UNIVERSITÉ DE LILLE (France)
&
UNIVERSITÉ DE M'SILA (Algérie)

UMR 9189 — Laboratoire Centre de recherche en informatique, signal et automatique de Lille.
Laboratoire de génie électrique-Faculté de technologie M'SILA

Thèse en cotutelle présentée pour le diplôme de doctorat

Par Mahdi Boukerdja

Discipline : Automatique et Informatique industrielle.

Sujet de thèse :

Commande avancée tolérante aux faute actives d'un système de microréseau DC, application à une plateforme de production d'hydrogène vert.

Date de soutenance : 02/11/2021 devant le jury composé de :

Rapporteurs

Mustapha HATTI	Maître de conférences HDR, Directeur de recherche, Unité de Développement des Équipements Solaires (UDES/CDER, Tipaza). Algérie
Nicolas HERAUD	Maître de conférences HDR, Université de Corse, France.

Président des jurys

Abderrahmen BOUGUERRA	Professeur, Université de M'Sila, Algérie.

Examinateurs

Anne-Lise GEHIN	Maître de conférences HDR, Université de Lille, France.
Zineb SIMEU-ABAZI	Professeure, Université de Grenoble Alpes, France.
Hafid HAFFAF	Professeur, Université d'Oran 1, Algérie.

Directeurs de thèse

Belkacem OULD BOUAMAMA	Professeur, Université de Lille, France.
Aissa CHOUDER	Professeur, Université de M'Sila, Algérie.

UNIVERSITY OF LILLE (France)
&
UNIVERSITY OF M'SILA (Algeria)

UMR 9189 — Laboratoire Centre de recherche en informatique, signal et automatique de Lille.
Laboratoire de génie électrique-Faculté de technologie M'SILA

Ph.D. thesis in cotutelle presented for the degree of Doctor of philosophy

By Mahdi Boukerdja

Academic Field: Automatique et Informatique industrielle.

Thesis subject:

Advanced active fault tolerant control of a DC microgrid system: application to a green hydrogen production platform.

Defense date: 02/11/2021. In front of the jury composed of:

Rapporteurs

Mustapha HATTI	Senior lecturer HDR, Research Director, Solar Equipment Development Unit (UDES/CDER, Tipaza), Algeria.
Nicolas HERAUD	Senior lecturer HDR, University of Corse, France.

President of jury

Abderrahmen BOUGUERRA	Professor, University of M'sila, Algeria.

Examiners

Anne-Lise GEHIN	Senior lecturer, University of Lille, France.
Zineb SIMEU-ABAZI	Professor, University of Grenoble Alpes, France.
Hafid HAFFAF	Professor, University of Oran 1, Algeria.

Supervisors

Belkacem OULD BOUAMAMA	Professor, University of Lille, France.
Aissa CHOUDER	Professor, University of M'Sila, Algeria.

Acknowledgment

This thesis work has been carried in cotutelle between the University of Lille and the University of M'sila. The thesis was funded by the ministry of higher education and research of Algeria, scholarship program profas B+, and European project E2C. I am grateful to the committee made by the collaboration between Algeria and France's higher education and research ministries related to Profas B+ scholarship program, where it put all its belief on me that I can achieve the objectives of the thesis and provided enough funding to perform this work. I am also grateful to both laboratories: **The electrical engineering laboratory of the M'sila University (LGE) and centre de recherche en informatique signale et automatique de Lille (CRIStAL).** They ensured the required equipment and a pleasant and supportive environment for my research.

My sincere gratitude goes to my supervisors **Professor Belkacem Ould Bouamama** of the University of Lille and **Professor Aissa Chouder** from the University of M'sila. I express my deep gratitude to them for their strong encouragement and guidance in completing this thesis. They put at my disposal all the tools and equipment available in the two laboratories **Cristal** and **LGE**, to realize this thesis. They trust me that I can add value to their research teams.

I also thank **Doctor Anne-Lise Gehin**, **Doctor Jean-Yves Dieulot**, and **Doctor Mathieu Bressel** for the opportunity to work with them and for their advice and strong encouragement.

I want to acknowledge **Professor Rochedi Merzouki**, the director of the **SoftE** team of CRIStAL laboratory, for the help he provided to me and for his permission to interact with his team members and use the equipment and tools of his team. I want to thank the members of the SoftE team: **Doctor Othman lakhal**, **Doctor Blaise Conrard**, **engineers Sepaldeep Singh Dhaliwal, Abdelkader Belarouci, Mouad Kahouadji,** and **Mario Sanz Lopez,** for the help and encouragement.

I also want to acknowledge **Professor Said Berkate** of the University of M'sila for his permission to interact with him and his helpful guidance to improve my English. Without forgetting to thank **Professeur Samir Zaghelache**, **Doctor Riad bouzidi**, **Doctor Smail Ghadeban**, **Doctor Ali djerioui**, **Doctor Riad Rouabhi**, **Doctor Abdelmalek Zorig**, **Doctor Issam Zorig,** and **Doctor Kenane Hadi** for the help that they provided to me.

Also, I want to thank all my friends from the CRIStAL laboratory: **Sumit Sood**, **Om Prakash**, **Rim Abdallah**, **Steeve Kamga Mbakop**, **Xinrui Yang**, **Naouel Daass**, **Bilal Daass, Balyogi**

Mohan Dash, Khoder Makkawi, **Manarshhjot Singh,** and all my friends of LGE laboratory: **Khalil Louassaa**, **Sidaali Ferahtia**, **Hafid Charefi,** and **Oussama Zagheba**.

I express all thanks to the jury committee: **Doctor Mustapha Hatti**, **Doctor Nicolas HERAUD**, **Professor Abderrahmen BOUGUERRA**, **Doctor Anne-lise Gehin**, **Professor Zineb Simeu-Abazi** and **Professor Hafid Haffaf** for giving their time to evaluate this thesis and I would like to thank them for their suggestion and advice to improve the work and enhance the manuscript.

I dedicate this thesis to my parents, **Khoudir boukerdja** and **Maissa Ghernoute**. Praying to God to protect them.

Abstract

Energy availability in DC microgrid is challenging due to the incremental negative impedance characteristic of constant power load and components faults, severely affecting the DC microgrid component. The negative incremental impedance and component faults decrease the damping factor of the DC microgrid component that yields an undamped oscillation in the electrical parameters (current and voltage). This undamped oscillation can damage the semiconductor components. Hence, the system stops operating, and the energy availability in DC microgrid will be lost. The thesis work proposes an advanced active fault tolerant control, applied to save energy availability from the loss by overcoming the instability issue due to the incremental negative impedance characteristic of constant power load and components faults. This active fault tolerant control consists of robust hierarchical control and online diagnosis. The robust hierarchical control consists of two levels of control: Primary and secondary control levels. They earn their robustness from two robust controllers performed based on the H_∞ norm: H_∞ and structured H_∞ based controls. The Golver Doyle and Nonsmooth optimization algorithms design these controllers using the augmented plants, deduced from the models of the DC/DC buck converter and parallel interconnection of DC microgrid components. These augmented plants include the weight functions that present the constraints of the optimization problem. The Golver Doyle and Nonsmooth optimization algorithms use these weight functions to obtain the robust controllers that will be implemented in the hierarchical control. Thanks to the robust online diagnosis that helps to reconfigure the robust hierarchical control is reconfigurable to mitigate components faults that severely affect the system. The robust online diagnosis consists of the analytical redundancy relations and generators of adaptive thresholds. The numerical evaluation of analytical redundancy relations gives the indicators of faults, comprised in the bounds limited by the adaptive thresholds when the faults do not occur. In the case of faults occurrence, the indicators of faults go outside the bound limited by the adaptive thresholds. Based on the fault isolation capability of the developed online diagnosis. The parameters variation caused due to faults can be estimated. The control reconfiguration process is implemented. It uses this estimation to reconfigure the control hierarchy by recalculating the H_∞ and structured H_∞ based controls. The developed technique effectiveness is validated using simulation and experimental studies.

Résumé :

La disponibilité de l'énergie dans le microréseau DC peut se perdre à cause de l'impédance négative incrémentale caractéristique de la charge à puissance constante et des défauts des composants, qui affectent gravement les composants du microréseau DC. L'impédance négative incrémentale et les défauts des composants diminuent le facteur d'amortissement des composants du microréseau DC, ce qui entraîne une oscillation non amortie des paramètres électriques (courant et tension). Cette oscillation non amortie peut endommager les composants semi-conducteurs. Par conséquent, le système cesse de fonctionner et la disponibilité de l'énergie dans le microréseau DC est perdue. Le travail de thèse propose une commande avancée tolérante aux défauts pour sauver la disponibilité d'énergie de la perte en surmontant le problème d'instabilité dû à la caractéristique d'impédance négative incrémentielle de la charge à puissance constante et des défauts des composants. Cette commande active tolérante aux fautes comprend un contrôle hiérarchique robuste et un diagnostic robuste en ligne. Le contrôle hiérarchique robuste se compose de deux niveaux de contrôle : les niveaux de contrôle primaire et secondaire. Ils obtiennent leur robustesse grâce à deux contrôleurs robustes basés sur la norme H∞ : le contrôleur H_∞ et le contrôleur H_∞ structuré. Les algorithmes d'optimisation de Golver Doyle et Nonsmooth conçoivent ces contrôleurs en utilisant les systèmes augmentés. Elles sont dérivées des modèles du convertisseur buck DC/DC et de l'interconnexion parallèle des composants microréseau DC. Ces systèmes augmentés comprennent les fonctions de pondération qui représentent les contraintes du problème d'optimisation. Les algorithmes d'optimisation de Glover Doyle et Nonsmooth utilisent ces fonctions de poids pour obtenir les contrôleurs qui assurent les performances souhaitées. La hiérarchie de contrôle robuste est reconfigurable avec l'aide du diagnostic en ligne robuste pour atténuer l'effet des défauts des composants qui affectent gravement le système. Le diagnostic en ligne robuste se compose des relations de redondance analytique et des générateurs de seuils adaptatifs. L'évaluation numérique des relations de redondance analytique donne les indicateurs de défauts. Ils sont compris dans les bornes limitées par les seuils adaptatifs lorsque les défauts ne se produisent pas. Dans le cas de l'apparition de défauts, les indicateurs de défauts sortent de la limite limitée par les seuils adaptatifs. Basé sur la capacité d'isolation des défauts du diagnostic en ligne développé. La variation des paramètres causée par les défauts peut être estimée. Le processus de reconfiguration du contrôle est mis en œuvre. Il utilise cette estimation pour reconfigurer la hiérarchie de contrôle en recalculant le contrôleur H_∞ et le contrôleur H_∞ structuré. L'efficacité de la technique développée est validée par une simulation et une étude expérimentale.

Acronyms

DC MG: DC microgrid.

CPL: Constant power load.

RES: Renewable energy sources.

GDOA: Golver Doyle optimization algorithm.

NOA: Nonsmooth optimization algorithm.

MPC: Model predictive control

SMC: Sliding mode control.

PBC: Passivity-based control.

BC: Backstepping control**.**

LFT: Linear fractional transformation.

BG: Bond graph.

FDI: fault detection and isolation.

ARR: analytical redundancy relation.

FTC: Fault-tolerant control.

List of figures

List of table

Contents

Introduction general

Context of the PhD

The work of this thesis is carried out under the collaboration between the PERSI (**https://www.cristal.univ-lille.fr/en/teams/persi/**) team of CRIStAL Laboratory University of Lille and CAGMOR (**https://www.univ-msila.dz/fr/?p=4863**) team of LGE Laboratory, University of M'sila. This collaboration between both laboratories aims to solve the research problems related to diagnosing and controlling the hybrid multi-source systems (HMS) for green hydrogen production. This complementary collaboration unifies the skills in the science of both teams, where the PERSI team focuses more on modeling the hybrid multiphysics systems. The models developed for such a system will be used for diagnosis (fault detection and isolation…….) and prognosis (remaining useful lifetime estimation). The head of PERSI team is Professor Belkacem Ould Bouamama. The CAGMOR team concentrates on enhancing the power converter architecture and developing novel control schemes for these power converters integrated into the Microgrid (MG) system. The head of the CAGMOR team is Doctor Smail Ghodbane.

The co-supervision thesis was officially started on 1 January 2020 under the supervision of Professors: Belkacem Ould Bouamama (University of Lille) and Professor Aissa Chouder (University of M'sila).

Research problem

DC Microgrid (MG) is such a power system developed to assist the utility grid in ensuring enough electrical energy for consumers. This power system integrates renewable energy sources (RESs) that do not harm the environment. For that, the application of DC MG in the industrial area is increasing. The DC MG can take a small size. Due to that, it can serve as an electrical supply for several loads such as the electric vehicle and aircraft [1–29]. The application of DC-MG could be more interesting if it is applied for green H_2 production. The use of H_2 fuel can improve the efficiency of DC-MG because the H_2 fuel is more effective than lead-acid batteries in storing surplus power. Also, this fuel can replace the transition line to transport the energy. In this case, the electrolyzer component produces the H_2 fuel using the electrical energy obtained from the RESs, and the produced H_2 fuel feeds the loads that must consist of the fuel cell. [30–31], for this reason, the DC-MG applied in green H_2 production takes the interest of thesis work.

The electrical power derived from the RESs is channeled from DC-MG electrical generators to the electrolyzer using a hierarchical control consisting of three control levels. Sometimes, a control equipping the electrolyzer lets this load consume constant power. In this case, the electrolyzer earns the incremental negative impedance (INI) characteristic of the constant power load (CPL). This INI is a perturbation destabilizing the system operation. The hierarchical control performed by using the conventional control cannot avoid the instability issue due to the INI of the CPL [45–70]. Besides the problem due to the presence of CPL, component faults can negatively affect the system in the same way as the presence of CPL in the system [71–97]. The INI and components faults decrease the damping factor of DC-MG components that let appearing an undamped oscillation in the electrical parameters (voltage and current). This undamped oscillation gives stress to the semiconductor elements of DC-MG. The DC-MG cannot operate, and the energy availability in DC-MG can be lost under these conditions [50,95].

Objectives of the thesis

In this thesis, an active fault-tolerant control (FTC) is developed, consisting of a robust online diagnosis and hierarchical control. This Active FTC is implemented in the DC-MG system to ensure energy availability, which can be lost due to instability arising from CPL and components faults. The robust hierarchical control increases the damping factor of the DC-MG in the presence of CPL. The developed robust hierarchical control consists of two levels of control: Primary and secondary control levels. The primary control level is implemented to ensure power-sharing among the DC-MG electrical generators.

On the other hand, the secondary control level is implemented to stabilize the DC-MG common bus's voltage and maintain the primary control's performance. The developed hierarchical control gets its robustness from two robust controllers: H_∞ and structured H_∞ based controllers integrated into the primary and secondary control levels, respectively. These controllers are performed using a design process consisting of Glover Doyle (GD) and Nonsmooth optimization algorithms. These algorithms require the augmented plants derived from the uncertain models of DC/DC converters and the parallel interconnection of DC-MG components. These augmented plants include the weight functions, which present the constraint of the optimization problem. The design process uses these weight functions to derive the required controllers.

Despite that, the developed hierarchical control increases the damping factor of DC-MG components sufficiently. A severe fault can decrease the damping of the system components operating under this robust hierarchical control. A robust online diagnosis is associated with the developed hierarchical control. It consists of the analytical redundancy relations (ARRs) and generators of adaptive thresholds, where numerical evaluations of ARRs are the fault indicators. These ARRs and generators of adaptive thresholds are derived from the model performed by linear fractional transformation bond graph (LFT-BG) modeling approach. This LFT-BG is a powerful tool for modeling the Hybrid multiphysics system as DC-MG and can include uncertainties and disturbances as part of the model. This robust online diagnosis minimizes the possibility of false alarms and detects and isolates the fault. Based on the developed online diagnosis. The change in the parameter that occurred due to faults can be estimated. This estimation reconfigures the hierarchical control by recalculating H_∞ and structured H_∞ based controllers to maintain the damping factor at the desired value to mitigate the effects of the severe faults.

Main contributions

The main contributions of the thesis are presented in the following points:

- The LFT-BG modeling approach is used to model the DC MG. This approach allows modeling the whole physics of the system and incorporating the uncertainties and disturbances.
- H_∞ and structured H_∞-based controls are proposed to improve the robustness of the DC MG control hierarchy. The improved control hierarchy maintains the stability of the system when the electrolyzer operates as CPL and mitigate the effect of components faults online diagnosis system developed using LFT-BG model of DC MG. This online diagnosis consists of the analytical redundancy relations, where their numerical evaluations are the signals of faults indicators called "residual signals." These residual signals are associated with the adaptive thresholds, which evolve with the parameters and measurement uncertainties and system inputs and outputs to minimize the false alarms.
- Active FTC is performed by the robust control hierarchy based on a robust online diagnosis layer. The possibility of the online diagnosis system to isolate the faults lets estimating the variation of DC-MG component parameters due to component faults. This estimation of parameters variation is used to reconfigure the robust control

hierarchy for corresponding to the actual state of the system. The reconfigured robust control hierarchy keeps the system performance at the acceptable one in the presence of the faults and maintains the stability of the DC MG.

- Online implementation of the fault-tolerant control system for complex green hydrogen system production.

Publications:

These results are presented in the following publications:

- **Peer-reviewed journals**
  1. **M. Boukerdja**, A. Chouder, L. Hassaine, B. Ould Bouamama, W. Issa, and K. Louassaa, "H∞ based control of a DC/DC buck converter feeding a constant power load in uncertain DC microgrid system," ISA Transactions, vol. 105, pp. 278–295, Oct. 2020.
  2. S. Sood, O. Prakash, **M. Boukerdja**, J.Y. Dieulot, B. Ould-Bouamama, M. Bresse l, and A.L. Gehin, "Generic Dynamical Model of PEM Electrolyzer under Intermit tent Sources," Energies, vol. 13, no. 24, p. 6556, Dec. 2020.
- **International conferences**
  1. **M. Boukerdja**, Y. Radi, O. Prakash, S. Sood, B. Ould-Bouamama, A. Chouder, A.L. Gehin, J.Y. Dieulot, M. Bressel, "LFT bond graph for online robust fault detection and isolation of hybrid multisource system," 2021 2nd International Conference on clean and green energy engineering, August 2021.
  2. **M. Boukerdja**, A. Chouder, and K. Louassaa, "Realizing the Accurate power-sharing in DC Microgrid Using Droop Control Strategy," 2019 International Conference on Advanced Electrical Engineering (ICAEE), Nov. 2019.
  3. O. Prakash, S. Sood, **M. Boukerdja**, B. Ould-Bouamama, J.-Y. Dieulot, A.-L. Ge hin, and M. Bressel, "A Model-based Prognosis approach to Proton Exchange Me mbrane Water Electrolysis System." European Control Conference (ECC), June. 2 021.
  4. S. Sood, O. Prakash, **M. Boukerdja,** B. Ould-Bouamama, J.Y. Dieulot, A.L. Gehin, and M. Bressel, "A Model-based diagnosis approach to Proton Exchange Membrane Water Electrolysis System." European Control Conference (ECC), June. 2021.

Two other publications are under preparation for submission, which will show the other results regarding the online application of fault-tolerant control.

Organization of thesis manuscript

The manuscript is organized as follows:

- **Chapter 1** presents an overview of the DC-MG system and its available architectures. This chapter also explains in detail the loss of energy availability due to the INI characteristics of CPL and components faults.
- **Chapter 2** presents the process to design the H_∞ based control used for output voltage regulation of the DC/DC buck converter. The H_∞ based control is derived from the Golver Doyle (DG) optimization algorithm. It aims to ensure the robustness of the DC/DC buck converter against perturbations arising from INI characteristics of CPL and the occurrence of component faults. The simulation study is carried out using Psim software to validate the proposed approach.
- **Chapter 3** explains in detail the use of GD and Nonsmooth optimization algorithms to perform a robust control hierarchy, which consists of two levels of control: Primary and secondary control levels. The H_∞ based controller resulting from the GD optimization algorithm is implemented in the primary control. The Nonsmooth optimization algorithm provided a structured H_∞ based controller, implemented in the secondary control level. This developed control hierarchy is validated by a simulation study performed in PSIM software.
- **Chapter 4** presents the development of a robust online diagnosis based on the LFT BG model of DC-MG. It defines the LFT-BG modeling approach, the different elements that the LFT-BG modeling approach uses to model the DC-MG components. The robust online diagnosis consists of the ARRs and generators of adaptive thresholds derived from the LFT-BG model of DC-MG performed under derivative causality. Based on the derived ARRs, the developed online diagnosis estimates the variations of the parameters caused by the components' faults. A process will use these estimations to reconfigure the control hierarchy to mitigate the effect of a severe fault.
- **Chapter 5** presents the experimental validation of the Active FTC elements (robust control hierarchy and online diagnosis) to verify their performances under several scenarios.

Chapter 1: State of the art

1.1. Introduction

Most industries and residential houses require the electrical power to operate their devices. This electrical power has been previously produced using generators based on non-renewable fuels such as natural gas and crude oil. These generators are good enough to satisfy the need for electrical energy. However, they cause the emission of greenhouse gases that harm the environment. Developing semiconductor switches and electronic devices yield new electrical generators based on renewable energy sources such as photovoltaic and wind turbine generators. These generators satisfy environmental protection requirements but do not sufficiently satisfy the need for electrical if they operate separately. The efficiency problem of this new kind of generator is solved by gathering all these generators in a single system. This way gives birth to a Microgrid (MG) system [32–39].

This chapter gives a review of the different architectures of MG system. Based on that, the choice to study the DC MG is justified. The hierarchical control has also been defined, which consists of three levels of control: Primary, secondary, and tertiary control levels, where the DC-MG operates under this hierarchical control to ensure a power flow needed to feed the load. The energy availability is not always ensured due to the current circulating and instability problem due to the incremental negative impedance (INI) characteristic of constant power load (CPL) and component (parametric) faults. The hierarchical has already avoided the current circulating. The instability due to the INI characteristic of CPL and component faults presents the worst issue that DC MG meets. Hence, this chapter explores in detail how the presence of CPL and component fault destabilize the system. Moreover, this chapter details the approaches used to improve the system robustness for the stable operation and their drawbacks. Based on these drawbacks, the work of this thesis will be justified.

1.2. Microgrid definition

The MG is a parallel connection of electrical generators integrating renewable energy sources to feed the local loads. This parallel connection can have AC or DC common bus. The power converters are implemented in such a system to control the power flow between the electrical generators and the local loads, which can take several forms. For instance, the local load can be the residential houses or chargers for the electric cars, as illustrated in Fig 1.2. Usually. These local loads require a stable production of the electrical power from the electrical generators to have the nominal operating conditions. But the MG cannot fill this requirement due to the intermittency of renewable energy sources (RESs) [37].

Hence, the storage device is incorporated in MG to deal with this unstable electrical production due to the intermittency of RES. This storage device stores the power surplus produced by the electrical generator, which is not consumed by the local loads. When the electrical generators cannot satisfy the power demand of the local loads, the storage devices will compensate for this power deficiency by the surplus of power already stored in the storage device [39,40].

In some cases, the storage device cannot be enough to store the surplus of power and compensate for the power deficiency. The MG may operate in connection with the utility grid to solve this problem. This connection helps to provide a surplus of power when the storage device is fully charged. Also, the utility grid's connection helps the MG get the power from the utility grid to compensate for the power deficiency. This method will be used when the storage device is fully or partially discharged and cannot compensate for this power deficiency [42–44].

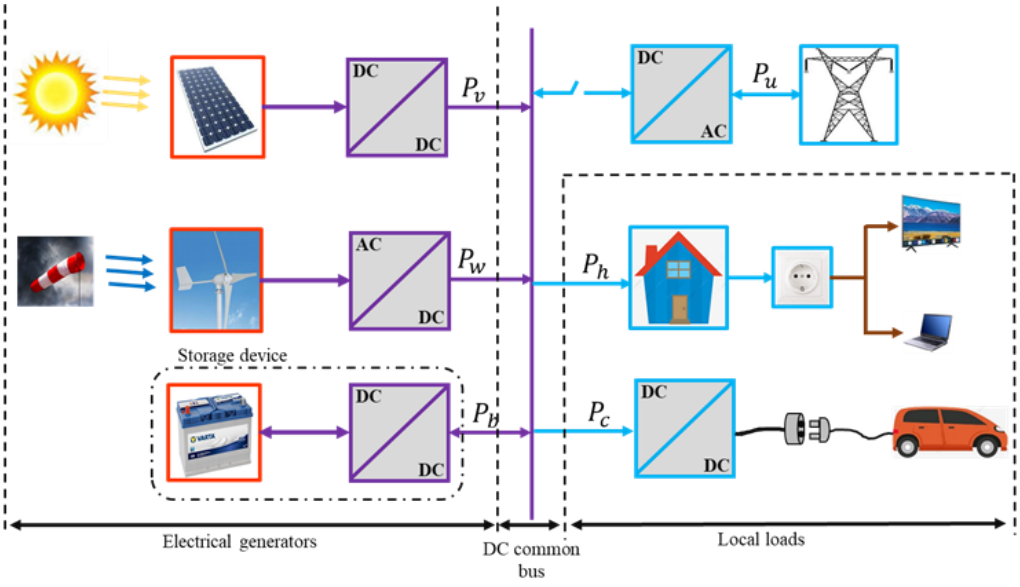

Fig 1.1. Microgrid system illustration.

However, this surplus power can be converted as a non-pollutant fuel, which can be again converted to electrical power. This fuel presents a method to store this surplus of power and has fewer disadvantages than batteries. In this case, the size of MG does not increase, and the use of this H_2 fuel facilitates the task of storing the power surplus. For that, the technology of the electrolyzer is involved in this task. The electrolyzer is considered as a converter that converts the electrical energy to green H_2 gas fuel stored in the metallic cylinders [30–31]. It uses electricity to decompose the molecules of H_2O into the O_2 and H_2 gases. When power is deficient in the system, the fuel cell compensates for the power deficiency by using the H_2

stored in metallic cylinders to produce the electrical power injected into the common DC bus, as illustrated in Fig 1.2.

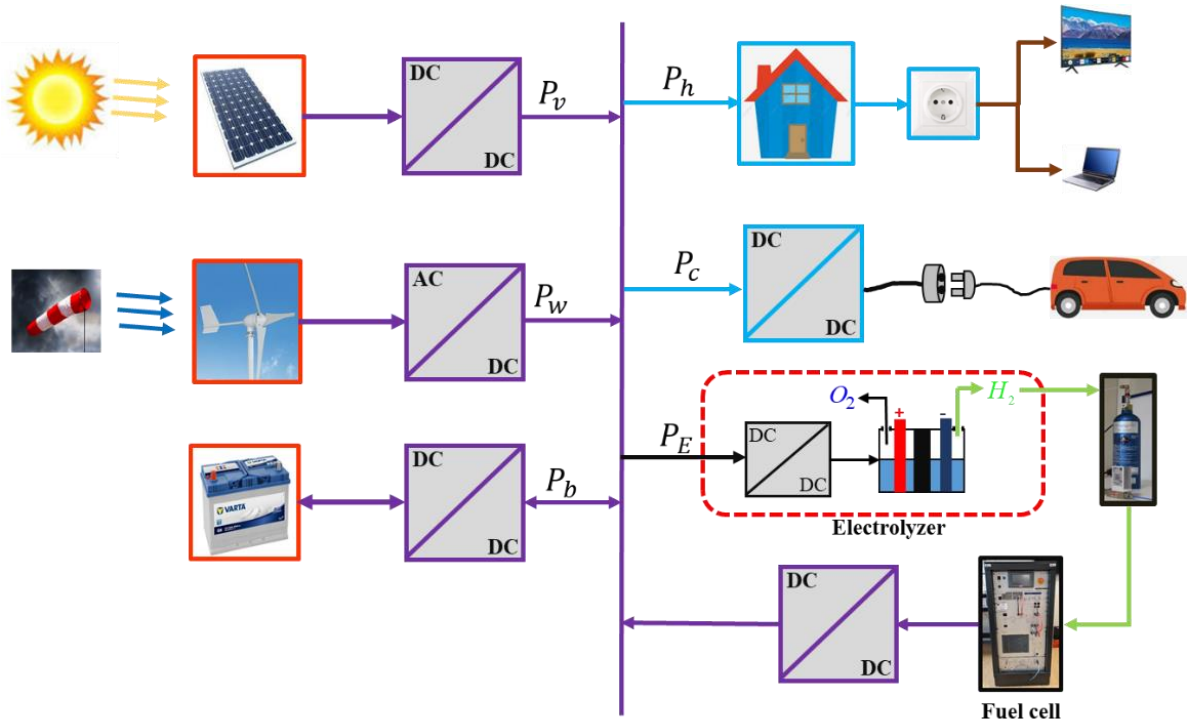

Fig 1. 2. Incorporating the electrolyzer and fuel cell in Microgrid to store the power surplus and compensate for this power deficiency.

1.2.1. Microgrid architectures

The MG architecture depends on the main components of MG: the electrical generators, storage devices, and local loads that can be controlled or not controlled. The nature of these MG components provides three types of MG architecture. These architectures are alternative current MG (AC MG), direct current MG (DC MG), and hybrid alternative current/direct current MG (Hybrid AC/DC MG) [32]. The AC MG architecture was historically the most widely employed since the electrical generators that provided AC form power were the most widely available. The AC MG is made up of the parallel connectivity of these electrical generators that provide AC power and are connected to a common AC-bus [33–35], as shown in Fig 1.3.

Electronic components' development in power conversion yields the electrical generators providing the DC form's power. The interconnection of these electrical generators in the common bus gives DC MG architecture, as illustrated in Fig 1.4, where the DC MG connection to the utility is performed through DC/AC converter [1–8].

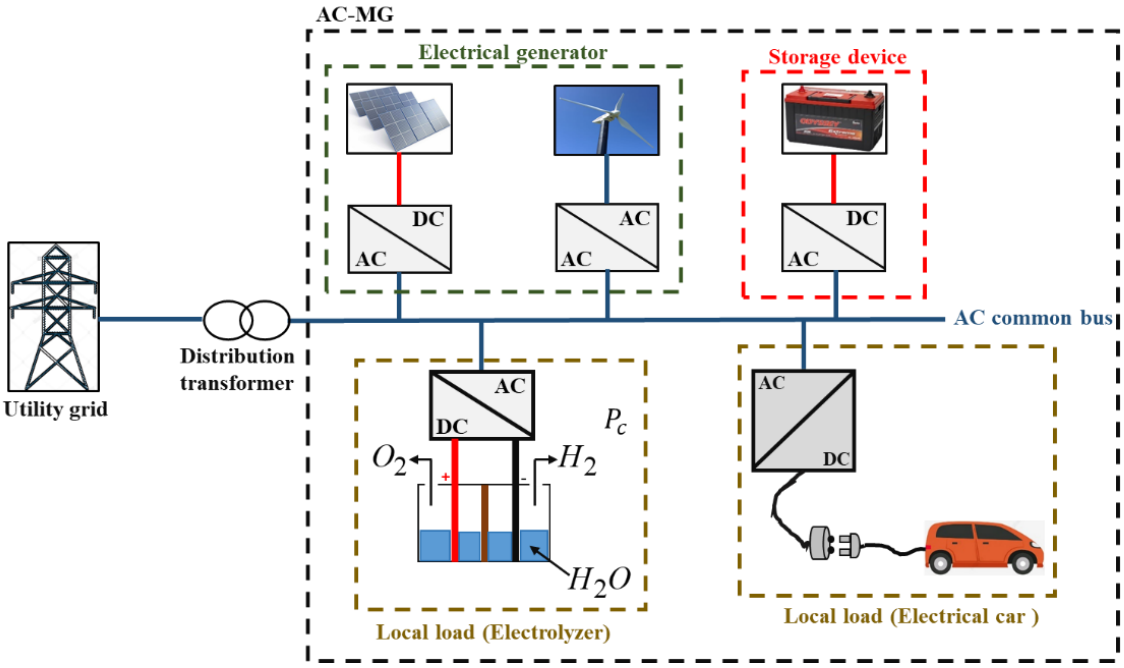

Fig 1.3. AC Microgrid architecture.

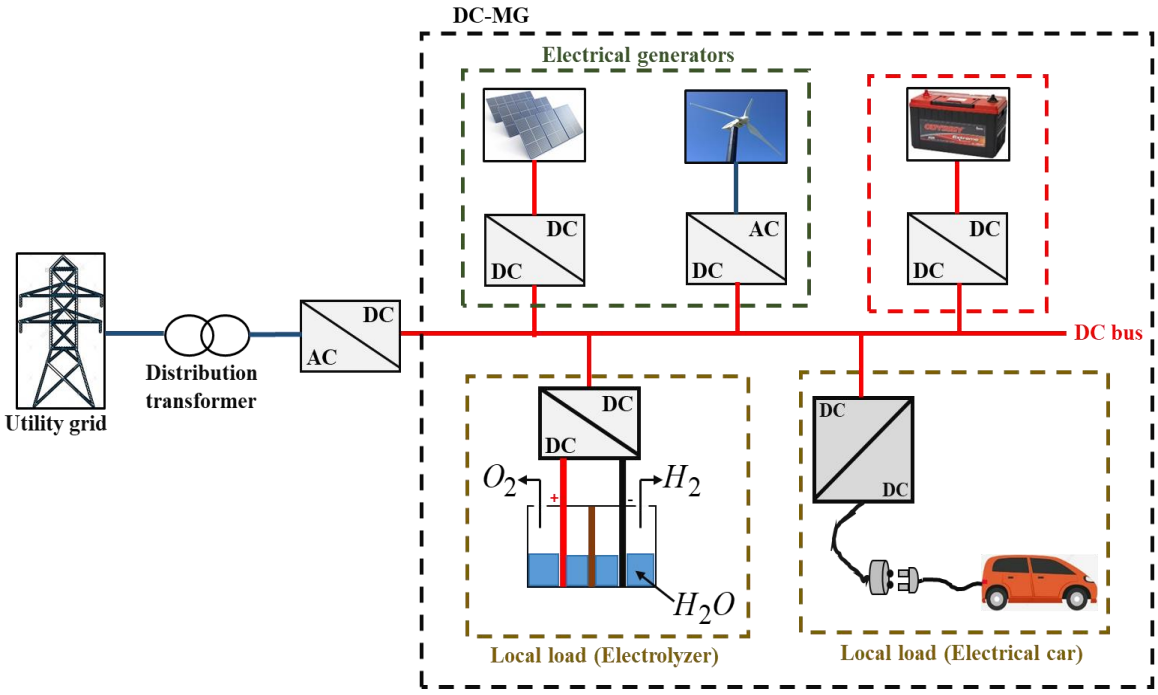

Fig 1.4. DC Microgrid architecture.

Hybrid AC/DC MG architecture incorporates both architectures: DC MG and AC MG, as illustrated in Fig 1.5, where the bidirectional AC/DC converter is used to connect the AC bus to the DC bus and transfers the power between AC MG and DC MG parts [12, 36–38].

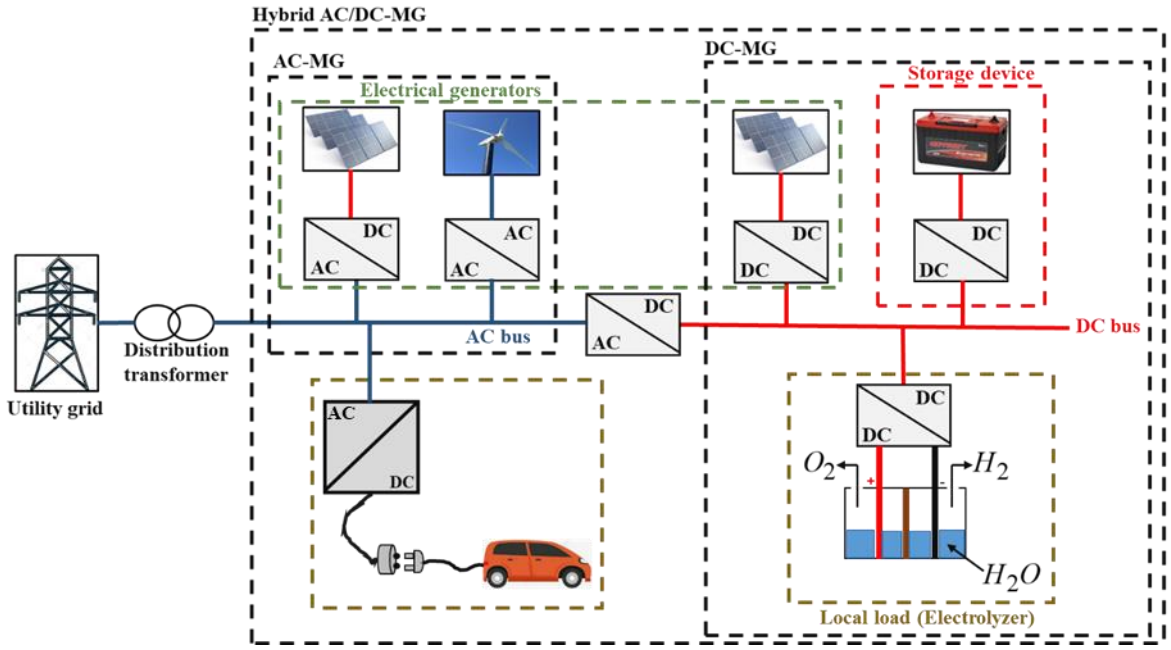

Fig 1.5. Hybrid AC/DC Microgrid architecture.

1.2.2. Why is DC Microgrid more preferred than the other architectures?

AC MG was the first adopted solution because all electrical generators were in AC form. However, the DC MG has more advantages compared to AC MG [42]. In terms of the power conversion stage, the architecture of DC-MG involves fewer power converters than AC MG. This advantage decreases the MG's size, making it more cost-effective and improving efficiency [12 16, 38]. Both MG architectures (AC MG and DC MG) require a power management control system. Incorporating this power management control system in DC MG is less complicated than AC MG architecture because voltage stabilization is only needed [25]. In contrast, AC-MG architecture has to deal with frequency stabilization [33–38].

Moreover, the absence of reactive power in DC MG lets DC MG become more efficient and reliable than AC MG. DC MG transmits only the active power in its lines that allows decreasing the size of the transmission lines. Contrary to AC MG architecture, it has to consider the reactive power. Besides, harmonic current issues due to the nonlinear loads do not arise in DC-MG architecture. Therefore, contrary to AC MG, there is no increase in power loss in the transmission lines due to the nonlinear loads that greatly increase the efficiency and reliability of DC MG compared to AC MG [20].

1.2.3. Hierarchical control of DC Microgrid

In DC MG, the electrical power produced by the electrical generators feeds the load component through the parallel interconnection of these components. This parallel interconnection faces the problem of current circulating, which is illustrated in Fig 1.6. It appears due to the different

magnitudes of the electrical generators output voltages ($v_1 < v_2$ or $v_1 > v_2$) and the difference between the transmission lines impedance. This current circulating causes several issues in the electrical generators, like the stress and damage of the semiconductor components and the impossibility to control the power flow, which must have this direction: from the electrical generators to the load [39, 44].

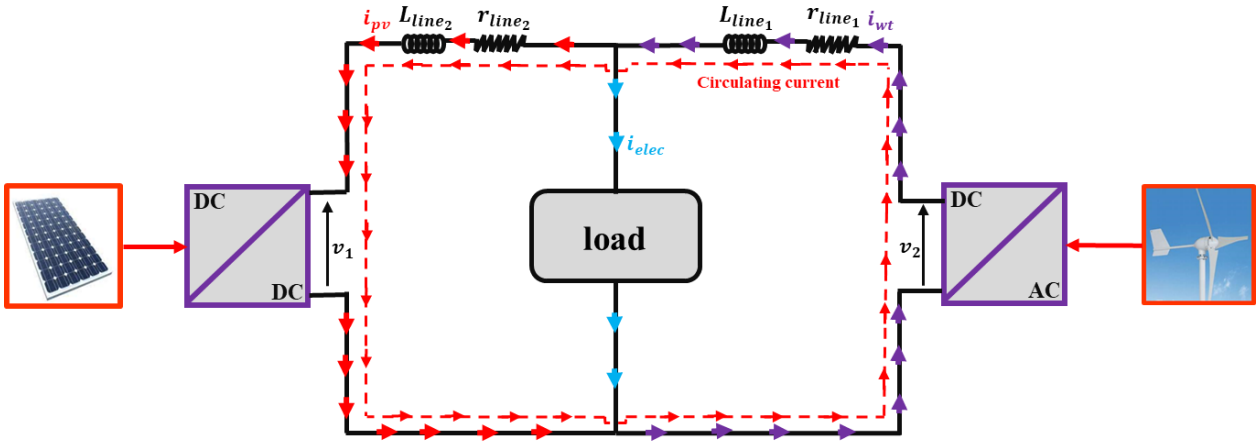

Fig 1.6. Current circulating problem in DC Microgrid.

Dealing with this problem requires: the common DC bus voltage must be maintained constant at the nominal value, and the output voltages of the electrical generators must be the same. In the case of the DC power injected in the common bus, these requirements are achieved when the DC MG operates under the hierarchical control consisting of three levels of control: primary, secondary, tertiary controls, illustrated in Fig 1.7. This hierarchical control is needed to keep the electrical parameters of the parallel connection of electrical generators at the nominal values and control the power flow between the electrical generators and electrolyzer, where the primary control is implemented to maintain the output voltages of the electrical generators at the same magnitude and control the flow of power, the secondary control is implemented to stabilize the voltage of the common DC bus to be kept at the nominal value, and the tertiary control is implemented to control the power flow between the utility grid and DC MG. This hierarchical control is also needed to apply the power management techniques to operate the DC-MG according to its optimal operating modes to ensure energy availability [44].

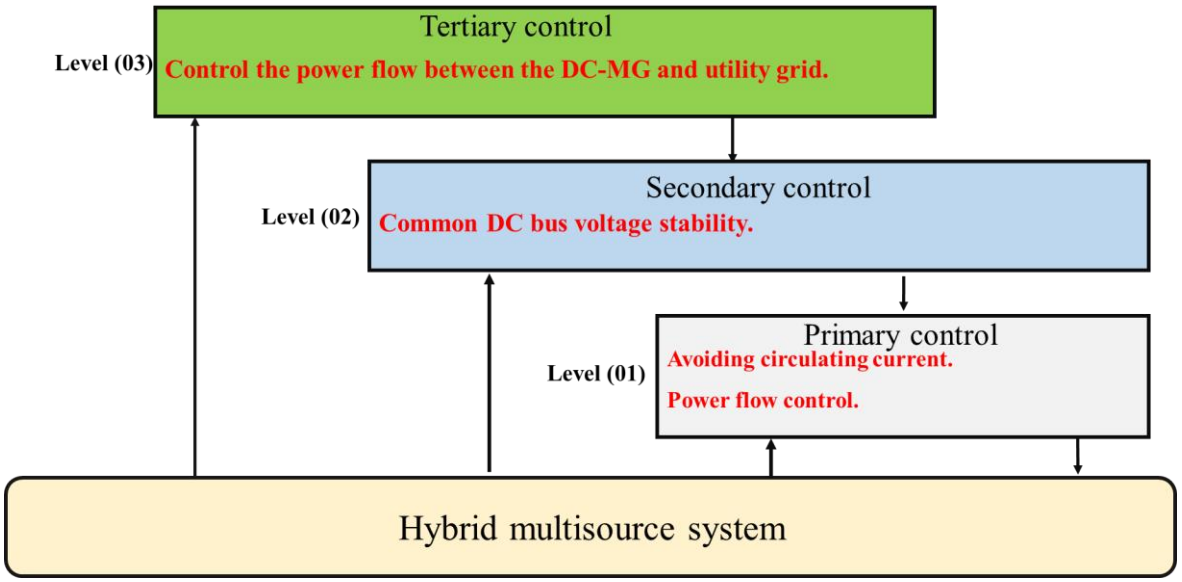

Fig 1.7. hierarchical control.

1.2.3.1. Primary Control

Primary control is the first level of hierarchical control, consisting of a set of decentralized controllers. Each decentralized controller is related to each electrical generator. All these decentralized controllers are implemented to control the direction of the power flow and avoid the current circulating problem [1, 6, 16, 23, 39].

Fig 1.8 shows one of the decentralized controllers' schemes incorporated in the primary control level. The droop control is implemented to mitigate the current circulating issue by introducing the virtual impedance R_v. This virtual impedance allows drooping the output voltage of electrical generators, as v_1, from the nominal voltage v^*, to force the electrical generators to provide the output current, as i_1 in the way that the power flow will be maintained, as illustrated in Fig 1.8 [1].

Voltage cascade control is implemented to ensure the power converter's stability and regulate the voltage and current simultaneously [6]. It receives the voltage reference from droop control, which can be written as follows:

$$v_{ref} = v^* - R_v \cdot i_1 \tag{1.1}$$

Voltage cascade control consists of two loops: Outer and inner loops. The outer loop's voltage control provides the current reference to the inner loop by exploiting the error resulting from the difference between v_{ref} and v_1 $\left(e = v_{ref} - v_1\right)$. The inner loop's current control exploits the

error resulting from $e = i_{ref} - i_1$ to provide the control law, converted to pulse width modular (PWM) signal through PWM block to operate the power converter.

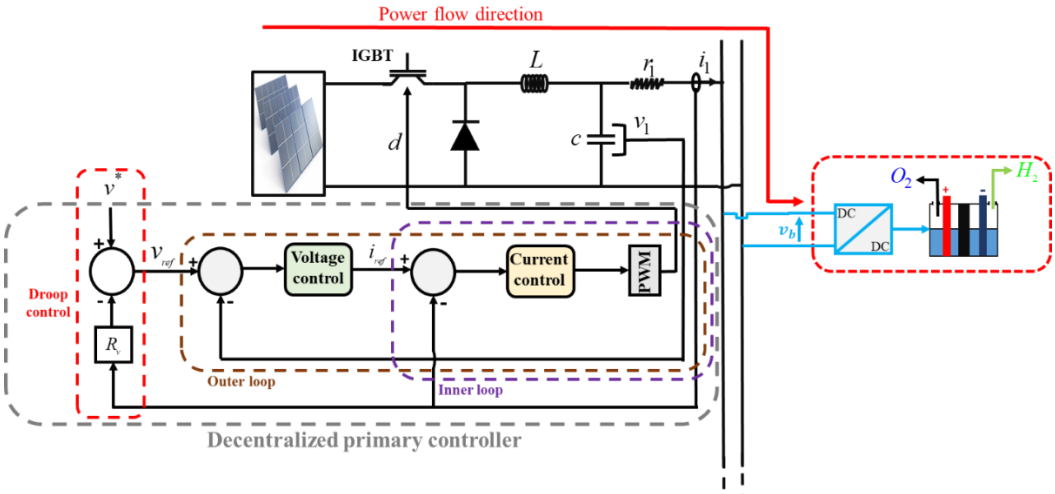

Fig 1.8. Decentralized primary controller scheme.

1.2.3.2. Secondary control

The primary control lets the common DC bus voltage v_b drops continuously by the increase of the output current i_1, which is consumed by the electrolyzer [39]. This continuous deviation of v_b imposes problems in the parallel connection of DC MG electrical generators as the electrolyzer may stop operating if v_b is very low, which prevents the power converter of the electrolyzer to ensure the power for green H_2 production. Therefore, the secondary control level is implemented to stabilize v_b at the nominal value v^*. This control allows avoiding the deviation of v_b without deteriorating the primary control performances [40].

The secondary control scheme has two configurations: Centralized and decentralized secondary control schemes. The centralized secondary control scheme consists of a unique controller, which generates the compensation voltage signal Δv to all decentralized primary controllers based on the error between v_b and v^*: $e = v^* - v_b$, as illustrated in Fig 1.9. This configuration of the decentralized secondary control has some limitations, such as it is easy to suffer from signal-point failures. Also, it cannot satisfy the play and plug requirements [41].

The decentralized secondary control scheme is developed to overcome the limitations of the centralized secondary control scheme. It consists of decentralized controllers, as illustrated in Fig 1.10, where each decentralized controller is related to each decentralized primary controller, and all these decentralized controllers generate the same compensation voltage

signal ($\Delta v_1 = \Delta v_2 = ... = \Delta v_t$). In this configuration, the communication network is required to exchange information regarding the common DC bus. In this decentralized secondary control, only one decentralized secondary controller has to measure v_b, and the other decentralized secondary controllers provide Δv based on the information regarding the common DC bus provided by the communication network [100].

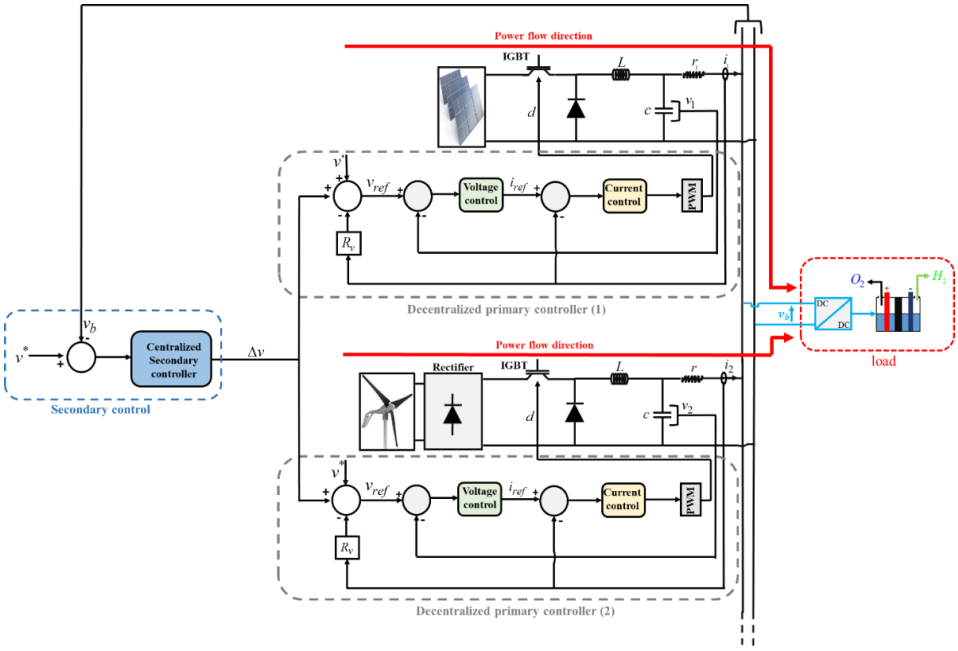

Fig 1.9. Centralized secondary control scheme.

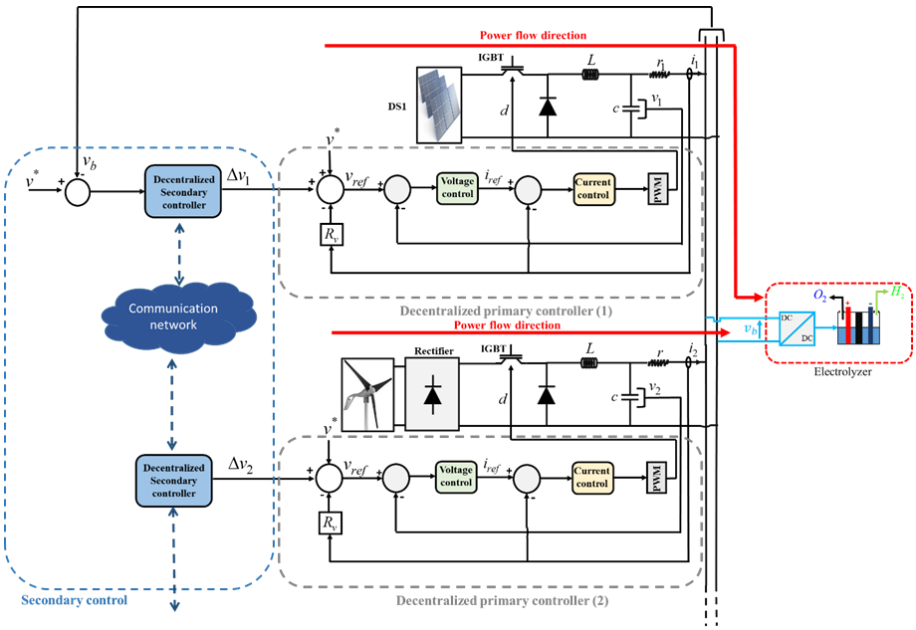

Fig 1.10. Decentralized secondary control scheme.

1.2.3.3.Tertiary control

The tertiary control is the third level of the DC MG hierarchical control. This control level is implemented when the DC MG is connected to the DC source or the utility grid through the distribution transformer and AC/DC power converter, representing a stiff DC grid, as illustrated in Fig 1.11. It controls the power flow between the stiff DC grid and DC MG. This control level is carried out by providing the voltage reference to the secondary control by exploiting the error $e = i_{G_{ref}} - i_G$ measured from the bypass switch [27].

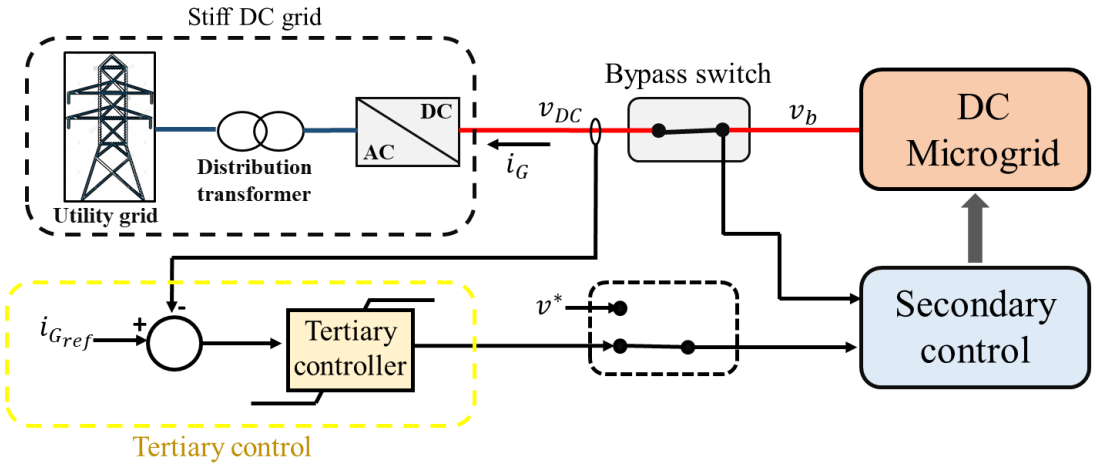

Fig 1.11. Tertiary control scheme.

1.3. DC Microgrid challenges

The DC MG faces the energy availability loss problem due to:

- Difficulty to control the power flow due to the power sharing imbalance and circulating current.
- DC MG operation loss due to the instability problem caused by the CPL and component faults.

The hierarchical control enables the system to avoid the current circulating [40]. The instability problem due to CPL and component faults is more worst issue. For this reason, it has taken the most interest of thesis work.

1.3.1. Instability issue due to constant power load

The DC MG can feed two types of local load: not controlled and controlled ones. A control equips these controlled loads to ensure certain operations conditions [28, 29]. In this case, usually, this controlled local load requires constant consumption of power. Then, it will behave as the CPL. The CPL has an "incremental negative impedance characteristic (INI)," which

causes the MG instability. Under this problem, the MG loses its nominal operating conditions [45–60].

The hierarchical control based on conventional techniques can't sufficiently increase the damping factor of DC MG components. The performance of the hierarchical control becomes mediocre due to the complexity and nonlinearity of DC MG, and the different physics included in DC MG generate several disturbances, which can also deteriorate the DC MG instability performance.

To understand the instability issue due to CPL, Fig 1.12 considers an example of a photovoltaic panel feeding the electrolyzer through DC/DC converters, where the DC/DC converter 1 receives the control signal from the hydrogen flow rate controller to fix the flow rate of the produced H_2 at the desired flow rate value. In this example, the part that gathers the DC/DC buck converter and electrolyzer behaves as the CPL. The DC/DC buck converter is implemented to control the power flow needed to run the electrolyzer.

By neglecting the power loss in the DC/DC buck converter, the electrolyzer consumes a power that can be described as follows:

$$P_{CPL} = v \cdot i = i_E \cdot v_E = c \tag{1.2}$$

where c is a constant value.

R_{CPL} denotes the INI characteristic of CPL. It can be written as follows [49]:

$$R_{CPL} = \frac{dv}{di} = -\frac{v}{i} = \frac{v^2}{P_{CPL}} \tag{1.3}$$

According to (1.2) and (1.3), the $v-i$ characteristic can describe the CPL behavior, as shown in Fig 1.13. This $v-i$ characteristic shows that the CPL current i decreases /increases by the increase/ decrease of the CPL terminal voltage v. R_{CPL} represents the tangential slope of the operating point [49].

The poles evolution, frequency, and phase-portrait analysis are depicted in Fig 1.14, Fig 1.15, and Fig 1.16, respectively, carried out on the example presented in Fig 1.12. These analyses require the dynamic model of a photovoltaic system, consisting of the photovoltaic panel and DC/DC buck converter. The following differential equations can represent this model:

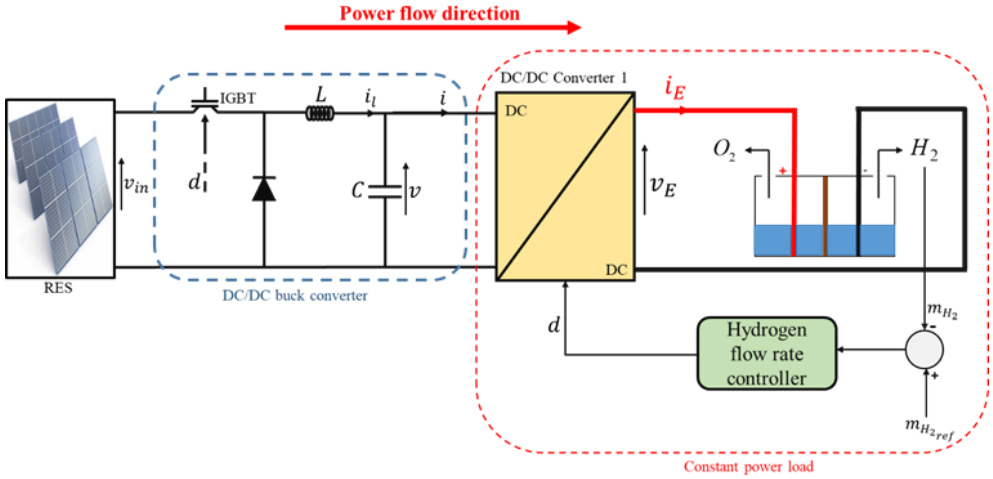

Fig 1.12. Example of a photovoltaic system feeding the electrolyzer.

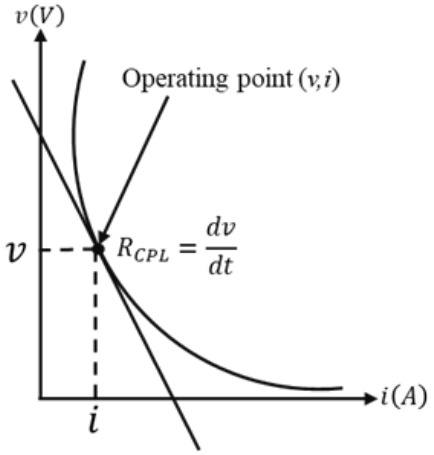

Fig 1.13. v-i characteristic of CPL.

$$\begin{cases} \dot{i}_L = \dfrac{v_{in}d}{L} - \dfrac{v}{L} \\ \dot{v} = \dfrac{i_L}{C} - \dfrac{P_{CPL}}{Cv} = \dfrac{i_L}{C} - \dfrac{v}{CR_{CPL}} \end{cases} \tag{1.4}$$

Phase portrait analysis is performed by using the model given in (1.4). But the Pole evolution and frequency analysis are carried out by using the transfer function obtained from the linearization of (1.5) around the operating point (v, i), which can be written as follows:

$$H(s) = \frac{v(s)}{d(s)} \frac{\dfrac{V_{in}}{LC}}{s^2 - \dfrac{P_{CPL}}{CV^2}s + \dfrac{1}{LC}} = \frac{\dfrac{V_{in}}{LC}}{s^2 + \dfrac{1}{CR'_{CPL}}s + \dfrac{1}{LC}} \tag{1.5}$$

where i_L is the inductance current, v_{in} is the input voltage, V_{in} is the nominal value of v_{in}, V is the nominal value of v, and R'_{CPL} is equal to $-P_{CPL}/V^2$. Pole evolution and frequency analysis are

performed by varying the P_{CPL} from 0 W to 100 W. On the other hand, phase portrait is carried out contrary to Pole evolution and frequency analysis. Under phase portrait analysis, P_{CPL} is kept at 100 W.

According to pole evolution analysis, the system poles lie on the right half zero-pole plan (RHP) due to the INI characteristic, where RHP presents the unstable region. The pole evolution analysis shows that the INI characteristic deteriorates the system stability performance. The frequency analysis also confirms what is seen in the pole evolution analysis. According to Fig 1.15, the system has a phase lower than $-\pi$ on all frequencies. That shows that the output voltage v has undamped oscillations due to the INI characteristic and doesn't converge to the steady state.

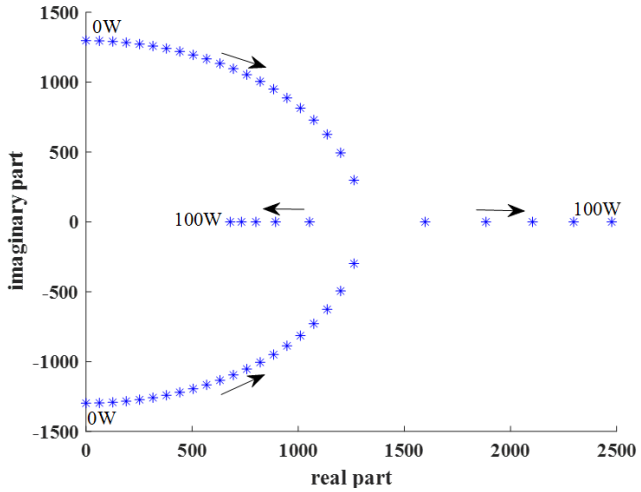

Fig 1.14. Pole evolution analysis carried out on the example presented in Fig 1.12.

Pole evolution and frequency analysis based on the linearized model clarify the CPL problem only around an operating point. This way may decrease the integrity of pole evolution and frequency analysis. For that, phase portrait is achieved to strengthen the pole evolution and frequency analysis. According to Fig 1.16, the system has an instability problem when the electrolyzer behaves as the CPL. Because the trajectory obtained under phase-portrait analysis doesn't converge to the equilibrium point. Moreover, the obtained trajectory forms several spiral cycles during the time, which shows that INI characteristic gives the not-damped oscillation during photovoltaic system operation.

In the case of the DC MG, the discussed issue will be worse than the system presented in Fig 1.12 due to the multiphysics and nonlinearity of DC MG. In these conditions, the system will lose its operation, and the energy availability will be lost. Hence, the seriousness of this problem let the work of the thesis interested in it.

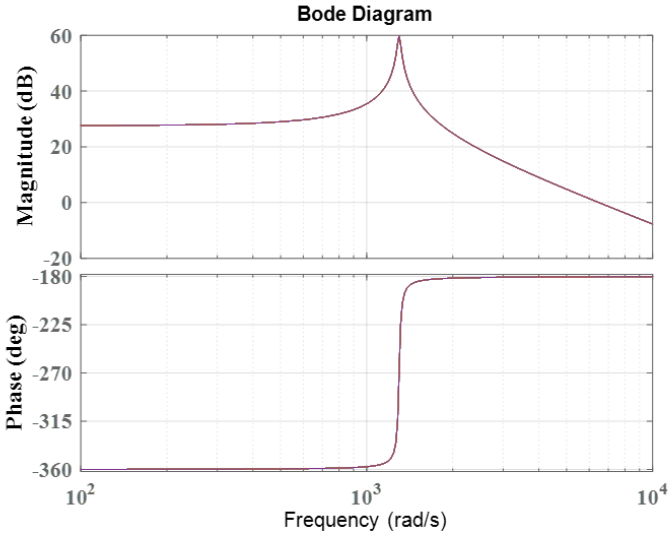

Fig 1.15. Frequency analysis carried out on the example presented in Fig 1.12.

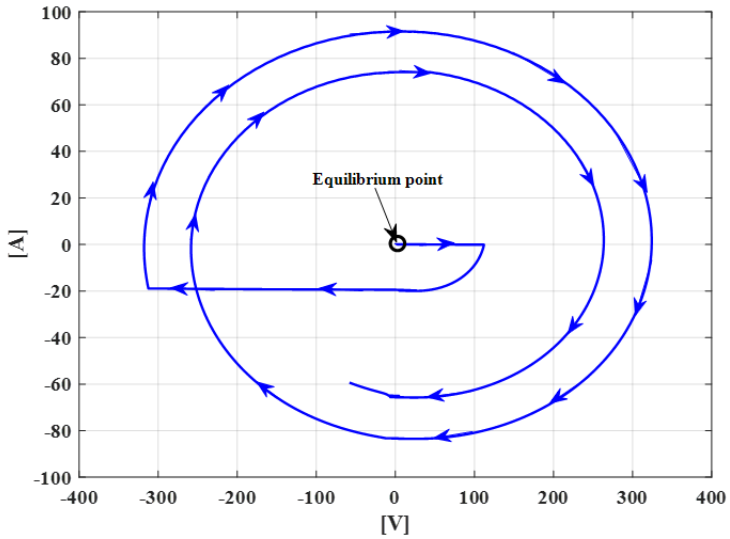

Fig 1.16. Phase portrait carried out on the example presented in Fig 1.12.

1.3.2. Instability issue due to components faults.

The component faults occur due to the disturbances, which let the system components degrade. These faults can deteriorate the stability performance of DC MG because they can decrease the damping factor of the DC MG components [72–87]. We consider the same example presented in Fig 1.12 modeled by (1.5) to understand this aforementioned issue. According to (1.5), the damping factor of the system can be written as follows:

$$\zeta = \frac{1}{CR'_{CPL}}\sqrt{\frac{1}{LC}} \tag{1.6}$$

Assuming that the control is applied for this system to mitigate the instability due to CPL. This controller aims to increase the system damping factor, which must be greater than 1. Therefore, the damping factor after applying this controller can be written as follows:

$$\zeta' = \varphi + \frac{1}{CR'_{CPL}}\sqrt{\frac{1}{LC}} \tag{1.7}$$

where φ is provided by the control to increase the damping factor of the system.

We assume that a component fault occurs in the DC/DC buck converter inductance that lets the value of L decreases or increases during the time. Due to this fault, a random variation can affect the damping factor of the system ξ', as illustrated in Fig 1.17. The random variation of ξ' deteriorates the system stability. When ξ' is lower than 1, the overshoots and oscillations appear in the electrical parameters of the system. The system loses completely its stability when ξ' goes down to 0. This system instability shows up in the undamped oscillation of the electrical parameters.

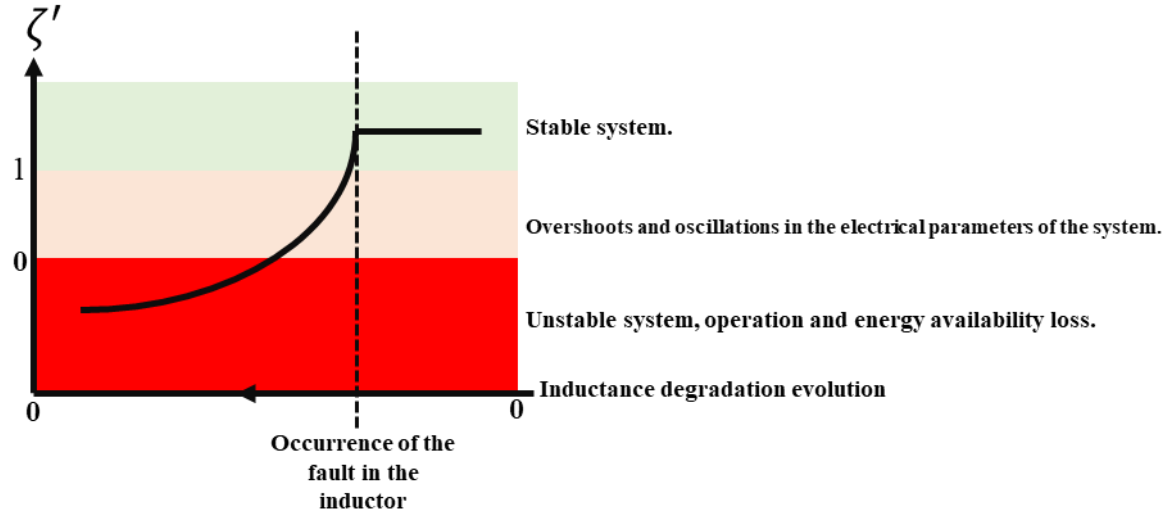

Fig 1.17. Evolution of system damping factor in the presence of component faults.

1.3. Active fault tolerant control of DC Microgrid.

Ensuring the energy availability in DC MG requires a robust hierarchical control to keep the system operating in stable and nominal conditions and avoid the negative impact of the INI characteristic and component faults [49,85]. In the case of this study, the robust hierarchical control consists only of the primary and secondary control levels. The primary and secondary control levels are performed based on the advanced robust control technique. This advanced robust control aims to increase the damping factor of DC MG components to compensate for

the INI characteristic and component fault effects [28–29]. Severe faults can decrease the damping factor despite the hierarchical control integrating the robust control. The hierarchical control must be reconfigured to keep the damping factor at the desired value. The robust online diagnosis is associated with the robust hierarchical control, as illustrated in Fig 1.18, to reconfigure the robust hierarchical control. This robust online diagnosis must have the ability to detect and isolate faults and the ability to minimize the possibility of false alarms. Based on this online diagnosis, the variation of the parameter that is occurred due to the fault can be estimated. The reconfiguration process will use this estimation to recalculate the parameters of the robust controls integrated into the primary and secondary control levels [76–80].

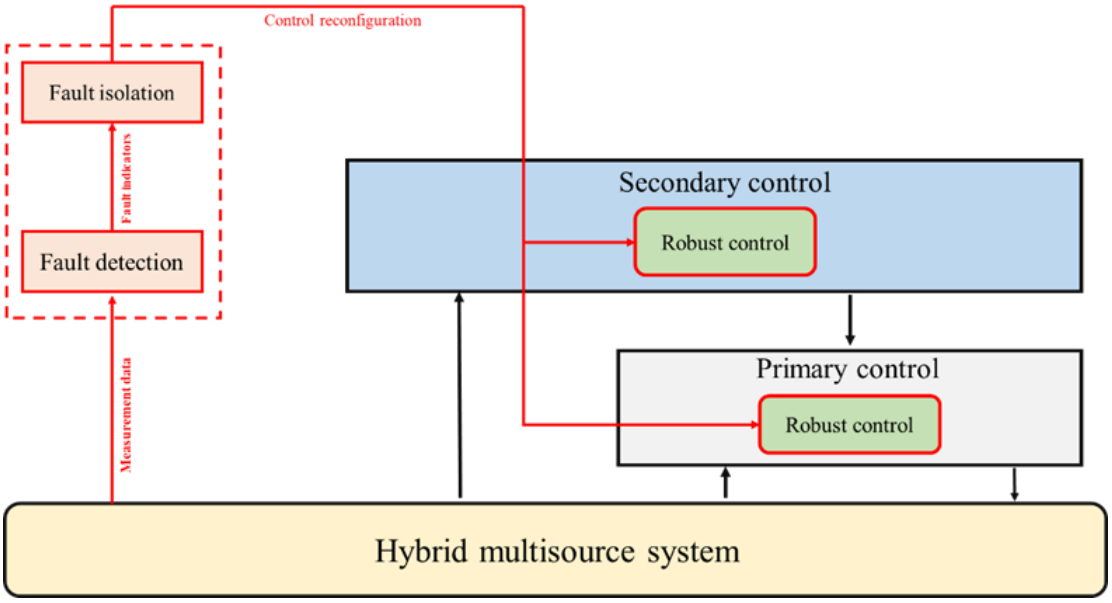

Fig 1.18. Reconfiguration of robust hierarchical control by using the robust online diagnosis.

This robust and reconfigurable hierarchical control comes under active fault tolerant control (FTC). The following sections review the control and diagnosis methods used to perform Active FTC.

1.4.1. Robust control techniques used to overcome faults and CPL issues.

Because of the nonlinearity of the power converters, the conventional controls cannot deal with the instability problem due to CPL and component faults [28, 29, 46, 47, 52, 58]. For that, several methods are proposed to solve the aforementioned issue. Among them: Passive damping, Active damping, and Nonlinear controls such as Sliding mode control, Model predictive control, Backstepping control, and Passivity-based control [45–47, 49–51, 53–60].

1.4.1.1. Passive damping

Passive damping is a simple approach to increase the damping factor of the DC MGs by adding the passive elements to the input filter of the power converters, as mentioned in [45–47]. This

approach can be divided into three methods: RC parallel damping, RL parallel damping, and RL series damping, as illustrated in Fig 1.19a, Fig 1.19b, and Fig 1.19c, respectively.

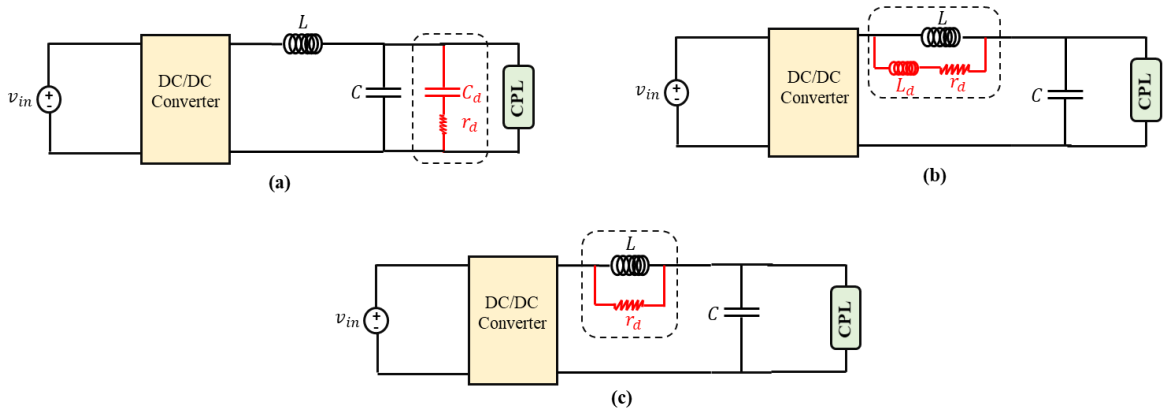

Fig 1.19. Passive damping technique: a) RC parallel damping, b) RL parallel damping, c) RL series damping.

The passive damping approach is simple to implement. It does not require the addition of any control terms to the control loop of the power converter. By using this method, the stability of DC MG is ensured. But the system efficiency is decreased due to the power loss caused by the passive elements.

1.4.1.2. Active damping

Active damping is another solution to overcome the instability problem. This approach is proposed to deal with the drawbacks of the passive damping approach. It aims to modify the DC MGs control loops in order to compensate for INI characteristics by increasing the damping factor of the power converters [49, 53, 57]. Three methods can be classified under active damping. The first method is source-side active damping, which aims to add a loop in loop control to improve the output impedance of the feeder converter to satisfy the impedance stability criterion, but this method is impossible to be applied to a system when the input stage is *LC* or uncontrolled rectifier. The second method is performed by injecting a current or power into the CPL control loops to modify the input impedance Z_{in} of the CPL. The third method is adding an auxiliary device that injects the desired compensating current within the system operation range [52, 61].

Besides, virtual impedance is one of the active damping methods proposed in [53, 57]. This method performs the improvement transfer function of the system. It forces the system poles to move towards the stable region (left half of s-plane). This approach does not cause any power dissipation because it modifies the system control loop by adding a virtual impedance, as illustrated in Fig 1.20.

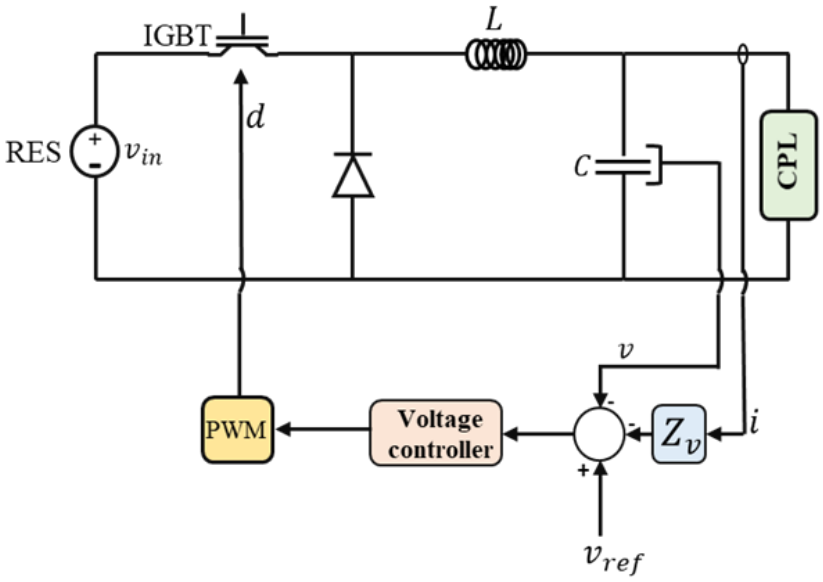

Fig 1.20. Adding virtual impedance to overcome the CPL instability problem.

Because of the effectiveness of the active damping approach in mitigating the instability problem due to the constant power load, active damping has received interest. However, it deteriorates system control performance and only compensates for the limited operation point [59].

1.4.1.3. Nonlinear control

Considering the DC/DC converter nonlinearity, nonlinear control techniques have been implemented, as illustrated in Fig 1.21, to stabilize the DC MG feeding CPL [54, 55, 59, 60, 61]. Among these nonlinear controls, Model predictive control (MPC) has been proposed by many authors [62–66]. For instance, in [62], the possibility of applying a finite control set model predictive control (FCS MPC) algorithm for dynamic stabilization of DC-MGS supplying the CPL is studied. In [63] and [64], the authors proposed the fuzzy MPC to stabilize DC-MGS feeding CPL. This proposed approach is based on Takagi-Sugeno (TS) fuzzy model and model predictive scheme. The MPC approach is effective in overcoming the CPL instability problem. But MPC is not suitable for plant-wide in real time due to its computational burden [66].

Sliding mode control (SMC) has been proposed to deal with the CPL instability problem and cover the MPC technique's drawbacks. As in [28–29] and [55]. In [29], the SMC technique is designed based on rigorous stability condition analysis to reach a suitable enhancement of the closed-loop system dynamic response. And in [55], a digital SMC (DSMC) is proposed for DC/DC converters under CPL conditions. This approach is effective in solving the CPL

problem. However, the SMC approach requires the capacitor current measurement, which is the cause of the ripple filtering degradation problem and causes the shattering problem [54].

Backstepping (BC) and passivity-based control (PBC) techniques are the most nonlinear controls proposed to deal with CPL issues. They can also cover the drawbacks of SMC and MPC techniques. For instance, in [67] and [68], the authors proposed backstepping control to deal with the CPL problem. They integrate the NDO (nonlinear disturbance observer) and 3rd-degree cabucative Kalman filter (CKF), respectively, for measurement estimation. In [54], instability due to the CPL is avoided by applying the PBC technique. The measurements used to generate the control law using this technique are estimated by the NDO observer. In [69] and [70], the authors proposed an improvement of the interconnection and damping assignment passivity-based control (IDA PBC) by developing an interconnection matrix to elaborate the internal link in a port-controlled Hamiltonian (PCH) model. This improvement will enhance the control law to deal with the CPL problem.

Although the nonlinear controls ensure suitable performances for DC-MG operating in the presence of CPL, they have several drawbacks. For instance, these techniques require a large use of sensors and the current power converter capacitor, which causes a ripple filtering degradation problems. Also, it isn't easy to realize the robust control hierarchy based on nonlinear control.

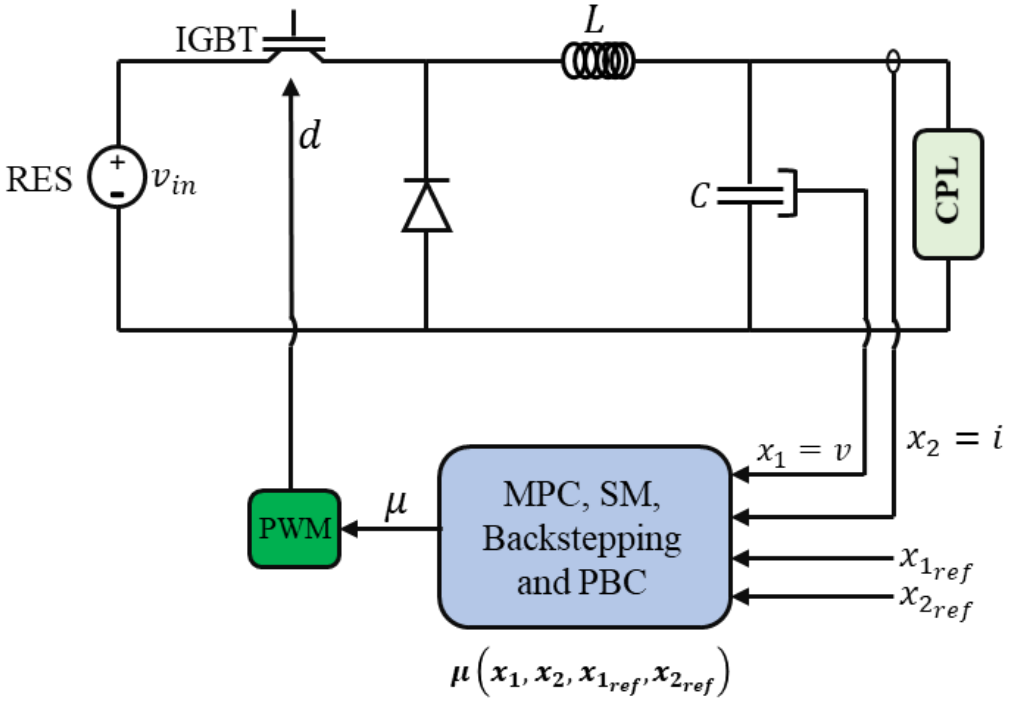

Fig 1.21. Nonlinear control to combat the CPL problem.

14.2. Techniques used to perform online fault diagnosis

1.4.2.1 Model-based techniques

The model-based technique is the first proposed to deal with the fault diagnosis issues in DC-MGS. It consists of analyzing the residual signals that are the fault indicators obtained through the error between the system's observations and the system model's output to detect the system's abnormalities, where the system model is fed by the same input acting on the real plant. The residual signals evolve with time near zero when the system operates in nominal conditions. They shift from zero to another value when an abnormality is present in the system [85–87]

The parity-space approach comes under the model-based technique. This approach is intended only for the linear system model. It uses the differential equations of the system presented in state-space equations to extract the analytical redundancy relations (ARRs), given in terms of the known signals, variables, and parameters in closed mathematical forms [88,-89], generating the residual signal using the system's observations. As in [90], the parity-space approach is proposed to detect the sensors and IGBT of power converter (actuator) faults in the DC-MGS. Also, in [91], the parity-space approach associated with l_2 gain analysis is performed to detect the DC power converter IGBT abnormalities in DC-MGS.

On the other hand, the system model can be used to develop the observers that can be used for the online fault diagnosis task. Here, the estimation error obtained from the difference between the system's observations and the real system output represents the residual signal [92]. The observer technique can also be applied to the nonlinear system model. As in [71, 93], the authors have proposed the optimal and unknown input observers to detect faults in the DC-MGS.

The residual signals derived from both methods are sensitive to faults, and they are limited to the fault detection and isolation (FDI) of sensors and actuators but not the parametric (component) faults. Thus, the parametric faults corresponding to the DC-MGS component cannot be detected under these methods. Because of many components of the DC-MG, simplistic models would yield no robust and poor FDI performances [94].

1.4.2.2. data-driven technique.

Data-driven based technique is proposed to deal with online fault diagnosis issues in DC-MGS when the accurate physics of the system is unknown. It consists of correlating the system's observation with the faulty or healthy system states. An analysis is performed on such

correlation to decide whether the fault is present or not in the system. The analysis performed on this correlation is conducted using artificial intelligence (AI) or statistics-based techniques. The AI techniques are usually used to solve the regression and classification problem, and the statistics-based techniques assign the probability of the system component being healthy or faulty, as in [94–95]. This technique has been proved to be successful in detecting and isolating both component and sensor faults.

In [94], the data-driven-based technique has been proposed for FDI in DC-MGS operating as the aircraft supply, where the neural network (NN) is used to solve the classification problem. In [96], the online fault diagnosis is realized based on the data-driven technique in the DC-MGS. In the studied case, the proposed approach exploits an artificial neural network (ANN) to analyze the measurements coming from the monitoring sensors to detect and isolate the faults in the system.

Even though the data-drive-based technique can detect and isolate all kinds of faults, it has several drawbacks. Among them: the data-drive-based technique requires adequate data of different working scenarios. It depends on the quality of the training data that has to be performed in the absence of system parameter uncertainties and sensor noises. Without good training data, this technique becomes ineffective with poor performance. Furthermore, this approach can only detect the predefined fault of the system [97].

1.5. Positioning of thesis work

Based on the given review of different methods that perform the layers of Active FTC, the thesis work proposed the alternative methods to perform the layers of Active FTC and overcome the drawbacks of the methods mentioned before and summarized in Tab 1.1 and Tab 1.2. The methods proposed by this thesis have to ensure the improvements presented in the following points:

- Avoid using passive elements as supplementary components helping the control hierarchy ensure stability system in the presence of CPL and components faults. The reason for that is these elements decrease the DC MG efficiency.
- Avoid using the virtual impedance incorporated in the control hierarchy because it can deteriorate the control performance.
- Possibility to implement the developed active FTC in the low-cost electronic board and prevent the occurrence of the computational burden problem.

- Avoid the use of capacitance current measurement that causes filtering degradation problems.
- Providing a robust online diagnosis can detect and isolate the defined and undefined components faults as much as possible.
- The capability of robust online diagnosis to provide the estimation of parameter variations caused due to components faults.

The robust control performed based on H_∞ norm, and robust online diagnosis based on the Linear fractional transformation bond graph (LFT) modeling approach has been proposed to achieve the aforementioned performances. The H_∞ based control is effective to ensure the stability system and mitigate the CPL and components. Performing the control hierarchy by using H_∞ based control is easy. Also, the implementation of this control hierarchy can be carried out in the low-cost electronic board.

The robust online diagnosis is realized based on the LFT-BG modeling approach, which is a powerful tool to model such a system as DC-MG. This tool can describe all system physics mathematically. Based on that, the developed can detect overall kinds of faults. In this case, parameter variations caused by the faults can be estimated. These estimations will be exploited to reconfigure H_∞ based control implemented in the control hierarchy.

The work presented by this thesis is a new contribution and an addition to the literature review.

Tab 1.1. Control methods summary

Methods	*Advantages*	*Drawbacks*
Passive damping [45–47].	Easy to implement	Decreases the efficiency
Active damping [49, 53, 57].	Overcomes the drawbacks of passive damping techniques. This method incorporates virtual impedance in control closed loops to increase the damping factor of DC/DC converters.	Modifies the control closed loops. The control performance can deteriorate.
Model predictive control (MPC) [54, 55, 59, 60, 61]	Powerful control approach for DC/DC converters. Under this approach, the stability system is guaranteed.	MPC is not suitable for plant-wide in real time due to its computational burden.
Sliding mode control (SMC) [29, 55]	Overcomes the drawbacks of SMC control. A low-cost electronic board can perform the implementation of SMC control.	The SMC approach requires the capacitor current measurement, which is the cause of the ripple filtering degradation problem and causes the shattering problem
Backstepping and passivity-based control [67–70, 54]	Overcomes the drawbacks of SMC techniques.	Give difficulties to build the control hierarchy.

Tab 1.2. Diagnosis methods summary.

Methods	*Advantages*	*Drawbacks*
Parity-space [88–91], Observers [92–93,71]	Have a high sensitivity to faults	limited to the FDI of sensors and actuators but not the parametric (component) faults. Because of many components of the DC-MG, simplistic models would yield no robust and poor FDI performances.
Data-driven techniques [94-96]	Overcomes the drawback of parity space and observer techniques. Sensitive to all kinds of faults.	Limited to the FDI of predefined faults. Depends on the quality of the training data that has to be performed in the absence of system parameter uncertainties and sensor noises. Without good training data, this technique becomes ineffective with poor performance.

1.6. Conclusion

This chapter provides the definition of MG in which the whole components forming the MG are presented. Moreover, the different MG architectures are explored in detail, and the choice to study the DC-MG is well justified. Also, the control hierarchy is well defined in this chapter, where each control level's objectives are mentioned, and explains how the presence of CPL and occurrence of component faults destabilize the system. The approaches available in the literature review are mentioned in this chapter with their drawbacks. Based on these drawbacks, we can justify the work of this thesis.

Chapter 2: H∞ bases control of DC/DC buck converter feeding constant power load

2.1. Introduction

This chapter explores the process of performing the robust control using the Golver Doyle optimization algorithm (GDOA). This GDOA is based on the H_∞ norm and requires the uncertain model of the system. The GDOA also uses the weight functions, presenting the constraints of the optimization problem. These weight functions help to reach the control performances wanted from the developed approach. The developed H_∞ based controller will be implemented in the primary control level to avoid the instability problem due to the presence of CPL and mitigate the negative effect of disturbances and components faults. The developed controller requires the voltage measurement and avoids using the current measurement that has issues such as ripple filtering degradation. The DC/DC buck converter is used to validate the proposed approach because it has a simple structure and is mostly used to incorporate the RES elements in DC-MG. Also, this chapter presents the small-signal values modeling approach to find the model of DC/DC buck converter, which also incorporates the mathematical representation to model the disturbances, uncertainties, and component faults.

The simulation study is performed by using Psim software. It consists of three scenarios carried out to validate the proposed approach. The first scenario is performed to verify the effectiveness of the H_∞ based control to avoid the instability problem due to the presence of CPL. The second and third scenarios are carried out to verify the ability of H_∞ based control to mitigate the effect of disturbances and component faults.

2.2. Average linear equivalent circuit of buck converter in continuous conduction mode.

Fig 2.1 Shows the main DC-MG component (DC/DC buck converter), which is used to integrate the RESs into DC-MG to supply the CPL, where a controlled current source shown in the buck converter electrical circuit represents the CPL, and the input voltage v_{in} can be the equivalent representation of any RES element. The DC/DC buck converter consists of the switching network (Transistor s and diode D_s) that regulates the output voltage according to the value of duty cycle d. It also consists of the low pass filter LC used to mitigate the current and voltage ripples caused by turning on/off the transistor s [39, 54].

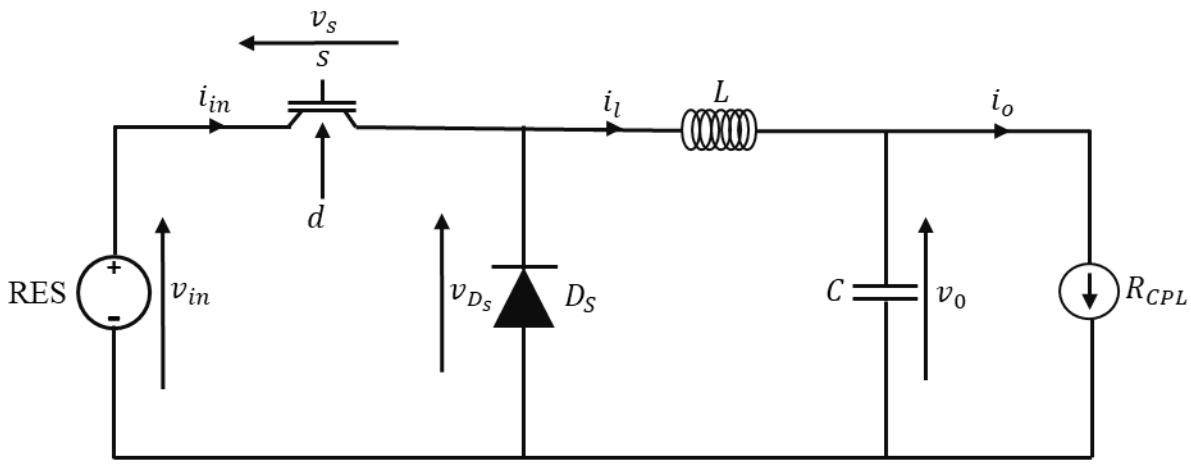

Fig 2.1. Electrical circuit of DC/DC buck converter.

where the output voltage v_o must be lower than v_{in}. It can be written as follows:

$$v_o = d \cdot v_{in} \tag{2.1}$$

where *d* is comprised between 0 and 1.

Considering that there is no loss of power in the DC/DC buck converter, the output current i_o can be written as follows [54]:

$$i_o = \frac{1}{d} \cdot i_{in} \tag{2.2}$$

Actually, the output current and voltage have ripples due to the PWM signal. Their ripples ($\Delta i,\ \Delta v$) depend on the switching frequency f_s related to the transistor *s* and the duty cycle *d* [98]. They can be written as follows:

$$\Delta i = \frac{V_0}{f_s \cdot L}\left(1 - D\right) \tag{2.3}$$

$$\Delta v = \frac{L}{2Cf_s} \tag{2.4}$$

where V_o and *D* are the DC nominal values of output voltage and duty cycle, respectively.

These expressions ($\Delta i,\ \Delta v$) are exploited to get the suitable values of C and L to properly mitigate these output current and voltage ripples. But The *LC* filter cannot completely mitigate these ripples. It still keeps the acceptable ripples allowed by the DC/DC buck converter specifications and must be known before calculating *C* and *L* values.

According to the previous definition of DC/DC buck converter. The DC/DC buck converter represents a nonlinearity and can be considered as a hybrid system due to the switching network (transistor *S* and diode D_s). The H_∞-based control approach does not require the average nonlinear model, representing the most accurate DC/DC buck converter model. The average linear model is then sufficient to develop this robust controller and guarantee the excepted performances [39].

The small-signal modeling method is the most common technique used to obtain the DC/DC buck converter average linear model for Continuous conduction mode (CCM) [98]. It also allows presenting the model obtained in the average linear circuit. This process of DC/DC buck converter modeling involves the following steps [99]:

1. Averaging the current and voltage waveforms of switching components over one switching period (knowing that the DC/DC buck converter operates under a PWM signal).
2. Replacement of switching component (*s* and D_s) with nonlinear dc dependent current and voltage sources.
3. Averaging the parasitic components of the switching devices over one switching period, such as transistor on-resistance, diode forward resistance, and diode offset voltage.
4. Perturbation of the average current, voltage, and duty ratio waveforms to obtain large-signal time-dependent waveforms.
5. Replacement of DC-dependent sources by nonlinear large-signal dependent current and voltage sources.
6. Splitting the large-signal current, voltage, and duty cycle waveforms into the DC and AC components.
7. Linearization of nonlinear dependent current and voltage sources.
8. Separation of DC and small-signal variables.
9. Representation of the DC variables by a DC circuit model and the small-signal AC variables by a small-signal AC circuit model.

This small-signal modeling method uses current and voltage-dependent sources and the law of the energy conversion to develop the DC/DC buck converter model for CCM. The current and

voltage-dependent sources are used to model the ideal switching network of DC/DC buck converter, and the law of energy conservation is used to model the parasitic component of switching devices, such as the transistor on-resistance, diode forward resistance, and diode offset voltage. Thus, the ideal dependent sources can model the ideal switching network of the DC/DC buck converter. On the other hand, the switched forward resistances of the transistor and diode are averaged using energy conservation law. The current, voltage and duty cycle are then perturbed in the average linear model of the DC/DC buck converter. Hence, the DC-dependent sources in the model are replaced by large-signal time-varying dependent sources. Therefore, large-signal current, voltage, and duty cycle contain DC and AC components. The large signal sources can be replaced by the DC-dependent sources and the AC small-signal dependent sources. If the magnitudes of the small-signal components are lows enough, the model can be linearized by neglecting the product of the AC components. Therefore, this leads to a linear circuit model containing both AC and DC components [99].

Before deriving the model for DC/DC buck converter, the following assumption must be taken into account [99]:

1. The transistor output capacitance and the diode capacitance are neglected. Therefore, the power losses in the power switch and diode are neglected.
2. The transistor on-resistance r_{DS} is linear, and the transistor off-resistance is infinite.
3. The diode in the on-state is modeled by a linear battery V_f and a linear forward resistance R_F. In the off-state, the diode is modeled by an infinite resistance.
4. Passive components are linear, time-invariant, and frequency independent.

The average linear model of the DC/DC buck converter is obtained by replacing the switching network with its corresponding average linear circuit. It is obtained based on the steady-state waveforms in the DC/DC buck converter switching network for CCM, illustrated in Fig 2.2, where the i_{in} is the current crossing the transistor s, v_d is the diode voltage, i_D is the current crossing the diode D and $f_s = 1/T_s$.

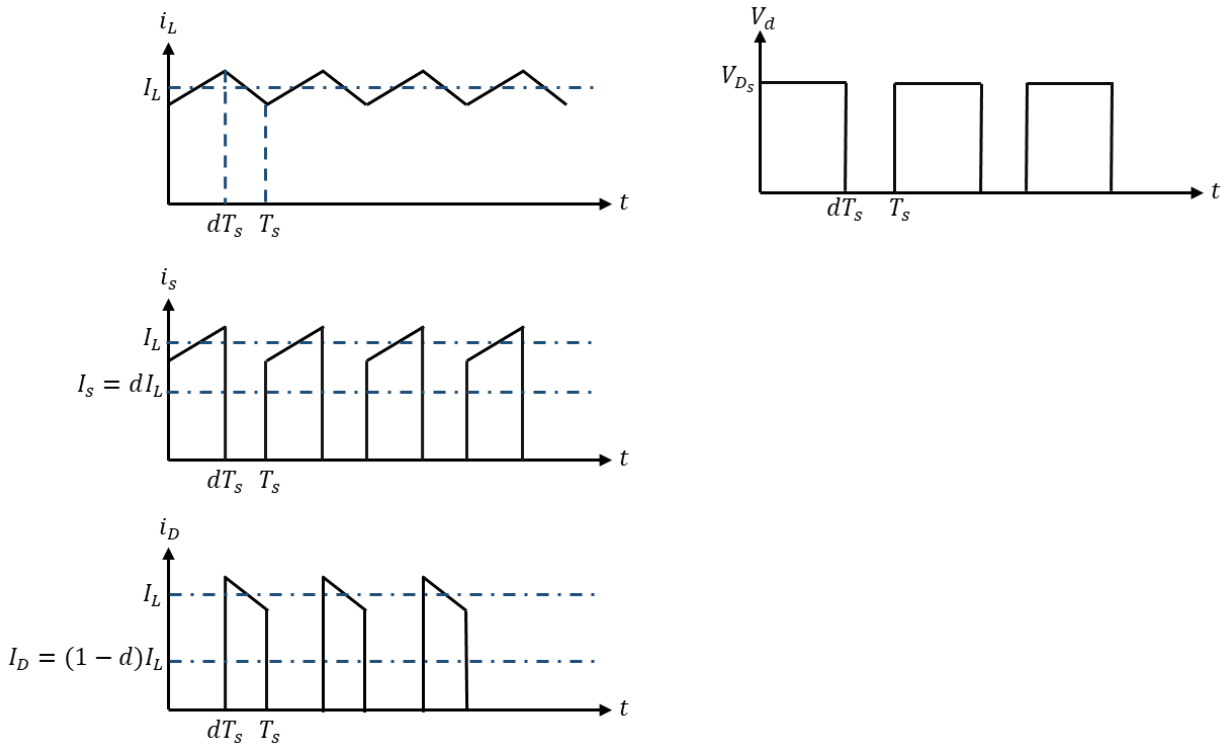

Fig 2.2. Steady-state waveforms in the switching network for CCM.

According to Fig 2.2, the steady-state waveform of i_{in} can be approximated by:

$$i_s \approx \begin{cases} I_L, \text{ for } 0 < t \le DT_s \\ 0, \text{ for } DT_s < t \le T_s \end{cases} \tag{2.5}$$

Then, the DC component of i_{in} can be written as follows:

$$I_s = \frac{1}{T_s}\int_0^{T_s} i_s dt = \frac{1}{T_s}\int_0^{dT_s} I_L dt = dI_L \tag{2.6}$$

where I_L is the DC nominal value of i_L .

According to Fig 2.2, the steady-state waveform of v_{D_s} can be approximated by:

$$v_{D_s} \approx \begin{cases} V_{D_s}, \text{ for } 0 < t \le dT_s \\ 0, \text{ for } \mathrm{dT_s} < t < T_s \end{cases} \tag{2.7}$$

Then, the DC component of v_{D_s} can be given as follows:

$$V_{D_s} = \frac{1}{T_s}\int_0^{T_s} v_{D_s} dt = \frac{1}{T_s}\int_0^{dT_s} V_{D_s} dt = dV_{D_s} \tag{2.8}$$

where $V_{D_s} = V_{in} - V_s$, V_{in} is the DC nominal value of v_{in} and V_s is the DC nominal value of v_s.

According to Fig 2.2, the steady-state waveform of i_D can be approximated as follow:

$$i_D \approx \begin{cases} 0, \text{ for } 0 < t \le dT_s \\ I_L, \text{ for } dT_s < t \le T_s \end{cases} \tag{2.9}$$

Then, the DC component of i_D is given as follows:

$$I_D = \frac{1}{T_s}\int_0^{T_s} i_D dt = \frac{1}{T_s}\int_{dT_s}^{T_s} I_L dt = I_L\left(1-d\right) \tag{2.10}$$

Using (2.6) and (2.10), I_L can be written as follows:

$$I_L = \frac{I_s}{d} = \frac{I_s}{\left(1-d\right)} \tag{2.11}$$

Using (2.5) and (2.6), the rms value of i_s is obtained as follow:

$$I_{s_{rms}} = \sqrt{\frac{1}{T_s}\int_0^{T_s} i_s^2 dt} = \sqrt{\frac{1}{T_s}\int_0^{dT_s} I_L^2 dt} = I_L\sqrt{d} = \frac{I_D\sqrt{d}}{1-d} \tag{3.12}$$

The power loss in the transistor on-resistance is given as follow:

$$\mathrm{P}_T = r_T I_{S_{rms}}^2 = \frac{r_T}{d} I_s^2 = r_{T_a} I_s^2 \tag{2.13}$$

where $r_{T_a} = r_T / d$.

Using (2.9), the rms value of i_D is obtained as follows:

$$I_{D_{rms}} = \sqrt{\frac{1}{T_s}\int_0^{T_s} i_D^2 dt} = \sqrt{\frac{1}{T_s}\int_{dT_s}^{T_s} I_L^2 dt} = I_L\left(1-d\right) = I_s\frac{\sqrt{(1-d)}}{d} = \frac{I_D}{\sqrt{(1-d)}} \tag{3.14}$$

The power loss in the forward diode resistance can be given as follow:

$$P_D = r_F I_{D_{rms}}^2 = \frac{r_F}{1-d} I_D^2 = r_{F_a} I_D^2 \tag{2.15}$$

where $r_{F_a} = r_F / (1-d)$.

Also, there is an amount of power lost in the diode offset voltage, which can be written as follows:

$$P_{VF} = V_F I_D \tag{2.16}$$

where V_F is the offset voltage of the diode.

According to (2.6) and (2.8) with exploiting the expressions of r_{a_T} and r_{F_a} . The nonlinear part of the DC/DC buck converter can be modeled in the steady-state by the voltage and controlled current sources, as illustrated in Fig 2.3a and Fig 2.3b, where the particles of this part causing power loss are modeled by r_{a_T} , r_{F_a} and V_F , and supposing that v_s is neglected. The circuit illustrated in Fig 2.3b is obtained after some mathematical manipulations based on Kirchhoff's laws.

The average linear circuit of the switching network, illustrated in Fig 2.3a and Fig 2.3b, is only useful for describing the steady-state behavior. To obtain the average linear circuit for the corresponding part, which can describe the whole behavior, is still based on the small-signal method definition.

Based on the small-signal method, v_{in}, i_L, d, and v_o can be written as follows:

$$v_{in} = \tilde{v}_{in} + V_{in} \tag{2.17}$$

$$i_L = \tilde{i}_L + I_L \tag{2.18}$$

$$d = \tilde{d} + D \tag{2.19}$$

$$v_o = \tilde{v}_o + V_o \tag{2.20}$$

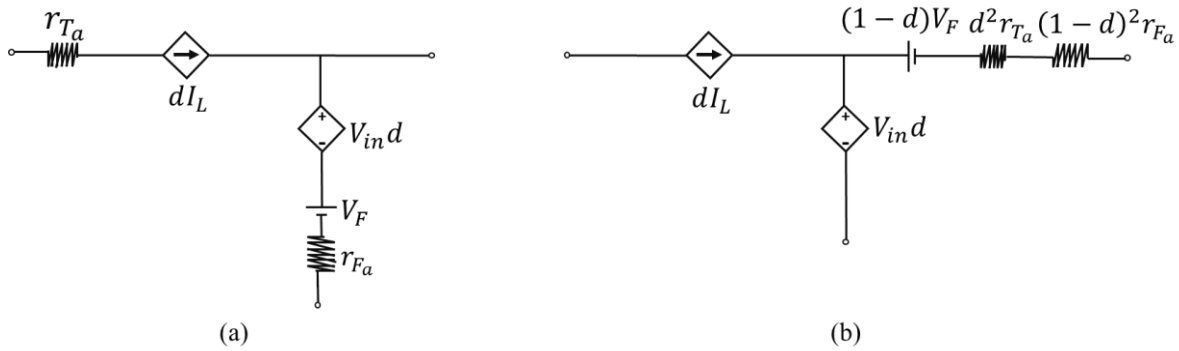

Fig 2.3. average linear circuit of the switch network in steady-state.

where $\tilde{v}_{in}, \tilde{i}_L$, $\tilde{d}$ and $\tilde{v}_o$ are the small-signal values of v_{in}, i_L, d, and v_o, respectively.

Neglecting the losses in the DC/DC buck converter and supposing that the average capacitance current is approximately zero, i_o can be approximated as follows:

$$i_o = i_L \tag{2.21}$$

Then, v_o and i_{in} can be approximated as follows:

$$v_o = d \cdot v_{in} \tag{2.22}$$

$$i_{in} = d \cdot i_L \tag{2.23}$$

Substituting (2.17), (2.18), (2.19) in (2.22) and (2.23), respectively. v_o and i_{in} will be expressed as follows:

$$\begin{aligned} v_o &= \left(\tilde{d} + D\right)\left(\tilde{v}_{in} + V_{in}\right) \rightarrow \tilde{v}_o + \cancel{V_o} = \cancel{\tilde{d}\tilde{v}_{in}}^{\approx 0} + V_{in}\tilde{d} + D\tilde{v}_{in} + \cancel{DV_{in}}^{\approx V_o} \\ &\rightarrow \tilde{v}_o = V_{in}\tilde{d} + D\tilde{v}_{in} \end{aligned} \tag{2.23}$$

$$\begin{aligned} i_{in} &= \left(\tilde{d} + D\right)\left(\tilde{i}_L + I_L\right) \rightarrow \tilde{i}_{in} + \cancel{I_{in}} = \cancel{\tilde{d}\tilde{i}_L}^{\approx 0} + D\tilde{i}_L + \tilde{d}I_L + \cancel{DI_L}^{\approx I_{in}} \\ &\rightarrow \tilde{i}_{in} = D\tilde{i}_L + \tilde{d}I_L \end{aligned} \tag{2.24}$$

According to (2.23), (2.24), and the average linear circuit presented in Fig 2.3a and Fig 2.3b, the average circuit that can describe the complete behavior of the DC/DC buck converter switching network is illustrated in Fig 2.4a and Fig 2.5b.

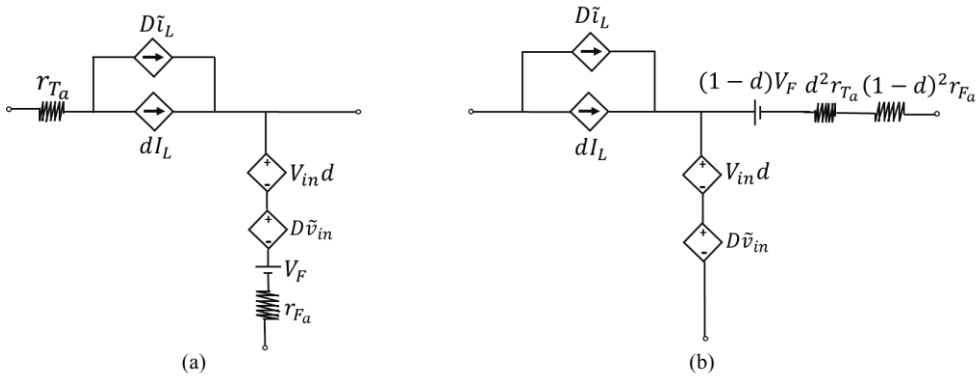

Fig 2.4. average linear circuit of the switch network describing the complete behavior.

Therefore, the average linear equivalent circuit of the DC/DC buck converter is easily obtained by replacing the switch network with its corresponding average linear circuit, as illustrated in Fig 2.5a, where the particles causing a power loss in this component are neglected to simplify the model. As a result, the average linear circuit of the DC/DC buck converter can be approximately illustrated as in Fig 2.5b based on (2.23).

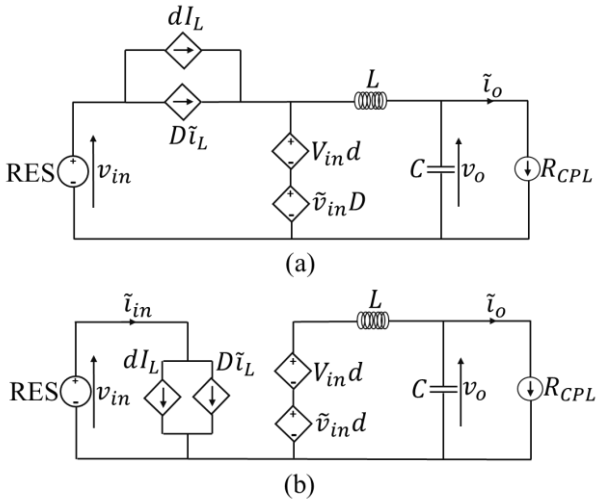

Fig 2.5. average linear circuit of DC/DC buck converter.

2.3. Transfer matrix of DC/DC buck converter.

Any control design used to perform a controller for the DC/DC buck converter in CCM requires a transfer function/ matrix or the differential equations presented in the state-space form, which is performed based on the average linear equivalent circuit of DC/DC buck converter [50, 99]. In the framework of the proposed control approach, the transfer function/matrix is the most used. The DC/DC buck converter can be considered as a multi-input single-output system (MISO), as illustrated in the diagram shown in Fig 2.6. This MISO can be presented by a transfer matrix, where the inputs are denoted by $\tilde{v}_{in}$, $\tilde{i}_o$ and d, and the output is denoted by $\tilde{v}_o$. It is worth pointing out that the only *d* is the variable of control, and $\tilde{v}_{in}$ and $\tilde{i}_o$ act on the DC/DC buck converter as the disturbances, and $T_p(s)$, $M_v(s)$ and $Z_0(s)$ are the gains of MISO transfer matrix, defined as follows:

- The Duty cycle-to-output voltage transfer function ($T_p(s)$).
- The input voltage-to-output voltage transfer function ($M_v(s)$).
- The output current-to-output voltage transfer function ($Z_0(s)$).

The output voltage v_o in the function of the MISO transfer matrix T_{MISO} is written as follows:

$$v_0 = \overbrace{\begin{bmatrix} T_p(s) & M_v(s) & Z_o(s) \end{bmatrix}}^{T_{MISO}} \cdot \begin{pmatrix} d \\ \tilde{v}_{in} \\ \tilde{i}_o \end{pmatrix} \tag{2.25}$$

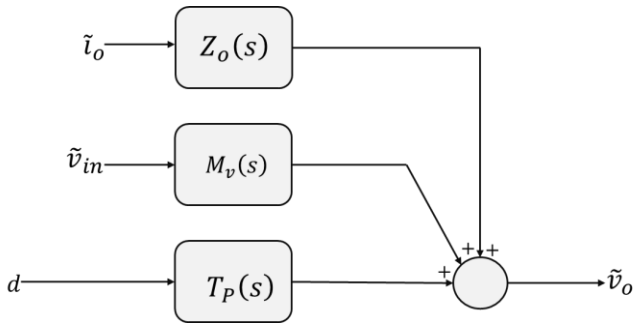

Fig 2.6. Block diagram of DC/DC buck converter transfer matrix.

Based on the average linear equivalent circuit presented in Fig 2.5b, $T_p(s)$ is calculated by supposing: $\tilde{v}_{in}=0$ and $\tilde{i}_o=0$. In this case, the average linear circuit of DC/DC buck converter becomes as illustrated in Fig 2.7, where

$$Z_1(s)=sL \tag{2.26}$$

$$Z_2(s)=\frac{R_{CPL}}{1+R_{CPL}Cs} \tag{2.27}$$

Using the circuit presented in Fig 2.7, $T_p(s)$ can be written as follows:

$$T_p(s)=\frac{v_o}{d}\bigg|_{\tilde{v}_{in}\approx 0,\tilde{i}_o\approx 0}=\frac{V_{in}Z_1(s)}{Z_2(s)+Z_1(s)}=\frac{\frac{V_{in}}{LC}}{s^2-\frac{P_{CPL}}{CV_o^2}s+\frac{1}{LC}} \tag{2.28}$$

where V_{in} and V_o are the DC nominal value of input and output voltages, respectively.

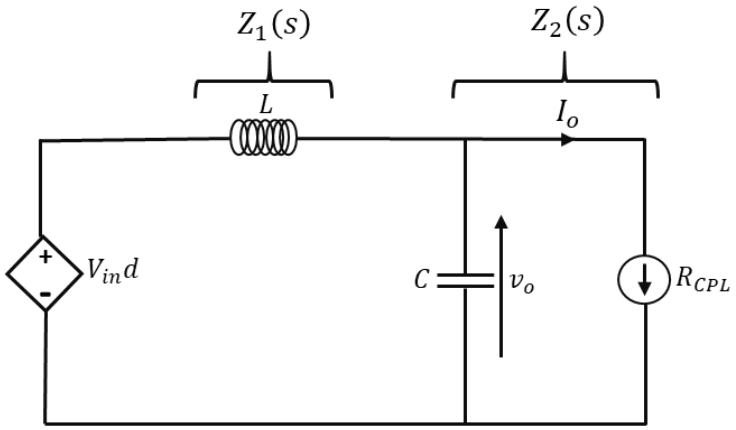

Fig 2.7. Average linear circuit of DC/DC buck converter obtained after supposing $\tilde{v}_{in}=0$.

$M_v(s)$ is calculated by supposing $d=0$ and $\tilde{i}_o=0$. After considering these suppositions, the average linear circuit becomes as illustrated in Fig 2.8.

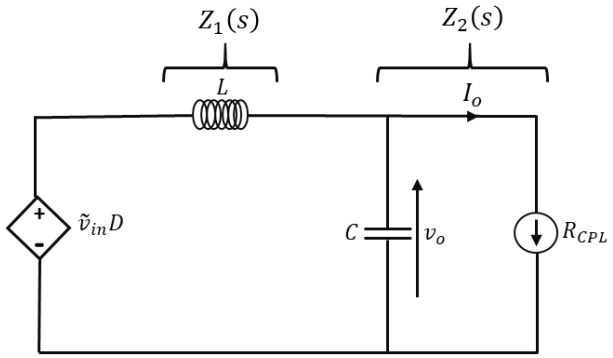

Fig 2.8. Average linear circuit of DC/DC buck converter obtained after supposing $d = 0$ ***and*** $\tilde{i}_o = 0$.

Using the circuit presented in Fig 2.8, $M_v(s)$ can be written as follows:

$$M_v(s) = \left.\frac{v_o}{v_{in}}\right|_{\tilde{d}=0,\tilde{i}_o\approx 0} = \frac{DZ_1(s)}{Z_1(s)+Z_2(s)} = \frac{\dfrac{D}{LC}}{s^2 - \dfrac{P_{CPL}}{CV_o^2}s + \dfrac{1}{LC}} \tag{2.29}$$

$Z_0(s)$ presents the output impedance of the DC/DC buck converter. It is calculated by putting the average linear equivalent circuit of the DC/DC buck converter under the voltage source v_t from its output with supposing: v_{in} and $d = 0$, as illustrated in Fig 2.9. Using the circuit presented in Fig 2.9, $Z_0(s)$ can be given through the following expression:

$$Z_o(s) = \frac{v_t}{i_t} \tag{2.30}$$

Then, $Z_0(s)$ can be written as follows:

$$Z_o(s) = \frac{Z_1(s)Z_2(s)}{Z_1(s)+Z_2(s)} = \frac{\dfrac{s}{C}}{s^2 - \dfrac{P_{CPL}}{CV_o^2}s + \dfrac{1}{LC}} \tag{2.31}$$

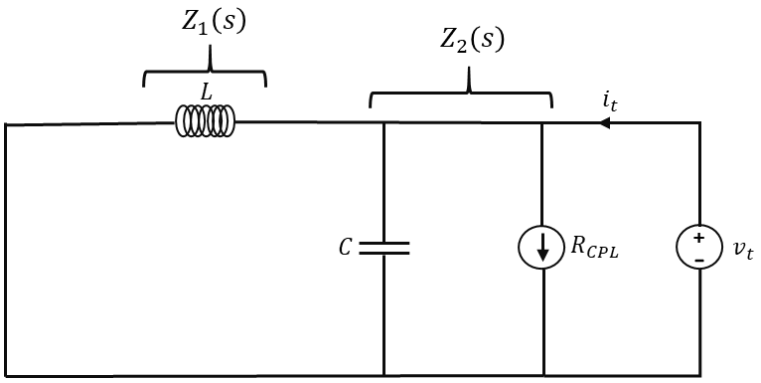

Fig 2.9. Average linear circuit of DC/DC buck converter used to obtain $Z_0(s)$.

2.4. Parameter uncertainties modeling

DC/DC buck converter parameter identification maybe not be achieved properly due to unknown disturbances. Otherwise, the DC/DC buck converter parameters have an uncontrolled random variation due to these unknown disturbances. In this case, the DC/DC buck converter parameter can be identified by an interval of values. Its minimum and maximum values are related to the uncertainty of the parameter and have the accepted limits given by the technical specifications of the DC/DC buck converter. Due to parametric (component) faults, the DC/DC buck converter parameters variate over the accepted limits. This unaccepted variation is considered an abnormality in the system, responsible for performance loss, reliability, and safety deteriorations. The proposed approach also addresses the issues mentioned above. It can also be considered a passive fault-tolerant control because it guarantees an acceptable performance for the faulty system. The proposed approach needs an uncertain model in which the parameter uncertainties mathematical presentation is incorporated [50].

The process of modeling the parameter uncertainties is based on definition3.1, which is given as follows:

Definition 2.1: Assuming ψ is a parameter of any system. The uncertainty on the parameter ψ can be additive or multiplicative, which can be written, respectively, as follows:

$$\psi = \psi_0 \pm \Delta\psi \tag{2.32}$$

$$\psi = \psi_0 \left(1 \pm \delta_\psi\right) \tag{2.33}$$

Based on **definition 2.1**, The parameters of $T_p(s)$, $M_v(s)$, and $Z_o(s)$ can be written as follows:

$$\begin{cases} a_1 = \dfrac{V_{in}}{LC} & a_1 = a_{1_0} + a_{1_0}\delta_{a_1} & a_{1_0} = \left(\dfrac{V_{in}}{LC}\right)_0 \\ a_2 = \dfrac{P_{CPL}}{CV_o^2} & a_2 = a_{2_0} + a_{2_0}\delta_{a_2} & a_{2_0} = \left(\dfrac{P_{CPL}}{CV_o^2}\right)_0 \\ a_3 = \dfrac{1}{LC} & a_3 = a_{3_0} + a_{3_0}\delta_{a_3} & a_{3_0} = \left(\dfrac{1}{LC}\right)_0 \end{cases} \tag{2.34}$$

$$\begin{cases} b_1 = \dfrac{D}{LC} & b_1 = b_{1_0} + b_{1_0}\delta_{b_1} & b_{1_0} = \left(\dfrac{D}{LC}\right)_0 \\ b_2 = \dfrac{P_{CPL}}{CV_o^2} & b_2 = b_{2_0} + b_{2_0}\delta_{b_2} & b_{2_0} = \left(\dfrac{P_{CPL}}{CV_o^2}\right)_0 \\ b_3 = \dfrac{1}{LC} & b_3 = b_{3_0} + b_{3_0}\delta_{b_3} & b_{3_0} = \left(\dfrac{1}{LC}\right)_0 \end{cases} \tag{2.35}$$

$$\begin{cases} c_1 = \dfrac{1}{C} & c_1 = c_{1_0} + c_{1_0}\delta_{c_1} & c_{1_0} = \left(\dfrac{1}{C}\right)_0 \\ c_2 = \dfrac{P_{CPL}}{CV_o^2} & c_2 = c_{2_0} + c_{2_0}\delta_{c_2} & c_{2_0} = \left(\dfrac{P_{CPL}}{CV_o^2}\right)_0 \\ c_3 = \dfrac{1}{LC} & c_3 = c_{3_0} + c_{3_0}\delta_{c_3} & c_{3_0} = \left(\dfrac{1}{LC}\right)_0 \end{cases} \tag{2.36}$$

where $\delta_{a_1}, \delta_{a_2}, ...\delta_{a3}$ are the relative uncertainties, comprised between -1 and -1.

According to (2.25) and substituting (2.34), (2.35), and (2.36) in $T_p(s)$, $M_v(s)$, and $Z_o(s)$, $\tilde{v}_o$ can be written as follows:

$$\begin{aligned} \tilde{v}_o = {} & \overbrace{\frac{a_{1_0}}{s^2 - a_{2_0}s + a_{3_0}}}^{T_{p0}(s)}(\omega_1 + \tilde{d} + (\omega_2 + \tilde{v}_{in}) \cdot \overbrace{\frac{b_{1_0}}{s^2 - b_{2_0}s + b_{3_0}}}^{M_{v0}(s)} \cdot \frac{1}{T_{p0}(s)} \\ & + (\omega_3 + \tilde{i}_o) \cdot \overbrace{\frac{c_{1_0}}{s^2 - c_{2_0}s + c_{3_0}}}^{Z_{o0}(s)} \cdot \frac{1}{T_{p0}(s)}) \end{aligned} \tag{2.37}$$

where:

$$\omega_1 = \overbrace{\frac{1}{T_{p0}(s)}\begin{bmatrix} \dfrac{a_{1_0}\delta_{a_1}}{s_2 - a_{2_0}s + a_{3_0}} & \dfrac{a_{2_0}\delta_{a_2} - a_{3_0}\delta_{a_3}}{s_2 - a_{2_0}s + a_{3_0}} \end{bmatrix}}^{\Delta_1(s)} \begin{pmatrix} \tilde{d} \\ \tilde{v}_o \end{pmatrix} \tag{2.38}$$

$$\omega_2 = \overbrace{\frac{1}{M_{v_0}(s)}\begin{bmatrix} \frac{b_{1_0}\delta_{b_1}}{s^2 - b_{2_0}s + b_{3_0}} & \frac{b_{2_0}\delta_{b_2} - b_{3_0}\delta_{b_3}}{s^2 - b_{2_0}s + b_{3_0}} \end{bmatrix}}^{\Delta_2(s)} \begin{pmatrix} \tilde{v}_{in} \\ \tilde{v}'_o \end{pmatrix} \tag{2.39}$$

$$\omega_3 = \overbrace{\frac{1}{Z_{o_0}(s)}\begin{bmatrix} \frac{c_{1_0}\delta_{c_1}}{s^2 - c_{2_0}s + c_{3_0}} & \frac{c_{2_0}\delta_{c_2} - c_{3_0}\delta_{c_3}}{s^2 - c_{2_0}s + c_{3_0}} \end{bmatrix}}^{\Delta_2(s)} \begin{pmatrix} \tilde{i}_o \\ \tilde{v}''_o \end{pmatrix} \tag{2.40}$$

$\Delta_1(s)$, $\Delta_2(s)$, and $\Delta_3(s)$ are the uncertain transfer matrix.

According to (2.37), it is concluded that the uncertain parameters and component faults disturb the control variable d (duty cycle). Therefore, these uncertainties and parametric faults can be included in the DC/DC buck converter average linear model, as illustrated in the block diagram depicted in Fig 2.10, where ω_T gathers the overall disturbance present in the DC/DC buck converter [50]

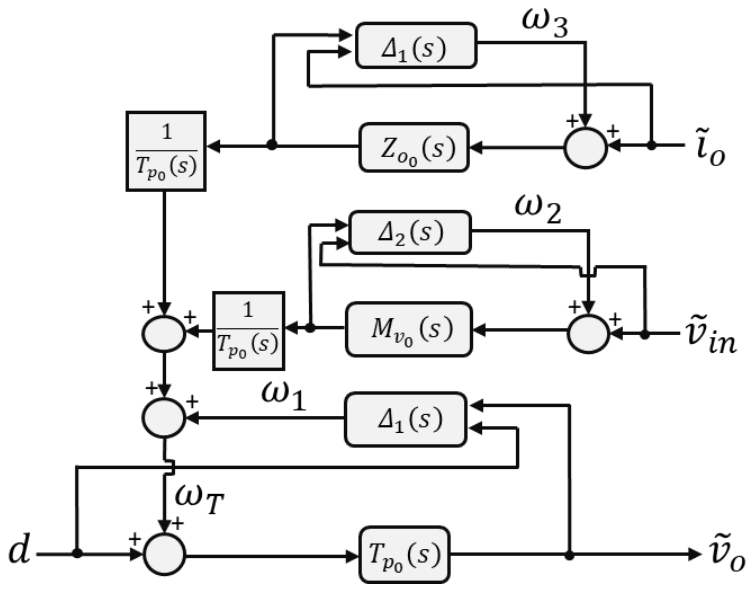

Fig 2.10. block diagram of DC/DC buck converter, including overall disturbances.

2.5. H∞ based control design

The H∞-based controller is the solution of an optimization problem, which is solved using the Golver Doyle optimization algorithm (GDOA). This GDOA is based on the H∞ norm and requires an augmented plant deduced from the control closed loop of DC/DC buck converter incorporating the model presented in section 2.4 (see Fig 2.10). This augmented plant represents the mathematical relationship of the error and control variable, with the variables

representing the disturbances. This augmented plant also comprises the weight functions, which impose the constraints helping to perform H∞-based controller that ensures the wanted performances. These weight functions must be determined before operating the algorithm [101-104].

In this section, certain definitions have to be mentioned to understand the design process of H∞-based controller, which are given as follows [50]:

Definition 2.2 (singular value): Assuming $G(s)$ is a transfer matrix. The singular values of $G(s)$ are defined as follows:

$$\sigma\left(G(s)\right)=\sqrt{\lambda\left(G^{*}(s)\cdot G(s)\right)} \tag{2.41}$$

And their proprieties used for mathematical manipulations are written as follows:

$$\begin{cases} \bar{\sigma}\left(G(s)\right)=0\rightarrow G(s)=0 \\ \forall\lambda\in\mathbb{C}\rightarrow\sigma\left(\lambda\cdot G(s)\right)=|\lambda|\cdot\sigma\left(G(s)\right) \\ \bar{\sigma}\left(G_1(s)+G_2(s)\right)\le\bar{\sigma}\left(G_1(s)\right)+\bar{\sigma}\left(G_2(s)\right) \\ \bar{\sigma}\left(G_1(s)\cdot G_2(s)\right)\le\bar{\sigma}\left(G_1(s)\right)\cdot\bar{\sigma}\left(G_2(s)\right) \\ \underline{\sigma}\left(G_1(s)\cdot G_2(s)\right)\le\underline{\sigma}\left(G_1(s)\right)\cdot\underline{\sigma}\left(G_2(s)\right) \end{cases} \tag{2.42}$$

Definition 2.3 (H∞ norm): assuming $G(s)$ is a transfer matrix, The H∞ norm of $G(s)$ is its biggest singular value of $G(s)$. It can be written as follow:

$$\left\|G(s)\right\|_{\infty}=\bar{\sigma}\left(G(s)\right) \tag{2.43}$$

Definition 2.4 (Algebraic Riccati equation): Assume *A*, *Q* and *R* are real *(n x n)* matrix, and *Q* and *R* are symmetric. The Algebraic Riccati equation is given as in the following matrix equation:

$$A^{*}\cdot X+X\cdot A+X\cdot R\cdot X+Q=0 \tag{2.44}$$

Let define another matrix *H*, which is obtained by concatenation of matrix *A*, *R*, and *Q* and can be written as follows:

$$H=\begin{bmatrix} A & R \\ -Q & A^{*} \end{bmatrix} \tag{2.45}$$

This *H* matrix is used to solve the Algebraic Riccati equation.

Definition 2.5 (Lower linear fractional transformation): consider an example of a system modeled by the transfer matrix $P(s)$, and $K(s)$ is a controller used to regulates the output of this system, which can be presented by the block diagram as illustrated in Fig 3.11a, where y, y_{in}, $e = y_{in} - y$ and u are the output of $P(s)$, input, error, and control variable, respectively.

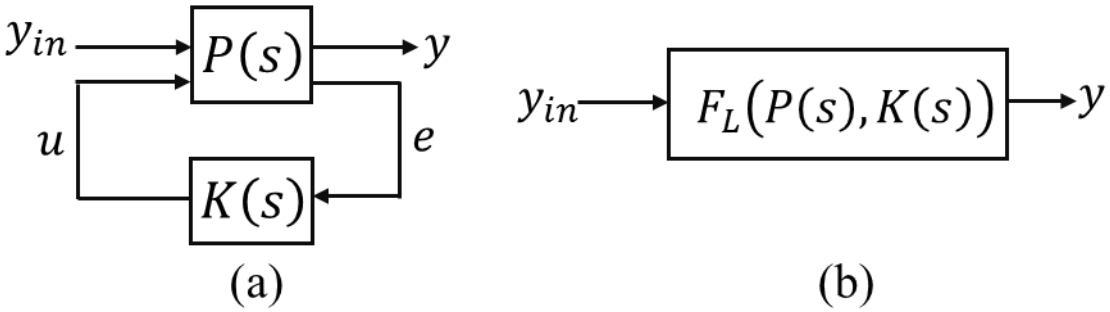

Fig 2.11. a) Augmented plant, b) Lower linear fractional transformation.

This system can be presented using the Lower linear fractional transformation (LLFT) as illustrated in Fig 2.11b, where $F_L(P(s),K(s))$ can be written as follows:

$$F_L(P(s),K(s)) = P_{11}(s) + P_{12}(s)\cdot K(s)\cdot\left(I - P_{22}(s)\cdot K(s)\right)^{-1}\cdot P_{21}(s) \quad (2.46)$$

where $P(s)$ is repartitioned as follows:

$$P(s) = \begin{bmatrix} P_{11}(s) & P_{12}(s) \\ P_{21}(s) & P_{22}(s) \end{bmatrix} \quad (2.47)$$

Remark: The transfer matrix $F_L(P(s),K(s))$ can be considered as the closed-loop transfer matrix.

2.5.1 Augmented plant

Fig 2.12 depicts voltage robust control closed-loop of DC/DC buck converter feeding CPL, where the uncertain model of DC/DC buck converter is shown in detail, and the H∞-based controller $K_\infty(s)$ and the weight function ($W_1(s)$, $W_2(s)$ and $W_3(s)$) are incorporated. These weight functions are the virtual filters that will not be present when $K_\infty(s)$ is implemented in the real system and are only used to design the $K_\infty(s)$. The augmented plant is extracted from

this voltage robust closed-loop control. It is a transfer matrix representing the mathematical relationship between $\{e_1, e_2, e\}$ and $\{V_{ref}, \omega, d\}$, which is required by the design process of H∞-based control that aims to mitigate the effect of the overall disturbance on the control variable and ensures the DC/DC buck converter stability in the presence of CPL. This augmented plant can be written as follows:

$$\begin{pmatrix} e_1 \\ e_2 \\ e \end{pmatrix} = \overbrace{\begin{bmatrix} W_1(s) & -W_1(s)\cdot T_{p0}(s)\cdot W_3(s) & -W_1(s)\cdot T_{p0}(s) \\ 0 & 0 & W_2(s) \\ 1 & -T_{p0}(s)\cdot W_3(s) & T_{p0}(s) \end{bmatrix}}^{[P(s)]} \cdot \begin{pmatrix} V_{ref} \\ \omega \\ \tilde{d} \end{pmatrix} \quad (2.48)$$

where:

$$d = K_\infty(s)\cdot e \quad (2.49)$$

e is the error $e = V_{ref} - \tilde{v}_o$, e_1 is the error e filtered by $W_1(s)$, e_2 is the control variable (duty cycle) d filtred by $W_2(s)$, and ω is the disturbances ω_T filtered by $W_3(s)$.

according to **definition 2.5**, LFT based on (2.48) and (2.49) is written as follows:

$$y = F_L\left(P(s), K_\infty(s)\right)\cdot y_{in} \quad (2.50)$$

where:

$$F_L\left(P(s), K_\infty(s)\right) = \begin{bmatrix} W_1(s)S(s) & W_1(s)S(s)T_{p0}(s)W_3(s) \\ W_2(s)S(s)K_\infty(s) & -W_2(s)T(s)W_3(s) \end{bmatrix} \quad (2.51)$$

$$y_{in} = \begin{pmatrix} V_{ref} \\ \omega \end{pmatrix} \quad (2.52)$$

$$y = \begin{pmatrix} e_1 \\ e_2 \end{pmatrix} \quad (2.53)$$

$S(s)$ and $T(s)$ are the sensitivity and complementary sensitivity functions, respectively, which are expressed as follows:

$$S(s) = \frac{1}{1 + K_\infty(s)T_{p0}(s)} \quad (2.54)$$

$$T(s)=1-S(s)=\frac{K_\infty(s)T_{p0}(s)}{1+K_\infty(s)T_{p0}(s)} \tag{2.55}$$

y is the output vector, and y_{in} is defined as the vector of disturbances.

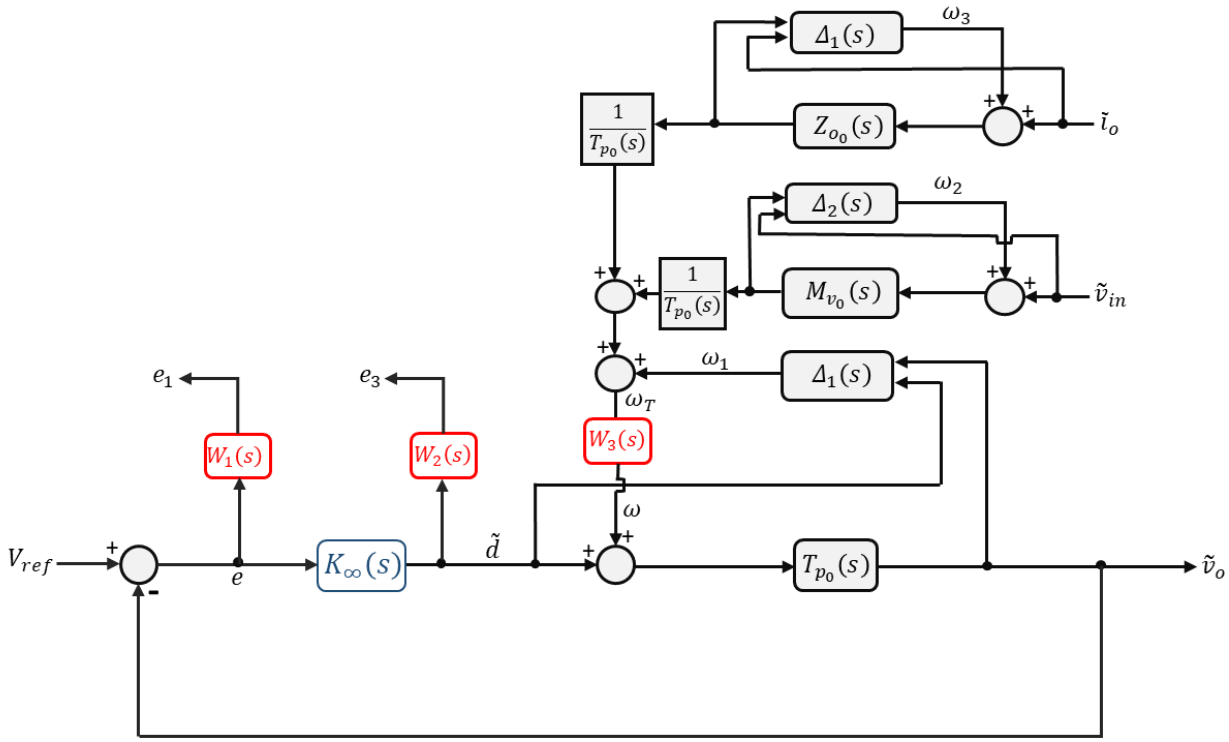

Fig 2.12. Robust control closed-loop incorporating $K_\infty(s)$ ***and the weight functions*** $W_1(s)$, $W_2(s)$ ***and*** $W_3(s)$.

2.5.2. Golver Doyle optimization algorithm

GDOA consists of solving an optimization problem to find $K_\infty(s)$, which minimizes as much as possible $\left\|F_L\left(P(s),K_\infty(s)\right)\right\|_\infty$ up to the control variable $d=K_\infty(s)\cdot e$ depends only on the error $e=V_{ref}-\tilde{v}_o$ ($d=K_\infty(s)\cdot e$) [50, 102]. This GDOA uses the state space presentation of the augmented plant, written in the following form:

$$\left[P(s)\right]=\begin{bmatrix} A & B_1 & B_2 \\ C_1 & D_{11} & D_{12} \\ C_2 & D_{21} & D_{22} \end{bmatrix} \tag{2.56}$$

where

$$P_1(s):\begin{cases}\dot{x} = A\cdot x + B_1\cdot y_{in} + B_2\cdot \tilde{d} \\ y = C_1\cdot x + D_{11}\cdot y_{in} + D_{12}\tilde{d} \\ e = C_2\cdot x + D_{21}\cdot y_{in} + D_{22}\tilde{d}\end{cases} \tag{2.57}$$

The GDOA is based on certain assumptions and theorems given as follows:

1. Assumption 1: the Controllability of (A, B_2) and the detectability of (A, C_2) must be verified.
2. Assumption 2: $rank(D_{11}) = n_{y_{in}}$ and $rank(D_{12}) = n_d$, where $n_{y_{in}}$ is the length of y_{in} and n_d is the length d.
3. Assumption 3: $\forall \omega \in R,\ rank\begin{pmatrix} A - j\omega I_n & B_2 \\ C_1 & D_{12}\end{pmatrix} = n + n_d = n+1$, where n is the order of the augmented plant $P(s)$.
4. Assumption 4: $\forall \omega \in R,\ rank\begin{pmatrix} A - j\omega I_n & B_1 \\ C_2 & D_{21}\end{pmatrix} = n + n_y = n+2$, where n_y is the length of y.
5. Assumption 5: $D_{12}^{*}\begin{bmatrix} C_1 & D_{21}\end{bmatrix} = \begin{bmatrix} 0 \\ I_{n_{\tilde{d}}}\end{bmatrix} = \begin{bmatrix} 0 \\ 1\end{bmatrix}$.
6. Theorem 1: The $K_\infty(s)$ can be designed if the following conditions are satisfied:

   The GDOA is based on the following matrix: H_∞ and J_∞, which are written as follow:

$$H_\infty = \begin{bmatrix} A & \gamma^{-2}B_1B_1^{*} - B_2B_2^{*} \\ -C_1^{*}C_1 & -A^{*}\end{bmatrix} \tag{2.58}$$

$$J_\infty = \begin{bmatrix} A^{*} & \gamma^{-2}C_1C_1^{*} - C_2C_2^{*} \\ -B_1^{*}B_1 & -A^{*}\end{bmatrix} \tag{2.59}$$

   Condition 1. H_∞, J_∞ must not have the eigenvalues in the imaginary axis.

   Condition 2. X_∞, Y_∞ are the algebraic Reccati equation solutions, where their known variables are the gains of (2.58) and (2.59).

7. Theorem 2: The resulted $K_\infty(s)$ stabilize the system if the following condition is satisfied, which is given as follows:

$$\left\| F_L\left(P(s), K_\infty(s)\right)\right\|_\infty \le \gamma, \gamma > 0 \tag{2.59}$$

Preferably, it is worth verifying the H_∞ norm of (2.59) by verifying the H_∞ norm of the gains of $\left\| F_L\left(P(s), K_\infty(s)\right)\right\|_\infty$, which must be lower than the y value resulting from the process of GDOA. That gives:

$$\begin{cases} \left\|W_1(s)S(s)\right\|_\infty \le \gamma & \rightarrow \quad \overset{a1}{\left|S(s)\right|} \le \overbrace{\dfrac{\gamma}{\left|W_1(s)\right|}}^{a2} \\ \left\|W_1(s)S(s)T_{p0}(s)W_3(s)\right\|_\infty \le \gamma & \rightarrow \quad \overbrace{\left|S(s)T_{p0}(s)\right|}^{a3} \le \overbrace{\dfrac{\gamma}{\left|W_1(s)W_3(s)\right|}}^{a4} \\ \left\|W_2(s)S(s)K_\infty(s)\right\|_\infty \le \gamma & \rightarrow \quad \overbrace{\left|S(s)K_\infty(s)\right|}^{a5} \le \overbrace{\dfrac{\gamma}{\left|W_2(s)\right|}}^{a6} \\ \left\|W_2(s)T(s)W_3(s)\right\|_\infty \le \gamma & \rightarrow \quad \overset{a7}{\left|T(s)\right|} \le \overbrace{\dfrac{\gamma}{\left|W_2(s)W_3(s)\right|}}^{a8} \end{cases} \tag{2.60}$$

where $K_\infty(s)$ can be given in the form of state-space representation as follows:

$$K_\infty(s) = \left[\begin{array}{c|c} A_\infty & Z_\infty Y_\infty C_2^* \\ \hline -B_2^* & 0 \end{array}\right] \tag{2.61}$$

A_∞ and Z_∞ are given as follows:

$$A_\infty = A + \gamma^{-2} B_1 B_1^* - B_2 B_2^* X_\infty - Z_\infty Y_\infty C_2^* C \tag{2.62}$$

$$Z_\infty = \left(I_n - \gamma^{-2} Y_\infty X_\infty\right)^{-1} \tag{2.63}$$

where $C = \begin{pmatrix} C_1 \\ C_2 \end{pmatrix}$

According to the assumptions and theorem mentioned above, the operation of GDOA is presented by the following steps:

- Step 1: forming the augmented plant $P(s)$.
- Step 2: determining the weight functions $W_1(s)$, $W_2(s)$ and $W_3(s)$.

- Step 3: giving an initial value for γ ($\gamma = \gamma_0$).
- Step 4: verifying assumptions 1, 2, 3, 4, and 5
- Step 5: verifying conditions 1 and 2 (see Theorem 1).
- Step 6: calculating $K_\infty(s)$ using (2.61).
- Step 7: verifying the condition (2.60).
- Step 8: if (2.60) is satisfied, the GDOA stops, and the wanted $K_\infty(s)$ is calculated in step5. If (2.60) is not satisfied, the algorithm's execution returns to step 5 after decreasing the γ value by a fixed-step $\Delta\gamma$ (the value $\Delta\gamma$ must be chosen before operating the algorithm of GDOA. when $\Delta\gamma$ is smaller, The GDOA is more reliable).

These steps of the GDOA process operation can be summarized in the flowchart, illustrated in Fig 2.13.

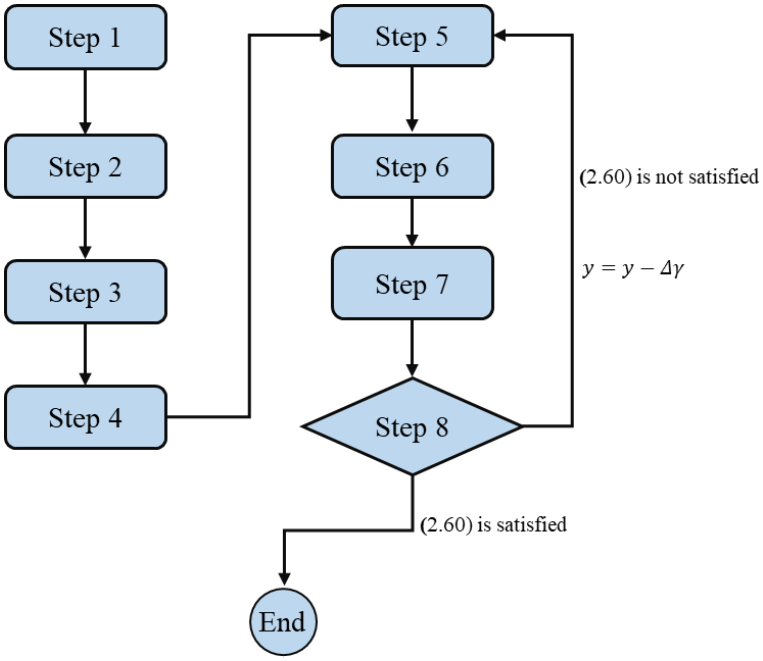

Fig 2.13. GDOA flowchart.

2.5.3. Weigh function determination

$K_\infty(s)$, which is designed with the help of the weight functions: $W_1(s)$, $W_2(s)$, and $W_3(s)$, ensures the control objectives by making the functions regathered in the set *SF* stable($SF = \{S(s), S(s)T_{p0}(s), S(s)K_\infty(s), T(s)\}$), which relate the disturbances V_{ref} and ω_T to the error ε and duty-cycle d , stable. To understand the way of determining the mathematical

expression of these weight functions with their known constant parameters. This section presents an example of the determination of $W_1(s)$ based on $S(s)$ behavior in the frequency domain.

$S(s)$ links the disturbance variable V_{ref} to the output e. If $S(s)$ is an unstable transfer function due to the CPL problem, disturbances, and ineffective control, in the frequency domain, the gain of $S(s)$ in dB ($20\log_{10}(|S(s)|)$) is bigger than 0 dB, and the phase of $S(s)$ is small then $-\pi$, as illustrated in Fig 2.14a, marked by (1) and (2), respectively, in the interval of the frequencies corresponding to the bandwidth ($\omega \in [0, \omega_c]$, where ω_c is the cutoff frequency). Also, the $S(s)$ phase could be smaller than $-\pi$ on overall frequencies in the instability case, as illustrated in Fig 2.14a marked by (3). If $K_\infty(s)$ is implemented in the studied system, the $S(s)$ gain in dB must become very low than 0 dB to mitigate the effect of V_{ref}, and $S(s)$ phase must become bigger than $-\pi$ in the interval of frequencies corresponding to the bandwidth, as illustrated in Fig 3.14b marked by (4) and (6). Also, $K_\infty(s)$ can provide to $S(s)$ a phase bigger than $-\pi$ on overall frequencies, as illustrated in Fig 2.14b marked by (5).

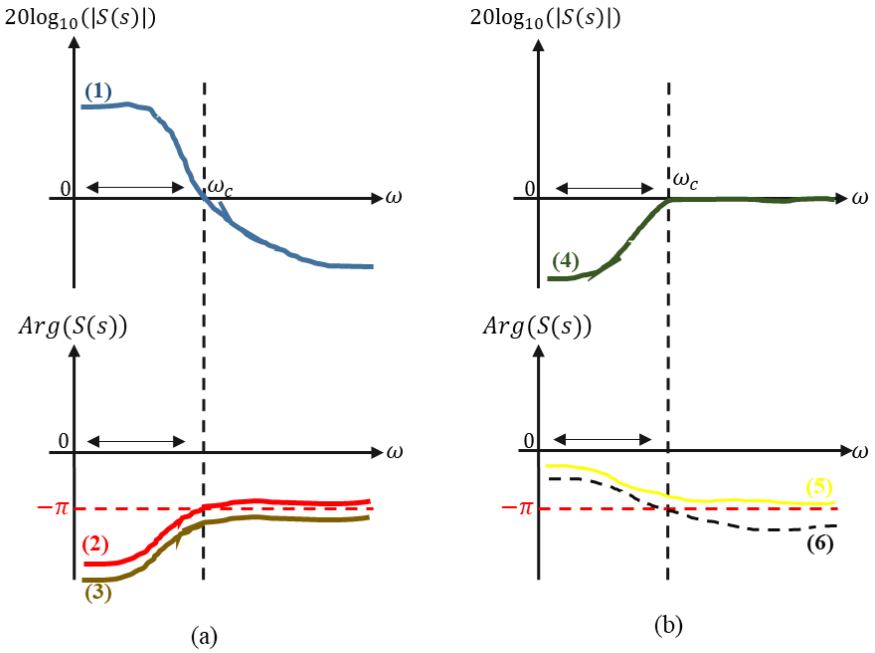

Fig 2.14. a) Frequency behavior of the unstable transfer function $S(s)$, b) Frequency behavior of the stable transfer function $S(s)$.

Therefore, $K_\infty(s)$ aims to assign the behavior to $S(s)$ in the frequency domain, as illustrated in Fig 2.15, where the maximum value of $S(s)$ gain in dB tends towards ΔG, which is the gain margin of the open-loop control that has the function presented by $K_\infty(s)T_p(s)$, and the minimum value of $S(s)$ gain in dB tends towards $20\log_{10}(\varepsilon)$, where ε is the steady-state error [104].

According to $S(s)$ behavior illustrated in Fig 2.15 and based on (2.60), $W_1(s)$ can be determined from the asymptotes of $S(s)$ and can have the mathematical expression written as follows:

$$W_1(s)=\frac{1}{K_1}\frac{s+\omega_1 K_1}{s+\omega_1 k_1} \tag{2.64}$$

The constant parameters of $W_1(s)$: K_1 and k_1 are identified from the extremum of $S(s)$ that can be written as follows:

$$K_1=e^{-\frac{\log(10)}{20}\Delta G} \tag{2.65}$$

$$k_1=\varepsilon \tag{2.66}$$

ω_1 can be chosen small than ω_c or equal to ω_c $(\omega_1\approx\omega_c)$, where ω_c, ε and ΔG represents the performances of the system that must be ensured by the controller, which are related to settling time and steady-state error.

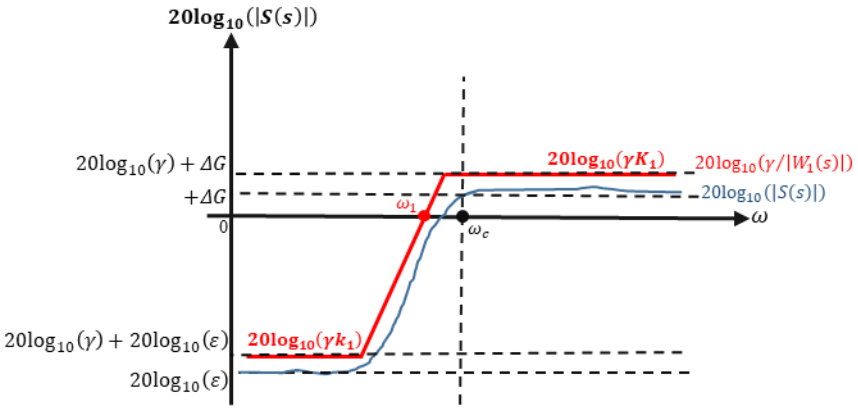

Fig 2.15. *$S(s)$ behavior assigned by $K_\infty(s)$.*

$W_2(s)$ and $W_3(s)$ are determined in the same way as $W_1(s)$ based on the stable behavior of $S(s)T_{p_0}(s), S(s)K_\infty(s)$ and $T(s)$. Their mathematical expression can be written as follows:

$$W_2(s) = \frac{1}{k_2}\frac{s+\frac{\omega_c}{K_2}}{s+\frac{\omega_c}{k_2}} \tag{2.67}$$

$$W_3(s) = K \tag{2.68}$$

Where their constant parameters are given as follows:

$$K_1 = K_2 \tag{2.69}$$

$$\omega_2 = \omega_1 \tag{2.70}$$

K can be chosen small than ε or equal to ε ($K \approx \varepsilon$).

2.6. Stability analysis

In this section, an analysis is carried out to verify if the functions gathered in the set $SF = \{S(s), S(s)T_{p_0}(s), S(s)K_\infty(s), T(s)\}$ have the behaviors in the frequency domain as the desired one described in section 2.5.3 when $K_\infty(s)$ is applied. Performing this analysis uses a singular value plot after obtaining $K_\infty(s)$ using the GDOA process performed in Matlab software, which uses the DC/DC converter parameter listed in Table 2.1.

Tab 2.1. DC/DC buck converter parameters.

Variables	Description	Values
V_{ref}	Output voltage reference	140V
V_{in}	Input voltage (provided by RES)	280V
C_0	Capacitance nominal value	220μF
L_0	Inductance nominal value	2.7mH
r_L	Inductance parasite resistance	0.8Ω
f_s	Switching frequency	25kHz

Based on the parameters of the DC/DC buck converter listed in Tab 2.1, the GDOA provides the following $K_\infty(s)$:

$$K_\infty(s)=\frac{733.6s^3+5.869\cdot10^3s^2+7.011\cdot10^3s+4.987\cdot10^{16}}{s^4+4.351\cdot10^6s^3+1.696\cdot10^{11}s^2+3.188\cdot10^5s+2.55\cdot10^5} \quad (2.71)$$

The weight functions used to perform $K_\infty(s)$ are written as follows:

$$\begin{cases} W_1(s)=\dfrac{0.75s+8\cdot10^3}{s+0.8} \\ W_2(s)=\dfrac{10^3s+6\cdot10^7}{s+6\cdot10^7} \\ W_3(s)=5\cdot10^{-5} \end{cases} \quad (2.72)$$

where $\gamma=1.28$ and $\omega_c=8.10^3 rad/s$.

According to the singular value plot illustrated in Fig 2.16, the conditions described in (2.60) are satisfied. The gain magnitudes of the functions gathered in the set *SF* are smaller than 0 dB in the interval of frequencies corresponding to the bandwidth. This singular value plot shows That the obtained controller $K_\infty(s)$ can mitigate the effect of the disturbances V_{ref} and ω_T as follows:

It is known that the functions gathered in set *SF* relate the disturbances to the duty cycle and steady-state error, which can be written as follows:

$$\begin{cases} e=S(s)\cdot V_{ref}+S(s)T_{p0}(s)\omega_T \\ \tilde{d}=S(s)K_\infty(s)\cdot V_{ref}-T(s)\omega_T \end{cases} \quad (2.73)$$

where (2.73) is obtained based on (2.51) without considering the presence of the weight functions. According to Fig 2.16, the magnitudes of the functions of SF are small than 1 ($|S(s)|<<1, |S(s)T_{p0}(s)|<<1,\quad |S(s)K_\infty(s)|<<1, |T(s)|<<1$). That shows that the disturbances do not have a considerable effect on the duty cycle and the error. The duty cycle only depends on the error.

According to Fig 2.17, the phases of the functions of *SF* are bigger than $-\pi$ in the frequencies interval corresponding to the bandwidth. That shows that the functions: $S(s)$, $S(s)T_{p0}(s)$, $S(s)K_{\infty}(s)$ and $T(s)$ are stable. Therefore, it can be concluded that, $K_{\infty}(s)$ ensure the stability of DC/DC converter by mitigating the effect of CPL.

The pole evolution analysis is carried out after and before applying $K_{\infty}(s)$, as illustrated in Fig 2.18, where the placement of the poles marked by the red color denotes the poles of the system before applying $K_{\infty}(s)$, and the placement of the poles marked by the blue color denotes the poles of the system after applying $K_{\infty}(s)$. This analysis is performed in the discrete-time domain. According to Fig 2.18, $K_{\infty}(s)$ assigns for the system the poles in the stable region. Before applying $K_{\infty}(s)$, the system has poles in the unstable region due to the presence of CPL. This analysis proves that the voltage control closed-loop is improved in terms of robustness and stability due to the application of $K_{\infty}(s)$. Here. The CPL and disturbances do not affect the system stability.

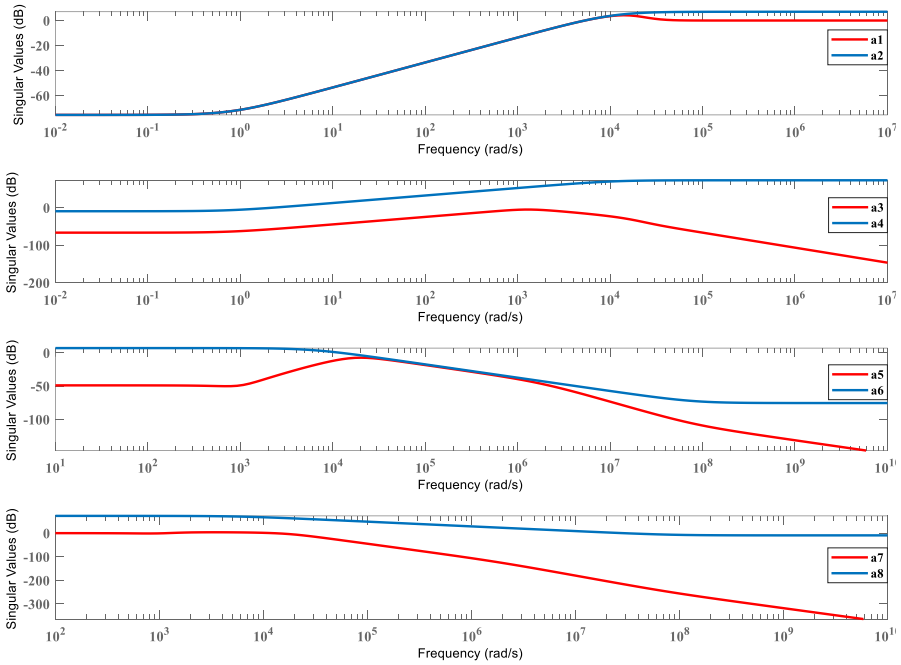

Fig 2.16. Gain behavior of $S(s)$, $S(s)T_{p0}(s)$, $S(s)K_{\infty}(s)$, $T(s)$, $\gamma / W_1(s)$, $\gamma / (W_1(s)W_3(s))$, $\gamma / W_2(s)$ ***and*** $\gamma / (W_2(s)W_3(s))$ ***marked by a1, a2, a3, a4, a5, a6, a7, and a8, respectively.***

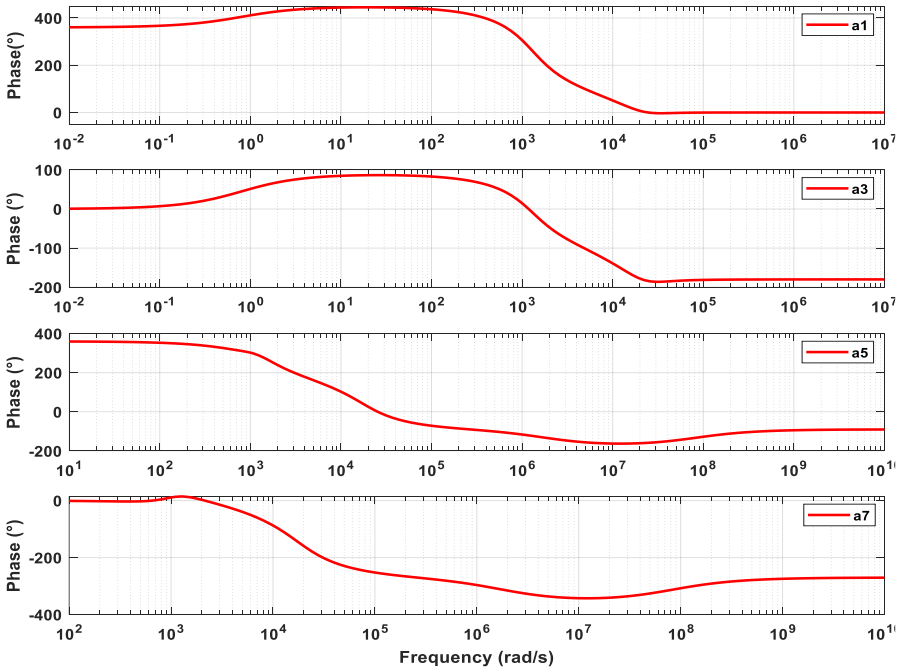

Fig 2.17. Phase behavior of $S(s)$, $S(s)T_{p_0}(s)$, $S(s)K_\infty(s)$ ***and*** $T(s)$ ***marked by a1, a3, a5, a7, respectively.***

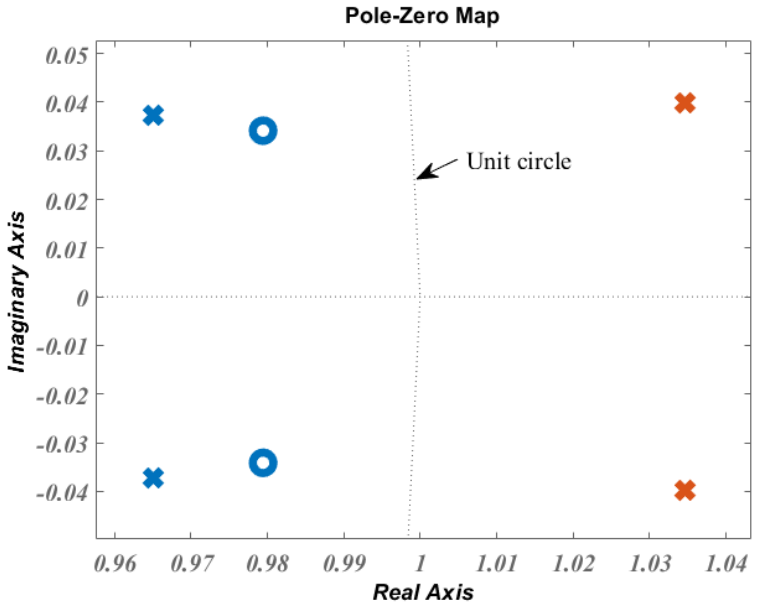

Fig 2.18. Pole evolution of the system after and before applying $K_\infty(s)$.

2.7. Simulation study

The simulation study is performed in PSIM software, as illustrated in Fig 2.9, to verify the $K_\infty(s)$ effectiveness to mitigate the CPL issue, disturbances, and parametric faults, where the parameter of the DC/DC buck converter are same listed in Tab 2.1 and $K_\infty(s)$ is the same calculated in section 2.7. The parametric faults represent the variation of the parameters, which

go over the accepted limits. For instance, in the presence of the parameter uncertainties, the value of inductance *L* in the nominal condition is given as follows: $L_0 - \delta_L L_0 \le L \le L_0 + \delta_L L_0$. If the fault occurs in *L*, the value of *L* may go over $L_0 + \delta_L L_0$ or down $L_0 - \delta_L L_0$, where the relative uncertainty δ_L is estimated at around 5% in the nominal condition of the system.

The simulation is subdivided into three scenarios. The first scenario is performed to assess the $K_\infty(s)$ effectiveness of maintaining the stability of the DC/DC buck converter feeding CPL. In the first scenario, the CPL is simulated using a controlled current source. Thus, it lets adjusting the power P_{CPL} demanded by the CPL, as illustrated in Fig 2.20. This way allows testing the $K_\infty(s)$ capability to maintain the DC/DC buck converter stability at different levels and mitigate the disturbances arising from the fluctuations of load current. In this scenario, v_{in} is kept at 280V, and the voltage reference is 140V.

The second scenario shows the $K_\infty(s)$ capability to attenuate the disturbance arising from the input voltage v_{in}. In this scenario, the disturbance is caused by a sudden variation of v_{in}, as illustrated in Fig 2.22. At the beginning of the simulation scenario, v_{in} is kept at 280V. At 2s, v_{in} decreases by 15V to reach 265 V. From 3s, v_{in} returns to 280V, where P_{CPL} is kept at 500W and the voltage reference is 140V.

The last scenario is realized to assess the $K_\infty(s)$ capability to ensure system performance in the presence of the parametric faults, which occur in the inductance *L* and capacitance *C*. These faults represent the parameter variations, which exceeds 5%, as illustrated in Fig 2.23. At the beginning of the simulation of this scenario. the values of *L* and *C* are kept at the nominal values. At 3s, the values of *L* and *C* decrease to reach $L = L_0 - 30\%L_0$ and $C = C_0 - 30\%C_0$. At 6s, the values of *L* and *C* increase to reach $L = L_0 + 30\%L_0$ and $C = C_0 + 30\%C_0$. All simulation results are depicted in Fig 2.21, Fig 2.22, and Fig 2.24**.** and the parameters of the simulated system are the same listed in Table 2.1.

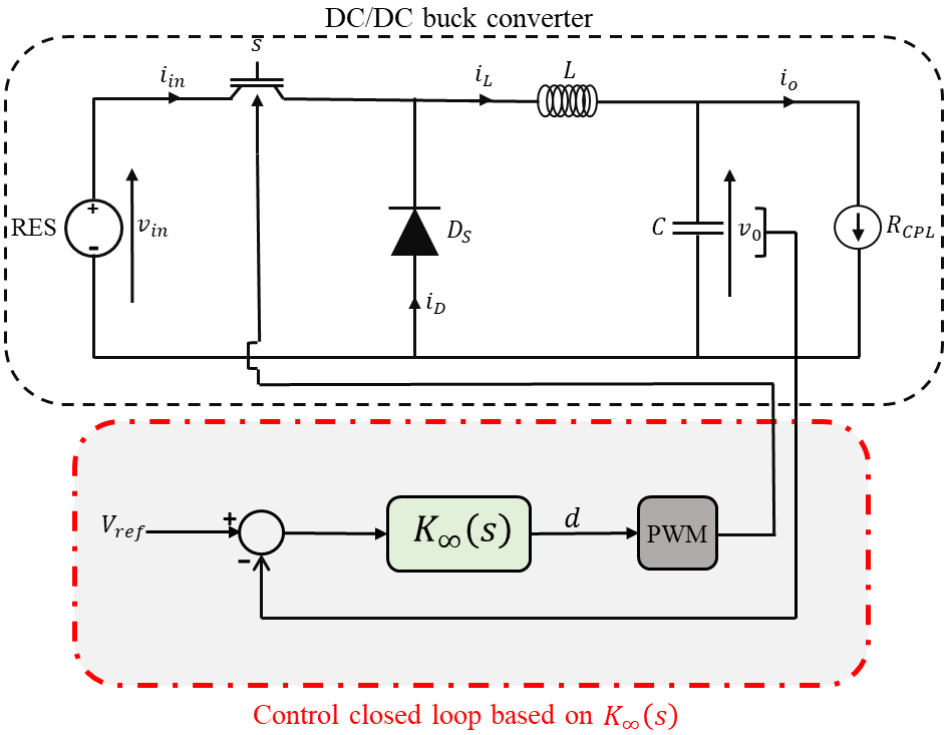

Fig 2.19. DC/DC buck converter operating under $K_\infty(s)$ simulated in PSIM software.

According to Fig 2.21, the v_0 response reaches the reference 140V after a settling time of 0.04s, and this response has no overshoot. Also, the i_0 fluctuation arising from the P_{CPL} step variations cause the transient small deviations that appear in the short duration, which are zoomed in and marked by A, B, and C. These transient deviations have the magnitude of 1.7V. After that, these deviations are smoothed and v_0 is kept at the reference value. As the v_0 response does not have an overshoot in the transient dynamic response and oscillations, it is concluded that the damping factor of the DC/DC buck converter increases due to the application of $K_\infty(s)$. Moreover, the disturbances arisen from the i_0 fluctuation do not have a considerable effect on the v_0 response due to the application of $K_\infty(s)$. Therefore, this scenario proves the effectiveness of $K_\infty(s)$ to maintain the stability of the DC/DC buck converter in the presence of CPL and mitigate the disturbances arising from the i_0 fluctuation.

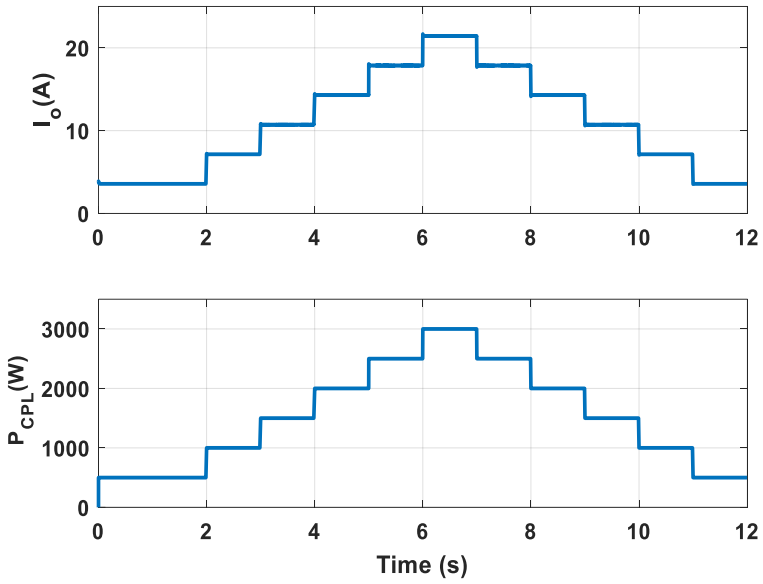

Fig 2.20. Behaviors of i_o and P_{CPL} resulted from the first scenario.

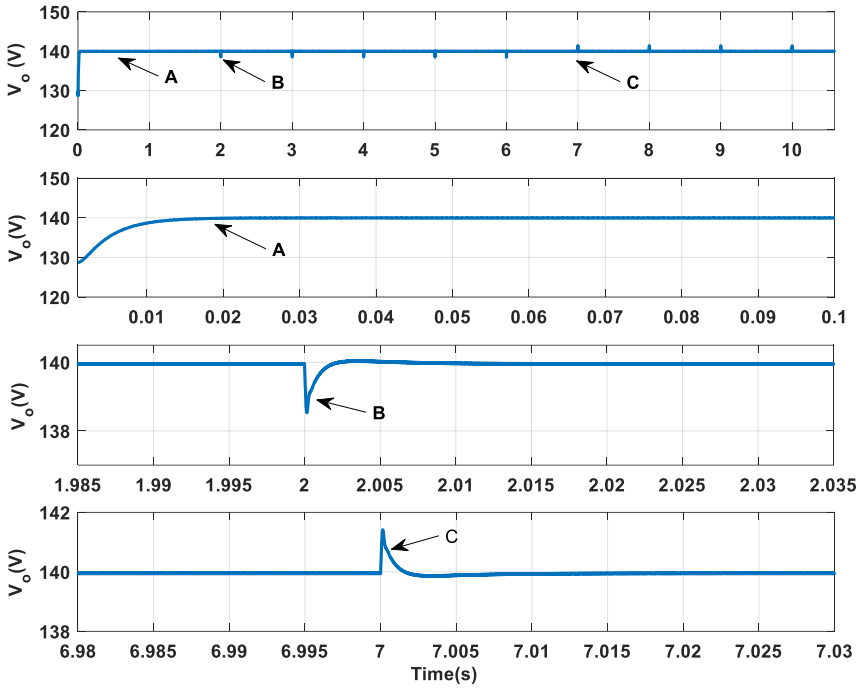

Fig 2.21. Behavior of V_0 resulted from the first scenario.

According to Fig 2.22, the disturbance arising from the sudden variation of v_{in} does not have a considerable effect as the fluctuations of i_0 when $K_\infty(s)$ is applied. The sudden variation of v_{in} causes two small transient deviations when v_{in} decreases to reach 265V and v_{in} increases to be kept at 280V. After that, these deviations are smoothed and v_0 is kept at 280V. Actually, this scenario is carried out to simulate the effect of the fluctuation of the RES output voltage due to

the natural elements' intermittency on the output voltage v_0 under the application of $K_\infty(s)$. According to Fig 3.1, the RES output voltage is illustrated by v_{in}. Therefore, this scenario shows that $K_\infty(s)$ can mitigate the disturbance arising from the RES output voltage fluctuations.

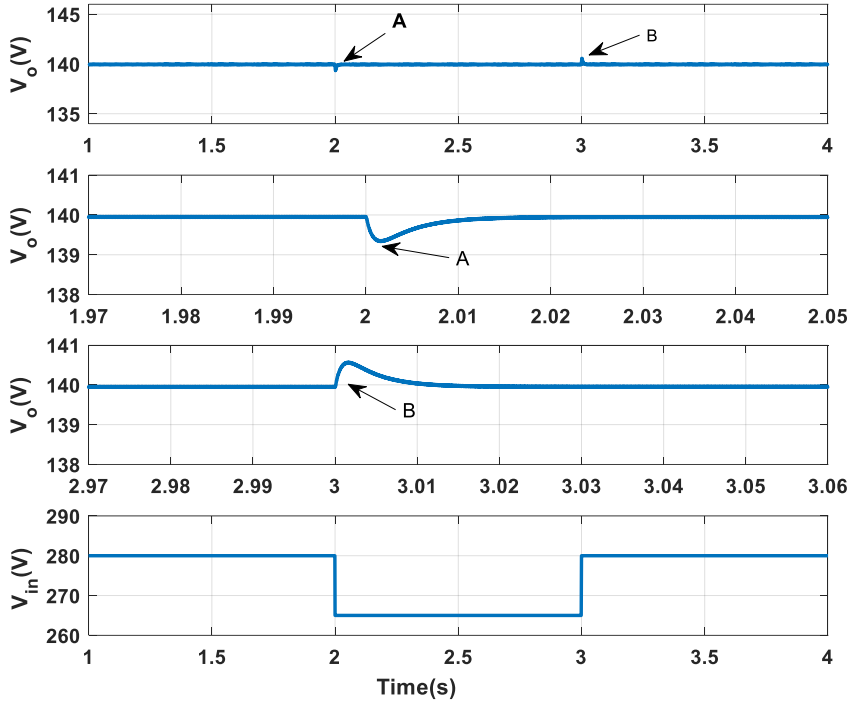

Fig 2.22. Behavior of V_0 resulted from the second scenario.

According to Fig 2.24, the components faults simulated in the components *L* and *C* of the DC/DC buck converter cause the transient deviations of, which are zoomed in and marked by A and B. these transient deviations have the magnitude of 20V and appear in short duration. According to obtained results of this scenario, the applied controller $K_\infty(s)$ smooths these deviations caused by the component faults by forcing the output voltage to return to the voltage reference value.

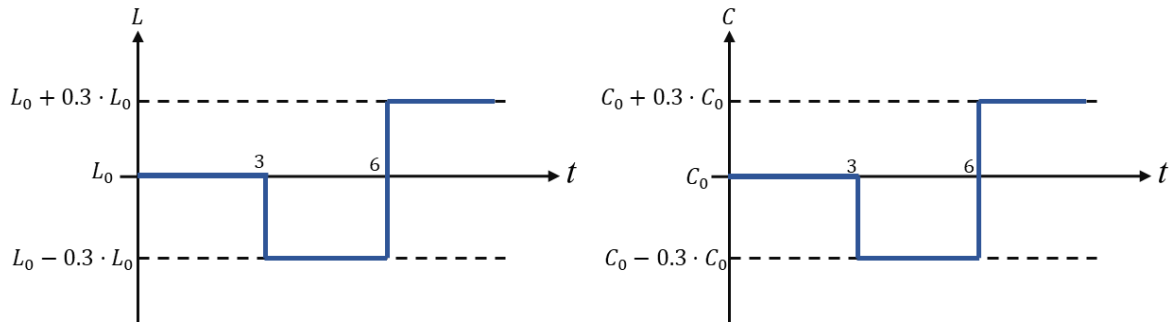

Fig 2.23. variation of C and L due to faults.

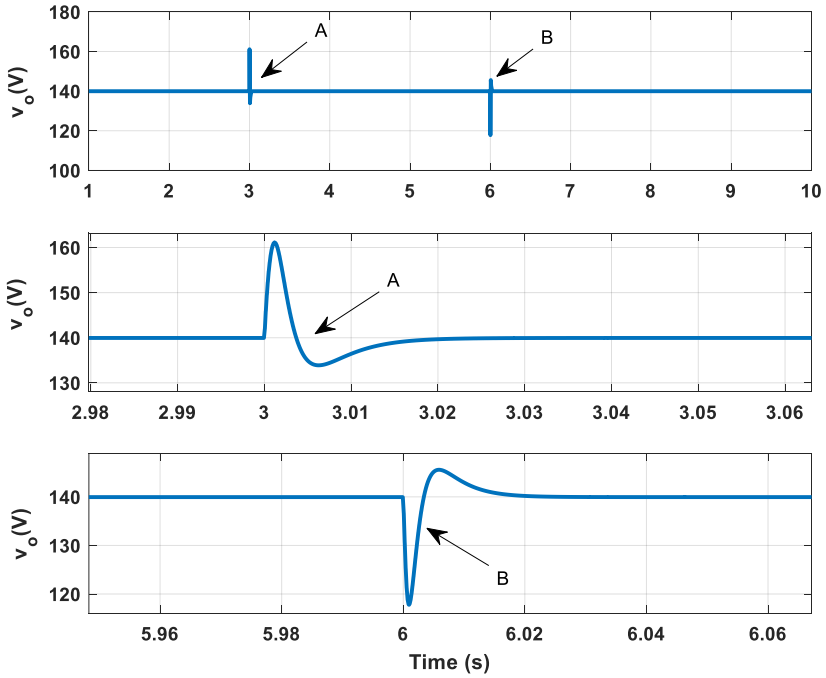

Fig 2.24. Behavior of V_0 resulted from the second scenario.

2.8. Conclusion

This chapter presents the process of designing H∞-based control using the GDOA algorithm, which requires an augmented plant obtained from the voltage robust control scheme. This augmented system incorporates the uncertain model and weight functions. These weight functions represent the constraints of the optimization problem to reach the control performances wanted from the proposed approach. The obtained results show the effectiveness of the H∞ based control to avoid the instability problem due to the presence of CPL for different levels of the consumed power P_{CPL} . Also, the developed approach mitigates the negative effect of the disturbances and component faults, where the system disturbances cause the small transient deviations, which will be smoothed due to the application of H∞ based control.

On the other hand, the component faults cause a considerable magnitude of transient deviations compared to the transient deviation caused by system disturbances. However, the H_∞ based control provides the necessary control law to avoid these deviations caused by component faults. Moreover, the simulation study proves the accuracy of determining the weight functions used to obtain the robust controller.

Chapter 3: Robust Hierarchical control of DC microgrid.

3.1. Introduction

Due to CPL's INI characteristic, the instability issue worsens when the CPL is present in the parallel connection of DC/DC buck converters and can worsen due to the disturbances and possibility of faults [45–60, 80]. In this case, the control hierarchy based on the conventional controllers meets the difficulties of regulating the electrical parameters (voltage and current), which are required to ensure a power flow needed to feed the load [45]. The robustness of this control hierarchy against the perturbation arising from the CPL and faults can be improved using the passive and active damping techniques and nonlinear controls. These techniques can be used to enhance the primary control level. In this case, the primary control level can sufficiently increase the damping factor of system components. However, these techniques have some drawbacks. These drawbacks are presented in the following points: the passive damping technique deteriorates the system efficiency due to the power loss. The active damping technique can deteriorate the performance of the control hierarchy. Performing the secondary control level becomes difficult or impossible if the primary control level is performed based on the nonlinear control techniques. This chapter presents in detail the process of H_∞ based control design used to enhance the control hierarchy robustness. This process design consists of GDOA and NOA algorithms, which provide H_∞ and structured H_∞ controllers [50,105].

The H_∞ controller is integrated into the primary control level, and the structured H_∞ controller is integrated into the secondary control level. This structured H_∞ controller has a fixed structure. This fixed structure is the same as the PI controller and is required by the secondary control level to satisfy certain conditions of secondary control operation. The GDOA is explored in detail in the third chapter. The NOA algorithm is presented in detail in this chapter. This NOA solves an optimization problem to obtain the structured H_∞ controller. It also requires an augmented system derived from the uncertain model of the parallel interconnection of DC/DC buck converter feeding CPL. This augmented plant also includes the weight functions determined using the same method presented in section 2.5.3. These weight functions present the constraint and help derive a robust controller that can ensure the wanted performances. The developed robust control hierarchy shares the most characteristic with the one developed by [40]. But the proposed approach provides some improvement by avoiding the use of current measurement that can cause filtering degradation. Also, the proposed approach avoids the use of the passive load to guarantee stable operation. Matlab and Psim software's are used to carry out the simulation study that is subdivided into four scenarios to validate the proposed approach

3.2. System and hierarchical control configuration

Fig 3.1 illustrates the complete DC-MG system, consisting of a parallel interconnection of electrical generators connected to a common DC bus through the transmission lines, where the transmission lines impedances are not neglected and presented by z_{line_1}, z_{line_2} ,….., z_{line_n} . Each electrical generator is performed by DC/DC buck converter and DC source, where the DC sources can be equivalent representations of RES elements, and in this study, we have chosen the DC/DC buck converter to be integrated into this DC-MG configuration since the DC/DC buck converter has a simple structure and is easy to be controlled.

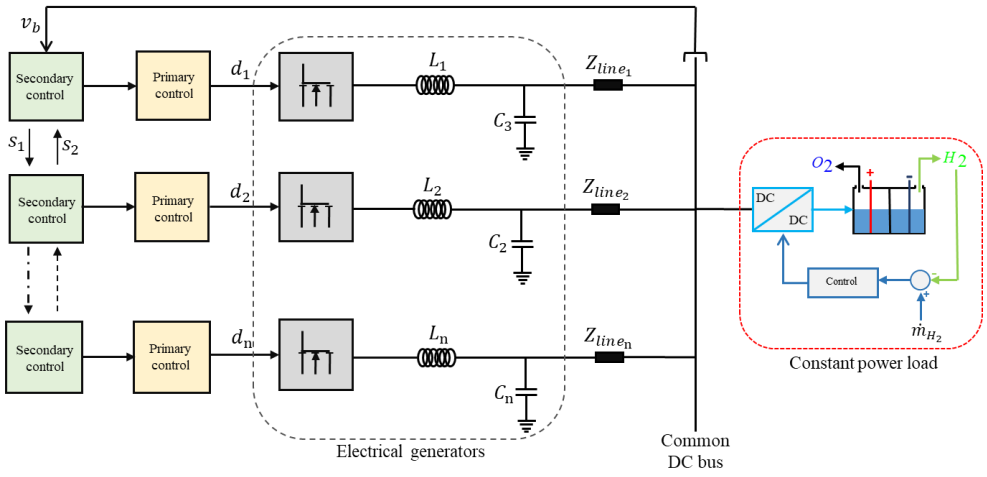

Fig 3.1. Parallel interconnection of electrical generators feeding constant power load.

In this configuration of DC-MG, all power produced by the electrical generators is consumed by the local. In this Fig 3.1, the local load is illustrated by the electrolyzer system, where the hydrogen production is controlled. Due to that, the electrolyzer consumes a constant power and earns the characteristic of CPL. Therefore. This configuration allows validating the effectiveness of the developed control to ensure better power-sharing and stability systems in the presence of CPL. The presented DC-MG does not incorporate the storage device since the DC sources provide unlimited power, and there is no surplus or power deficiency.

The developed robust control that will be validated using the DC-MG configuration, illustrated in Fig 3.1, consists of two levels: primary and secondary controls. The robust hierarchical control scheme is illustrated in Fig 3.2. This robust hierarchical control scheme shares almost the same characteristics as the one developed by [40]. However, it cannot have better power-sharing and robustness against the instability and components faults in the presence of CPL. The developed work aims to avoid these issues by enhancing this hierarchical control scheme.

This enhanced hierarchical control scheme will incorporate the H∞ and structured H∞ based controls.

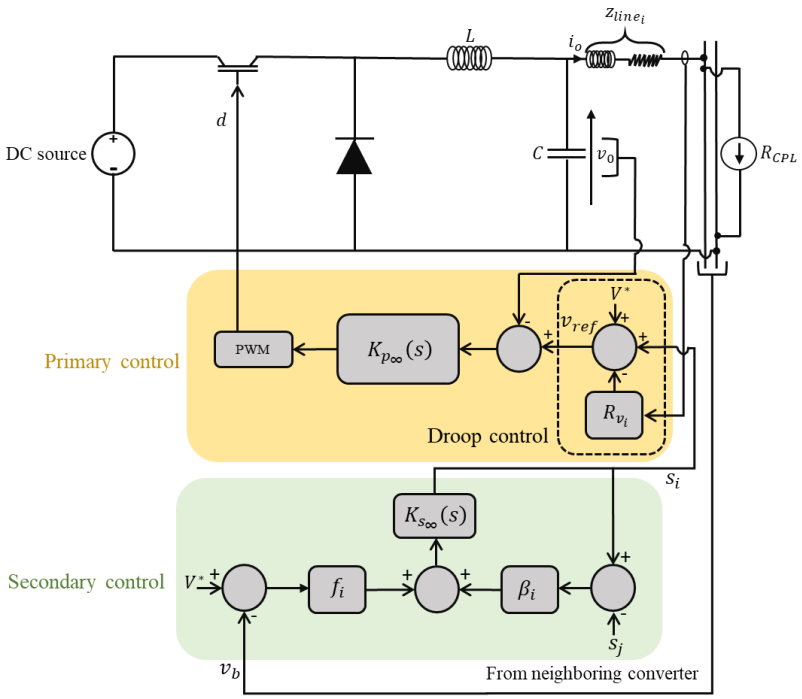

Fig 3.2. Robust hierarchical control scheme.

According to Fig 3.2, the primary control consists of the robust voltage loop and droop controls. The robust voltage loop control incorporates the robust controller $K_{P_\infty}(s)$ whose process of design is presented in chapter 2. This robust controller provides the control law (duty-cycle) by using the signal error ($v_{ref} - v_o$). The control law given by $K_{P_\infty}(s)$ is converted to PWM signal to operate the DC/DC buck converter. The voltage reference v_{ref} is provided by the droop control. It can be written as follow:

$$v_{ref} = v^* - R_v \cdot i_o + s_i \tag{3.1}$$

where R_v is the virtual impedance employed by the droop control to avoid the current circulating and s_i is the compensation voltage signal.

The secondary control is decentralized, developed to maintain the DC bus voltage at the related value v^*. Thus, the voltage deviation caused by the primary control will be avoided. According to Fig 3.2, each decentralized secondary has the same structured H∞ based controller $K_{s_\infty}(s)$. All the decentralized secondary controllers provide the same compensation voltage signals:

$s_1 = ... = s_i = ... = s_n$, where i is the index of DC/DC buck converter and n is the number of DC/DC buck converters integrated into the system. In this decentralized secondary control scheme, $K_{s_\infty}(s)$ must have a fixed structure, which has the same structure as PI control. It can be written as follows:

$$K_{s_\infty}(s) = K_{p_\infty} + \frac{K_{i_\infty}}{s} \tag{3.2}$$

where K_{p_∞} and K_{i_∞} are the gain of structured H_∞ based controller calculated based on Nonsmooth optimization algorithm (NOA).

The structured H_∞ based controller $K_{s_\infty}(s)$ generates s_i by using the error signal, which is given as follows:

$$e = f_i \cdot \left(v^* - v_b\right) + \beta_i \left(s_i - s_j\right) \tag{3.3}$$

The compensation voltage signal s_j is provided by the neighboring DC/DC buck converter through a network, which has the characteristic of a laplacian graph. This network is performed at the secondary control level. It lets the decentralized secondary controllers exchange information regarding their compensation voltage signal. Also, this network improves the performances of the hierarchical control as the possibility of providing the v_b measurement to one decentralized secondary controller. No need to provide v_b measurement to all decentralized secondary controllers.

The coefficients f_i and β_i have to be chosen properly to ensure a stable operation for the secondary control. These coefficients (f_i, β_i) are obtained when the following criteria is satisfied:

Let define the matrix Z that is written as follows:

$$Z = -\left(-f\left|R_{CPL}\right|1_{n\times 1} \cdot 1_{n\times 1}^T \cdot A^{-1} + \beta L\right) \tag{3.4}$$

The secondary control has a sable operation when the matrix Z is Hurwitz. Therefore, f and β have to be chosen properly to make Z a Hurwitz matrix

where f and β are the diagonal matrix written as follows:

$$f = diag\left(f_1,...,f_i,...,f_n\right) \tag{3.5}$$

$$\beta = diag\left(\beta_1,...,\beta_i,...,\beta_n\right) \tag{3.6}$$

R_v and Z_{line} are the diagonal matrix including the virtual impedance used by the primary controllers and the impedance of transmission lines, respectively. They are written as follows:

$$R_v = diag(R_{v_1},...,R_{v_i},...,R_{v_n}) \tag{3.7}$$

$$Z_{line} = diag\left(z_{line_1},...,z_{line_i},...z_{line_n}\right) \tag{3.8}$$

A is given as follows:

$$\gamma = \gamma_0 - \Delta\gamma \tag{3.9}$$

3.3. Modeling of the parallel interconnection of DC/DC buck converters

Carrying out the robust hierarchical control requires a model That describes the physical relation between the DC bus voltage and the output voltages of the DC/DC buck converter. Also, this model has to include the disturbance and overall uncertainties. The process to obtain this model starts with the average linear equivalent circuit of the DC/DC buck converter, as illustrated in Fig 3.2, where the impedance of the transmission line is not neglected, and this equivalent circuit shows the interconnection of DC/DC buck converter with the other DC/DC buck converters.

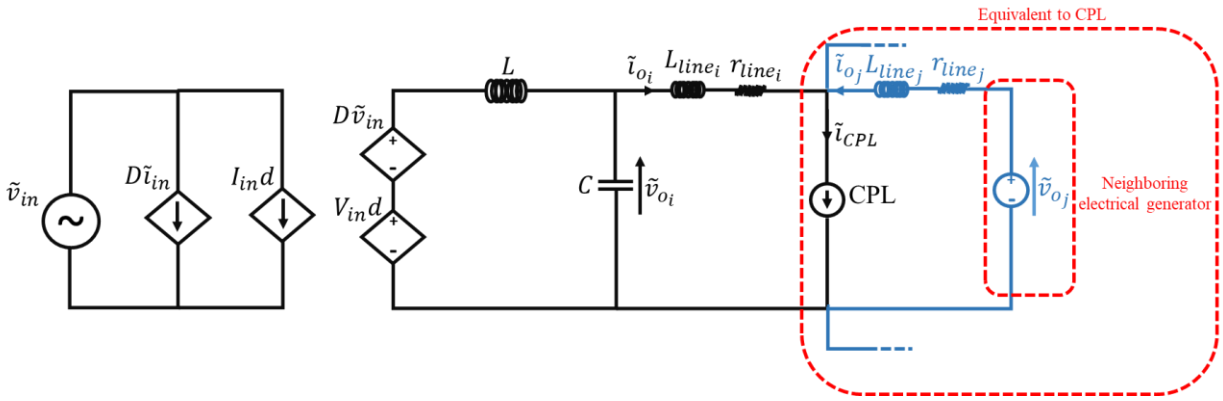

Fig 3.3. Equivalent circuit of DC/DC buck converter interacting with the other DC/DC buck converter.

Supposing that the power lost in the transmission line is neglected, the primary control is applied, and the power sharing is maintained in the system, the DC/DC buck converters will

provide the same output current. Hence, the part, which gathers the CPL and the neighboring DC/DC buck converters can be equivalent to CPL, which consumes P_{CPL}/n.

According to this supposition and section 2.3, the DC/DC buck converter is considered a MISO system, as illustrated by the block diagram in Fig 3.4, where $T_p(s)$, $M_v(s)$ and $Z_o(s)$ are the transfer functions that link the input variables: $\tilde{v}_{in}$, $\tilde{i}_{o_i}$ and *d* with the output variable $\tilde{v}_i$.

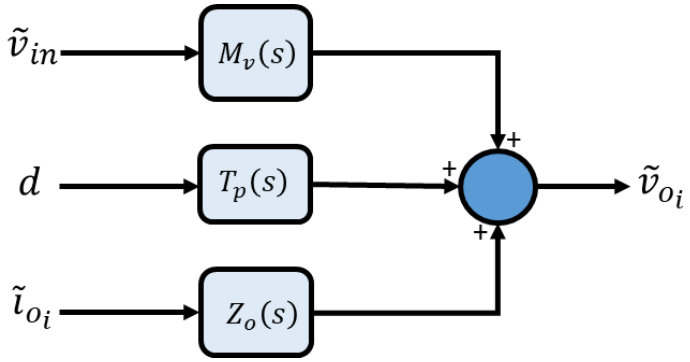

Fig 3.4. Block diagram of DC/DC buck converter model considering the presence of transmission line impedance.

In this case, the DC/DC buck converter model considers the transmission line impedance denoted by the following terms: L_{line_i} and r_{line_i}. The terms L_{line_i} and r_{line_i} are included in the mathematical expression of these transfer functions: $T_p(s)$, $M_v(s)$ and $Z_o(s)$. They are written as follows:

$$T_p(s) = V_{in}\frac{\left(r_{line_i}+R_{CPL}\right)+L_{line_i}s}{Ls\left(1+\left(r_{line_i}+R_{CPL}\right)Cs+CL^2s^2\right)+L_{line_i}s+r_{line_i}+R_{CPL}} \quad (3.10)$$

$$M_v(s) = D\frac{\left(r_{line_i}+R_{CPL}\right)+L_{line_i}s}{Ls\left(1+\left(r_{line_i}+R_{CPL}\right)Cs+CL^2s^2\right)+L_{line_i}s+r_{line_i}+R_{CPL}} \quad (3.11)$$

$$Z(s) = \frac{Ls\left(r_i+R_{CPL}+L_is\right)}{Ls\left(1+\left(r_{line_i}+R_{CPL}\right)Cs+CL^2s^2\right)+L_{line_i}s+r_{line_i}+R_{CPL}} \quad (3.12)$$

Exploiting the study presented in section 2.4 and definition 2.1, the robust closed loop of the primary control can be presented as illustrated in Fig 3.5. It includes the uncertain model of DC/DC buck converter, where $\Delta_1(s)$, $\Delta_2(s)$ and $\Delta_3(s)$ are the uncertain transfer matrix that

describes the whole uncertainties of the system and ω_T are the variable, which is the sum of the known disturbances that act on the control variable d .

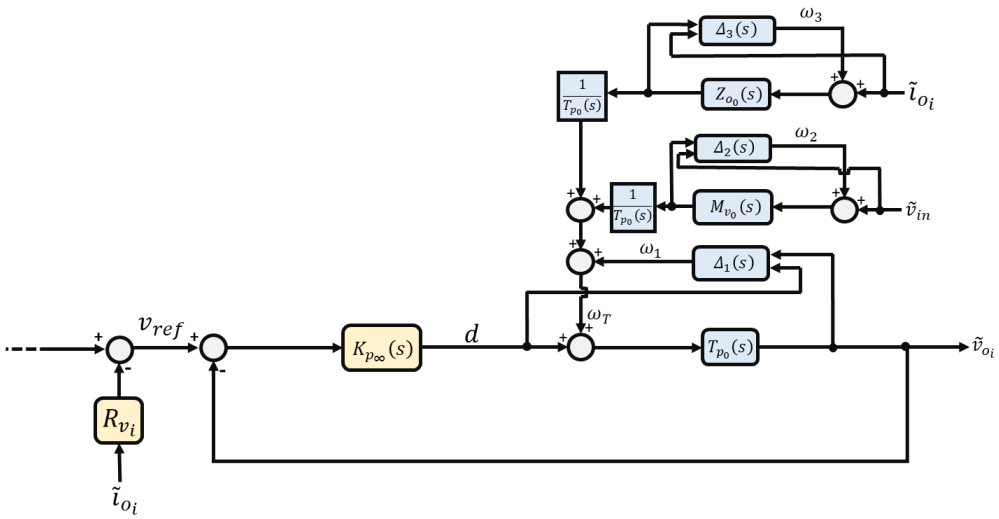

Fig 3.5. robust primary control closed loop.

The remaining part of this section focuses on modeling the physical relation between the DC bus voltage v_b and the output voltages of the DC/DC buck converters ($v_1,\ldots,v_i,\ldots,v_3$). This modeling uses the equivalent circuit of the parallel interconnection of DC/DC buck converters, illustrated in Fig 3.6.

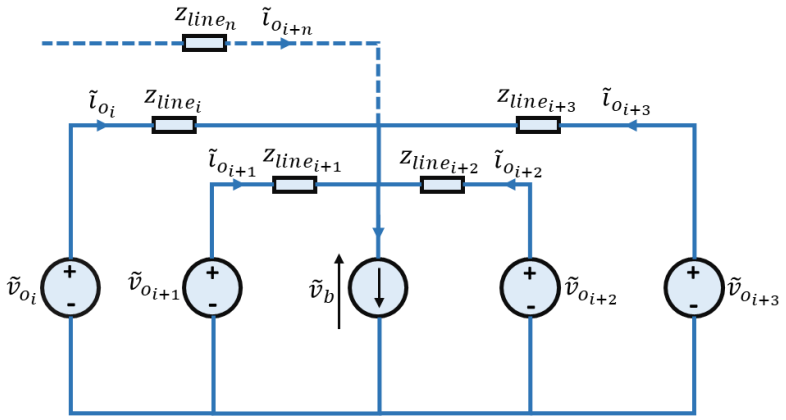

Fig 3.6. equivalent circuit of the parallel interconnection of DC/DC buck converters.

Definition 3.1 (Superposition theorem): consider an example of an electrical circuit that supplies an impedance load consisting of three voltage DC sources, as illustrated in Fig 3.7. In this example, we aim to find how i_1 , which flows in the branch marked by (1), can be described by the other parameter of the electrical circuit (v_1 , v_2 , v_3 , z_1 , z_2 and z_3).

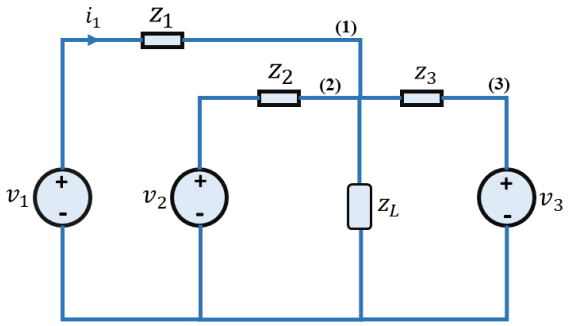

Fig 3.7. Electrical interconnection integrating three voltage sources to supply the load z_L.

Based on the superposition theorem, i_1 can be given as follows:

$$i_1 = \sum_{t=1}^{3} i_t' = i_1' + i_2' + i_3' \tag{3.13}$$

where

- t goes from 1 to 3 because the number of the sources integrated into the electrical circuit is three.
- Case 1: v_1 provides i_1' by considering $v_2 = 0$ and $v_3 = 0$.
- Case 2: v_2 provides i_2' by considering $v_1 = 0$ and $v_3 = 0$.
- Case 3: v_3 provides i_3' by considering $v_1 = 0$ and $v_2 = 0$.

Therefore, i_1', i_2' and i_3' are obtained using the electrical circuit illustrated in Fig 3.8a, Fig 3.8b, Fig 3.8c under the supposition that v_1, v_2 and v_3 are short-circuited according to the cases (case 1, case 2, and case 3) mentioned before.

Based on the Kirchhoff laws i_1', i_2' and i_3' are written as follows:

$$i_1' = v_1 \frac{1}{z_1 + \left(\sum_{k=1}^{3} \frac{1}{z_k} + \frac{1}{z_L} - \frac{1}{z_1} \right)^{-1}} \tag{3.14}$$

$$i_2' = -v_2 \frac{1}{z_1} \cdot \frac{\left(\sum_{k=1}^{3} \frac{1}{z_k} + \frac{1}{z_L} - \frac{1}{z_2} \right)^{-1}}{z_2 + \left(\sum_{k=1}^{3} \frac{1}{z_k} + \frac{1}{z_L} - \frac{1}{z_2} \right)^{-1}} \tag{3.15}$$

$$i_3^{'} = -v_3 \frac{1}{z_1} \frac{\left(\sum_{k=1}^{3} \frac{1}{z_k} + \frac{1}{z_L} - \frac{1}{z_3}\right)^{-1}}{z_3 + \left(\sum_{k=1}^{3} \frac{1}{z_k} + \frac{1}{z_L} - \frac{1}{z_3}\right)^{-1}} \tag{3.16}$$

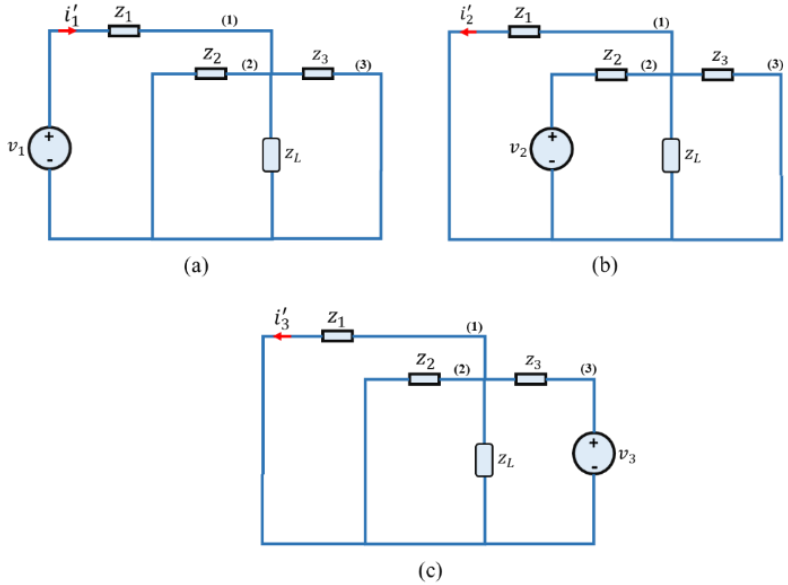

Fig 3.8. Electrical interconnection, where a) v_2 and v_3 are short-circuited, b) v_1 and v_3 are short-circuited, c) v_1 and v_2 are short-circuited.

Substituting (3.14), (3.15), and (3.16) in (3.13), i_1 can be expressed as follows:

$$\begin{aligned} i_1 = v_1 \frac{1}{z_1 + \left(\sum_{k=1}^{3} \frac{1}{z_k} + \frac{1}{z_L} - \frac{1}{z_1}\right)^{-1}} - v_2 \frac{1}{z_1} \cdot \frac{\left(\sum_{k=1}^{3} \frac{1}{z_k} + \frac{1}{z_L} - \frac{1}{z_2}\right)^{-1}}{z_2 + \left(\sum_{k=1}^{3} \frac{1}{z_k} + \frac{1}{z_L} - \frac{1}{z_2}\right)^{-1}} \\ - v_3 \frac{1}{z_1} \frac{\left(\sum_{k=1}^{3} \frac{1}{z_k} + \frac{1}{z_L} - \frac{1}{z_3}\right)^{-1}}{z_3 + \left(\sum_{k=1}^{3} \frac{1}{z_k} + \frac{1}{z_L} - \frac{1}{z_3}\right)^{-1}} \end{aligned} \tag{3.17}$$

According to Fig 3.6, the DC bus voltage v_b is written as follows:

$$v_b = \tilde{v}_{o_i} - z_{line_i} \tilde{i}_{o_i} \tag{3.18}$$

Based on definition 3.1, $\tilde{i}_{o_i}$ can be written as follows:

$$\tilde{i}_{o_i} = \tilde{i}_{o_i}^{'} - \sum_{t=1}^{n-1} \tilde{i}_{o_{i+t}}^{'} \tag{3.19}$$

$\tilde{i}_{o_i}^{'}$ and $\tilde{i}_{o_{i+t}}^{'}$ are written as follows:

$$\tilde{i}_{o_i}^{'} = \frac{\tilde{v}_{o_i}}{z_{line_i} + \left(\sum_{k=0}^{n} \frac{1}{z_{Line_{i+k}}} + \frac{1}{|R_{CPL}|} - \frac{1}{z_{line_i}} \right)^{-1}} \tag{3.20}$$

$$\tilde{i}_{o_{i+t}}^{'} = \frac{1}{Z_{Line_i}} \frac{\tilde{v}_{o_{i+t}} \left(\sum_{k=0}^{n} \frac{1}{z_{Line_{i+k}}} + \frac{1}{|R_{CPL}|} - \frac{1}{z_{line_{i+t}}} \right)^{-1}}{z_{line_{i+t}} + \left(\sum_{k=0}^{n} \frac{1}{z_{Line_{i+k}}} + \frac{1}{|R_{CPL}|} - \frac{1}{z_{line_{i+t}}} \right)^{-1}} \tag{3.21}$$

Substituting (3.20) and (3.21) in (3.19), $\tilde{i}_{o_i}$ can be written as follows:

$$\begin{aligned} \tilde{i}_{o_i} = & \frac{\tilde{v}_{o_i}}{z_{line_i} + \left(\sum_{k=0}^{n} \frac{1}{z_{Line_{i+k}}} + \frac{1}{|R_{CPL}|} - \frac{1}{z_{line_i}} \right)^{-1}} \\ & - \sum_{t=1}^{n-1} \frac{1}{Z_{Line_i}} \frac{\tilde{v}_{o_{i+t}} \left(\sum_{k=0}^{n} \frac{1}{z_{Line_{i+k}}} + \frac{1}{|R_{CPL}|} - \frac{1}{z_{line_{i+t}}} \right)^{-1}}{z_{line_{i+t}} + \left(\sum_{k=0}^{n} \frac{1}{z_{Line_{i+k}}} + \frac{1}{|R_{CPL}|} - \frac{1}{z_{line_{i+t}}} \right)^{-1}} \end{aligned} \tag{3.22}$$

In this system, the primary control provides to DC/DC buck converters the same output voltages. Based on that, $\tilde{v}_{o_i}$ is equal to $\tilde{v}_{o_{i+t}}$ ($\tilde{v}_{o_i} = \tilde{v}_{o_{i+t}}$). Then, $\tilde{i}_{o_i}$ can be written as follows:

$$\begin{aligned} \tilde{i}_{o_i} = & \frac{\tilde{v}_{o_i} \left(\sum_{k=0}^{n} \frac{1}{z_{Line_{i+k}}} + \frac{1}{|R_{CPL}|} - \frac{1}{z_{line_i}} \right)}{\left(\sum_{k=0}^{n} \frac{1}{z_{Line_{i+k}}} + \frac{1}{|R_{CPL}|} - \frac{1}{z_{line_i}} \right) z_{line_i} + 1} \\ & - \frac{1}{Z_{Line_i}} \frac{\tilde{v}_{o_i}(n-1)}{\left(\sum_{k=0}^{n} \frac{1}{z_{Line_{i+k}}} + \frac{1}{|R_{CPL}|} - \frac{1}{z_{line_{i+t}}} \right) z_{line_{i+t}} + 1} \end{aligned} \tag{3.23}$$

All the decentralized secondary controls must have the same controller $K_{s_\infty}(s)$. But, it is not possible to achieve that because the transmission lines have different impedance. There is a trick to solve this problem: consider this difference of the line impedance as the uncertainties.

It is defined that Y is an admittance and written as follows:

$$Y = \frac{1}{Z_{Line_i}} \tag{3.24}$$

Based on definition 3.1, Y and Z_{Line_i} comprising the uncertainties are written as follows:

$$Y = Y_0 + Y_0\delta_Y \tag{3.25}$$

$$z_{Line_i} = z_{line_{i0}} + z_{line_{i0}}\delta_{z_{Line_i}} \tag{3.26}$$

Based on (3.25) and (3.26), $\tilde{i}_{o_i}$ can be written as follows:

$$\tilde{i}_{o_i} = \frac{Y_0 + Y_0\delta_Y + \dfrac{1}{|R_{CPL}|}}{\left(nY_0 + n\delta_Y Y_0 + \dfrac{1}{|R_{CPL}|}\right)\left(z_{Line_{i0}} + z_{Line_{i0}}\delta_{z_{line_i}}\right)+1}\cdot\tilde{v}_{o_i} \tag{3.27}$$

Substituting (3.27) in (3.18), v_b is written as follows:

$$v_b = \tilde{v}_{o_i}\left(1-\left(z_{Line_{i0}} + \delta_{z_{Line_i}} z_{Line_{i0}}\right)\frac{Y_0 + Y_0\delta_Y + \dfrac{1}{|R_{CPL}|}}{\left(nY_0 + n\delta_Y Y_0 + \dfrac{1}{|R_{CPL}|}\right)\left(z_{Line_{i0}} + z_{Line_{i0}}\delta_{z_{Line_i}}\right)+1}\right)$$

(4.28)

Among the advantages of $K_{p_\infty}(s)$ is to mitigate the effect of the disturbances $\tilde{v}_{in}$, $\tilde{i}_{o_i}$ and ω_T, it is concluded that:

$$\tilde{v}_{in}\cdot\frac{M_v(s)T_{p0}(s)}{1+K_{p_\infty}(s)T_{p0}(s)} \approx 0 \tag{3.29}$$

$$\tilde{i}_{o_i}\cdot\frac{Z_0(s)T_{p0}(s)}{1+K_{p_\infty}(s)T_{p0}(s)} \approx 0 \tag{3.30}$$

$$\omega_T\cdot\frac{T_{p0}(s)}{1+K_{p_\infty}(s)T_{p0}(s)} \approx 0 \tag{3.31}$$

According to (3.29), (3.30), (3.31), and robust primary control closed-loop illustrated in Fig 3.5, $\tilde{v}_{o_i}$ can be written as follows:

$$\tilde{v}_{o_i} \approx \frac{K_{p_\infty}(s)T_{p_0}(s)}{1+K_{p_\infty}(s)T_{p_0}(s)} \cdot v_{ref} \tag{3.32}$$

Substituting (3.32) in (3.28), v_b can be written as follows:

$$v_b = \left(1-\left(z_{Line_{i_0}} + \delta_{z_{Line_i}} z_{Line_{i_0}}\right)\frac{Y_0 + Y_0\delta_Y + \frac{1}{|R_{CPL}|}}{\left(nY_0 + n\delta_Y Y_0 + \frac{1}{|R_{CPL}|}\right)\left(z_{Line_{i_0}} + z_{Line_{i_0}}\delta_{z_{Line_i}}\right)+1}\right) \cdot \frac{K_{p_\infty}(s)T_{p_0}(s)}{1+K_{p_\infty}(s)T_{p_0}(s)} \cdot v_{ref} \tag{3.33}$$

After some mathematical manipulations carried out on (3.33), v_b can also be written as follows:

$$v_b = H_0(s)B_1(s)\left(v_{ref} + \omega_b\right) \tag{3.34}$$

where $H_0(s)$ and $B_1(s)$ are given as follows:

$$H_0(s) = \frac{K_{p_\infty}(s)T_{p_0}(s)}{K_{p_\infty}(s)T_{p_0}(s)+1} \tag{3.35}$$

$$B_1(s) = \frac{Y_0 Z_{line_0}(n-1)+1}{nY_0 Z_{line_0} + \frac{Z_{line_0}}{|R_{CPL}|}+1} \tag{3.36}$$

ω is the variable of the disturbances arising from the uncertainties of transmission line impedance. It can be written as follows:

$$\omega_b = \Delta_4(s)\begin{pmatrix} v_{ref} \\ v_b \end{pmatrix} \tag{3.37}$$

$\Delta_4(s)$ is the uncertain transfer matrix, which is given as follows:

$$\Delta_4(s) = \frac{1}{B_1(s)}\begin{pmatrix}\Phi_1 & \Phi_2\end{pmatrix} \tag{3.38}$$

where

$$\Phi_1 = H_0(s)(n-1)\frac{\delta_{z_{line_i}} z_{line_{i0}} Y_0 + \delta_Y z_{line_{i0}} Y_0}{nY_0 z_{line_{i0}} + \frac{z_{line_{i0}}}{|R_{CPL}|} + 1} \tag{3.39}$$

$$\Phi_2 = \frac{\delta_{z_{line_i}} \left(nY_0 z_{line_{i0}} + \frac{z_{line_{i0}}}{|R_{CPL}|} \right) + \delta_Y Y_0 z_{line_{i0}}}{nY_0 z_{line_{i0}} + \frac{z_{line_{i0}}}{|R_{CPL}|} + 1} \tag{3.40}$$

Based on the robust primary control closed-loop, (3.34) and (3.37). The robust secondary control closed loop is obtained as illustrated in Fig 3.9, where the uncertain model of the system is included, ω_T gathers the disturbances arising from the input voltage $\tilde{v}_{in}$, output current $\tilde{i}_{o_i}$, and uncertain parameters of the DC/DC buck converters, and ω is the variable of the disturbances arising from the uncertainties of transmission line impedance and acting on the variable v_{ref} .

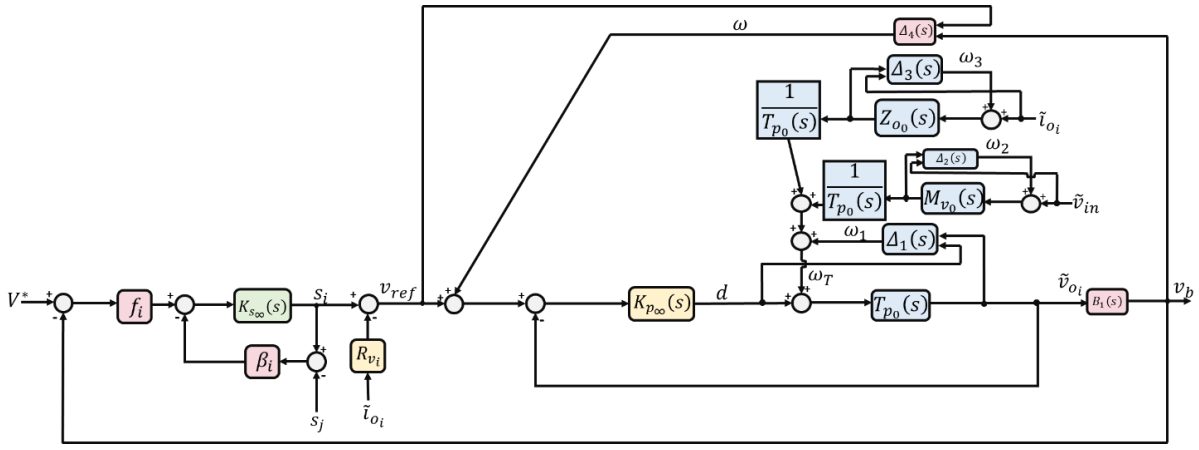

Fig 39. Robust decentralized secondary control closed loop.

3.4. Robust hierarchical control design process.

The design process of robust hierarchical control aims to obtain the controllers $K_{p_\infty}(s)$ and $K_{s_\infty}(s)$. This design process consists of the GDOA and NOA [102, 105]. These algorithms require two augmented plants, including the weight functions that help obtain the wanted controllers for ensuring the desired performances. The augmented plants are derived from the robust decentralized secondary control, where the weight functions are included, as illustrated

in Fig 3.10. These weight functions are only used to design these robust controllers and will not be present when $K_{p_\infty}(s)$ and $K_{s_\infty}(s)$ are applied.

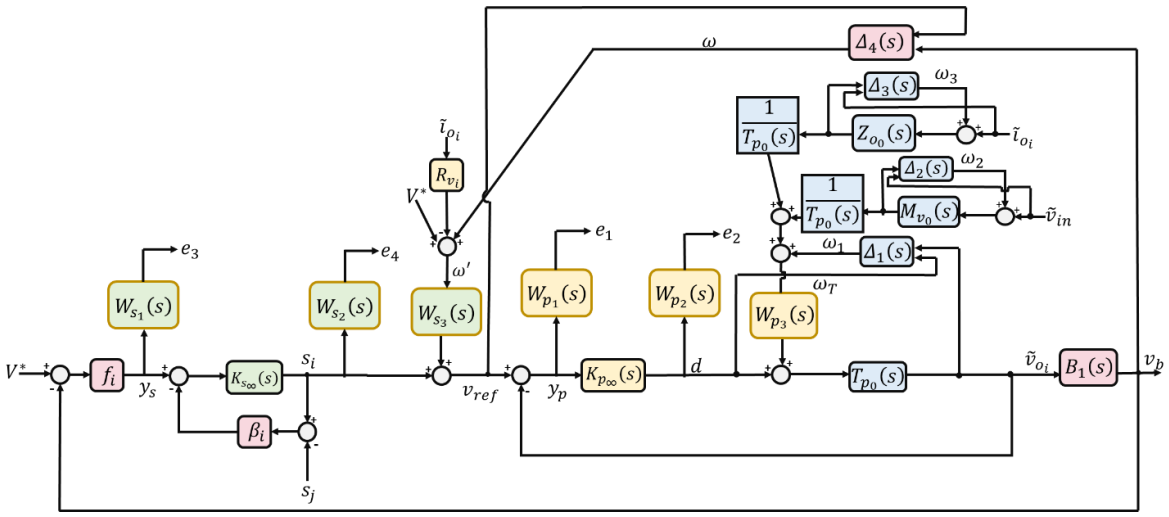

Fig 3.10. Robust decentralized secondary control, including the weight functions.

According to Fig 3.10, the augmented plants ($P_1(s), P_2(s)$) needed by the design process are given as follows:

$$\begin{pmatrix} e_1 \\ e_2 \\ y_p \end{pmatrix} = \overbrace{\begin{bmatrix} W_{p_1}(s) & -W_{p_1}(s)T_{p_0}(s)W_{p_3}(s) & -W_{p_1}(s) \\ 0 & 0 & W_{p_2}(s) \\ 1 & -T_{p_0}(s)W_{p_3}(s) & T_{p_0}(s) \end{bmatrix}}^{P_1(s)} \begin{pmatrix} v_{ref} \\ \omega_T \\ d \end{pmatrix} \tag{3.41}$$

$$\begin{pmatrix} e_3 \\ e_4 \\ y_s \end{pmatrix} = \overbrace{\begin{bmatrix} W_{s_1}(s)f_i & -W_{s_1}(s)H_0(s)B_1(s)f_iW_{s_3}(s) & -W_{s_1}(s) \\ 0 & 0 & W_{s_2}(s) \\ 1 & -H_0(s)B_1(s)W_{s_3}(s) & H_0(s)B_1(s) \end{bmatrix}}^{P_2(s)} \begin{pmatrix} V^* \\ \omega' \\ s_i \end{pmatrix} \tag{3.42}$$

where

$$d = K_{p_\infty}(s)y_p \tag{3.43}$$

In the steady-state, All the decentralized secondary controllers provide the same compensation voltage signals ($s_1 = .. = s_i = ... = s_i = ... = s_n$). Thus, s_i can be approximately written as follows:

$$s_i = K_{s_\infty}(s)\, y_s \tag{3.44}$$

Based on definition 3.5, two LFTs can be defined as follows:

$$y_1 = F_L\left(P_1(s), K_{p_\infty}(s)\right)\cdot y_{in_1} \tag{3.45}$$

$$y_2 = F_L\left(P_2(s), K_{s_\infty}(s)\right)\cdot y_{in_2} \tag{3.46}$$

where

$$F_L\left(P_1(s), K_{p_\infty}(s)\right) = \begin{pmatrix} W_{p1}(s)S_p(s) & W_{p1}(s)S_p(s)T_{p0}(s)W_{p3}(s) \\ W_{p2}(s)S_p(s)K_{p_\infty}(s) & -W_{p2}(s)\varpi_p(s)W_{p3}(s) \end{pmatrix} \tag{3.47}$$

$$F_L\left(P_2(s), K_{s_\infty}(s)\right) = \begin{pmatrix} W_{s_1}(s)S_s(s) & W_{s_1}(s)S_s(s)H_0(s)B_1(s)W_{ps}(s) \\ W_{s_2}(s)S_s(s)K_{s_\infty}(s) & -W_{s_2}(s)\varpi_s(s)W_{s_3}(s) \end{pmatrix} \tag{3.48}$$

where y_{in_1}, y_{in_1}, y_1 and y_2 are written as follows: $y_{in_1} = \begin{pmatrix} v_{ref} \\ \omega_T \end{pmatrix}$, $y_{in_2} = \begin{pmatrix} V^* \\ \omega' \end{pmatrix}$, $y_1 = \begin{pmatrix} e_1 \\ e_2 \end{pmatrix}$ and $y_2 = \begin{pmatrix} e_3 \\ e_4 \end{pmatrix}$.

$S_p(s)$, $S_s(s)$, $\varpi_p(s)$ and $\varpi_s(s)$ are the sensitivity functions. These sensitivity functions are written as follows:

$$S_p(s) = \frac{1}{1+K_{p_\infty}(s)T_{p0}(s)} \tag{3.49}$$

$$S_s(s) = \frac{1}{1+K_{s_\infty}(s)H_0(s)B_1(s)} \tag{3.50}$$

$$\varpi_p(s) = \frac{K_{p_\infty}(s)T_{p0}(s)}{1+K_{p_\infty}(s)T_{p0}(s)} \tag{3.51}$$

$$\varpi_p(s) = \frac{K_{s_\infty}(s)B_1(s)H_0(s)}{1+K_{p_\infty}(s)B_1(s)H_0(s)} \tag{3.52}$$

To verify if the designed controllers $K_{p_\infty}(s)$ and $K_{s_\infty}(s)$ are good enough to reach the control objectives, these controllers must satisfy the conditions written as follows [102,105]:

$$\left\| F_L\left(P_1(s), K_{p_\infty}(s)\right)\right\|_\infty \le \gamma_1 \tag{3.53}$$

$$\left\| F_L\left(P_2(s), K_{s_\infty}(s)\right)\right\|_\infty \le \gamma_2 \tag{3.54}$$

Therefore, the design process must be based on the conditions presented in (3.53) and (3.54) and the good selection of the weight functions. Preferably, it is worth verifying the conditions (3.53) and (3.54) by verifying the H_∞ norm of the gains of the transfer matrix $F_L\left(P_1(s), K_{p_\infty}(s)\right)$ and $F_L\left(P_2(s), K_{s_\infty}(s)\right)$, which have to be lower than γ_1 and γ_2, respectively. That gives:

$$\begin{cases} \left\|S_p(s)\right\|_\infty \le \dfrac{\gamma_1}{\left\|W_{p1}(s)\right\|_\infty} \rightarrow & \left|S_p(s)\right| \le \dfrac{\gamma_1}{\left|W_{p1}(s)\right|} \\ \left\|S_p(s)T_{p0}(s)\right\|_\infty \le \dfrac{\gamma_1}{\left\|W_{p1}(s)W_{p3}(s)\right\|_\infty} \rightarrow & \left|S_p(s)T_{p0}(s)\right| \le \dfrac{\gamma_1}{\left|W_{p1}(s)W_{p3}(s)\right|} \\ \left\|S_p(s)K_{p_\infty}(s)\right\|_\infty \le \dfrac{\gamma_1}{\left\|W_{p2}(s)\right\|_\infty} \rightarrow & \left|S_p(s)K_{p_\infty}(s)\right| \le \dfrac{\gamma_1}{\left|W_{p2}(s)\right|} \\ \left\|\varpi_p(s)\right\|_\infty \le \dfrac{\gamma_1}{\left\|W_{p2}(s)W_{p3}(s)\right\|_\infty} \rightarrow & \left|\varpi_p(s)\right| \le \dfrac{\gamma_1}{W_{p2}(s)W_{p3}(s)} \end{cases} \tag{3.55}$$

$$\begin{cases} \left\|S_s(s)\right\|_\infty \le \dfrac{\gamma_2}{\left\|W_{s1}(s)\right\|_\infty} \rightarrow & \left|S_s(s)\right| \le \dfrac{\gamma_2}{\left|W_{s1}(s)\right|} \\ \left\|S_s(s)H_0(s)B_1(s)\right\|_\infty \le \dfrac{\gamma_2}{\left\|W_{s1}(s)W_{s3}(s)\right\|_\infty} \rightarrow & \left|S_s(s)H_0(s)B_1(s)\right| \le \dfrac{\gamma_2}{\left|W_{s1}(s)W_{s3}(s)\right|} \\ \left\|S_s(s)K_{s_\infty}(s)\right\|_\infty \le \dfrac{\gamma_2}{\left\|W_{s2}(s)\right\|_\infty} \rightarrow & \left|S_s(s)K_{s_\infty}(s)\right| \le \dfrac{\gamma_2}{\left|W_{s2}(s)\right|} \\ \left\|\varpi_s(s)\right\|_\infty \le \dfrac{\gamma_2}{\left\|W_{s2}(s)W_{s3}(s)\right\|_\infty} \rightarrow & \left|\varpi_s(s)\right| \le \dfrac{\gamma_2}{\left|W_{s2}(s)W_{s3}(s)\right|} \end{cases} \tag{3.56}$$

where γ_1 and y_2 are also resulted from GDOA and NOA, respectively.

The design process of the robust hierarchical control can be summarized in the steps given as follows:

- Step 1: selecting the weight functions $W_{p1}(s)$, $W_{p2}(s)$, $W_{p3}(s)$, $W_{s1}(s)$, $W_{s2}(s)$ and $W_{s3}(s)$.
- Step 2: forming the augmented system $P_1(s)$.
- Step 3: performing $K_{p\infty}(s)$ by using GDOA.
- Step 4: forming the augmented system $P_2(s)$.
- Step 5: performing $K_{s\infty}(s)$ by using NOA.

The design process of the proposed control can be depicted by a flowchart, as illustrated in Fig 3.11.

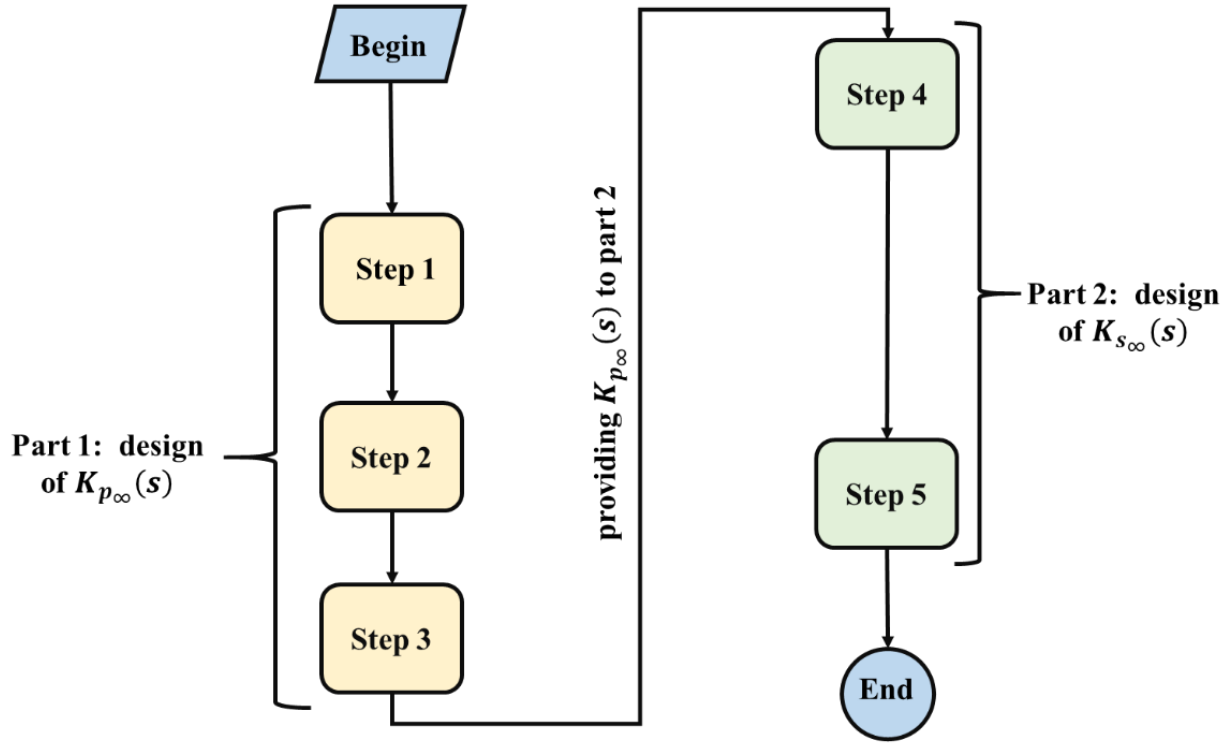

Fig 3.11. Flowchart of robust hierarchical control process design.

The same way, presented in section 2.5.3, is used to determine the mathematical expressions of the weight function employed to derive $K_{p\infty}(s)$ and $K_{s\infty}(s)$. The mathematical expressions of these weight functions are given as follows:

$$\begin{cases} W_{p_1}(s) = \dfrac{1}{K_{p_1}} \cdot \dfrac{s + \omega_{c_p} K_{p_1}}{s + \omega_{c_p} k_{p_1}} \\ W_{s_1}(s) = \dfrac{1}{K_{s_1}} \cdot \dfrac{s + \omega_{c_s} K_{s_1}}{s + \omega_{c_s} k_{s_1}} \end{cases} \tag{3.57}$$

$$\begin{cases} W_{p_2}(s) = \dfrac{1}{k_{p_2}} \cdot \dfrac{s + \dfrac{\omega_{c_p}}{K_{p_2}}}{s + \dfrac{\omega_{c_p}}{k_{p_2}}} \\ W_{s_2}(s) = \dfrac{1}{k_{s_2}} \cdot \dfrac{s + \dfrac{\omega_{c_s}}{K_{s_2}}}{s + \dfrac{\omega_{c_s}}{k_{s_2}}} \end{cases} \tag{3.58}$$

$$\begin{cases} W_{p_2}(s) = \dfrac{1}{k_{p_2}} \cdot \dfrac{s + \dfrac{\omega_{c_p}}{K_{p_2}}}{s + \dfrac{\omega_{c_p}}{k_{p_2}}} \\ W_{s_2}(s) = \dfrac{1}{k_{s_2}} \cdot \dfrac{s + \dfrac{\omega_{c_s}}{K_{s_2}}}{s + \dfrac{\omega_{c_s}}{k_{s_2}}} \end{cases} \tag{3.59}$$

$$\begin{cases} W_{p_3}(s) = K_1^{'} \\ W_{s_3}(s) = K_2^{'} \end{cases} \tag{3.60}$$

where K_{p_1}, K_{s_1}, $k_{p_1}, k_{s_1}, K_{p_2}, K_{s_2}, k_{p_2}$ and k_{s_2} are given as follows:

$$K_{p_1} = K_{p_2} = K_{s_1} = K_{s_2} = e^{-\frac{\log(10)}{20}\Delta G} \tag{3.61}$$

$$k_{s_1} = k_{s_2} = k_{p_1} = k_{p_2} = \varepsilon \tag{3.62}$$

$K_1^{'}$ and $K_2^{'}$ have to be chosen less then ε. ω_{c_p} and ω_{c_s} are the cutoff frequencies having an impact on the dynamic responses of the secondary and primary control, which can be fast responses if these cutoff frequencies have large values. As the dynamic response of the primary control is faster than the dynamic response of the secondary control, ω_{c_p} has to be chosen bigger

than ω_{c_s}. ε and ΔG are the steady-state error and gain margin, corresponding to the system performances. The following section explores in detail the basics of NOA and how the NOA process will be performed. On the other hand, GDOA will be not discussed because it is explored in detail in section 2.5.2

3.4.1. Nonsmooth optimization algorithm

The NOA solves an optimization problem: finding the structured controller $K_{s_\infty}(s)$ to minimize the H_∞ norm of $F_L\left(P_2(s), K_{s_\infty}(s)\right)$ as much as possible to attenuate the effect of the disturbances y_{in_2} and stabilize $P_2(s)$ [105]. This optimization problem can be presented as follows:

$$\begin{aligned} &\underset{w\in R}{minimize} \ \left\| F_L\left(P_2(s), K_{s_\infty}(s)\right)\right\|_\infty \\ &subject\ to\ K_{s_\infty}(s)\ stablizes\ P_2(s) \end{aligned} \tag{3.62}$$

where *w* is the frequency variable that belongs to real interval values *R*, $K_{s_\infty}(s)$ has a fixed structure as PI control presented in (3.2). The operation of NOA is based on the derivative of the Clarke subdifferentiable function defined as follows [105]:

Definition 3.1 (Clarke subdifferentiable function): let consider two functions $f(x)$ and $G(x)$, where $f(x)$ is equal to the H_∞ norm of $G(x)$. $f(x)$ can be written as follows:

$$f(x) = \left\| G(x)\right\|_\infty \tag{3.63}$$

The Clarke subdifferentiable function derived from $f(x) = \left\| G(x)\right\|_\infty$ is written as follows:

$$\delta f(x) = \wp'(x) \cdot \min\left(\phi\left(\wp(x)\right)\right)$$

(4.64)

where $\wp(x)$ is the smooth operator, mapping R^n on the space H_∞ of the $G(x)$, $\wp'(x)$ is the adjoint of $\wp(x)$ and $\phi\left(\wp(x)\right)$ is the subgradient of $\wp(x)$ at $G(x)$.

Definition 3.2 (smooth operator): let consider a function $G(x)$ that links the outputs vector y to the inputs vector u. This mathematical relationship between u and y is expressed as follows:

$$y = G(x)u \tag{3.65}$$

where u and y can be written as follows:

$$y = \begin{pmatrix} y_1 \\ y_2 \\ : \\ : \\ y_j \end{pmatrix} \tag{3.66}$$

$$u = \begin{pmatrix} u_1 \\ u_2 \\ : \\ : \\ u_i \end{pmatrix} \tag{3.67}$$

$G(x)$ can be subdivided into many smooth operators, where the smooth operator is the subfunction derived from $G(x)$. This subfunction links a single input to a single output as written in the following equation:

$$y_j = \underset{u_i \to y_j}{G}(x) \cdot u_i \tag{3.68}$$

$\underset{u_i \to y_i}{G}(x)$ denotes the smooth operator.

Definition 3.3 (smooth operator subgradient): Let's consider a function $G(x)$ **,** and $\underset{u_i \to y_i}{G}(x)$ is a smooth operator derived from $G(x)$. The subgradient of $\underset{u_i \to y_i}{G}(x)$ at $G(x)$ is given as follows:

$$\phi\left(\underset{u_i \to y_i}{G}(x)\right) = \left\|G(x)\right\|_{\infty}^{-1} \mathrm{Re}\left(Tr\left(G(x)^{*}\, \underline{u} \cdot \underline{u}^{*}\, \underset{u_i \to y_i}{G}(x)\right)\right) \tag{3.69}$$

Let consider $G(x)=U\Sigma V^*$ is the singular value decomposition. $\underline{u}$ is the first column of U, $\underline{u}^*$ is the adjoint of $\underline{u}$, and $G(x)^*$ is adjoint of $G(x)$.

Based on definition 3.2, the smooth operators derived from $F_L\left(P_2(s),K_{s_\infty}(s)\right)$ are given as follows:

$$e_3 = \underset{V^*\to e_3}{F_L}\left(P_2(s),K_{s_\infty}(3)\right)\cdot V^* \tag{3.70}$$

$$e_3 = \underset{\omega'\to e_3}{F_L}\left(P_2(s),K_{s_\infty}(3)\right)\cdot \omega' \tag{3.71}$$

$$e_4 = \underset{V^*\to e_4}{F_L}\left(P_2(s),K_{s_\infty}(3)\right)\cdot V^* \tag{3.72}$$

$$e_4 = \underset{\omega'\to e_4}{F_L}\left(P_2(s),K_{s_\infty}(3)\right)\cdot \omega' \tag{3.73}$$

Based on definition 3.3, the subgradients of (4.70), (4.71), (4.72), and (4.73) at $F_L\left(P_2(s),K_{s_\infty}(s)\right)$ are written as follows:

$$\begin{aligned}\phi\left(\underset{V^*\to e_3}{F_L}\left(P_2(s),K_{s_\infty}(s)\right)\right) = \left\|F_L\left(P_2(s),K_{s_\infty}(s)\right)\right\|_\infty^{-1}\,\mathrm{Re}(Tr(F_L\left(P_2(s),K_{s_\infty}(s)\right)^* \\ \cdot \underline{u}_1\cdot\underline{u}_1^*\cdot \underset{V^*\to e_3}{F_L}\left(P_2(s),K_{s_\infty}(s)\right)))\end{aligned} \tag{3.74}$$

$$\begin{aligned}\phi\left(\underset{\omega'\to e_3}{F_L}\left(P_2(s),K_{s_\infty}(s)\right)\right) = \left\|F_L\left(P_2(s),K_{s_\infty}(s)\right)\right\|_\infty^{-1}\,\mathrm{Re}(Tr(F_L\left(P_2(s),K_{s_\infty}(s)\right)^* \\ \cdot \underline{u}_1\cdot\underline{u}_1^*\cdot \underset{\omega'\to e_3}{F_L}\left(P_2(s),K_{s_\infty}(s)\right)))\end{aligned} \tag{3.75}$$

$$\begin{aligned}\phi\left(\underset{V^*\to e_4}{F_L}\left(P_2(s),K_{s_\infty}(s)\right)\right) = \left\|F_L\left(P_2(s),K_{s_\infty}(s)\right)\right\|_\infty^{-1}\,\mathrm{Re}(Tr(F_L\left(P_2(s),K_{s_\infty}(s)\right)^* \\ \cdot \underline{u}_1\cdot\underline{u}_1^*\cdot \underset{V^*\to e_4}{F_L}\left(P_2(s),K_{s_\infty}(s)\right)))\end{aligned} \tag{3.76}$$

$$\phi\left(\underset{\omega'\to e_4}{F_L}\left(P_2(s),K_{s_\infty}(s)\right)\right)=\left\|F_L\left(P_2(s),K_{s_\infty}(s)\right)\right\|_\infty^{-1}\mathrm{Re}(Tr(F_L\left(P_2(s),K_{s_\infty}(s)\right)^* \cdot \underline{u}_1\cdot\underline{u}_1^*\cdot \underset{\omega'\to e_4}{F_L}\left(P_2(s),K_{s_\infty}(s)\right))) \tag{3.77}$$

where the singular value decomposition of $F_L\left(P_2(s),K_{s_\infty}(s)\right)$ is written as follows:

$$F_L\left(P_2(s),K_{s_\infty}(s)\right)=U_1\Sigma V_1^* \tag{3.78}$$

$\underline{u}_1$ is the first column.

Based on definition 3.1, Clarke subdifferentiable function obtained based on (3.74), (3.75), (3.76), and (3.77) are written as follows:

$$\delta f_1(x)=\underset{V^*\to e_3}{F_L}\left(P_2(s),K_{s_\infty}(s)\right)^*(x)\cdot\min_{w\in R}\left(\phi\left(\underset{V^*\to e_3}{F_L}\left(P_2(s),K_{s_\infty}(s)\right)(x)\right)\right) \tag{3.79}$$

$$\delta f_2(x)=\underset{\omega'\to e_3}{F_L}\left(P_2(s),K_{s_\infty}(s)\right)^*(x)\cdot\min_{w\in R}\left(\phi\left(\underset{\omega'\to e_3}{F_L}\left(P_2(s),K_{s_\infty}(x)\right)\right)(x)\right) \tag{3.80}$$

$$\delta f_3(x)=\underset{V^*\to e_4}{F_L}\left(P_2(s),K_{s_\infty}(s)\right)^*(x)\cdot\min_{w\in R}\left(\phi\left(\underset{V^*\to e_4}{F_L}\left(P_2(s),K_{s_\infty}(s)\right)\right)(x)\right) \tag{3.81}$$

$$\delta f_4(x)=\underset{\omega'\to e_4}{F_L}\left(P_2(s),K_{s_\infty}(s)\right)^*(x)\cdot\min_{w\in R}\left(\phi\left(\underset{\omega'\to e_4}{F_L}\left(P_2(s),K_{s_\infty}(s)\right)\right)(x)\right) \tag{3.82}$$

where *x* comprise the data of the controller $K_{s_\infty}(s)$. It can be given as follows:

$$x=\left(K_{p_\infty}\ K_{i_\infty}\right) \tag{3.83}$$

The NOA operates based on the subgradients and Clarke subdifferentiable functions presented in (3.74), (3.75), (3.76), (3.77), (3.79), (3.80), (3.81), and (3.82), respectively. The NOA operation can be summarized in the steps as follows:

- Step 1: initialize x by giving a large initial value as much as possible $x=x^+$

- Step 2: Find the minimum values of (3.74), (3.75), (3.76), and (3.77) on the whole interval of frequencies. This step corresponds to the process of obtaining the solution for a convex optimization problem.
- Step 3: Substitute the minimum values of (3.74), (3.75), (3.76), and (3.77) in (3.79), (3.80), (3.81), and (3.82). If (3.79), (3.80), (3.81), and (3.82) are all different than zero. *x* decreases by Δx $\left(x = x^{+} - \Delta x\right)$, where Δx is calculated as follows:

$$\Delta x = \begin{pmatrix} \Delta K_p & \dfrac{\Delta K_p}{\|d\|} \end{pmatrix}$$

where ΔK_p has to be chosen small as much as possible, and *d* is a column vector formed by the subgradients of a smooth operator at $F_L\left(P_2(s), K_{s_\infty}(s)\right)$ and can be written as follows:

$$d = \begin{pmatrix} \phi\left(\underset{V^* \to e_3}{F_L}\left(P_2(s), K_{s_\infty}(s)\right)\right) \\ \phi\left(\underset{\omega' \to e_3}{F_L}\left(P_2(s), K_{s_\infty}(s)\right)\right) \\ \phi\left(\underset{V^* \to e_4}{F_L}\left(P_2(s), K_{s_\infty}(s)\right)\right) \\ \phi\left(\underset{\omega' \to e_4}{F_L}\left(P_2(s), K_{s_\infty}(s)\right)\right) \end{pmatrix} \tag{3.84}$$

Replace the value of x^{+} by the value of *x* and return to step 2. If only one of (3.79), (3.80), (3.81), and (3.82) is equal to zero. Verify the condition presented in (3.56), where the controller parameters $K_{s_\infty}(s)$ take their values from *x*. If the conditions (4.56) are satisfied. Stop running the algorithm program and take the controller $K_{s_\infty}(s)$, which is used to verify the conditions presented in (3.56) (3.56) as the solution of the optimization problem presented in (3.62). If the conditions presented in (3. 56) go to step 4. The value of γ_2 is resulted by using the following formula:

$$Ss_e : v_{L_2} \tag{3.85}$$

- Step 4: determine other mathematical expressions of $W_{s_1}(s)$, $W_{s_2}(s)$ and $W_{s_3}(s)$, and go to step 1.

The algorithm does not go up to step 4 since the weight functions ($W_{s1}(s)$, $W_{s2}(s)$ and $W_{s3}(s)$) are well determined and effective for obtaining $K_{s_\infty}(s)$. The NOA operation process can be presented in the flowchart, as illustrated in Fig 3.12.

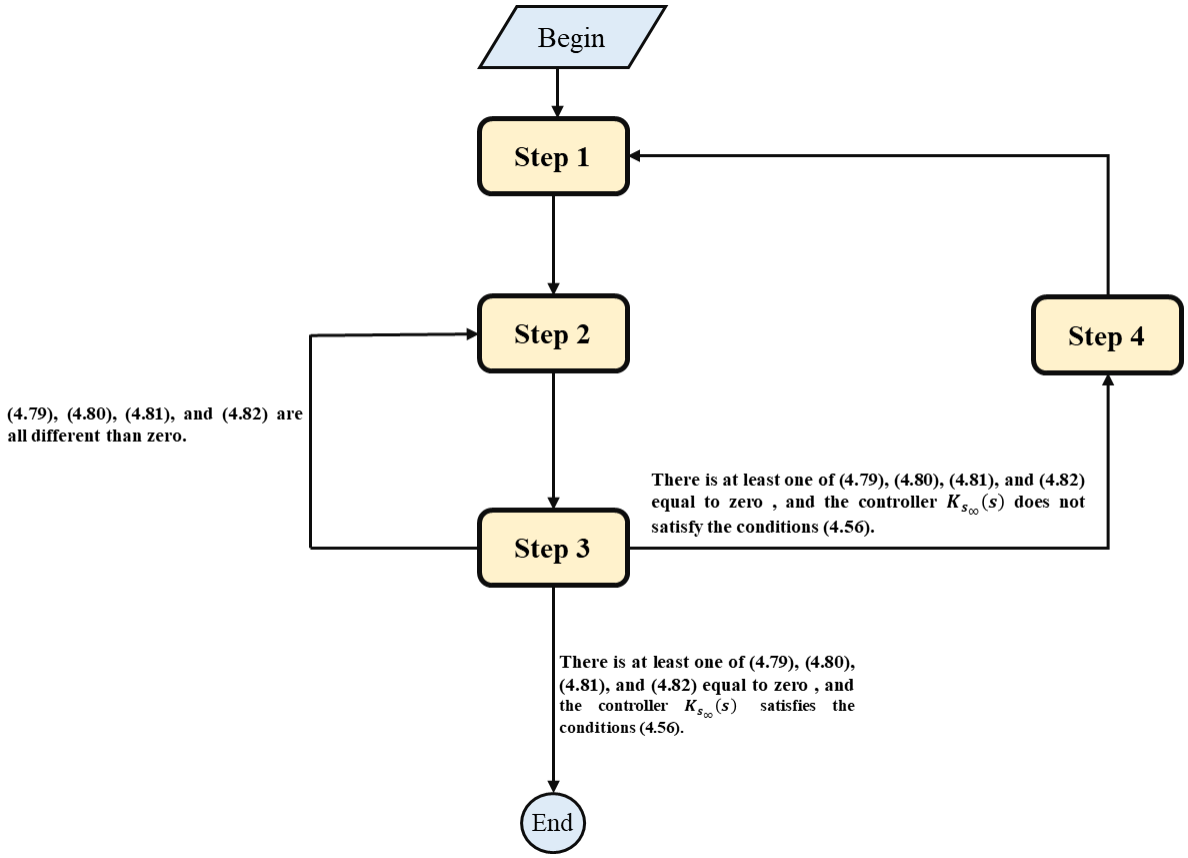

Fig 3.12. NOA flowchart

3.5. Stability analysis

This section presents the stability analysis operating under the developed robust control hierarchy. This stability analysis is carried out in the same way presented in section 3.6, which aims to verify if the functions presented in set (3.86) have the behavior in the frequency domain when $K_{p_\infty}(s)$ and $K_{s_\infty}(s)$ are applied. This stability analysis is performed based on the singular value and phase plot performed after obtaining $K_{p_\infty}(s)$ and $K_{s_\infty}(s)$ using the process design performed in Matlab software. The system parameters used to perform the stability study are listed in Tab 3.1.

$$\begin{aligned}\{&S_p(s), S_p(s)T_{p0}(s), S_p(s)K_{p_\infty}(s), \varpi_p(s)\\ &, S_s(s), S_s(s)H_0(s)B_1(s), S_s(s)K_{s_\infty}(s), \varpi_s(s)\}\end{aligned} \tag{3.86}$$

$K_{p_\infty}(s)$ and $K_{s_\infty}(s)$ are resulted as follows:

$$K_{p_\infty}(s) = \frac{3332s^3 + 2.665\cdot10^{11}s^2 + 1.099\cdot10^3 s + 9.705\cdot10^{15}}{s^4 + 8.928\cdot10^6 s^3 + 9.899\cdot10^{10}s^2 + 4.576\cdot10^{14}s + 3.66\cdot10^4} \quad (3.87)$$

$$K_{s_\infty}(s) = 7.05\cdot10^{-3} + 512\frac{1}{s} \quad (3.88)$$

The weight functions used to perform $K_{p_\infty}(s)$ and $K_{s_\infty}(s)$ are given as follows:

$$\begin{cases} W_{p_1}(s) = \dfrac{0.5s + 8\cdot10^3}{s + 0.8} & W_{s_1}(s) = \dfrac{0.5s + 321.5}{s + 0.3120} \\ W_{p_2}(s) = \dfrac{10^4 s + 4\cdot10^7}{s + 0.8\cdot10^7} & W_{s_2}(s) = \dfrac{10^3 s + 15.6250\cdot10^4}{s + 31.52\cdot10^4} \\ W_{p_2}(s) = 3\cdot10^{-4} & W_{s_3}(s) = 3\cdot10^{-4} \end{cases} \quad (3.89)$$

γ_1 and γ_2 are resulted as follows:

$$\gamma_1 = 3.85 \quad (3.90)$$

$$\gamma_2 = 0.80 \quad (3.91)$$

f_i and β_i are selected for each DC/DC buck converter as follows:

$$f_i = 1 \quad (3.92)$$

$$B_i = 1 \quad (3.93)$$

Tab 3.1. DC microgrid parameters.

Variables	Descriptions	Values
L_o	Nominal inductance	$12mH$
C_o	Nominal capacitance	$2200\mu F$
v_{in}	Input voltage	$100V$
v_o	Output voltage	$48V$
V^*	Nominal DC bus voltage	$48V$
z_{line}	Transmission line impedance	$40(mH) + 30(\mu H)\cdot J$

The singular value and phase plots are depicted in Fig 3.12, Fig 3.13, Fig 3.14, Fig 3.15, and Fig 3.16, Fig 3.17, Fig 3.18, and Fig 3.19.

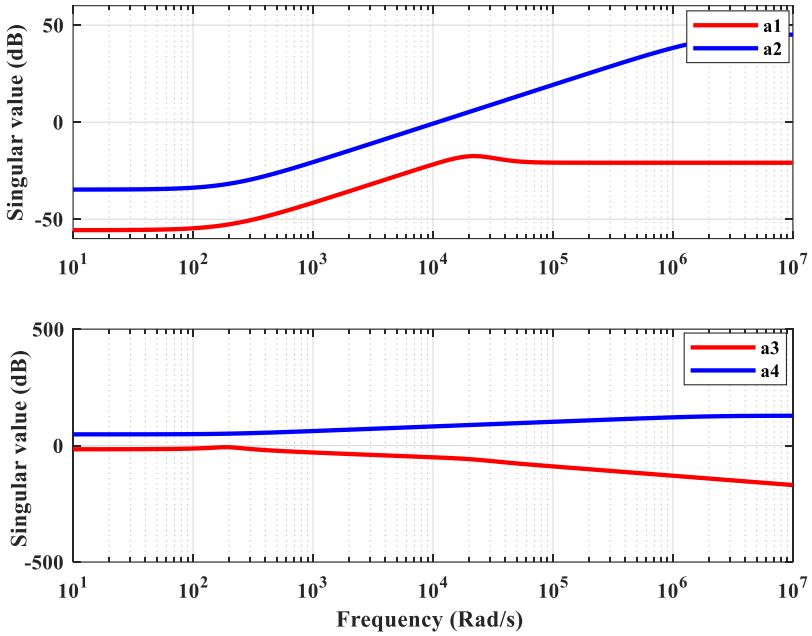

Fig 3.12. Singular value plot of $S_p(s)$, $\gamma_1 / W_{p_1}(s)$, $S_p(s)T_{p_0}(s)$ ***and*** $\gamma_1 / \left(W_{p_1}(s)W_{p_3}(s)\right)$ ***marked by a1, a2, a3, and a4, respectively.***

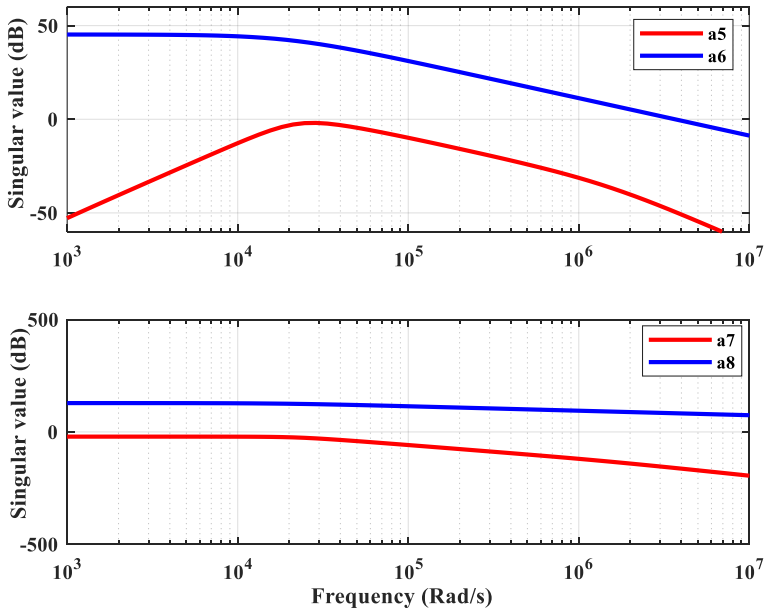

Fig 3.13. Singular value plot of $S_p(s)K_{p_\infty}(s)$, $\gamma_1 / W_{p_2}(s)$, $\varpi_p(s)$ ***and*** $\gamma_1 / \left(W_{p_2}(s)W_{p_3}(s)\right)$ ***marked by a5, a6, a7, and a, respectively.***

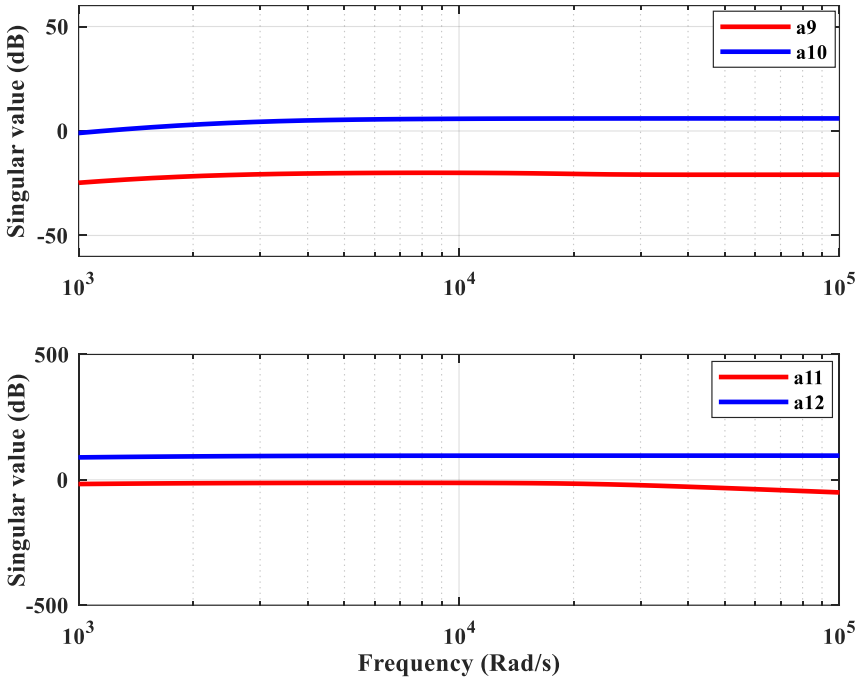

Fig 3.14. Singular value plot of $S_s(s)$, $\gamma_2 / W_{s_1}(s)$, $S_s(s)H_0(s)B_1(s)$ ***and*** $\gamma_2 / \left(W_{s_1}(s)W_{s_3}(s)\right)$ ***marked by a9, a10, a11, and a12, respectively.***

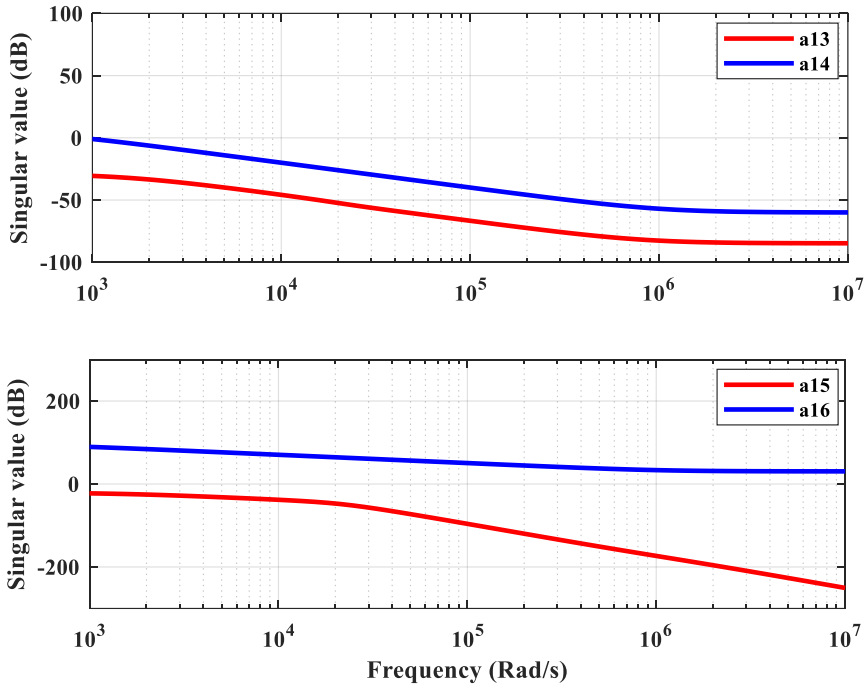

Fig 3 .15. Singular value plot of $S_s(s)K_{s_\infty}(s)$, $\gamma_2 / W_{s_2}(s)$, $\varpi_s(s)$ ***and*** $\gamma_2 / \left(W_{s_2}(s)W_{s_3}(s)\right)$ ***marked by a13, a14, a15, and a16,*** **respectively.**

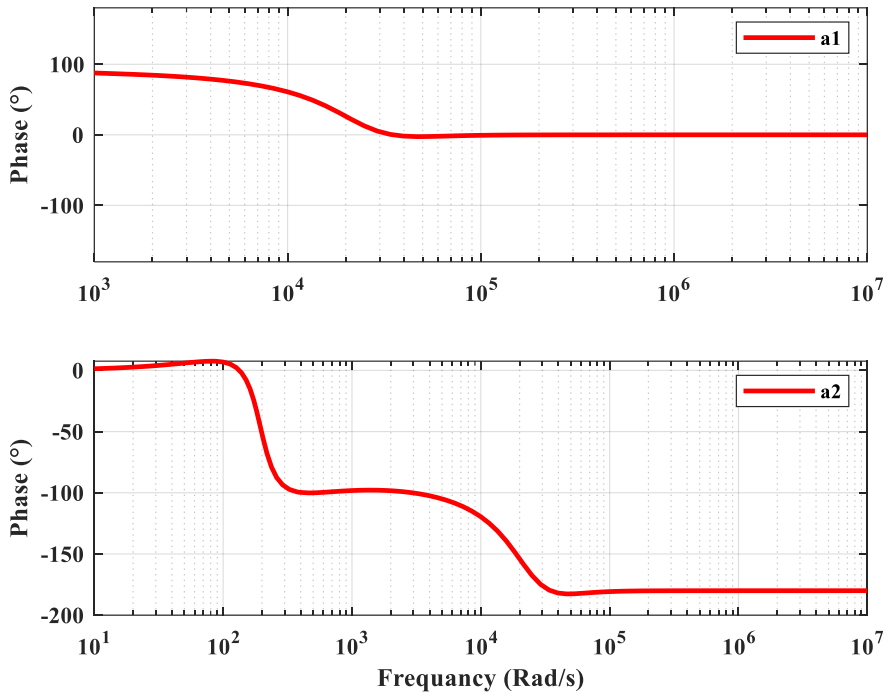

Fig 3.16. Phase plot of $S_p(s)$ ***and*** $S_p(s)T_{p0}(s)$ ***marked by a1 and a2, respectively.***

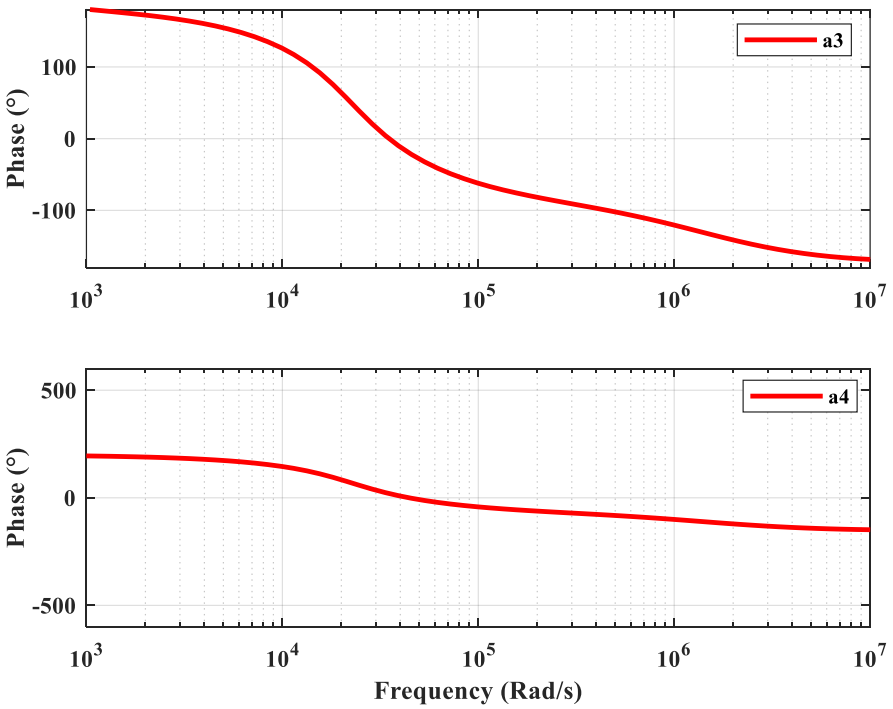

Fig 3.17. Phase plot of $S_p(s)K_{p_\infty}(s)$ ***and*** $\varpi_p(s)$ ***marked by a3 and a4, respectively.***

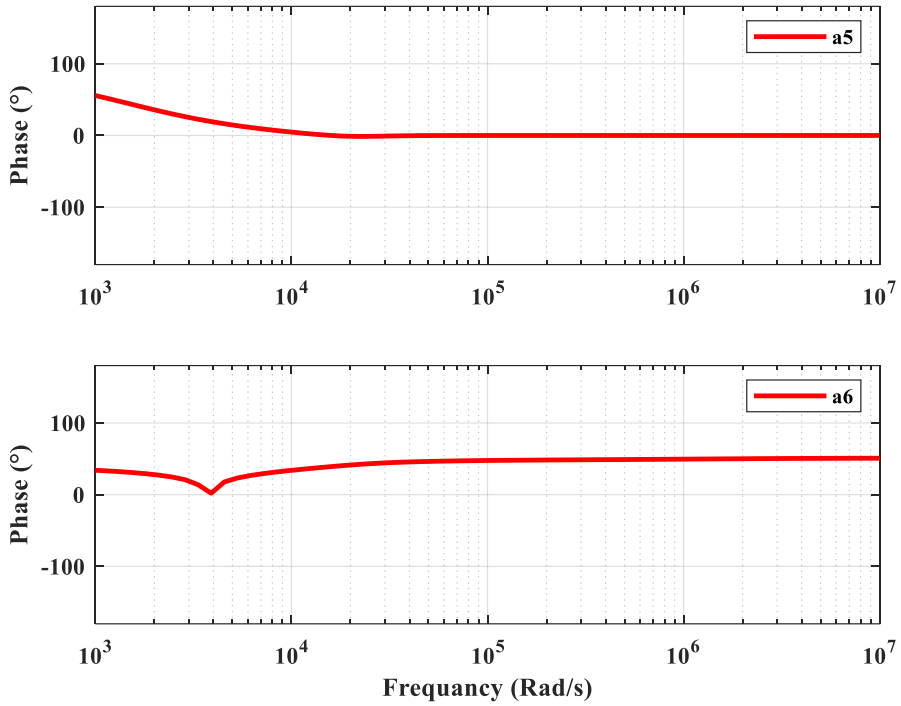

Fig 3.18. Phase plot of $S_s(s)$ ***and*** $S_s(s)H_0(s)B_1(s)$ ***marked by a5 and a6, respectively.***

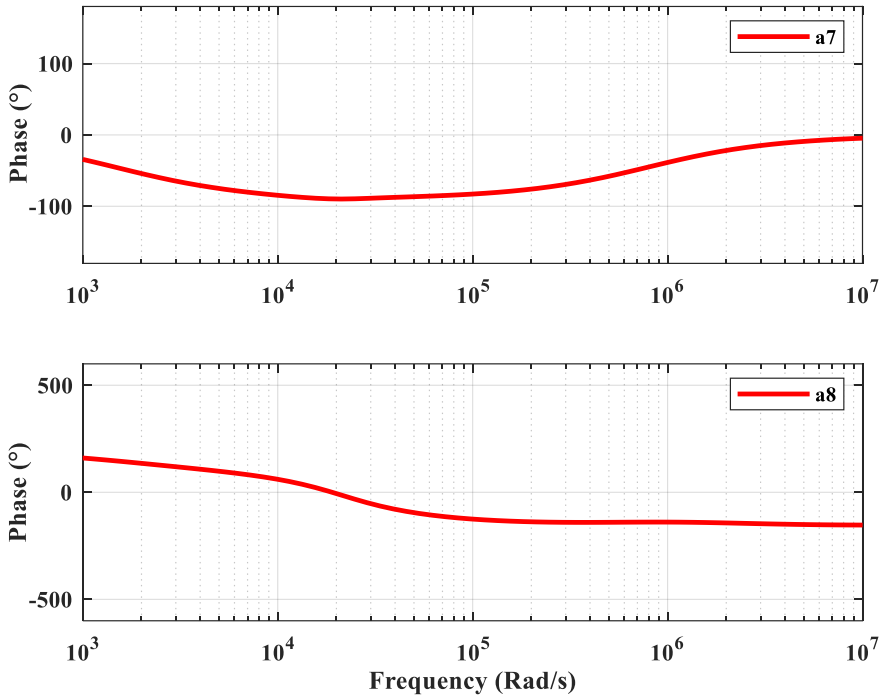

Fig 3.19. Phase plot of $S_s(s)K_{s_\infty}(s)$ ***and*** $\varpi_s(s)$ ***marked by a7 and a8, respectively.***

According to Fig 3.12, Fig 3.13, Fig 4.14, and Fig 3.15, The conditions described in (3.55) and (3.56) are satisfied. The gain magnitudes in dB of (3.86) are lower than 0 dB in the interval of the frequencies corresponding to the bandwidth. That shows the ability of the Robust

hierarchical control to mitigate the whole disturbances (ω_T and ω') present in the system. The effectiveness of $K_{p_\infty}(s)$ and $K_{s_\infty}(s)$ can also be demonstrated as follows:

Based on Fig 3.10 and neglecting the presence of the weight functions in the robust hierarchical control closed loop. The error y_p ($y_p = v_{ref} - \tilde{v}_{o_i}$), duty cycle d , error y_s ($y_s = V^* - v_b$), and voltage compensation signal s_i can be written as follows:

$$\begin{cases} y_p = S_p(s)\cdot v_{ref} + S_p(s)T_{p0}(s)\cdot\omega_T \\ d = S_p(s)K_{p_\infty}(s)\cdot v_{ref} - \varpi_p(s)\cdot\omega_T \\ y_s = S_s(s)\cdot V^* + S_p(s)T_{p0}(s)\cdot\omega' \\ s_i = S_s(s)K_{s_\infty}(s)\cdot V^* - \varpi_s(s)\omega' \end{cases} \tag{3.94}$$

According to obtained singular plots, the magnitudes of (3.86) lower than 1 ($|S_p(s)| \ll 1$, $|S_p(s)T_{p0}(s)| \ll 1, |S_p(s)K_{p_\infty}(s)| \ll 1, |\varpi_p(s)| \ll 1, |S_p(s)H_0(s)B_1(s)| \ll 1$). That means the impact of the disturbance variables (V^*, v_{ref} , ω' and ω_T) on the y_p , y_s , d and s_i is neglected. Therefore, according to (3.43) and (3.44), y_p and y_s depend only on d and s_i .

According to the phases plot depicted in Fig 3.16, Fig 3.17, Fig 3.18, and Fig 3.19, the phases of the functions presented in (3.86) are bigger than $-\pi$. That shows these functions are stable. That means the controller $K_{p_\infty}(s)$ and $K_{s_\infty}(s)$ implemented in the hierarchical control can avoid the stability problem caused by the INI characteristic of CPL.

The pole evolution analysis is carried out to strengthen the previous stability analysis based on singular values and phase plots. This pole evolution analysis is depicted in Fig 3.20. it carried out before and after applying the controllers $K_{p_\infty}(s)$ and $K_{s_\infty}(s)$, where the poles and zeros of the system, primary control closed-loop (PCCL) and secondary control closed-loop (SCCL) marked by the yellow, blue and red colors, respectively. The pole evolution analysis shows that the INI characteristic of the CPL assigns to the system the poles located outside the unit circle, which correspond to the unstable region. On the other hand, the application of the controllers $K_{p_\infty}(s)$ and $K_{s_\infty}(s)$ assign to the system the poles located inside the unit circle, which correspond to the stable region. This analysis confirms what is seen in the previous stability analysis based on the singular and phase plots. Indeed, the application of $K_{p_\infty}(s)$ and $K_{s_\infty}(s)$

improves the robustness of the control hierarchy, and the system earns robustness against the INI characteristic of CPL and disturbances.

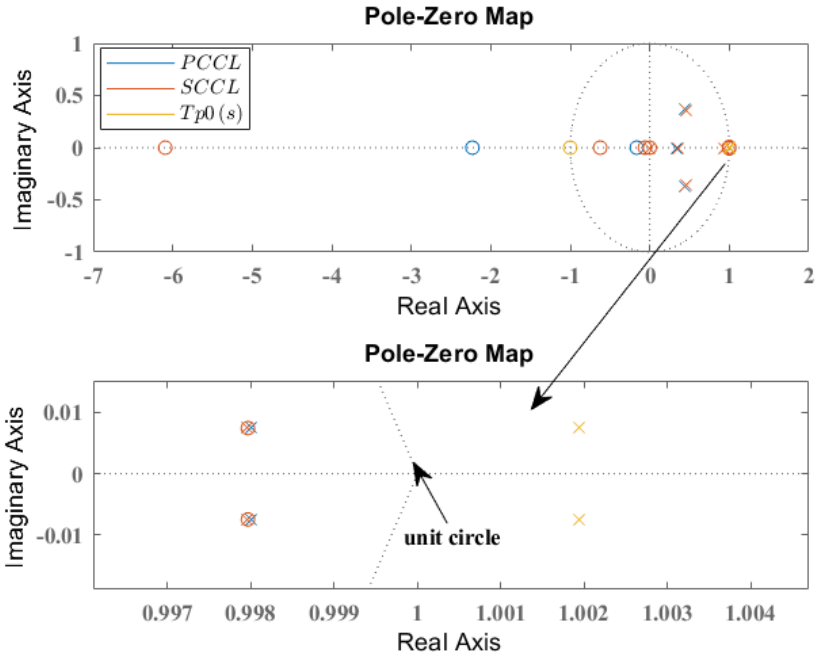

Fig 3.20. Poles evolution analysis carried out after and before applying the controllers $K_{p_\infty}(s)$ ***and*** $K_{s_\infty}(s)$.

3.6. Simulation results

The simulation study is performed using PSIM software to validate the proposed approach. This simulation consists of DC-MG having the same configuration illustrated in Fig 3.1 and operating under the proposed approach. The DC-MG used for this simulation consists of four DC/DC buck converters connected in parallel to feed a load. The input voltages of these DC/DC buck converters are provided by DC sources, which can be considered as an equivalent representation of RESs. In this simulation, two kinds of loads: resistive load and CPL, are used to carry out this simulation. But, these loads are not present simultaneously during the simulation. That allows verifying the performance of the system operating under the proposed approach in the presence of resistive load and CPL. The parameters of DC/DC buck converters are the same listed in Tab 3.1. In this simulation, we consider that transmission line impedances are different, where their parameter values are listed in Tab 3.2.

Tab 3.2. transmission line impedance parameters.

Z_{line_1} of DC/DC buck converter 1	
$r_{line_1} = 0.4\Omega$	$L_{line_1} = 30mH$
Z_{line_2} of DC/DC buck converter 2	
$r_{line_2} = 0.6\Omega$	$L_{line_2} = 9mH$
Z_{line_3} of DC/DC buck converter 3	
$r_{line_3} = 0.6\Omega$	$L_{line_3} = 30mH$
Z_{line_4} of DC/DC buck converter 4	
$r_{Line_4} = 0.2\Omega$	$L_{line_4} = 9mH$

This simulation study is subdivided into four scenarios. The first scenario is performed to validate the effectiveness of the robust hierarchical control to avoid the current circulating, stabilize the system in the presence of CPL and maintain the bus voltage at the nominal value V^*. This scenario is carried out as follows: the primary control is activated from the beginning of this scenario simulation, where the virtual impedances R_v employed in the droop controls are the same, having the value of 8Ω. The secondary control is activated at 1s. In the case of the presence of CPL in the system. The CPL consumes 100W from the beginning of the simulation up to 2s. At 2s, a sudden change of the power consumed by the CPL occurs that let's increase the power consumed by the CPL to reach 200W. In the case of the presence of resistive load in the system. The system supplies a resistive load of 30Ω from the beginning of the simulation of this scenario up to 2S. a sudden change occurs in the resistive load. This sudden change decreases the value of the resistive load that lets the resistive load reaches a value of 15Ω. The sudden change that occurs in the loads is implemented in the simulation to validate the capability of the robust hierarchical control to mitigate the disturbances arising from the load current. The simulation results of this scenario are presented in Fig 3.21, Fig 3.22, and Fig 3.23.

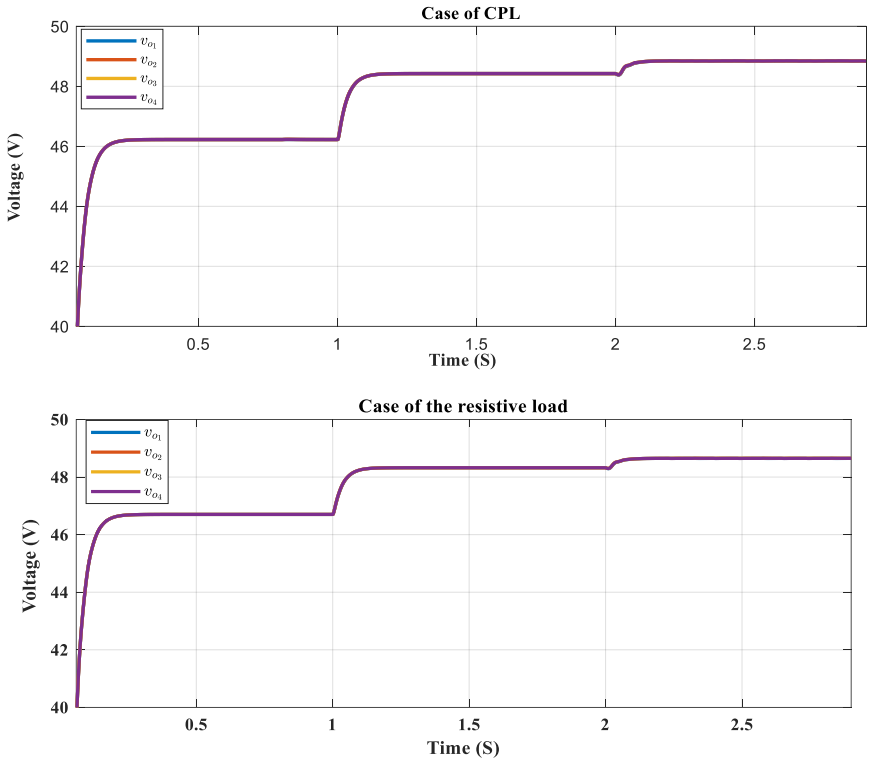

Fig 3.21. Behavior of the output voltages of DC/DC buck converters resulted from the first scenario.

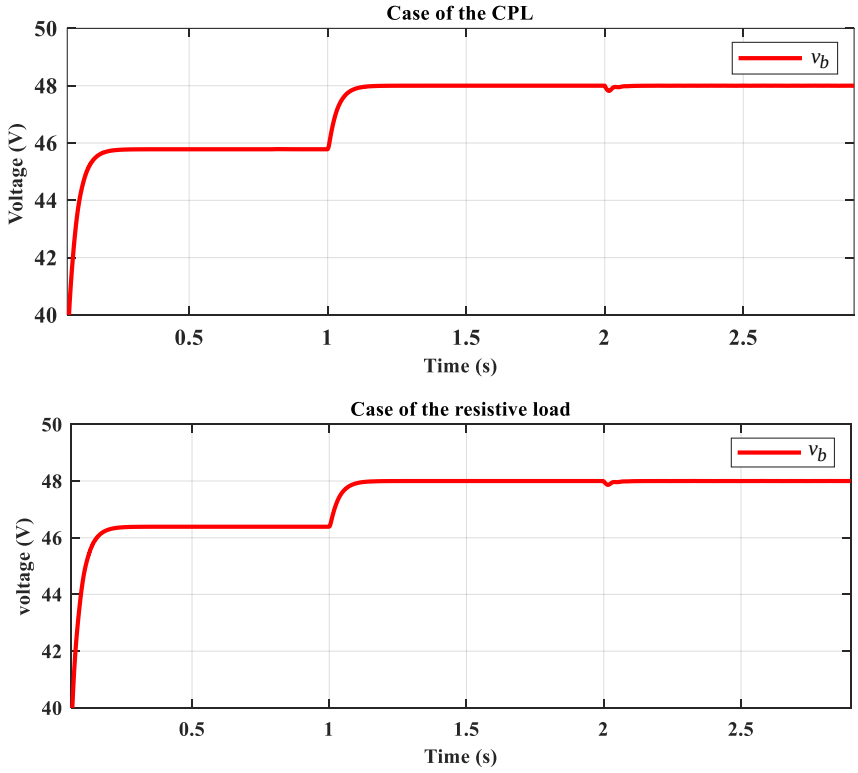

Fig 3.22. Behavior of the bus voltage resulted from the second scenario.

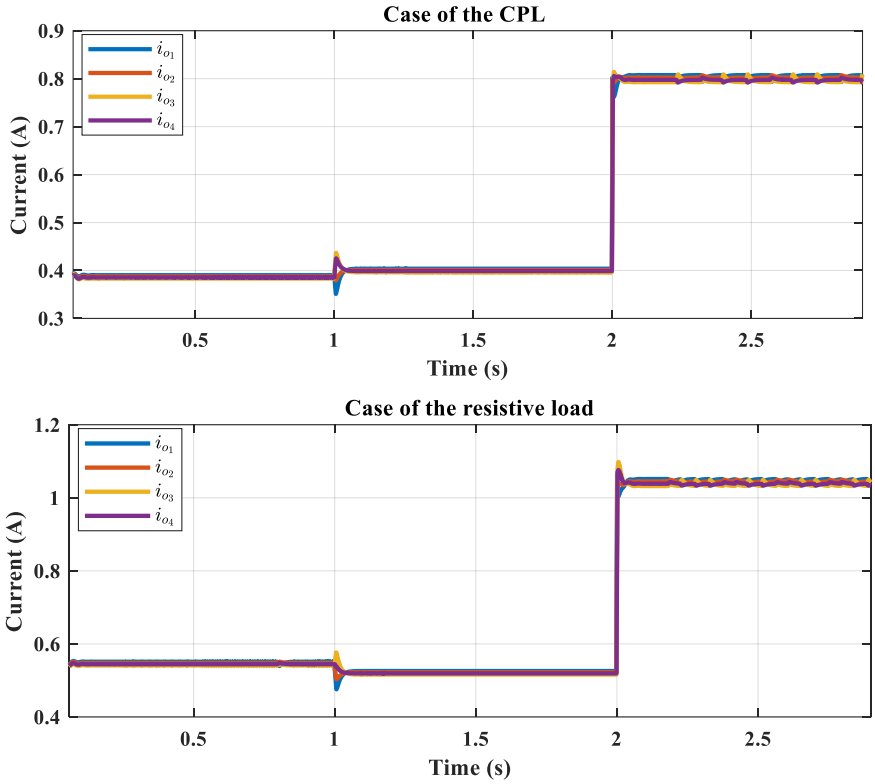

Fig 3.23. Behavior of the output currents of the DC/DC buck converters resulted from the first scenario.

The second scenario is carried out to verify the effectiveness of the robust hierarchical control to mitigate the disturbances, which arise from connecting or disconnecting one or more DC/DC buck converters from the common DC bus. This second scenario is performed as follows: the third DC/DC buck converter is disconnected from the common DC bus from the beginning of the scenario simulation. At 2s, this third DC/DC buck converter is connected again to the common DC bus. Under this scenario, the primary and secondary are activated and operate from the beginning of this scenario simulation. Also, in this scenario, we consider a DC-MG, which supplies a CPL consuming power of 100W. The simulation results of this scenario are presented in Fig 3.24, Fig 3.25, and Fig 3.26.

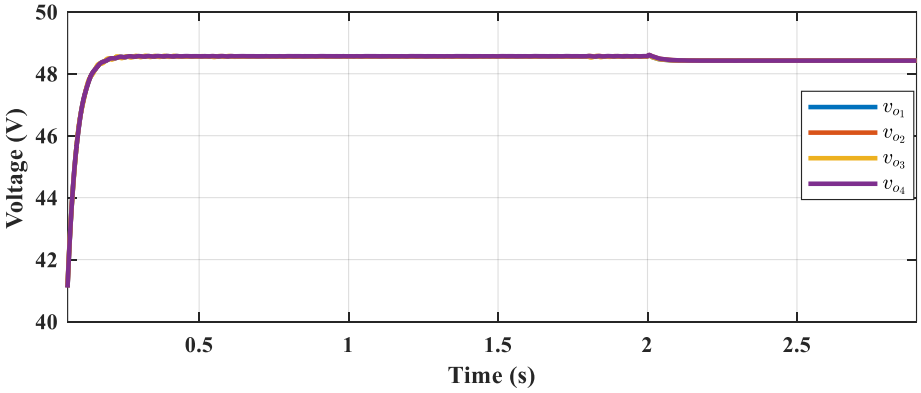

Fig 3.24. Behavior of the output voltages of the DC/DC buck converter resulted from the second scenario.

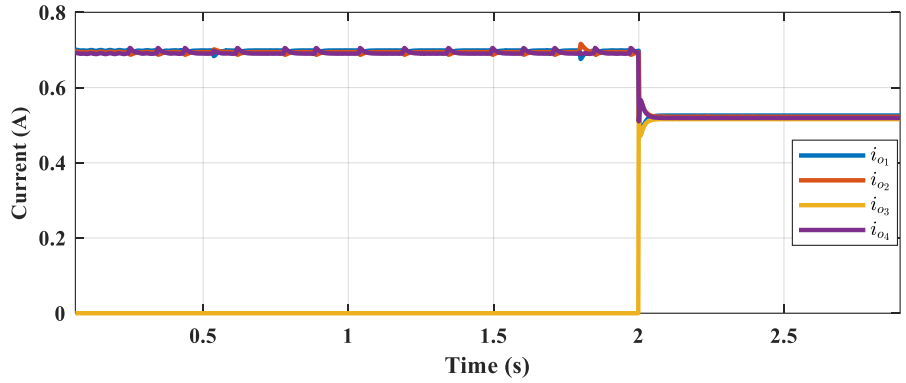

Fig 3.25. Behavior of the output currents of the DC/DC buck converter resulted from the second scenario.

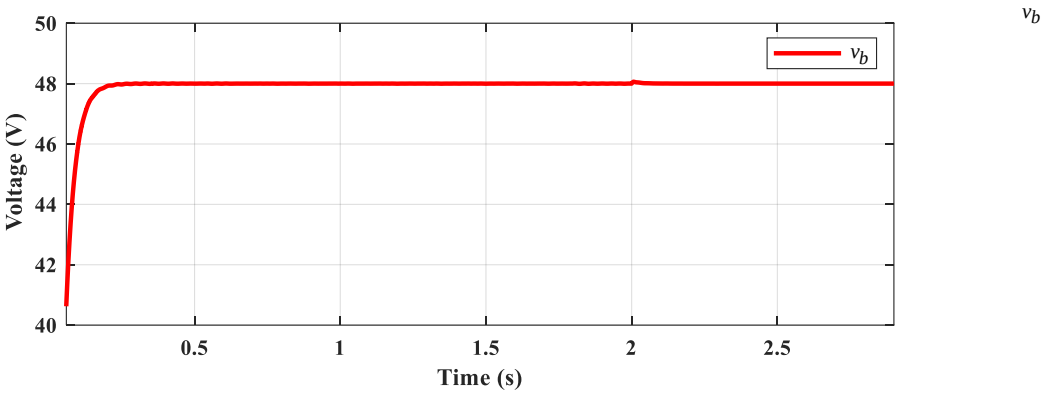

Fig 3.26. Behavior of the bus voltage resulted from the second scenario.

The third scenario is to validate the effectiveness of the robust hierarchical control to mitigate the disturbances arising from the sudden changes, which occur in one or more DC/DC buck converters' input voltages. This scenario is achieved as follows: the sudden change occurs only in the input voltages of the first and fourth DC/DC buck converters. From 0s to 2s, the input voltages v_{in_1} and v_{in_2} are kept at 100V. At 2s, the sudden change occurs, where v_{in_1} decreases by 20V and v_{in_2} increases by 20V, as illustrated in Fig 3.27. Under this scenario, the system supplies the CPL consuming power of 100 W. The simulation results of this scenario are presented in Fig 3.28, Fig 3.29.

The fourth scenario is carried out to verify the effectiveness of the robust hierarchical control to mitigate the effect of component faults. In this scenario simulation, the component faults are included in the filters (LC) elements of the second and third DC/DC buck converter in the same way presented in section 2.7. These faults are represented by the parameter variation of the inductance *L* and capacitance *C*, which exceed 5%. This scenario is performed as follows: From 0s to 2s, parameters *L* and *C* are kept at the nominal values ($L = L_0$ and $C = C_0$). At 2s, the

sudden change occurs in the parameters L and C as follows: $L = L_0 + 30\% \cdot L_0$ and $C = C_0 + 30\% \cdot C_0$. Under this scenario, only the CPL is present in the system and consumes a power of 100W. The simulation results of this scenario are presented in Fig 3.30 and Fig 3.31.

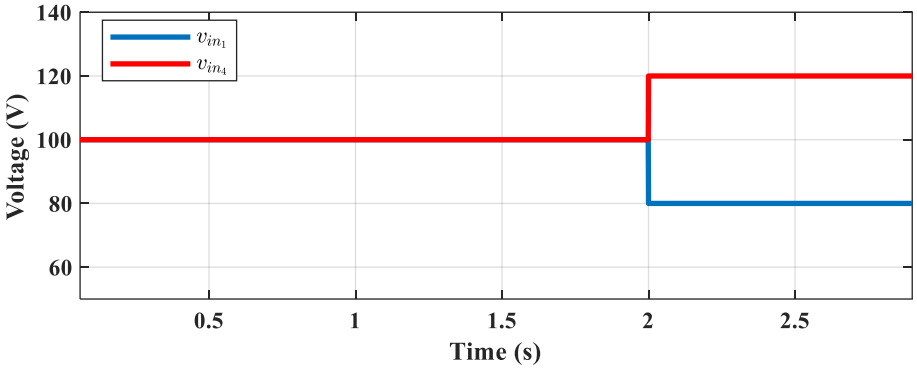

Fig 3.27. Behavior of inputs voltages v_{in_1} and v_{in_2} resulted from the third scenario.

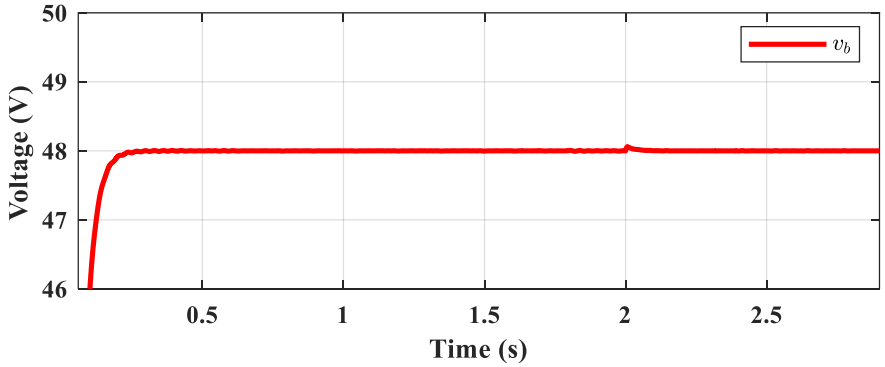

Fig 3.28. Behavior of bus voltage resulted from the third scenario.

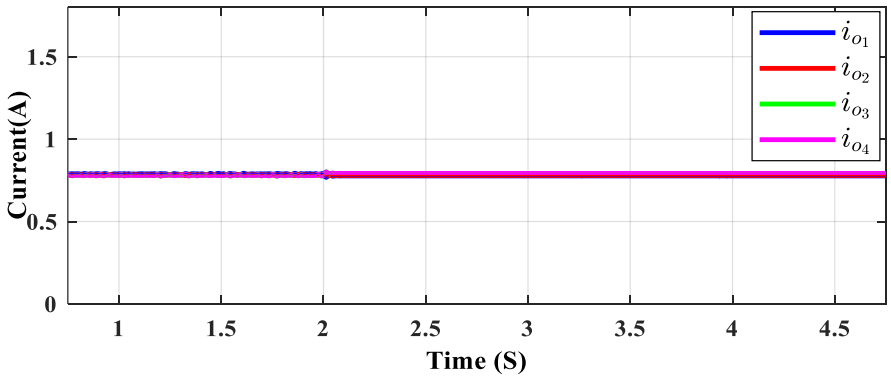

Fig 3.29. Behavior of the output currents of the DC/DC buck converters resulted from the third scenario.

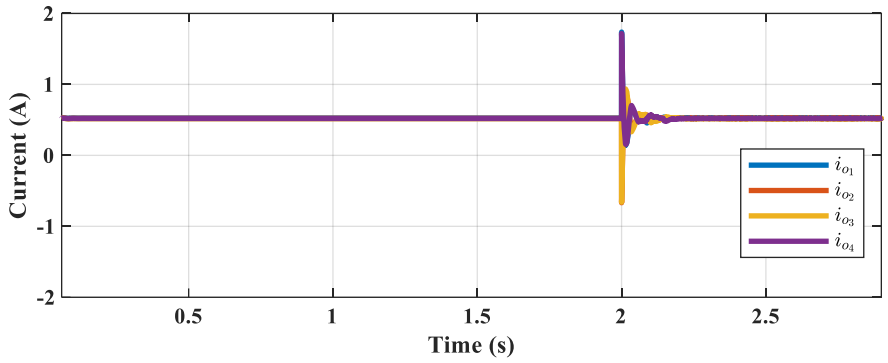

Fig 3.30. Behavior of the output currents of the DC/DC buck converters resulted from the fourth scenario.

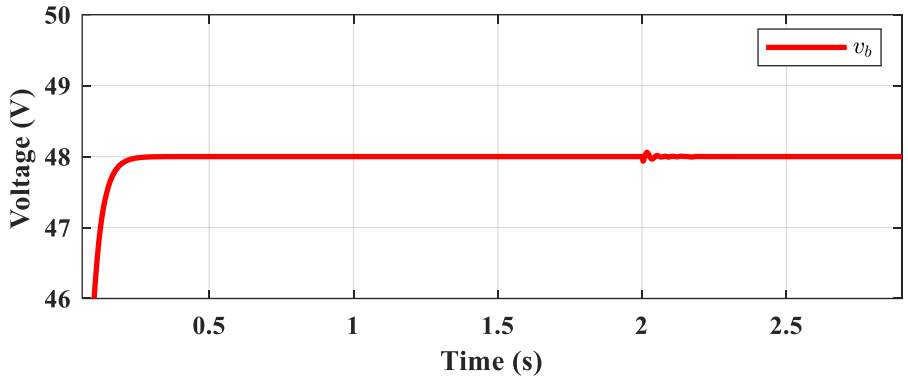

Fig 3.31. Behavior of the bus voltage resulted from the fourth scenario.

According to Fig 3.21, Fig 3.22, and Fig 3.23, the output and bus voltages are deviated from the nominal value v^* due to the droop controls of the primary control level. Also, it is noticed that all the DC/DC buck converters provide the same output currents and voltages because the droop controls employ the same virtual impedance R_v. These results show that the primary control level avoids the magnitudes difference of the DC/DC buck converters output voltages that prevent the occurrence of current circulating. It is also noticed that the application of $K_{p_\infty}(s)$, which is integrated into the primary control, avoids the instability problem caused by the presence of CPL due to the increase of the damping factors of system elements.

The activation of the secondary control level lets avoiding the voltage deviation, which appears due to the primary control level. This secondary control level restores the bus voltage to maintain at the nominal value $v^* = 48V$ and avoids the instability problem caused by the presence of CPL. When CPL increases its consumption power, by the way, the CPL current Also increases, the small voltage deviation appears in the bus voltage during a short duration. After that, this voltage deviation will be smoothed. Moreover, these results show that the robust hierarchical control guarantees the same in the presence of the resistive load, which does not cause any instability problem, and CPL, where the presence of the resistive load in place of

CPL affects the dynamic of the system. But that does not affect the performance of the proposed approach.

According to Fig 3.24, Fig 3.25, and Fig 3.26, it is noticed that the disconnected DC/DC buck converter does not provide the current. On the other hand, the output voltage of this disconnected DC/DC buck converter is provided due to the standby mode applied in this DC/DC buck converter. This standby mode must be applied in any DC/DC buck converter before connecting it to the system under operation to prevent any damage. These scenario results show that connecting the disconnected DC/DC buck converter again to the common DC bus causes a very small voltage deviation, which appears for a short duration. After that, this deviation will be smoothed. This perturbation that arises from connecting the DC/DC buck converter does not affect the system's stable operation despite that CPL is present in the system, what it is shown by the results of the second scenario. It is the same shown by the results of the third scenario depicted in Fig 3.28 and Fig 3.29. the sudden changes in the inputs voltage also cause small voltage and current deviations. After that, these deviations are smoothed and do not affect the operation of the system.

According to Fig 3.30 and Fig 3.31, the component faults do not considerably affect the bus voltage. But the fault occurrence causes the current fluctuation and current circulating during a short time interval, which will be smoothed out after some time. Also, the results presented in Fig 3.30 and Fig 3.31 show that the occurrence of component faults does not affect the system's stability. Therefore, these component faults do not decrease the damping factor of system elements when the system operates under the robust hierarchy control.

3.7. Conclusion

In this chapter, the results obtained from the simulation study prove that the proposed approach enhanced the robustness of the hierarchical control against the INI characteristic of CPL, faults, and disturbances and ensures a better regulation of the bus voltage and output voltages and currents of DC/DC buck converters in the presence of CPL and faults. This robust hierarchical control avoids the difference in the output voltages magnitudes that prevent the occurrence of current circulating and ensure the power flow needed to supply the load. Also, these obtained results show the capability of the design process consisting of GDOA and NOA to perform the robust control. The developed approach is validated by the presence of two kinds of load: resistive load and CPL. These loads were not simultaneously present in the system during the simulation. The change of loads in the system has a considerable effect on the system.

Therefore, this validation proves that the change of system dynamic does not affect the performances of the developed robust control.

Chapter 4: Active fault tolerant control of DC microgrid system.

4.1. Introduction:

The stability of the DC-MG system is not saved from the effect of the severe component faults despite that DC-MG operates under the developed robust control hierarchy. The robust Hierarchical control can not maintain the damping factor of system components at the desired value due to some faults, which cause parameter variations that exceed the accepted limits. Therefore, the robust Hierarchical control needs a process used to reconfigure the robust controllers (H_∞ and structured H_∞ based controllers) for being adapted. In this case, the Hierarchical control earns the ability to keep the damping factor at the desired value in order to save the DC MG from the instability problem.

This chapter develops an active fault-tolerant control (FTC). It consists of the robust online diagnosis and the reconfiguration process exploited to recalculate the robust controllers when the faults occur in the DC MG. The Robust online diagnosis is developed using the linear fractional transformation bond graph (LFT BG) modeling approach, a powerful tool for modeling hybrid multi-physical systems such as DC MG. This modeling tool can include the disturbances and uncertainties as a part of the model. The developed Robust online diagnosis can estimate the variations of the parameter arising due to faults. The control reconfiguration will use them to update the robust controllers. The chapter also presents the simulation study consisting of two parts is carried out using 20SIM software. This simulation gives results that prove the effectiveness of the proposed approach to mitigate the effect of the components. In this study, the sensors and actuator faults and the faults in the semiconductor components are not taken into account. The study focuses more on the components faults, which affect the stability of the system.

4.2. Conventional bond graph

BG is a modeling tool used to model multi-physical systems in the form of a graph. This graph shows the physical cause and effect and energy exchange between system elements. This graphical modeling presentation can be used to generate the analytical equations of the system automatically with the help of the software, which is familiar with this BG modeling tool [105]. The BG approach is wildly used in the industry of mechatronics and power systems. It has several advantages as:

- It is a unique language for all physical domains.
- It clearly shows the cause and effect relations in the model.
- It allows further possible development and evolution of the model.

- It is also a tool for analyzing the system's structural properties.

The BG is a union of two sets of elements: $s = \theta \cup A$, where *A* is the set of the power bonds, which show the exchange of the powers between the system elements. In contrast, θ is the set of the elements used to model the system components, which consists of the passive elements {*R*, *C*, I}, Active elements {*Se*, *Sf*}, transformer elements {TF, GY}, junctions {1,0} and sensor elements {*De*, *Df*}. Moreover, the BG formalism is known by the causal properties used to carry out the simulation study of the system and perform the online diagnosis for the modeled system [106].

4.2.1. Power bond

Power bond is illustrated by the half arrow, as shown in Fig 2.1. This power bond is used to show the exchange of power between the system elements [106]. The power in BG formalism is written as a product of two variables as given in the following expression:

$$P = e \cdot f \tag{4.1}$$

where *e* (effort) and *f* (flow) are the power variables.

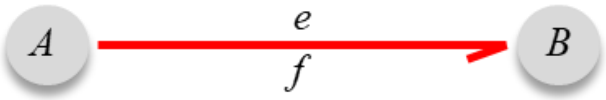

Fig 4.1. Power bond.

The nature of *e* and *f* change from one physical domain to another. Table 2.1 gives the efforts and flows for some physical domains.

Tab 4.1. Power variables in the bond graph.

Domaine	Effort:	Flow:	Power:
Electrical	Voltage *v* [V]	Current *i*	$P = v \cdot i$
Mechanical rotation	Torque *T* [N.m]	Angular velocity ω [rad/s]	$P = T \cdot \omega$
Mechanical translation	Force *F* [N]	Velocity $\dot{x}$ [m/s]	$P = F \cdot \dot{x}$

4.2.2. Passive elements

The passive elements model the system components, which receive the power. This power can be either dissipated or stored as potential energy or kinetic energy. Passive elements are classified into resistive (*R),* capacitive(*C),* and inductive (*I*) elements [105].

4.2.2.1. Resistive R element

The R element models the components that have the linear dynamic and dissipates the energy, as the electrical resistive and mechanical damper, illustrated in Fig 2.2a and Fig 2.2b, respectively. Its constitutive equation can be written as follows:

$$\Phi_R(e, f) = e - R \cdot f = 0 \tag{4.2}$$

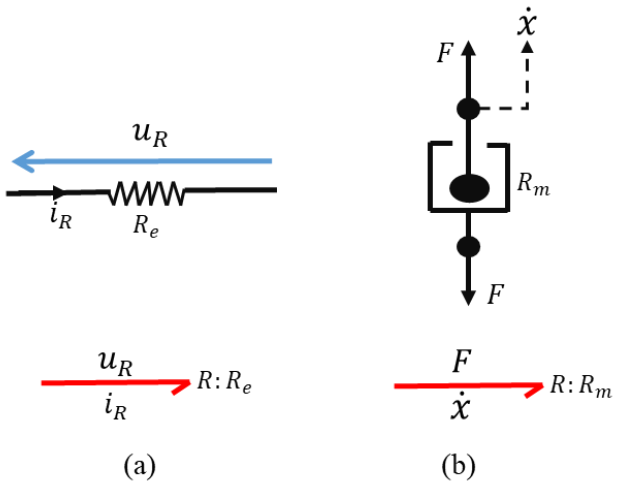

Fig 4.2. a) Electrical resistance, b) Mechanical damper.

The R element can be modulated by the external signal. For example, consider a normal diode if the diode is conductive. It can be considered a closed interrupter, as illustrated in Fig 2.3a. If the diode is not conductive. It can be considered an open interrupter, as illustrated in Fig 2.3b. This component can be modeled by a modulated resistive elements *MR*, as illustrated in Fig 2.3c, where m is an external signal that gives the state of diode and R_0 is the internal resistance of the diode. *MR* can be written as follows:

$$MR = \begin{cases} \dfrac{R_0}{m} = R_0 \text{ if } m = 1 \text{ (diode is conductive)} \\ \dfrac{R_0}{m} \approx \infty \text{ if } m = 0 \text{ (diode is not conductive)} \end{cases} \tag{4.3}$$

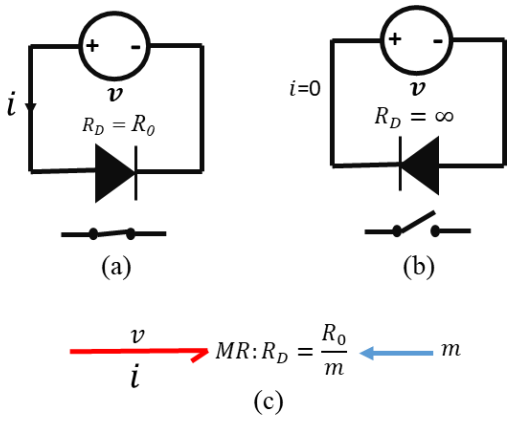

Fig 4.2. a) Conducive diode, b) Not a conductive diode, c) BG model of the diode.

4.2.2.2. Capacitive C element

The capacitive *C* element is used to model the system components, transforming the received energy into the potential energy without loss, as the electrical capacitor and spring, illustrated in Fig 2.4a and Fig 2.4b, respictevely. The constitutive equation of the *C* element can be written as follows:

$$\Phi_C\left(e, \int f \cdot dt\right) = e - \frac{1}{C}\int f dt = 0 \tag{4.4}$$

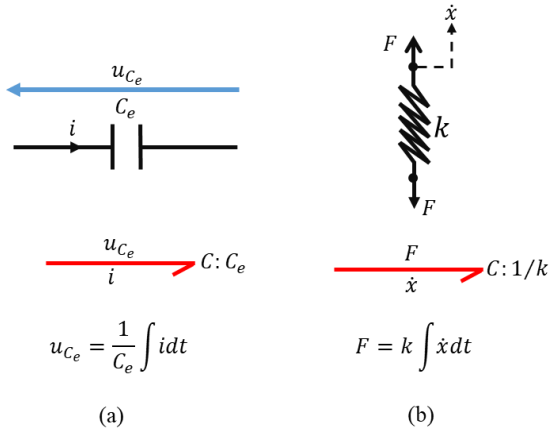

Fig 4.3. a) Electrical capacitor, b) Spring.

4.2.2.2. Inductive I element

The *I* element models the system components, transforming the received energy into kinetic energy without loss, as the electrical inductor and motor shaft, illustrated in Fig 2.5a and Fig 2.5b, respectively. The constitutive equation of the *I* element can be written as follows:

$$\Phi_I\left(e, I\frac{df}{dt}\right) = e - I\frac{df}{dt} = 0 \tag{4.5}$$

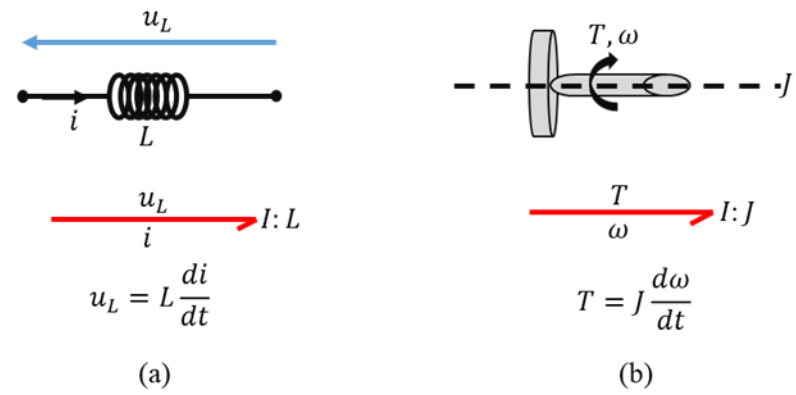

Fig 4.4. a) Electrical inductor, b) Motor shaft.

4.2.3. Active elements

The elements S_e and S_f model the system component providing the power in the form of effort and flow, respictevely [105]. For instance, the voltage and current sources are the components that provide electrical power. Under the BG approach, these electrical sources are modeled by the active elements, as illustrated in Fig 4.6a and Fig 4.6b, respectively.

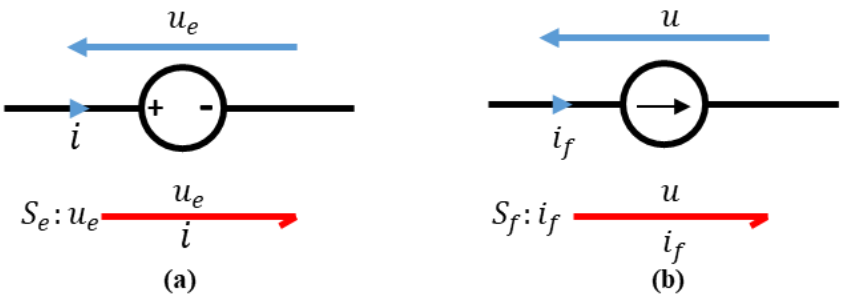

Fig 4.6. a) Electrical voltage source, b) Electrical current source.

These active elements can be modulated (MS_e and MS_f). In this case, the effort and flow depend on an external signal. The modulated active elements can model, for example, the electrical dependent sources, as illustrated in Fig 4.7, marked by (1) and (2), where v_x is an external signal.

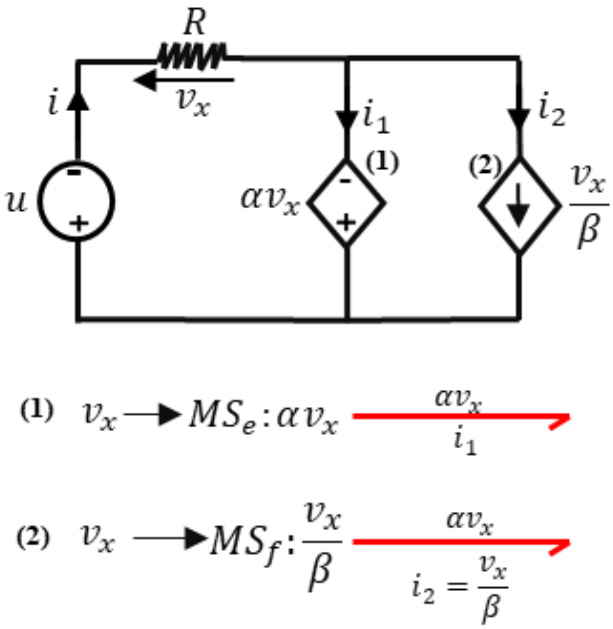

Fig 4.7. Modeling the electrical dependent sources using the modulated active elements.

4.2.4. Transformer and gyrator

The transformer element denoted by *TF* models the system components, which transform and transport the power from one part of the system to another [106]. For instance, the *TF* element can model the electrical power transformer, as illustrated in Fig 4.8a, where the input effort e_1 is proportional to the output effort e_2, and the output flow f_2 is proportional to the input flow f_1 . The constitutive equation of TF can be written as follows:

$$Tf \rightarrow \begin{cases} e_1 = me_2 \\ f_2 = mf_1 \end{cases} \tag{4.6}$$

The TF element can be modulated. In this case, the magnitude of the ratio m depends on an external signal. For instance, in the case of the electrical power transformer illustrated in Fig 4.8c, the transformation ration m can depend on the magnetic permeability μ of the ferromagnetic material of the electrical power transformer. This electrical power transformer can be modeled by a modulated *TF element (MTF)*, where the magnetic permeability is an external signal under the BG approach.

The gyrator element denoted by *GY* models the system components that transform the power and transport it from one part of the system to another. But this element changes the physical nature of the power. For instance, the GY can model the electromechanical part of the DC motor, as illustrated in Fig 4.8b, the input effort e_1 is proportional to the output flow f_2 , and

output effort e_2 is proportional to the input flow f_1 . The constative equation of GY can be written as follows:

$$GY \rightarrow \begin{cases} e_1 = rf_2 \\ e_2 = rf_1 \end{cases} \tag{4.7}$$

The GY element can be modulated. The magnitudes of the ratio *r* of *GY* depend on an external signal. Considering the example of the electromechanical part of the DC motor, the modulated *GY* element (*MGY*) can model the DC motor electromechanical part when the ratio *r* depends on the current i_H , which is used to produce the magnetic field required to turn the shaft of the DC motor, as illustrated in Fig 4.8d. In this example, under the BG approach i_H is the external signal.

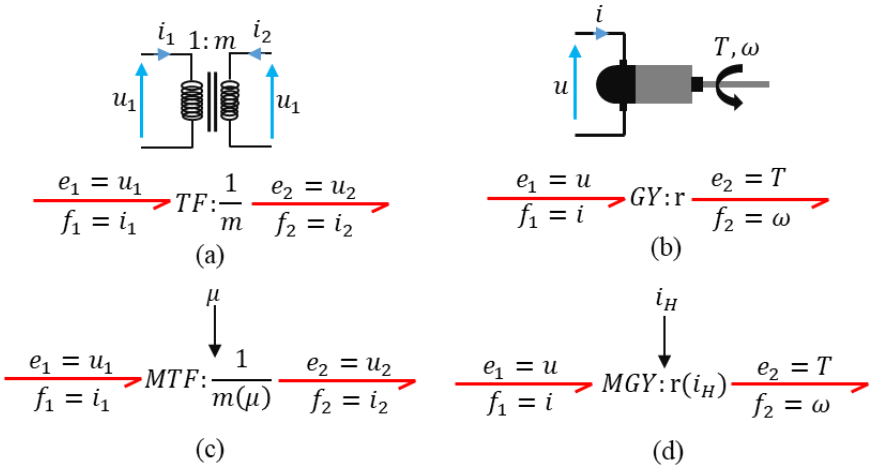

Fig 4.8. a) BG model of the electrical transformer, b) BG model of the electromechanical part of the DC motor, c) Modulated MTF element, d) modulated MGY element.

4.2.5. Junctions

The junctions "1" and "0" link between BG elements and gather them in the same graph, as shown in the example of the electrical circuit BG model depicted in Fig 4.9. The power bonds linked to junction "1" must have the same flow. On the other hand, the sum of the efforts of the incoming power bonds is equal to the sum of the efforts of the outgoing power bond, as shown in the junction "1" marked by (1) of the example of the BG model of the electrical circuit. The power bonds linked to junction "0" must have the same effort. On the other hand, the sum of the flows of incoming power bonds is equal to the sum of the flows of the outgoing power bonds, as shown in the junction "0" marked by (2) of the example of the electrical circuit BG model [105-106].

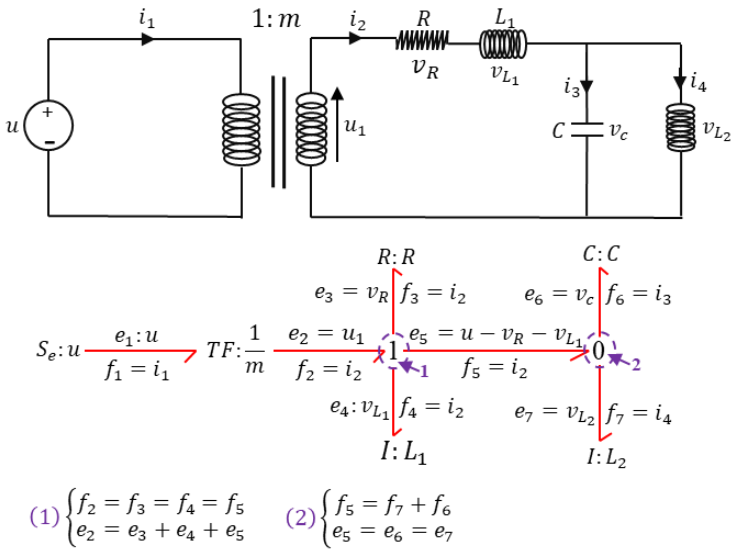

Fig 4.9. Electrical circuit BG model.

4.2.6. Effort and flow detectors

Under the BG approach, the sensors used to measure power variables: effort and flow are presented by effort and flow detectors: D_e and D_f [105]. The D_e and D_f are linked to the junction "0''and "1", respectively, to measure the effort and flow. These detectors are linked to the junctions using an information bond depicted by the full arrow, as illustrated in the example of the RLC electrical circuit shown in Fig 4.10, where i_m and v_{L_m} denote the measurements of i and v_L. This information bond represents the signal transmission of effort and flows measurement.

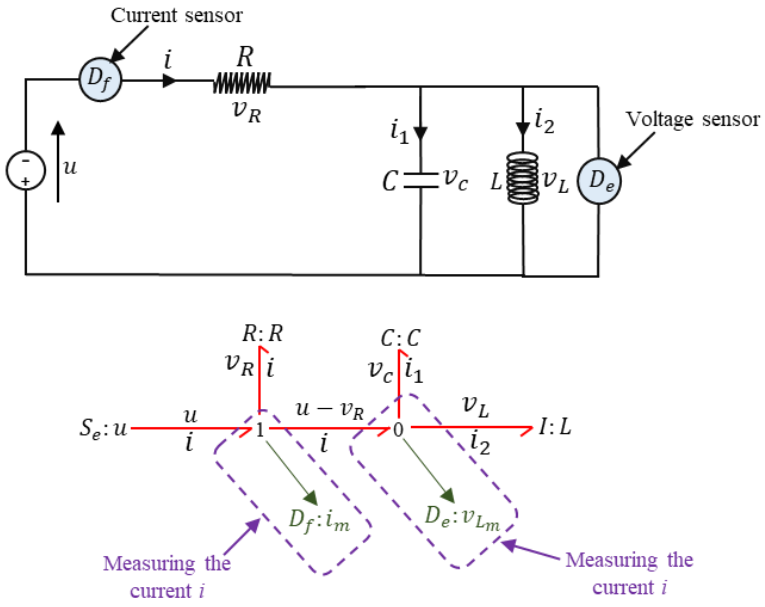

Fig 4.10. RLC electrical circuit BG model incorporating the detector elemenst for measuring current and voltage.

4.2.7. Causality

BG formalism is known by the causal properties, which are the integral and derivative causal properties. These properties are the way to know how the system components act between them, as illustrated in Fig 4.11. The causal properties are presented in BG by the cross-stroke in one of the power bond sides. S_1 acts on S_2 by an effort, and S_2 replies to S_1 by a flow (effort causality) if the cross-stroke is placed on the right side. On the other hand, the cross-stroke placement on the left side shows S_1 acts on S_2 by a flow, and S_2 replies to S_1 by an effort (flow causality). The use of integral and derivative causal properties simulates the dynamic of modeled multi-physical systems and develops online monitoring for FDI, respectively, before the online implementation [107]. The cross-stroke assignment in integral and derivative causal properties is performed by respecting the rules well explained in [105]. Under derivative causal property, the elements of effort and flow sensors D_e and D_f become the effort and flow signal sensors SS_e and SS_f, respectively [106].

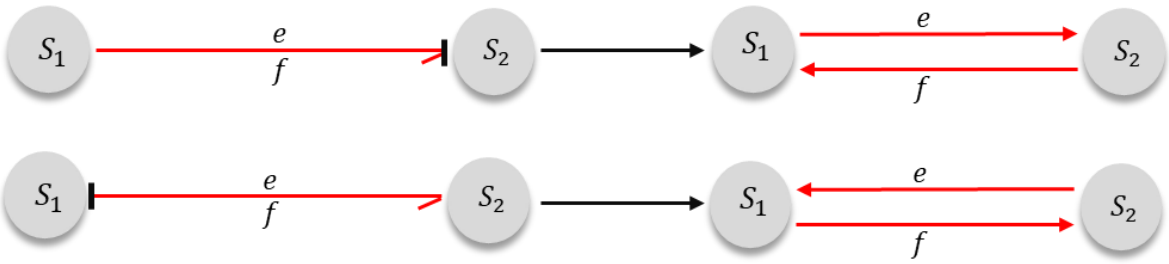

Fig 4.11. Causality presentation.

4.3. Linear fractional transformation for modeling the uncertainties under bond graph approach

The real process DC-MG parameter identification meets issues, which prevents obtaining the nominal values. In this case, each DC-MG parameter can be expressed by an interval of values, where its minimum and maximum values are related to the parameter's uncertainty. Also, the DC-MG parameters may vary in the range that can arise due to unknown disturbance, even in the case of the absence of faults. The minimum and maximum of this range are related to the parameter uncertainties. This problem complicates FDI's task performed for DC-MG and is considered as the main cause of false alarms. For more robustness of the FDI algorithm, linear fractional transformation presentation is used to incorporate the uncertain part of the DC-MG parameter in the BG model [108].

Using the LFT methodology, uncertainties on parameters are considered as an additive or multiplicative, as written in (4.8) and (4.9), where β is an example of any system parameter to

illustrate the LFT methodology, β_n is the β nominal value, δ_β is the relative uncertainty, and Δ_β is the absolute uncertainty.

$$\beta = \beta_n \pm \Delta\beta \tag{4.8}$$

$$\beta = \beta_n \left(1 \pm \delta_\beta\right) \tag{4.9}$$

To illustrate how uncertainty is integrated into the BG using the LFT presentation methodology, consider the BG *R* element's case. Let consider $R = R_n\left(1 \pm \delta_R\right)$ the real value of the *R* element.

Assume that the causality of this element *R* is assigned on the left side. Then, the effort of *R* is written as follows:

$$\begin{aligned} e_R &= R \cdot f_R = R_n\left(1 \pm \delta_R\right) f_R = R_n f_R \pm \delta_R R_n f_R \\ &= e_{R_n} + e_{\delta_R} \end{aligned} \tag{4.10}$$

According to (4.10), the uncertainty of *R* integrated into BG when the causality is assigned on the left side is shown in Fig 4.12a, where D_e^* is used to measure e_{R_n} and e_R is introduced by MSe^*.

Assume now the causality of *R* is assigned on the right side. Then, the flow is given as follows:

$$\begin{aligned} f_R &= \frac{1}{R} e_R = \frac{e_R}{R_n\left(1 \pm \delta_R\right)} = \frac{1}{R_n}\left(1 \pm \delta_{1/R}\right) e_R \\ &= \frac{e_R}{R_n} \pm \frac{\delta_{1/R} e_R}{R_n} = f_{R_n} + f_{\delta_{1/R}} \end{aligned} \tag{4.11}$$

According to (4.11), the uncertainty of *R* integrated into BG under effort causality is shown in Fig 4.8b, where D_f^* is used to measure f_{R_n} and MS_f^* introduces $f_{\delta_{1/R}}$.

The LFT presentation of elements *C*, *I*, *GY*, and *TF* in BG can be performed in the same way as the element *R* [109].

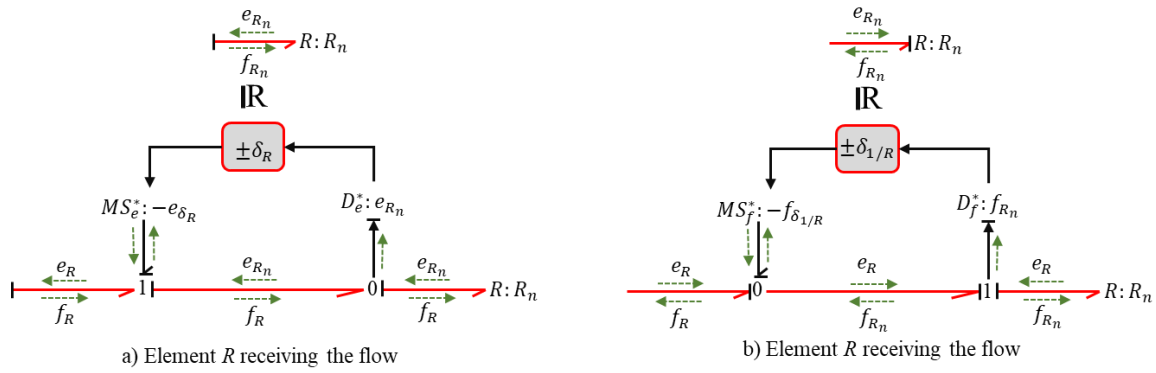

Fig 4.12. LFT-BG model of R element.

4.4. Robust online diagnosis based on linear fractional transformation bond graph

The robust online diagnosis consists of the *ARRs* and generators of adaptive thresholds. They are derived from the LFT-BG model by using the properties of the junctions ("0" and "1") where there is a SS_e or SS_f that corresponds to the sensors used for monitoring. The *ARR* is the sum of efforts of incoming power bonds minus the sum of efforts of outgoing power bonds if the junction "1" is used. Also, the *ARR* can be the sum of flows of incoming power bonds minus the sum of flows of outgoing power bonds if the junction "0" is used. All *ARR* parameters must be known, and the uncertain parts are neglected [110]. The mathematical expression of *ARR* can be written as follows:

$$\begin{aligned} ARR &= \Sigma\left(e_{in_n} + \cancelto{0}{e_{in_\delta}}\right) - \Sigma\left(e_{out_n} + \cancelto{0}{e_{out_\delta}}\right) \\ &= \Psi\left(\Sigma SSe, \Sigma SSf, \Sigma Se, \Sigma Sf, \theta_n\right) \end{aligned} \tag{4.12}$$

or

$$\begin{aligned} ARR &= \Sigma\left(f_{in_n} + \cancelto{0}{f_{in_\delta}}\right) - \Sigma\left(f_{out_n} + \cancelto{0}{f_{out_\delta}}\right) \\ &= \Psi\left(\Sigma SSe, \Sigma SSf, \Sigma Se, \Sigma Sf, \theta_n\right) \end{aligned} \tag{4.13}$$

where e_{in}, e_{out}, f_{in}, f_{out} and θ_n are the nominal incoming effort, outgoing effort, incoming flow, outgoing flow and BG elements parameters, and e_{in_δ}, e_{out_δ}, f_{in_δ} and $f_{out\delta}$ are the neglected incoming effort, outgoing effort, incoming flow, and outgoing flow, respectively, generated by the uncertain parts. The generator of adaptive threshold a is the sum of the absolute value of uncertain parts neglected in (4.12) or (4.13) and the uncertainties arising from the sensors [108]. It can be written as follows:

$$\begin{aligned} a &= \Sigma\left|e_{in_\delta}\right| + \Sigma\left|e_{out_\delta}\right| + \Sigma\left|\xi\right| \\ &= \Psi\left(\Sigma SSe, \Sigma SSf, \Sigma Sf, \Sigma Se, \theta_n, \delta_\theta\right) + \left|\Sigma\zeta\right| \end{aligned} \tag{4.14}$$

or

$$\begin{aligned} a &= \Sigma\left|f_{in_\delta}\right| + \Sigma\left|f_{out_\delta}\right| + \Sigma\left|\xi\right| \\ &= \Psi\left(\Sigma SSe, \Sigma SSf, \Sigma Sf, \Sigma Se, \theta_n, \delta_\theta\right) \end{aligned} \tag{4.15}$$

where $\delta_\theta = \left\{\delta_R, \delta_C, \delta_L, \delta_{TF}, \delta_{GY}\right\}$ and $\theta_n = \left\{R_n, C_n, I_n, GY_n, TF_n\right\}$. The fault indicators are the numerical evaluation of *ARRs* called "residual signals." $r = eval(ARR)$. Theoretically, *r* should be zero, but *r* is not zero due to noises and parameter uncertainties. If $-\left|a\right| \le r \le \left|a\right|$, then the system operates in the nominal conditions (no faults). Else, faults occur in the system [110].

4.6. Linear fractional transformation bond graph of DC Microgrid

In this section, the process of obtaining the LFT-BG model of DC-MG, illustrated in Fig 4.13, is briefly explained, where the causality of the model is assigned under the derivative causality propriety. This DC-MG system has the same configurations described in the previous chapters. But the only difference is the RESs: the wind turbine, photovoltaic panel, and storage device are included in the system. This model is obtained by joining the nominal BG models of DC-MG components in the single model and including the parameter uncertainties using LFT presentation. The obtained DC-MG LFT-BG model will be used to drive the ARRs and generators of the adaptive thresholds to monitor the whole components of the DC-MG.

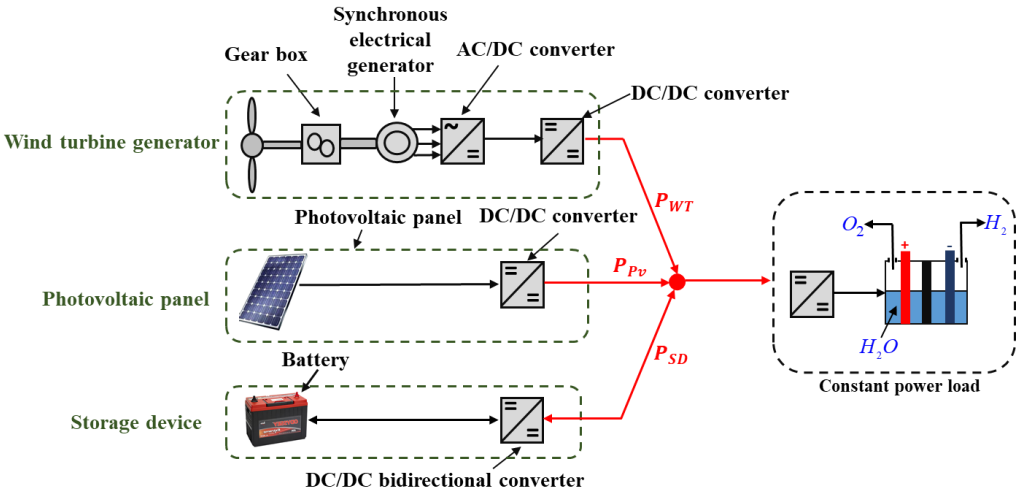

Fig 4.13 DC-MG incorporating the renewable energy source.

4.6.1. Wind turbine generator nominal BG model

The wind turbine (WT) component consists of a mechanical part deriving the synchronous electrical generator. The mechanical part is illustrated in Fig 4.14a, and its BG nominal model is illustrated in Fig 4.14b. It consists of the propeller driving a gearbox. This mechanical part is connected to the electrical synchronous machine through a shaft characterized by two parameters: J is the inertia moment, and σ is the viscous friction coefficient. The propeller, which is the generator of torque T_{ear} deduced from the wind speed W_S and direction W_D, converts the wind's kinetic power to mechanical power. The Gearbox provides the suitable torque and rotational speed Ω to derive the synchronous electrical generator for generating the electrical power, where the torque provided by Gearbox is equal to $T_{ear} = Jd\Omega/dt + f\Omega$ [110]. In the BG approach, the power variables are as follows: e is the torque, and f is the rotational speed. The source of effort MS_e models the propeller: T_{ear} and the Gearbox by $TF:1/G$ element. As the same Ω drives all shaft particles, the shaft part is modeled by $I:J$ and $R:\sigma$ connected to junction "1".

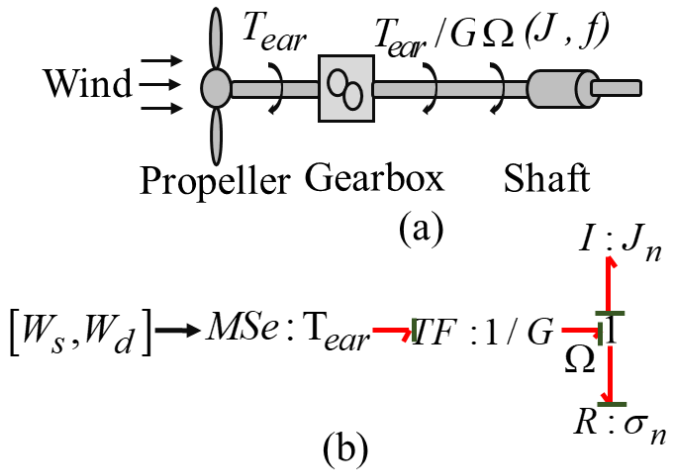

Fig 4.14. a) Mechanical part of the wind turbine, b) Nominal BG model of the wind turbine mechanical part.

The synchronous electrical generator of the WT component illustrated in Fig 4.15a consists of two parts: the moving and the fixed parts. It converts the mechanical power provided by the mechanical part to the electrical power when the moving part rotates due to shaft rotation. The permanent magnet used to make the moving part generates a magnetic field circulation, which excites the fixed part's winding to produce the electrical current. The nominal BG model illustrated in Fig 4.15b of the synchronous electrical generator (Power variables: e is the voltage; f is current) is obtained based on the park transformation technique [112]. The elements $MGY : (3/2)\, pL_{d_n} i_q \Omega$, $MGY : (-3/2)\, pL_{q_n} i_d \Omega$ and $GY : (3/2)\, p\lambda\Omega$ model the interaction of magnetic field circulation with the winding of the fixed part when the moving part is rotating, p is the generator pole pairs and λ is the flux density of the permanent magnet, and the elements $R : R_{d_n}$, $R : R_{q_n}$, $I : I_{d_n}$, $I : I_{q_n}$, v_d, v_q, i_d and i_q refer to the electrical characteristic of the fixed part winding, where R_{d_n} and R_{q_n} are the resistances in the direct and quadratic axis, respectively, L_{d_n} and L_{q_n} are the inductances in direct and quadratic axis, respectively, v_d and v_q are the winding voltages in the direct and quadratic axis, respectively, and i_d and i_q are the winding currents in the direct and quadratic axis, respectively. The synchronous electrical generator's real outputs are i_a, i_b, i_c, v_a, v_b, and v_c. They are obtained using the inverse Park transformation of v_d, vq, i_d and i_q.

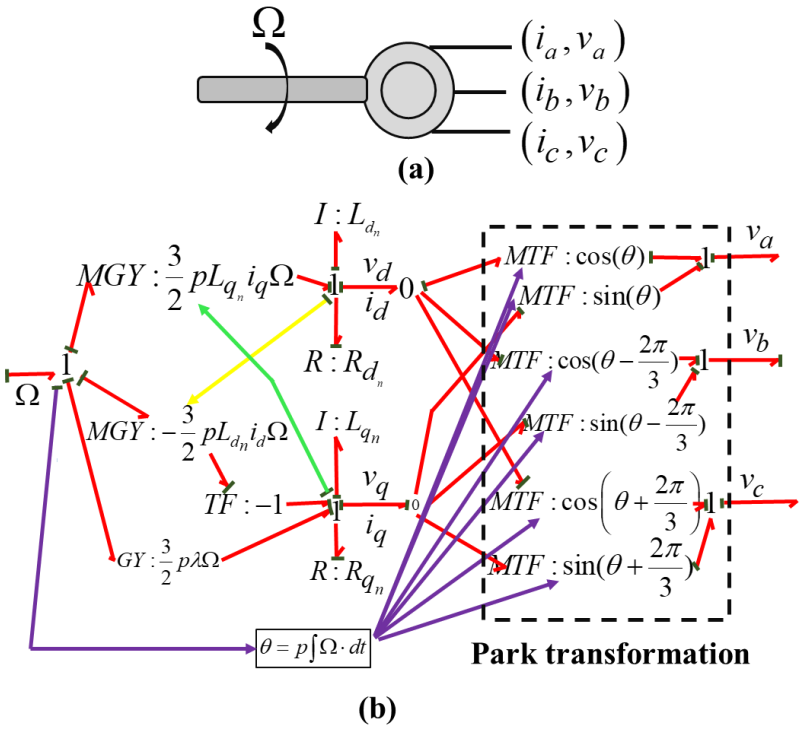

Fig 4.15. a) Synchronous electrical generator, b) Nominal BG model of the synchronous electrical generator.

4.6.2. Photovoltaic panel nominal BG model.

The photovoltaic panel (PV) component consists of a series of solar cells that capture solar irradiation (*S*) and convert it to electrical power. This PV component can be considered as the current source producing i_{ph} as depicted in Fig 4.16a, and its nominal BG model is illustrated in Fig 4.16b, where *MSf:*i_{ph} is used to model the i_{ph} current source and *R:* R_{shn}, *R:* $R_{Dn,}$ and *R:* R_{sn} are used to model the particles causing the power loss, where R_{shn}, $R_{Dn,}$ and R_{sn} are the equivalent shunt resistance, the equivalent resistance of diode deduced from the semiconductor characteristic of the panel, and equivalent series resistance, respectively. This component's output power is the product of i_p and v_p, which are photovoltaic current and voltage, respectively [113].

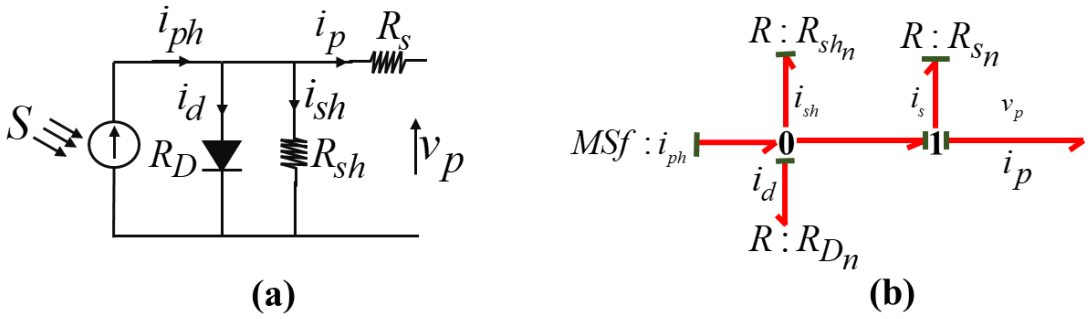

Fig 4.16. a) Photovoltaic panel equivalent electrical circuit, b)nominal BG model of the photovoltaic panel.

4.6.3. Storage device nominal BG model.

The storage device (SD) component consists of the lead-acid battery, which can be considered as a voltage source V_{oc} (the V_{oc} value depends on the state of charge SOC of Battery) and is represented by the equivalent circuit as shown in Fig 4.17a. The nominal BG model of this component is illustrated in Fig 4.17b, where $MS_e : V_{OC}$ is used to model the voltage sources, $C : C_{dl}$ is used to model the double-layer capacitance of lead-acid battery, and $R : R_{dl}$ and $R : R_i$ are used to model the particles causing the loss of power, which are the charge transfer and internal resistances, respectively. This component's output power is the product of i_b and v_b, which are the lead-acid battery current and voltage, respectively [114].

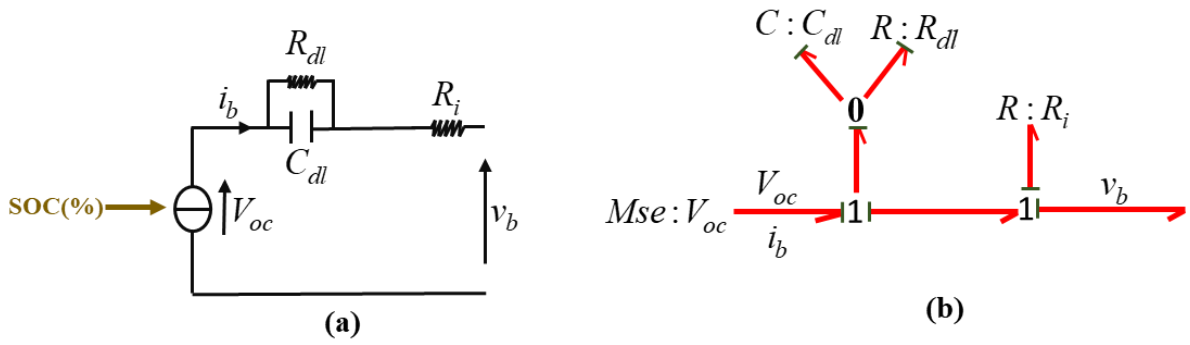

Fig 4.17. a) Electrical circuit lead-acid battery, b) Nominal BG model of equivalent electrical circuit of lead-acid battery.

4.6.4. DC/DC converter Nominal BG model

Consider that the DC/DC converters used to integrate the RESs and SD into the DC-MG system are the DC/DC buck and bidirectional converters, illustrated in Fig 4.18a and Fig 4.19a, respectively. The DC/DC buck converter is implemented to integrate the WT and PV into the DC-MG system, while the DC/DC bidirectional converter is implemented to integrate the storage device.

The nominal BG model of the DC/DC buck converter is illustrated in Fig 4.18b, where the controlled junction 1_C is used to model the semiconductor switch s, and the modulated $MR : R_D / m$ element is used to model the freewheel diode. The filter LC elements of the DC/DC buck converter are modeled by the inductance element $I : L$ and $C : C$. The PWM signal acts on the semiconductor switch s to regulate the output voltage v_o. Therefore. This semiconductor switch s has two states: closed and open states.

For this reason, the controlled junction 1_C is used to model the physical behavior of switch s in this nominal BG model, where the PWM block provides a signal to this controlled junction 1_C for changing its state: if PWM signal=1, $i_s = i_{in}$ else $i_s = 0$. The freewheel diode is implemented in the DC/DC buck converter to dissipate the energy stored in the inductive element L when the switch s is in its open state. In this case, the diode current i_D is equal to the inductance current i_L. The diode current i_D will be zero when the switch s is in its closed state. In this case, the diode is considered as an infinite impedance. In the nominal BG model of the DC/DC buck converter, the physical behavior of the freewheel diode is modeled by the modulated $MR: R_D / m$ element. The parameter m takes its value from the reverse of the PWM signal, where $m = 1$ presents the case of $i_D = i_L$ and $m = 0$ presents the case of $i_D = 0$ ($MR: \infty$). The resistance R_D is the internal resistive of the diode.

The nominal model of the DC/DC bidirectional converter is obtained using almost the same BG elements utilized to perform the DC/DC buck converter, as illustrated in 4.19b, where the switch s_1 is modeled by 1_c, the switch s_2 is modeled by 0_c and the freewheel diodes D_1 and D_2 are modeled by $MR: R_{D_1} / m$ and $MR: R_{D_2} / m$, respectively. The switches s_1 and s_2 do not operate simultaneously. For that, the process control incorporates the variable k to select which switch must operate according to the operation case of the battery (charging or discharging the battery).

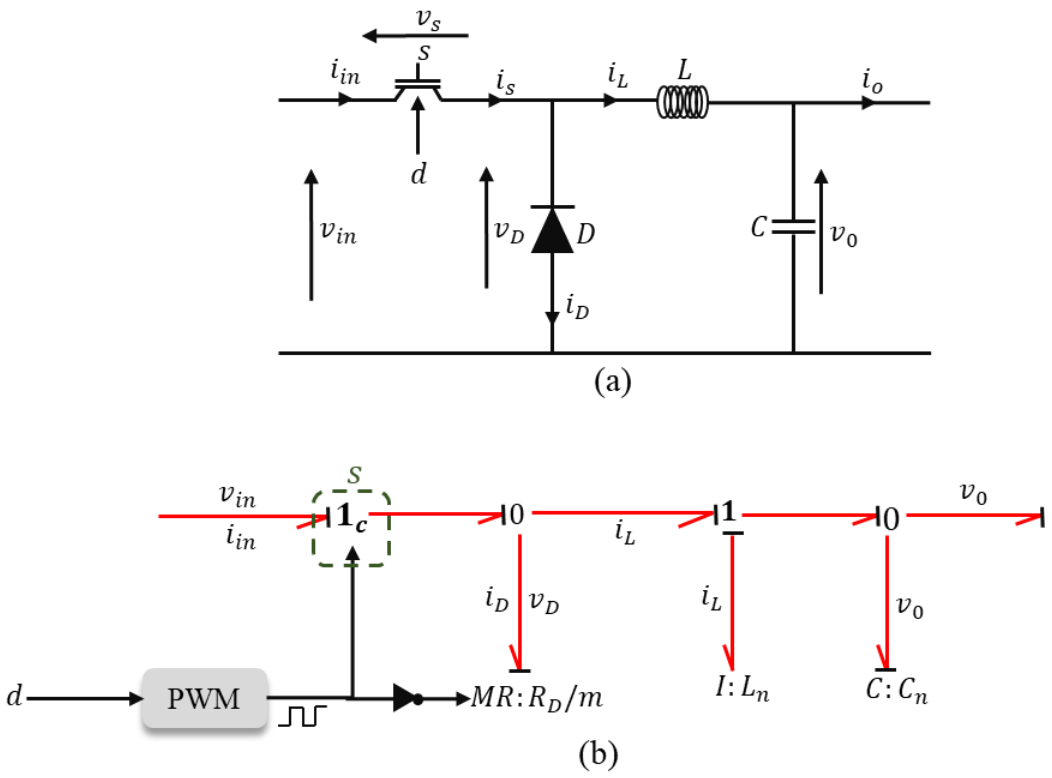

Fig.4.18. a) Electrical circuit of DC/DC buck converter, b) Nominal BG model of DC/DC buck converter.

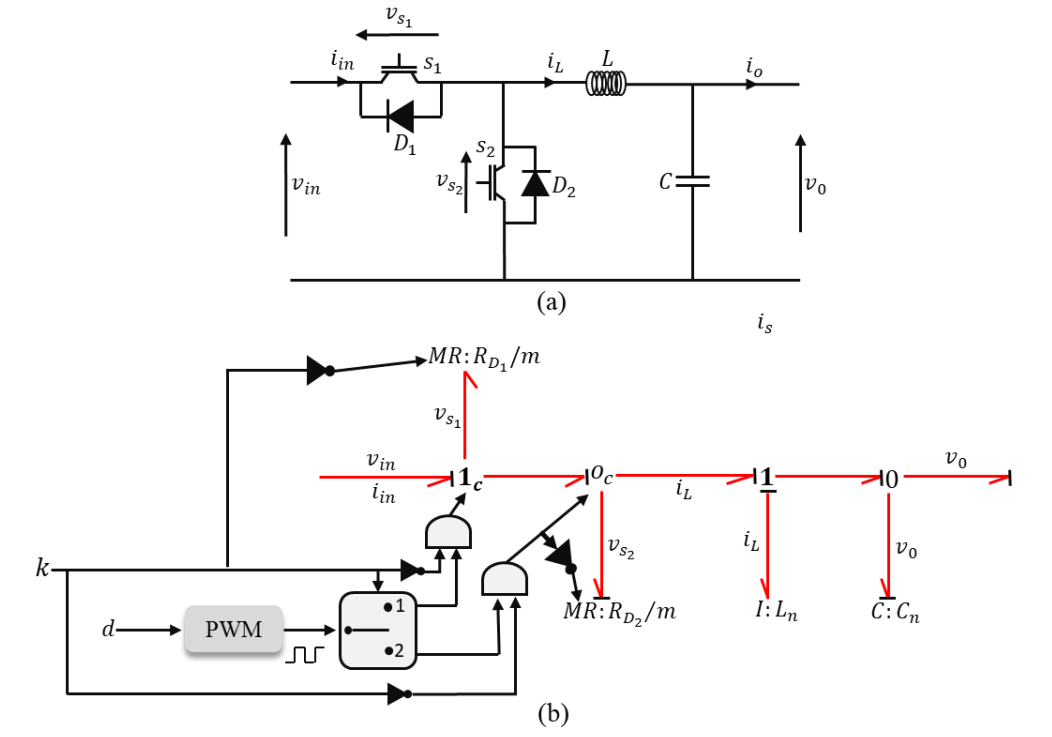

Fig 4.19. a) DC/DC bidirectional converter electrical circuit, b) Nominal BG model of DC/DC Bidirectional converter.

4.7. Robust online diagnosis of DC Microgrid system

The whole LFT-BG of DC-MG is obtained by gathering all the nominal BG models of DC Microgrid components in a single model. After that, the uncertainties of the system are incorporated in the model using LFT presentation, as illustrated in Fig 4.20, where the sensors used to monitor the system are: $SS_{f_1}, SS_{f_2}, SS_{f_3}, SS_{f_4}, SS_{f_5}, SS_{f_6}, SS_{f_7}, SS_{f_8}, SS_{e_1}, SS_{e_2}, SS_{e_3}$, SS_{e_4} which are used to get the measurements of $\Omega_m, i_{d_m}, i_{q_m}, i_{p_m}, i_{b_m}, i_{L_{1_m}}, i_{L_{2_m}}, i_{L_m}, i_{L_m}$, $v_{C_{dl_m}}, v_{o_{1_m}}, v_{o_{2_m}}$ and v_{o_m}. Actually, there are no real sensors that can be installed in the system to measure i_{d_m} i_{p_m} and $v_{C_{dl_m}}$. However, these measurements can be performed in another way. The measurement of i_{d_m} and i_{p_m} are carried out by using the transformation park performed on the measurement of v_{a_m}, v_{b_m} and v_{c_m}, while the measurement of $v_{C_{dl_m}}$ is performed using the observer's technique.

We do not consider the uncertainties arising from the internal resistance of the diode because this internal diode resistance is very small. Therefore, the uncertainties arising from the diode component do not have a considerable effect on the system. The system modeling does not consider the rectifier because the developed approach focuses more on the faults, which can deteriorate the system stability performance.

Luenberger observer is used to estimate the measurement of $SS_{e_1} : v_{C_{dl_m}}$. It can be expressed by the state-space representation written as follow:

$$\begin{cases} \dot{x} = A \cdot x + B \cdot u + K_{obs}\left(\tilde{y} - y\right) \\ \tilde{y} = C \cdot \tilde{x} + D \cdot U \end{cases} \tag{4.20}$$

where $\tilde{y} = v_{C_{dl_m}}$ and The gain of the Luenberger observer K_{Obs} is obtained by identifying the characteristic polynomial of the observer with the desired polynomial to place the poles of the observer.

The BG approaches facilitate the calculation of the matrices *A*, *B*, and *C*. These matrices can be easily deduced from the observer BG model. This BG model of the observer can be easily derived from the nominal BG model of the battery component, as illustrated in Fig 4.21, where the observer provides two outputs $\tilde{y}_1$ and $\tilde{y}_2$. The $\tilde{y}_1$ can be measured (y_{1m}) and $\tilde{y}_2$ corresponds to the suited estimation ($\tilde{v}_{C_{dl_m}}$), while the term of $K_{obs}\left(\tilde{y} - y\right)$ is included in the observer BG model by MS_f.

Fig 4.22 presents a part of the LFT BG model of the DC-MG system (Corresponding to the SD component) to illustrate the process to derive the ARRs and the adaptive threshold generators. According to the junction where $SS_{e_1} : v_{C_{dl}m}$ is placed. It is obtained that:

$$i_b - i_{C_{dl}} - i_{R_{dl}} = i_b - \left(f_{C_{dl_n}} + f_{\delta_{C_{dl}}} \right) - \left(f_{R_{dl_n}} + f_{\delta_{1/R_{dl}}} \right) \tag{4.21}$$

Neglecting $f_{\delta_{C_{dl}}}$ and $f_{\delta_{1/R_{dl}}}$, the mathematical expression of the ARR can be written as follows:

$$ARR_5 = i_b - f_{C_{dl_n}} - f_{R_{dl_n}} = i_{b_m} - C_{dl_n} \frac{dv_{C_{dl_m}}}{dt} - \frac{v_{C_{dl_m}}}{R_{dl_n}} \tag{4.22}$$

where i_{b_m} is the measurement of i_b obtained by SS_{f_5}. The adaptive threshold generator associated with ARR_5 is the sum of the neglected flows: $f_{\delta_{C_{dl}}}$ and $f_{\delta_{1/R_{dl}}}$ and the uncertainties arising from SS_{f_5} and SS_{e_1}, which can be written as follows:

$$a_5 = \left| f_{\delta_{C_{dl}}} \right| + \left| f_{\delta_{1/R_{dl}}} \right| = \left| \pm \delta_{C_{dl}} C_{dl_n} \frac{dv_{C_{dl_m}}}{dt} \right| + \left| \pm \delta_{1/R_{dl}} \frac{v_{C_{dl_m}}}{R_{dl_n}} \right| + \left| \delta_{v_{C_{dl}}} \right| + \left| \delta_{i_b} \right| \tag{4.23}$$

The other ARR_s are derived in the same way as ARR_5. They are given as follows:

$$ARR_1 = \frac{3}{2} p L_{q_n} i_{q_m} \Omega_m - L_{d_n} \frac{di_{d_m}}{dt} - R_{d_n} i_{d_m} - v_{d_m} \tag{4.23}$$

$$ARR_2 = \frac{3}{2} p \Omega_m \left(\lambda - L_{d_n} i_{d_m} \right) - L_{q_n} \frac{di_{q_m}}{dt} - R_{q_n} i_{q_m} - v_{q_m} \tag{4.24}$$

$$ARR_3 = T_{ear} - J_n \frac{d\Omega_m}{dt} - \sigma_n \Omega_m - \frac{3}{2} p \lambda i_{q_m} \tag{4.25}$$

$$ARR_4 = \frac{R_{sh_n} R_{D_n}}{R_{sh_n} + R_{D_n}} \left(i_{ph} - i_{p_m} \right) - R_{s_n} i_{p_m} - v_{p_m} \tag{4.26}$$

$$ARR_6 = \left(V_{oc} - v_{C_{dl_m}} \right) - v_{b_m} - R_{i_n} i_{b_m} \tag{4.27}$$

$$ARR_7 = d \cdot v_{WT_m} - v_{o_{1_m}} - L_{1_n} \frac{di_{L_{1_m}}}{dt} \tag{4.28}$$

$$ARR_8 = \frac{i_{in_{1_m}}}{d} - i_{o_{1_m}} - C_{1_n} \frac{dv_{o_{1_m}}}{dt} \tag{4.29}$$

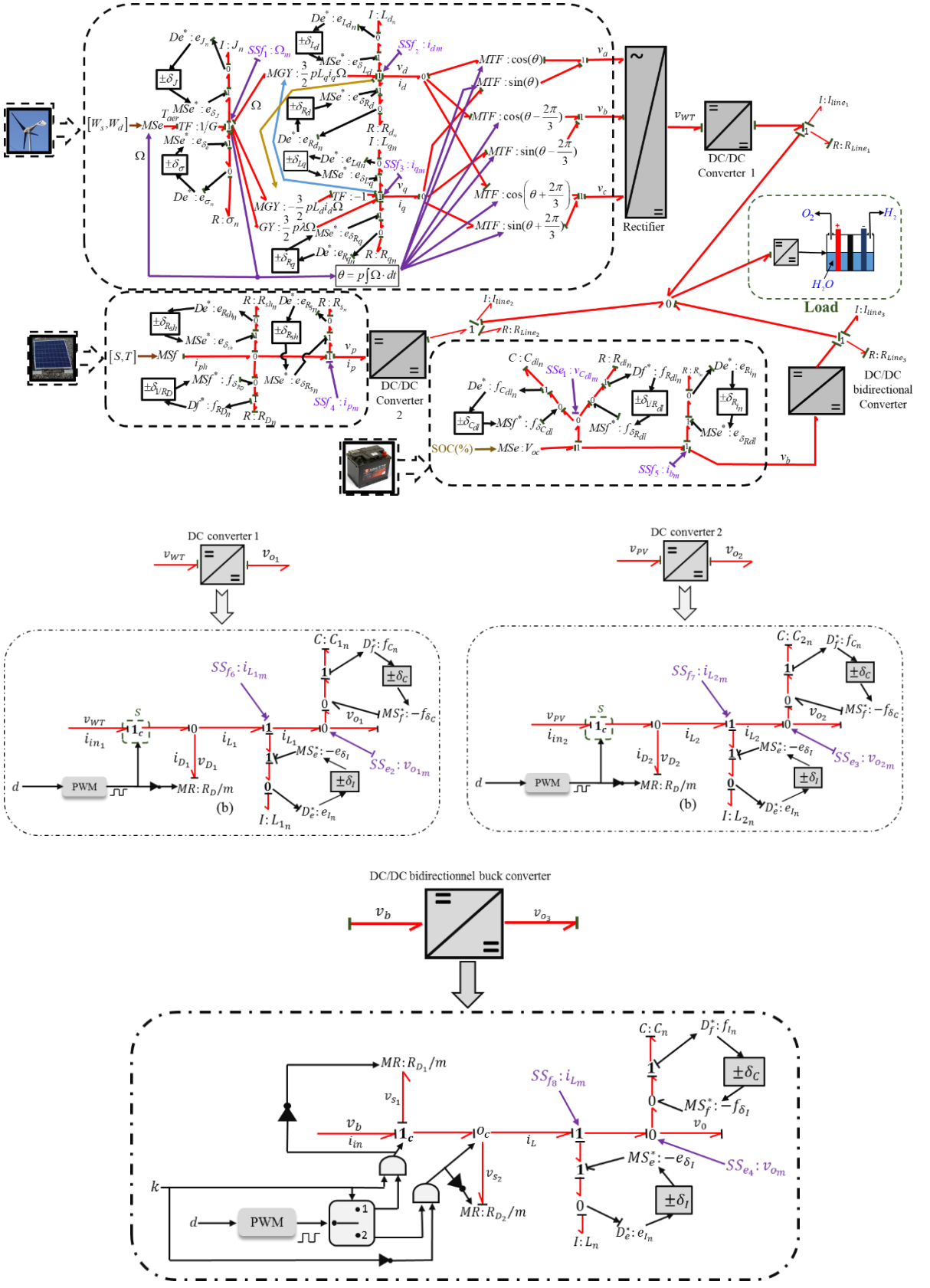

Fig 4.20. LFT-BG model of DC-Microgrid generated under derivative causality.

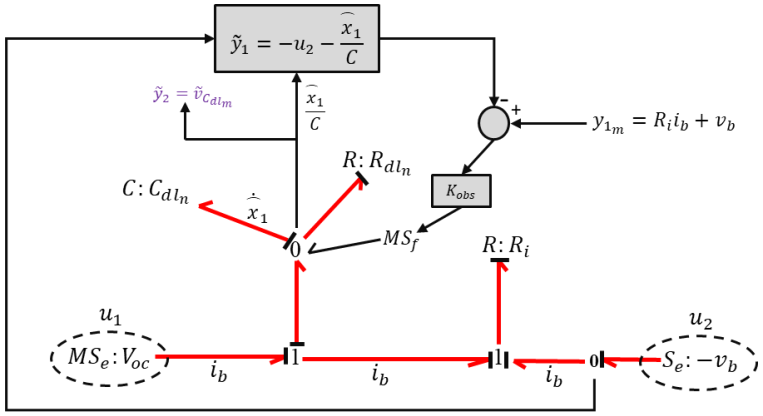

Fig 4.21. Observer BG model.

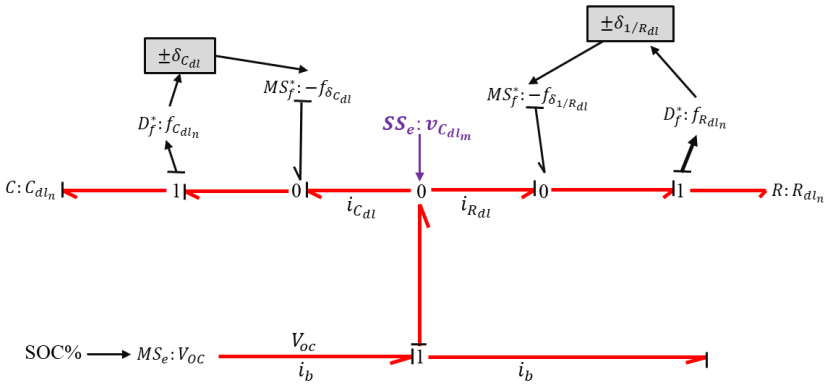

Fig 4.22. Part of the LFT-BG model used for illustrating the process to derive the ARR and adaptive threshold generator.

$$ARR_9 = d \cdot v_{pv_m} - v_{o2_m} - L_{2_n} \frac{di_{L_{2_m}}}{dt} \tag{4.30}$$

$$ARR_{10} = \frac{i_{in_{2_m}}}{d} - i_{o_{2_m}} - C_{2_n} \frac{dv_{o_{2_m}}}{dt} \tag{4.31}$$

$$ARR_{11} = d \cdot v_{b_m} \cdot k - (1-k) v_{b_m} - L_n \frac{di_{L_n}}{dt} - v_{o_m} \frac{(-1)^{2+(1-k)}}{1+(1-k)d} \tag{4.32}$$

$$ARR_{12} = i_{L_m} - i_{o_m} - C_n \frac{dv_{o_m}}{dt} \tag{4.33}$$

The adaptive threshold generators associated with these ARRs are written as follows:

$$a_1 = \left|\frac{3}{2}\delta_{L_q} pL_{q_n} i_{q_m} \Omega_m\right| + \left|\delta_{L_d} L_{d_n} \frac{d_{i_{d_m}}}{dt}\right| + \left|\delta_{R_d} R_{d_n} i_{d_m}\right| + \left|\xi_\Omega\right| + \left|\xi_{i_d}\right| + \left|\xi_{i_q}\right| + \left|\xi_{v_d}\right| \tag{4.34}$$

$$a_2 = \left|\frac{3}{2}\delta_{L_d} pL_{d_n} i_{d_m} \Omega_m\right| + \left|\delta_{L_q} L_{q_n} \frac{di_{q_m}}{dt}\right| + \left|\delta_{R_q} R_{q_n} i_{q_m}\right| + \left|\xi_\Omega\right| + \left|\xi_{i_d}\right| + \left|\xi_{i_q}\right| + \left|\xi_{v_q}\right| \tag{4.35}$$

$$a_3 = \left|\delta_J J_n \frac{d\Omega_m}{dt}\right| + \left|\delta_\sigma \sigma_n \Omega_m\right| + \left|\frac{3}{2}\delta_{i_q} p\lambda i_{q_m}\right| + \left|\xi_\Omega\right| + \left|\xi_{iq}\right| \quad (4.36)$$

$$a_4 = \left|\delta_{R_{eq}} R_{eq}\left(i_{ph} - i_{p_m}\right)\right| + \left|\delta_{R_s} R_{s_n} i_{p_m}\right| + \left|\xi_{v_p}\right| + \left|\xi_{i_p}\right| \quad (4.37)$$

$$a_6 = \left|\delta_{R_i} R_{i_n} i_{b_m}\right| + \left|\xi_{v_{C_{dl}}}\right| + \left|\xi_{v_b}\right| \quad (4.38)$$

$$a_7 = \left|\delta_{L_1} L_{1_n} \frac{di_{L_{1_m}}}{dt}\right| + \left|\xi_{v_{WT}}\right| + \left|\xi_{v_{o_1}}\right| \quad (4.39)$$

$$a_8 = \left|\delta_C C_{1_n} \frac{dv_{o_{1_m}}}{dt}\right| + \left|\xi_{i_{in_1}}\right| + \left|\xi_{i_{o_1}}\right| \quad (4.40)$$

$$a_9 = \left|\delta_{L_2} L_{2_n} \frac{di_{2_m}}{dt}\right| + \left|\xi_{v_{o_2}}\right| + \left|\delta_{v_p}\right| \quad (4.41)$$

$$a_{10} = \left|\delta_{C_2} C_{2_n} \frac{dv_{o_{2_m}}}{dt}\right| + \left|\xi_{i_{in_2}}\right| + \left|\xi_{i_{o_2}}\right| \quad (4.42)$$

$$a_{11} = \left|\delta_L L_n \frac{di_{L_n}}{dt}\right| + \left|\xi_{v_b}\right| + \left|\xi_{v_o}\right| \quad (4.43)$$

$$a_{12} = \left|\delta_C C_n \frac{dv_{o_m}}{dt}\right| + \left|\xi_{i_L}\right| + \left|\xi_{i_o}\right| \quad (4.44)$$

The fault signature matrices illustrated in Tab 4.2 and Tab 4.3 are performed based on the obtained ARRs. They consist of the signatures of the component faults for carrying out the monitorability and isolability analysis. These analyses help to verify the capability of the developed robust online diagnosis to detect and isolate the faults. According to Tab 4.2 and Tab 4.3, all faults can be detected. The faults that may occur in the DC/DC converter and in R_d and R_i can be isolated. The faults may occur in C_{dl}, R_{dl}, L_d, L_q, R_q, J, σ, R_{sh}, R_{D_s} and R_s can be not isolated. However, these faults can be isolated by sets depicted in Tab 4.2 in different colors. Each set gathers the faults that have the same signatures. At least. This way allows localizing the faults at the specific part of DC-MG where they may occur.

The faults that cannot be isolated separately by the developed diagnosis system cause the fluctuation in the voltages v_{WT}, v_{pv} and v_b, which can be estimated by the derived *ARRs*. Because of the possibility of isolating the faults in the DC/DC converters, the variations of the

parameters can be estimated. This estimation of the voltage fluctuation and parameter variations caused due to fault is used to reconfigure the control hierarchy.

Tab 4.2. signature matrix of Fault that may occur in the sources.

Faults→ ARRs ↓	C_{dl}	R_{dl}	L_d	L_q	R_d	R_q	J	σ	R_{Sh}	R_{D_S}	R_S	R_i
ARR_1	0	0	1	1	1	0	0	0	0	0	0	0
ARR_2	0	0	1	1	0	1	1	1	0	0	0	0
ARR_3	0	0	0	0	0	0	0	0	0	0	0	0
ARR_4	0	0	0	0	0	0	0	0	1	1	1	0
ARR_5	1	1	0	0	0	0	0	0	0	0	0	0
ARR_6	0	0	0	0	0	0	0	0	0	0	0	1
ARR_7	0	0	0	0	0	0	0	0	0	0	0	0
ARR_8	0	0	0	0	0	0	0	0	0	0	0	0
ARR_9	0	0	0	0	0	0	0	0	0	0	0	0
ARR_{10}	0	0	0	0	0	0	0	0	0	0	0	0
ARR_{11}	0	0	0	0	0	0	0	0	0	0	0	0
ARR_{12}	0	0	0	0	0	0	0	0	0	0	0	0
M_b	1	1	1	1	1	1	1	1	1	1	1	1
I_b	0	0	0	0	1	0	0	0	0	0	0	1

Tab 4.3. Signature matrix of faults may occur in DC/DC converters.

Faults→ ARRs ↓	L_{1_n}	C_{1_n}	L_{2_n}	C_{2_n}	L_n	C_n
ARR_1	0	0	0	0	0	0
ARR_2	0	0	0	0	0	0
ARR_3	0	0	0	0	0	0
ARR_4	0	0	0	0	0	0
ARR_5	0	0	0	0	0	0
ARR_6	0	0	0	0	0	0
ARR_7	1	0	0	0	0	0
ARR_8	0	1	0	0	0	0
ARR_9	0	0	1	0	0	0
ARR_{10}	0	0	0	1	0	0
ARR_{11}	0	0	0	0	1	0
ARR_{12}	0	0	0	0	0	1
M_b	1	1	1	1	1	1
I_b	1	1	1	1	1	1

4.8. Robust Hierarchical control reconfiguration

The process of the robust Hierarchical control reconfiguration is presented in the following steps:

-Step 1: detection and localization of the occurred faults.

-Step 2: Estimation of voltage and parameter variations: this estimation depends on the localization of the faults. If the faults occur in all or one of $\{L_d, L_q, R_d, R_q, J, \sigma\}$, the variation of the voltage v_{WT} is needed for the control reconfiguration. It can be obtained as follows:

$$\Delta v_{WT} = v_{WT_F} - v_{WT_0} \tag{4.46}$$

where v_{WT_0} is the voltage value when the fault is not present in $\{ L_d , L_q , R_d , R_q , J , \sigma \}$. v_{WT_F} is written as follows:

$$v_{WT_F} = \max\left(v_{a_F}(t), v_{b_F}(t), v_{c_F}(t)\right) \tag{4.45}$$

$v_{a_F}(t)$, $v_{b_F}(t)$ and $v_{c_F}(t)$ is obtained by using the reverse transformation. they can be written as follows:

$$\begin{bmatrix} v_{a_F} \\ v_{b_F} \\ v_{c_F} \end{bmatrix} = \left[P\left(\int \Omega_m dt\right)\right]^{-1} \begin{bmatrix} v_q \\ v_d \end{bmatrix} \tag{4.46}$$

v_q and v_d are derived from the residual signals r_1 and r_2 generated from *ARR1* and *ARR2*, respictevely. They are written as follows:

$$v_d : \begin{cases} v_d = -(r_1 - a_1) + \dfrac{3}{2} p L_{q_n} i_{q_m} \Omega_m - L_{d_n} \dfrac{di_{d_m}}{dt} - R_{d_n} i_{d_m} & \text{If } (r_1 > 0) \\ v_d = -(r_1 + a_1) + \dfrac{3}{2} p L_{q_n} i_{q_m} \Omega_m - L_{d_n} \dfrac{di_{d_m}}{dt} - R_{d_n} i_{d_m} & \text{If } (r_1 < 0) \end{cases} \tag{4.47}$$

$$v_q : \begin{cases} v_q = -(r_2 - a_2) + \dfrac{3}{2} p \Omega_m \left(\lambda - L_{d_n} i_{d_m}\right) - L_{q_n} \dfrac{di_{q_m}}{dt} - R_{q_n} i_{q_m} & \text{If } (r_2 > 0) \\ v_q = -(r_2 + a_2) + \dfrac{3}{2} p \Omega_m \left(\lambda - L_{d_n} i_{d_m}\right) - L_{q_n} \dfrac{di_{q_m}}{dt} - R_{q_n} i_{q_m} & \text{If } (r_2 < 0) \end{cases} \tag{4.48}$$

If the faults occur in all or one of $\{ R_{sh} , R_{s_n} , R_{D_s} \}$, the voltage variation of v_{pv} is needed for the control reconfiguration. This voltage variation is written as follows:

$$\Delta v_{pv} = v_{pv_F} - v_{pv_0} \tag{4.49}$$

where v_{pv_0} is the value of v_{pv} when the fault is not present in $\{ R_{sh} , R_{s_n} , R_{D_s} \}$. v_{pv_F} is obtained from the residual signal r_4 generated from *ARR4* and can be written as follows:

$$v_{pv_F}:\begin{cases} v_{pv_F} = -\left(r_4 - a_4\right) + \dfrac{R_{sh_n} R_{D_n}}{R_{sh_n} + R_{D_n}}\left(i_{ph} - i_{p_m}\right) - R_{s_n} i_{p_m} \text{ If } \left(r_4 > 0\right) \\ v_{pv_F} = -\left(r_4 + a_4\right) + \dfrac{R_{sh_n} R_{D_n}}{R_{sh_n} + R_{D_n}}\left(i_{ph} - i_{p_m}\right) - R_{s_n} i_{p_m} \text{ If } \left(r_4 < 0\right) \end{cases} \quad (4.50)$$

If the faults occur in all or one of $\{C_{dl}, R_{dl}, R_i\}$, the voltage variation of v_b is needed for the Hierarchical control configuration. It is obtained as follows:

$$\Delta v_b = v_{b_F} - v_{b_0} \quad (4.51)$$

where v_{b_0} is the value of v_b when the fault is not present in $\{C_{dl}, R_{dl}, R_i\}$. v_{b_F} is obtained from the residual r_6 generated from *ARR6*. It is written as follows:

$$v_{b_F}:\begin{cases} v_{b_F} = -\left(r_6 - a_6\right) + \left(V_{oc} - v_{Cdl_m}\right) - R_{i_n} i_{b_m} \text{ If } \left(r_6 > 0\right) \\ v_{b_F} = -\left(r_6 + a_6\right) + \left(V_{oc} - v_{Cdl_m}\right) - R_{i_n} i_{b_m} \text{ If } \left(r_6 < 0\right) \end{cases} \quad (4.52)$$

The parameter variation of L_1 is needed for the Hierarchical control when the fault occurs and affects this parameter. It can be written as follows:

$$\Delta L_1 = L_{1_F} - L_{1_n} \quad (4.53)$$

L_{1_F} is obtained from the residual signal r_7 generated from *ARR7*.

$$L_{1_F}:\begin{cases} L_{1_F} = \dfrac{1}{i_{L_{1_m}}} \int \left(-\left(r_7 - a_7\right) + d \cdot v_{WT} - v_{0_{1_m}}\right) \cdot dt \text{ If } (r_7 > 0) \\ L_{1_F} = \dfrac{1}{i_{L_{1_m}}} \int \left(-\left(r_7 + a_7\right) + d \cdot v_{WT} - v_{0_{1_m}}\right) \cdot dt \text{ If } (r_7 < 0) \end{cases} \quad (4.54)$$

L_{1_F} can also be written as follows:

$$L_{1_F}:\begin{cases} L_{1_F} = \left(\dfrac{di_{L_{1_m}}}{dt}\right)^{-1} \left(-\left(r_7 - a_7\right) + dv_{WT} - v_{o_{1_m}}\right) \text{ If } \left(r_7 > 0\right) \\ {}_{1_F} = \left(\dfrac{di_{L_{1_m}}}{dt}\right)^{-1} \left(-\left(r_7 + a_7\right) + dv_{WT} - v_{o_{1_m}}\right) \text{ If } \left(r_7 > 0\right) \end{cases} \quad (4.55)$$

But this formula can be nor implemented due to the zero value of $i_{L_{1_m}}$ that is given when $i_{L_{1_m}}$ is a continuous signal.

The parameter variations of C_1, L_2, C_2, L and C are obtained in the same context and way as L_1. They can be written as follows:

$$\Delta C_1 = C_{1_F} - C_{1_0} \tag{4.56}$$

$$\Delta L_2 = L_{2_F} - L_{2_0} \tag{4.57}$$

$$\Delta C_2 = C_{2_F} - C_{2_0} \tag{4.58}$$

$$\Delta L = L_F - L_0 \tag{4.59}$$

$$\Delta C = C_F - C_0 \tag{4.60}$$

C_{1_F}, L_{2_F}, C_{2_F}, L_F and C_F are given as follows:

$$C_{1_F}: \begin{cases} C_{1_F} = \dfrac{1}{v_{o1_m}} \int \left(-\left(r_8 - a_8\right) + \dfrac{i_{in1_m}}{d} - i_{o1_m} \right) \text{ If } \left(r_8 > 0\right) \\ C_{1_F} = \dfrac{1}{v_{o1_m}} \int \left(-\left(r_8 + a_8\right) + \dfrac{i_{in1_m}}{d} - i_{o1_m} \right) \text{ If } \left(r_8 < 0\right) \end{cases} \tag{4.61}$$

$$L_{2_F}: \begin{cases} L_{2_F} = \dfrac{1}{i_{L2_m}} \int \left(-\left(r_9 - a_9\right) + d \cdot v_{pv_m} - v_{02_m} \right) \cdot dt \text{ If } (r_9 > 0) \\ L_{2_F} = \dfrac{1}{i_{L2_m}} \int \left(-\left(r_9 + a_9\right) + d \cdot v_{pv_m} - v_{01_m} \right) \cdot dt \text{ If } (r_9 < 0) \end{cases} \tag{4.62}$$

$$C_{2_F}: \begin{cases} C_{2_F} = \dfrac{1}{v_{o2_m}} \int \left(-\left(r_{10} - a_{10}\right) + \dfrac{i_{in2_m}}{d} - i_{o2_m} \right) \text{ If } \left(r_{10} > 0\right) \\ C_{2_F} = \dfrac{1}{v_{o2_m}} \int \left(-\left(r_{10} + a_{10}\right) + \dfrac{i_{in2_m}}{d} - i_{o2_m} \right) \text{ If } \left(r_{10} < 0\right) \end{cases} \tag{4.63}$$

$$L_f: \begin{cases} L_f = \dfrac{1}{i_m} \int \left(-\left(r_{11} - a_{11}\right) + d v_{b_m} k - \left(1-k\right) v_{b_m} - v_{o_m} \dfrac{\left(-1\right)^{2+(1-k)}}{1+\left(1+k\right)d} \right) \text{ If } \left(r_{11} > 0\right) \\ L_f = \dfrac{1}{i_m} \int \left(-\left(r_{11} + a_{11}\right) + d v_{b_m} k - \left(1-k\right) v_{b_m} - v_{o_m} \dfrac{\left(-1\right)^{2+(1-k)}}{1+\left(1+k\right)d} \right) \text{ If } \left(r_{11} < 0\right) \end{cases} \tag{4.64}$$

$$C_f : \begin{cases} C_f = \dfrac{1}{v_{o_m}} \int \left(-\left(r_{12} - a \right) + i_{L_m} - i_{o_m} \right) \text{ If } \left(r_{12} > 0 \right) \\ C_f = \dfrac{1}{v_{o_m}} \int \left(-\left(r_{12} + a \right) + i_{L_m} - i_{o_m} \right) \text{ If } \left(r_{12} > 0 \right) \end{cases} \quad (4.65)$$

-Step 3: in the case of DC-MG illustrated in Fig 4.13, there are three H∞ based controllers: { $K_{p_\infty}(s)_1, K_{p_\infty}(s)_2, K_{p_\infty}(s)_3$ } and three structured H∞ based controllers: { $K_{s_\infty}(s)_1 = K_{s_\infty}(s)_2 = K_{s_\infty}(s)_3 = K_{s_\infty}(s)$ }. These controllers will be recalculated using the estimations provided by step 2.

The controller $K_{p_\infty}(s)_1$ is recalculated when the faults occur in the DC/DC buck converter 1 or WT generator or in both of these components. The recalculation of $K_{p_\infty}(s)_1$ exploits the estimations: $\Delta v_{WT}, \Delta L_1$ and ΔC_1. But the use of these estimations depends on which fault or faults occur. For instance, if the fault occurs in L_1, the recalculation of $K_{p_\infty}(s)_1$ use only ΔL_1 and Δv_{WT} and ΔC_1 has zero values because there are no faults occurred which affect v_{WT} and C_1 .

The controllers $K_{p_\infty}(s)_2$ and $K_{p_\infty}(s)_3$ are recalculated when the faults occur in {PV panel, DC/DC buck converter 2} and {Battery, DC/DC bidirectional converter}. The recalculation of $K_{p_\infty}(s)_2$ and $K_{p_\infty}(s)_3$ Also exploits the estimations: Δv_b , Δv_{pv} , ΔC_2 , ΔL_2 , ΔC and ΔL_2 in the same way as the recalculation of $K_{p_\infty}(s)_1$.

On the other hand, the recalculation of $K_{s_\infty}(s)$ happens when one or several recalculations occur in { $K_{p_\infty}(s)_1, K_{p_\infty}(s)_2, K_{p_\infty}(s)_3$ } and at least one of the conditions presented in (4.55) and (4.65) must be not satisfied. These conditions must be tested three times. In each time, the controller $K_{p_\infty}(s)$ is substituted by $K_{p_\infty}(s)_1, K_{p_\infty}(s)_2$ and $K_{p_\infty}(s)_3$.

Actually, the estimation will be used to recalculate the coefficients of the transfer functions of each converter. Then the GA et Nonsmooth optimization algorithms will use these updated transfer functions to derive the H∞ and structured H∞ controllers.

4.9. Simulation study:

The simulation study carried out using 20SIM software is subdivided into two parts. These two parts are performed to validate the robust online diagnosis and active Fault tolerant control, which is based on the developed robust online diagnosis to reconfigure the robust Hierarchical control when the fault occurs in the system. The filters LC of the converters (DC/DC Buck converter 1, DC/DC buck converter, and DC/DC bidirectional converter) have the same parameters values ($C_1 = C_2 = C = 2200\mu F$ and $L_1 = L_2 = L = 12mH$). The semiconductor switches of the DC/DC converters operate under the same switching frequency ($f = 25kHz$). The renewable energy sources (WT and PV) and battery parameters are listed in Tab a.1.

The simulation of the first part consists of the LFT-BG model of DC-MG, which is derived under the integral causal property to simulate its physical behavior under the operation state (System operate under control hierarchy), and the online diagnosis system that consists of the ARRs and their generators of the adaptive thresholds, as illustrated in Fig 4.23. The process to vary the parameters randomly in the DC-MG model is included to simulate the effect of the uncertainties in the system. One scenario is performed to validate the developed robust online diagnosis. In this scenario, several component faults are injected into the parameters: L_d, R_q, σ, R_s, R_i, L_1, C_1, L_2, L_2, C_2 and C at the instances: 50s, 12s, 30s, 38s, 45s, 10s, 50s, 40s, 20s, 36, respectively. The obtained results are illustrated in Fig 4.24, Fig 4.25, Fig 4.26, and Fig 4.27.

According to the obtained results, the residuals signals generated from the developed *ARRs* are not in the zero value and vary randomly due to the parameter uncertainties. Their thresholds are adaptively evolving with the evolution of system variables. The thresholds' adaptive evolution helps prevent the residual signals from going out of their thresholds bounds when there is no fault. When faults occur in the HMS, the residuals generated by ARR_1, ARR_2, ARR_3, ARR_4, ARR_6, ARR_7, ARR_8, ARR_9, ARR_{10}, and ARR_{12} go out of their thresholds bounds at different times due to the presence of faults. When the faults are avoided, the residual signals generated by the *ARRs*, which are previously mentioned, return to the threshold bounds. It is noticed that only the residual signals generated by ARR_5 and ARR_{11} are not affected and kept inside their thresholds bounds during the whole simulation time. According to the monitorability and isolability carried out in section 4.7, ARR_5 and ARR_{11} are not sensitive to any fault simulated in this scenario. For this reason, the residual signals of ARR_5 and ARR_{11} are not affected by these faults. This part of the validation scenario and the presence of faults at different times have

been performed to verify the monitorability and isolability analysis discussed in section 4.7 based on the Fault signature matrices depicted in Tab 4.2 and Tab 4.3

The second part of the simulation is performed by the LFT-BG model of DC-MG derived under integral derivative causality, robust online diagnosis, and the process to reconfigure the Hierarchical control when the faults occur in the system, as illustrated in Fig 4.28. one scenario is also performed for this simulation part, which aims to inject the faults in: L_d , L_2 and C in the same time at 2s. This scenario is carried out in the presence (with reconfiguration process (WRP)) and in the absence (Without reconfiguration process) of the process, which is used to reconfigure the control hierarchy. The injected faults cause the variation of 30% in L_d and L_2 and variation of -30% in C . In this simulation, the CPL consumes 185W, and the bus voltage is stabilized around 24V. The obtained results are illustrated in Fig 4.29 and Fig 4.30.

According to the obtained results, when the reconfiguration process is not implemented in the system. The occurrence of faults causes fluctuations in the output currents and DC bus voltage. These fluctuations have a magnitude around 3A or 2A of output currents and 1V of DC bus voltage. They appear during the duration of 0.05s noticed in the behavior of the output currents and the duration of 1.1s noticed in the behavior of the DC bus voltage. When the reconfiguration process is implemented in the system, we noticed from the obtained results that the fluctuations arising due to faults are almost smoothed. That shows that the damping factor of DC-MG components is increased. Therefore. These obtained results show that the fault-tolerant control consisting of the robust online diagnosis, robust control hierarchy, and the control reconfiguration process effectively mitigates the effect of the severe faults.

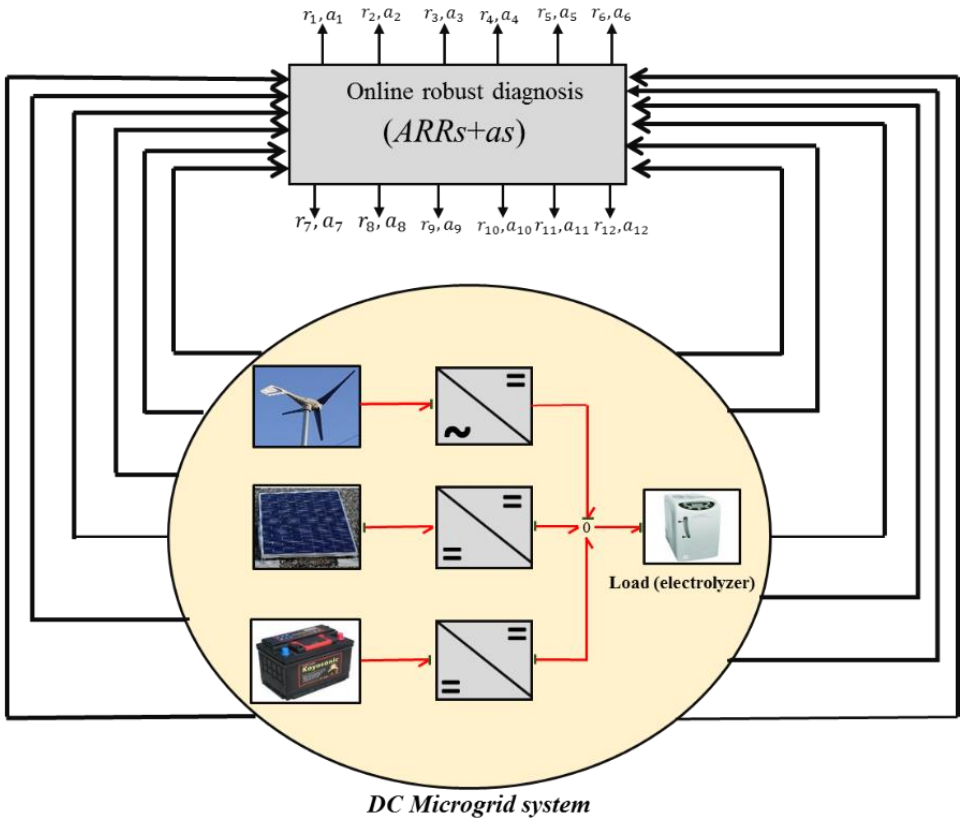

Fig 4.23. Simulation of DC-MG monitored by an online diagnosis performed in 20SIM software.

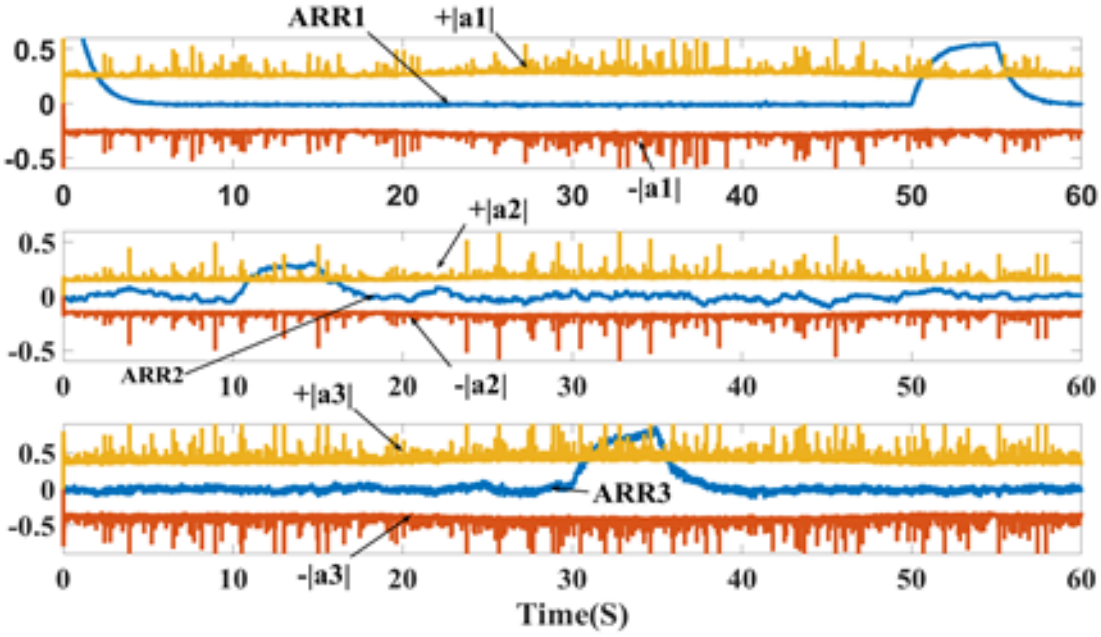

Fig 4.24. Numerical evaluation of ARR_1, ARR_2, and ARR_3 with their adaptive thresholds.

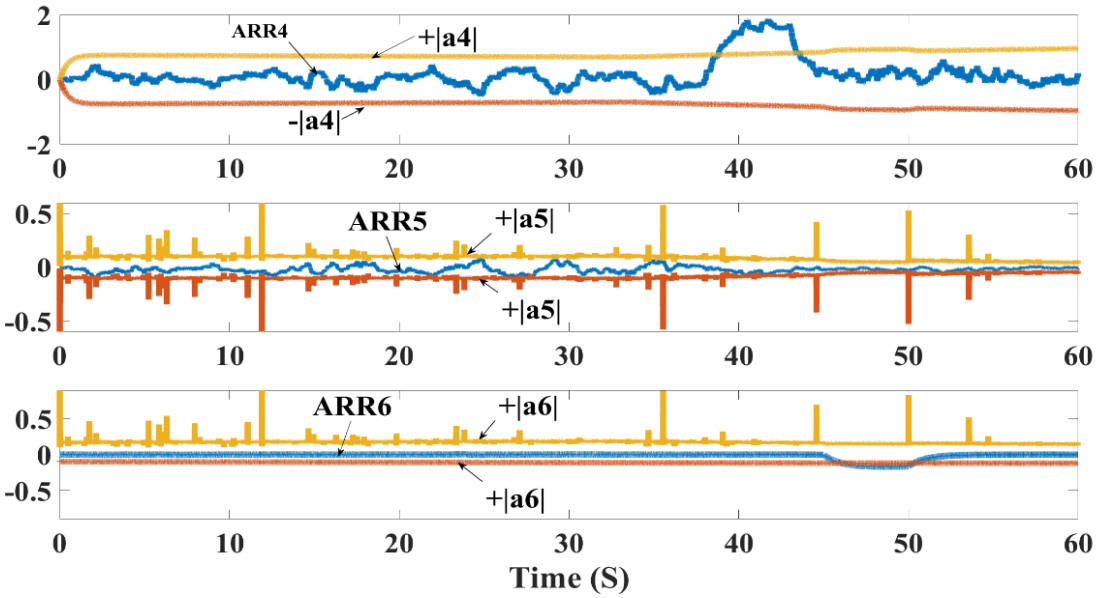

Fig 4.25. Numerical evaluations of ARR_4, ARR_5, and ARR_6 with their adaptive thresholds

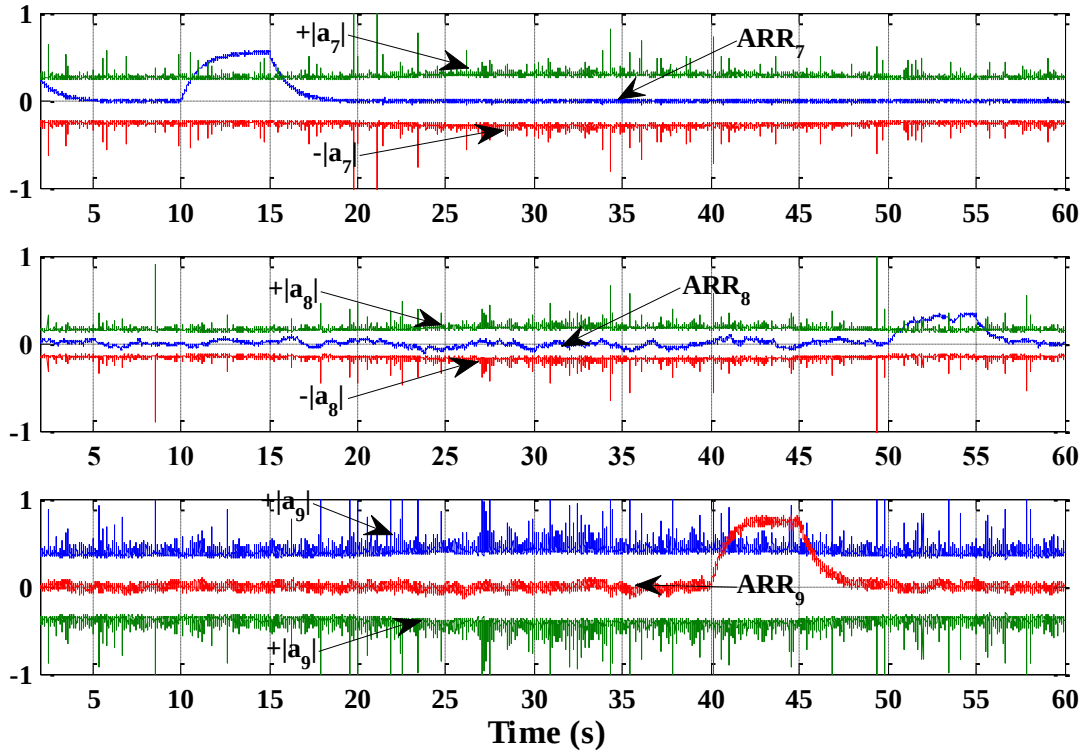

Fig 4.26. Numerical evaluation of ARR7, ARR8, and ARR9 with their adaptive thresholds.

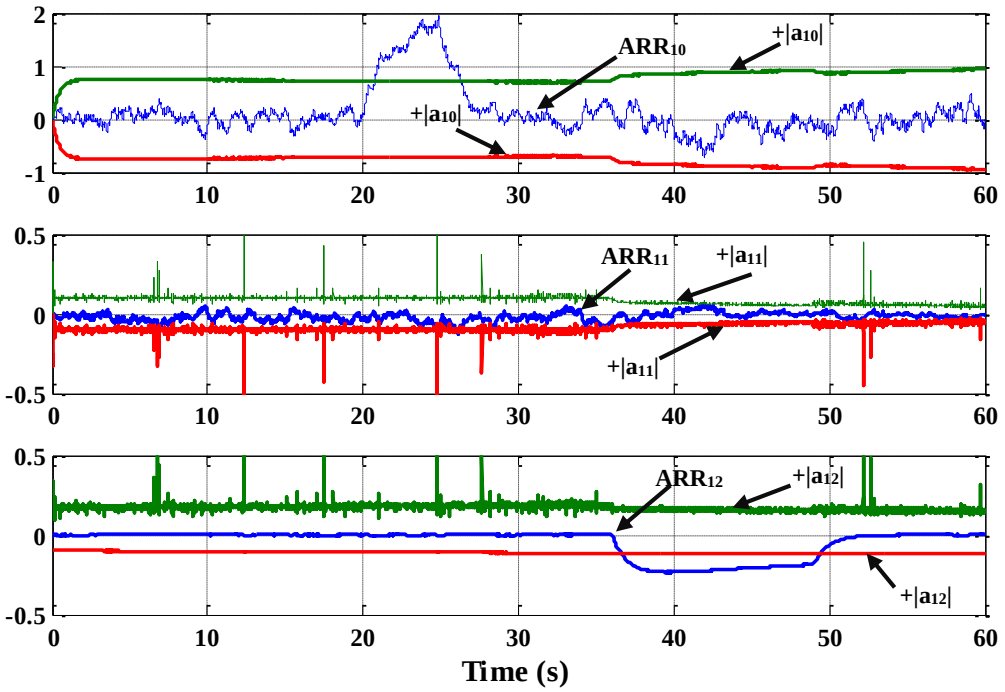

Fig 4.27. Numerical evaluations of ARR_{10}, ARR_{11}, and ARR_{12} with their adaptive thresholds.

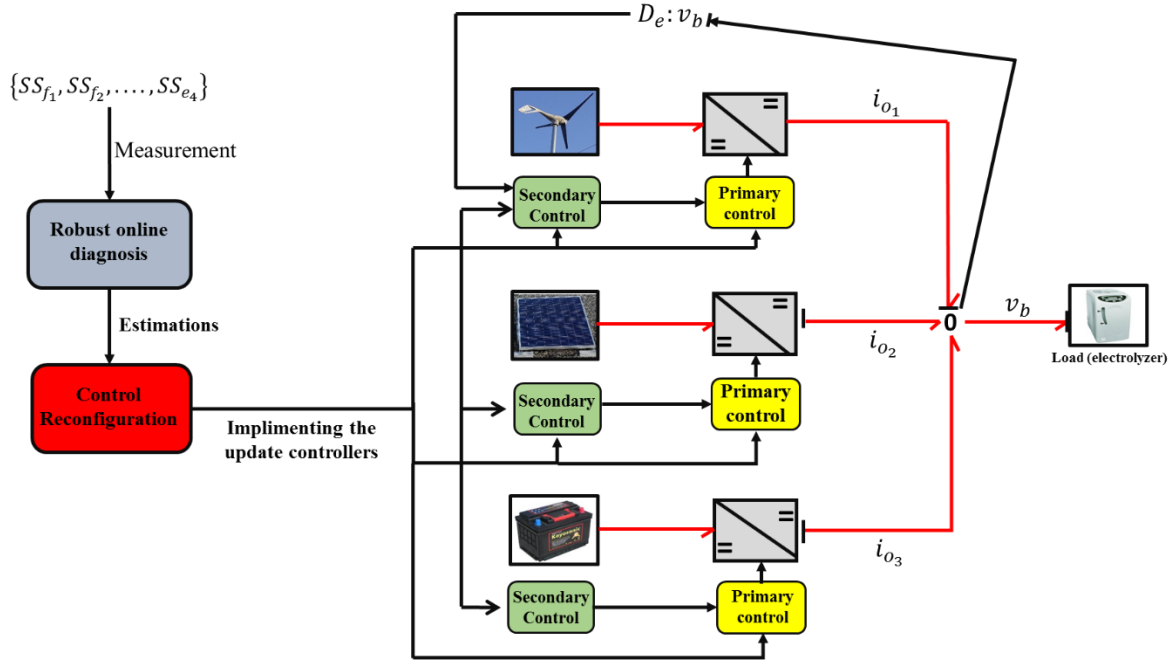

Fig 4.28. DC-MG operating under fault-tolerant control simulated in 20SIM software.

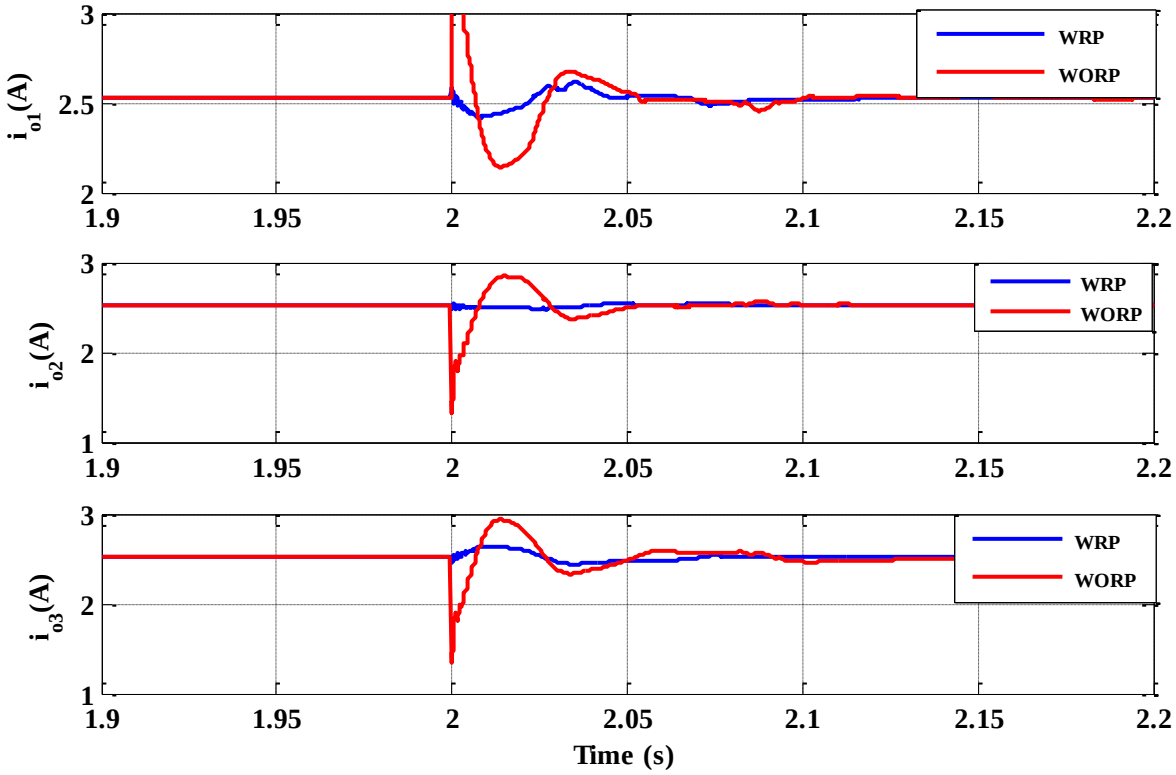

Fig 4.29. Behavior of DC/DC converters output current resulted from the scenario of the second part of the simulation.

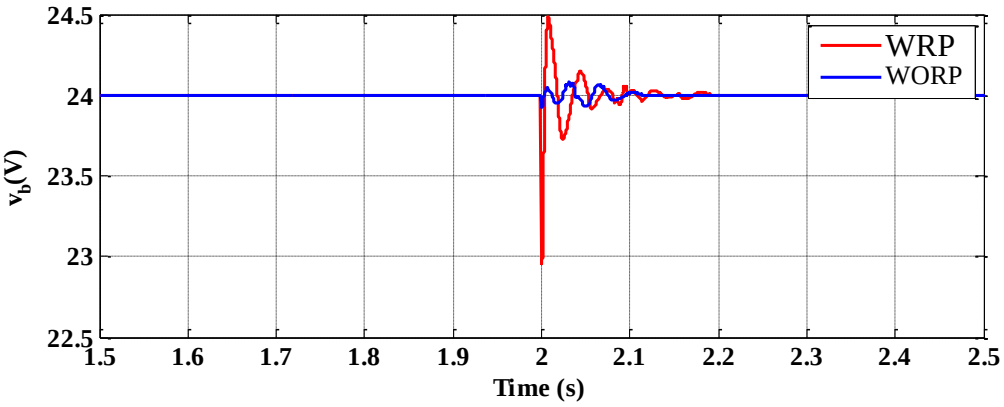

Fig 4.30. Behavior of DC bus voltage resulted from the scenario of the second part of the simulation.

4.10. Conclusion

This chapter explores in detail the process to develop the active fault-tolerant control of DC-MG, which consists of the Robust online diagnosis, control reconfiguration process, and robust control hierarchy. The robust online diagnosis consists of the analytical redundancy relation and the generators of the adaptive thresholds. The numerical evaluations of the analytical redundancy relations are the indicators of faults. These indicators of faults are comprised in the bounds limited by the adaptive thresholds when there is no fault in the system. These adaptive

thresholds evolve with the system inputs and outputs and system uncertainties to avoid the possibility of false alarm. The Robust online diagnosis can estimate the parameter variations caused by faults based on the derived analytical redundancy relation. These estimations will be used to recalculate the robust controller of primary and secondary control levels. The obtained results show the developed Active fault-tolerant control's effectiveness in maintaining the stability system and avoiding the current and voltage fluctuations.

Chapter 5: Experimental validation.

5.1. Introduction

This chapter presents the experimental validation of the elements of active FTC (Robust hierarchical control and robust online diagnosis) applied in the DC-MG. They are validations by using two experimental setups under several scenarios. The robust hierarchical control is validated by an experimental setup consisting of two DC sources that emulate the RES_s. These DC sources are integrated into the parallel interconnection through two DC/DC buck converters. In this experimental setup, the CPL is emulated using DC/DC boost converter. In this validation, the hierarchical control is designed based on parameters different from the experimental setup parameters. This way can verify the robustness of the control against the parameter variations, which exceed the accepted limits. In the real system, these unaccepted parameter variations occur due to faults.

Another platform of DC-MG applied in the green H_2 production is exploited to validate the robust online diagnosis. The platform consists of real RESs. The components faults are injected in PV panel and battery by using a rheostat.

5.2. Experimental validation of H_∞ based control

The experimental setup shown in Fig 5.1 is built in the laboratory to validate the H_∞-based control's effectiveness, consisting of a DC source, DC/DC buck converter, and a boost converter acting as a CPL. The load side converter (boost converter) feeds a resistive load whose output voltage is firmly regulated. The power demand of the CPL is adjusted by changing the resistance load. Two experimental tests are carried out: the first is a variation test of CPL power demand (the resistance of boost converter adjusts CPL power), and the second test is an input voltage variation. The desired output voltage is 15 V, and the DC source voltage is 28 V. The experimental results are depicted in Fig 5.2, Fig 5.3, and Fig 5.4

It is worth mentioning here that the capacitance and inductance values used in the experimental setup are different from those listed in Tab 5.1, while the controller is designed using the parameters listed in Tab 5.1 to validate its robustness against the parameter variations. The adopted parameters for the experiment purpose are listed in Tab 5.2. The designed controller is implemented in a low-cost DSP of Texas Instrument TMS320F28335. Using the controller order reduction algorithm [66], the designed controller converted to a discrete-time is given as follows:

$$K_\infty(z) = \frac{4.47z^2 - 4.37z + 4.379}{z^3 - 1.177z^2 + 0.186z - 0.009} \tag{5.1}$$

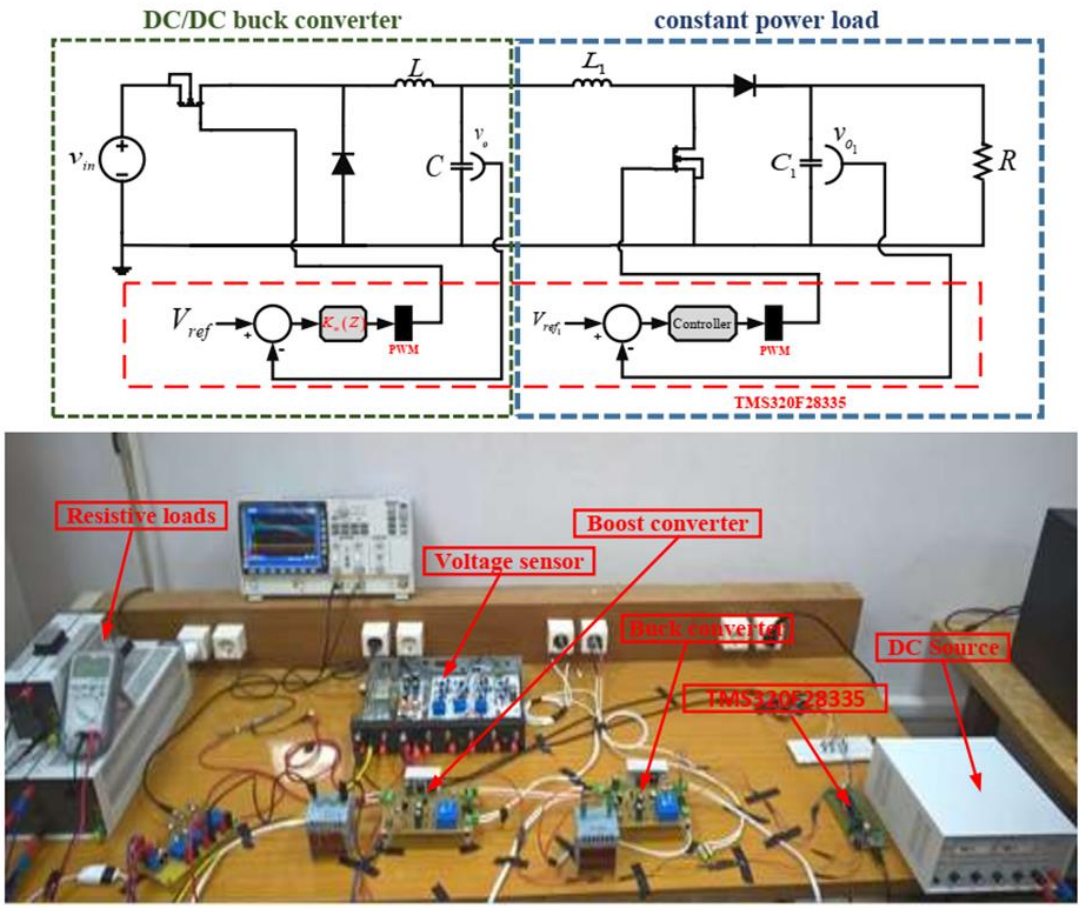

Fig 5.1. experimental setup developed to validate the H_∞ based control

Tab 5.1. experimental setup parameters

Buck converter	Boost converter
$v_{ref} = 15V$	$v_{ref} = 20V$
$v_{in} = 28V$	$v_0 = 15V$
$C = 470\mu F$	$C = 470\mu F$
$L = 2.87mF$	$L = 0.5mF$
$f_s = 25kHz$	$f_s = 25kHz$
/	$R = 9\Omega(45W)$ $R = 13\Omega(31W)$ $R = 25\Omega(15W)$

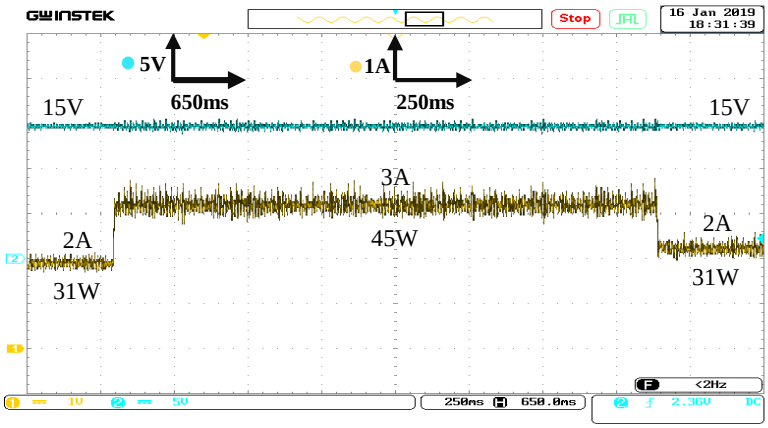

Fig 5.2. Experimental results of CPL consumed power variation test.

According to Fig. 24, Fig. 25, and Fig. 26, the system operation has a short transient dynamic, corresponding to a small settling time of less than 0.04 s. The output voltage has an allowed overshoot and remains at the desired value. Moreover, the system stability is maintained under several changes in the power consumed by the CPL. The controller is robust against the parameter variations and avoids the perturbations brought by the CPL current and input voltage fluctuations. Any transient voltage deviation appeared when a substantial change occurred in CPL's input voltage and power consumed.

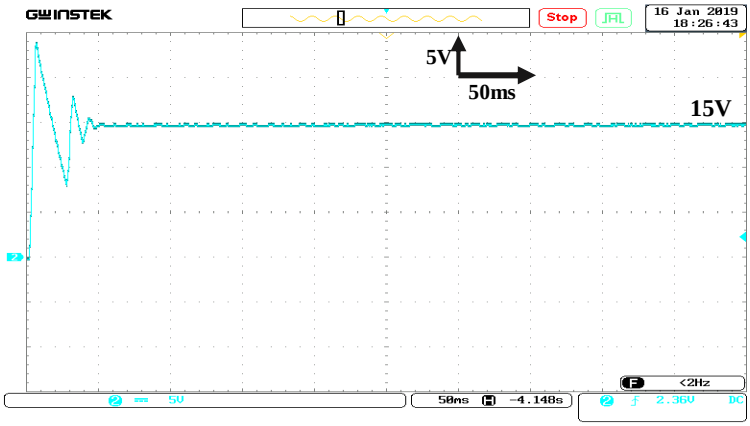

Fig 5.3. Transit dynamic of output voltage response.

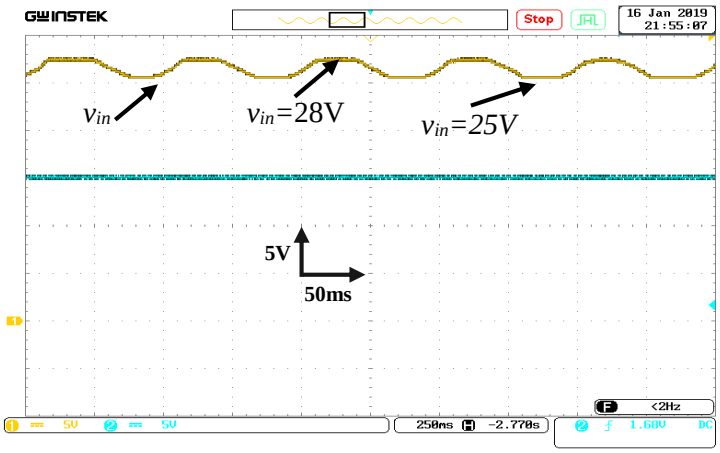

Fig 5.4. Experimental results of input voltage variation test.

5.3. Experimental validation of robust hierarchy control

Fig 23 presents the experimental setup built in the laboratory, which is exploited to validate the effectiveness of the proposed approach for achieving the control objectives. This experimental setup is a prototype of a DC MG system that contains two DC voltage input sources used to emulate renewable energy sources. These DC input sources supply the CPL through two DC buck converters, which are separately put in the system and connected in parallel to the common DC bus, with two rheostats are used to emulate the transition line impedances. The CPL is emulated using the DC Boost converter supplying the resistive load to test the implemented algorithm for different levels P_{CPL}. All parameters of experimental setup components are listed in Table 3. Knowing that the DC buck converters parameters are chosen differently, and the controllers $K_{p_\infty}(s)$ and $K_{s_\infty}(s)$ are designed using the parameters listed in Table 1. This way allows approximately validating the robustness of the designed control against the parameters variation.

The designed control algorithm is implemented in the TMS320F28935 electronic card after converting $K_{p_\infty}(s)$ and $K_{s_\infty}(s)$ to the discrete-time domain. Using the controller order reduction algorithm (ref). $K_{p_\infty}(s)$ is given in discrete-time domain as follows:

$$K_{p_\infty}(z)=\frac{39.5034z^3-3.3729z^2-39.5016z+39.38014}{z^3-0.49772z^2-0.7814z+0.281223} \qquad (5.2)$$

$K_{s_\infty}(s)$ has the PI structure. Therefore, there is no need to use the controller order reduction algorithm. $K_{s_\infty}(s)$ is given in discrete-time domain as follows:

$$K_{s_\infty}(z) = \frac{0.002287z - 0.001722}{z - 1} \tag{5.3}$$

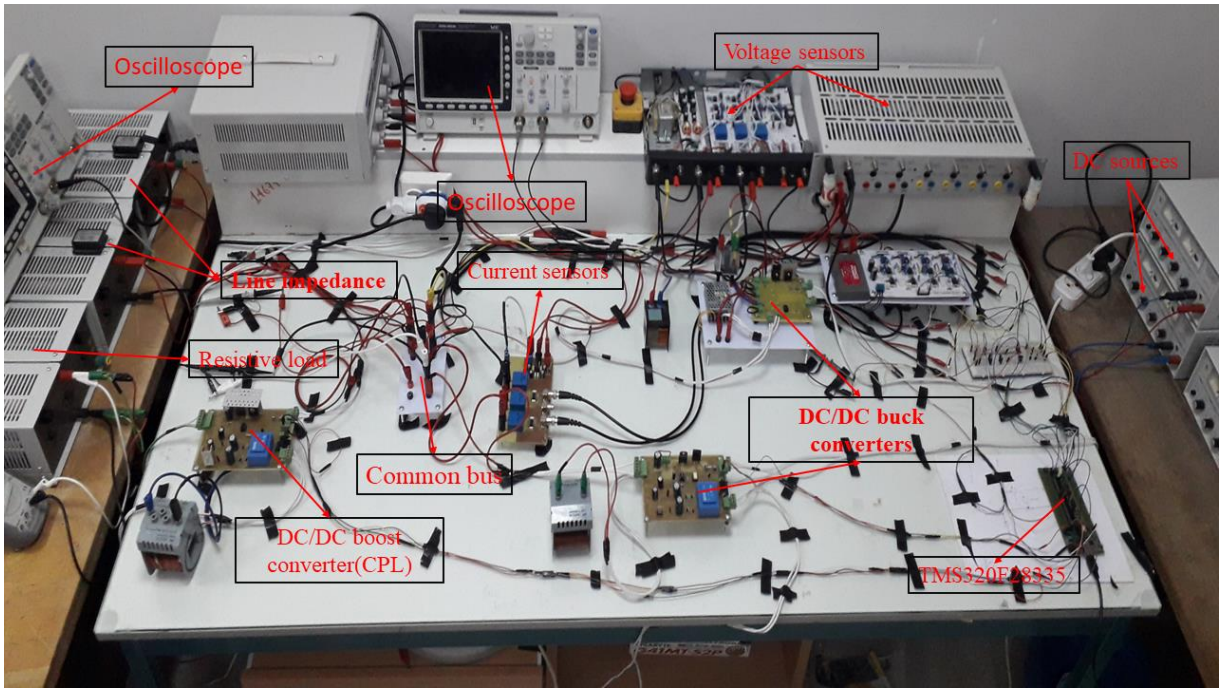

Fig 5.5. experimental setup used to validate the developed robust control hierarchy.

Tab 5.2. Experimental setup parameters

Buck converter 1	
$L_1 = 2.7mH$	$C_1 = 470\mu F$
$r_{line_1} = 1.8\Omega$	$v_{in_1} = 30V$
Buck converter 2	
$L_2 = 6mH$	$C_2 = 220uF$
$r_{line_2} = 1.8\Omega$	$v_{in_2} = 30V$
Boost converter	
$L = 0.5mH$	$C = 470\mu F$
$v_{in} = v^* = 15V$	
Switching frequency	
$f_s = 25khZ$	
Bus voltage nominal value	
$v^* = 15V$	

The experimental study is subdivided into three scenarios: The first scenario is carried out to show the effectiveness of the designed control for maintaining the power-sharing and remaining the voltage of the DC common bus at the rated value. This scenario is performed in two cases, which correspond to the presence of two different kinds of load: resistive and CPL load that are not connected at the same time in the system. This way allows exhibiting that the change of load type does not affect the system operation stability under the designed control application. The first scenario is performed as follows: the system supplies the fixed load (20Ω for the case of the resistive load, P_{CPL}=20 for the case of the CPL.). At the beginning of the experimental time, the DC buck converters operate in stand-alone mode. Then, the decentralized primary controls are activated at 0.95s and 1.57s in both cases. After a certain time of the decentralized primary controls activation, the decentralized secondary controls are activated at 2.35s and 2.4s in both cases. All first scenario results are depicted in Fig 5.6, Fig 5.7, and Fig 5.8.

According to the obtained results, the transient dynamic of the system operating under the proposed control has a settling time less than 0.5s. Moreover, there is no overshot during the transient dynamic. The decentralized primary controls maintain the current power-sharing by avoiding the circulating current and voltage difference between DC buck converters outputs during its activation. However, it is caused by a large deviation of voltage seen in the output voltages of the DC buck converter and common DC bus voltage. The common DC bus voltage is restored at the rated value v^* when the decentralized secondary controls are activated. Furthermore, the voltage deviation caused by the decentralized primary controls are avoided by maintaining the sharing of the current generated by DC buck converters. These scenario results also show that the change of load type does not affect the system operating under the designed control, and the stability is maintained during its operation in the presence of CPL load.

Knowing that the controllers $K_{p_\infty}(s)$ and $K_{s_\infty}(s)$ are designed using the system parameters different from the parameters listed in Tab 5.2. According to the obtained results, the performances of system operation are maintained. Therefore, because of $K_{p_\infty}(s)$ and $K_{s_\infty}(s)$, system control earns the robustness against the parameters variation.

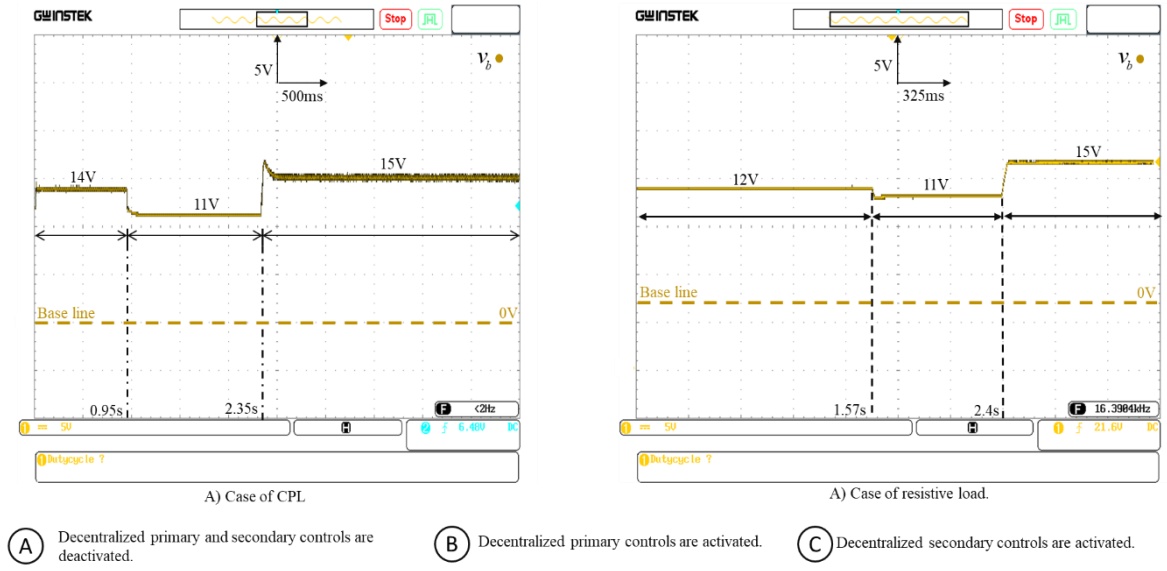

Fig 5.6. Common DC bus voltage resulted from the first scenario in the case of CPL and resistive load.

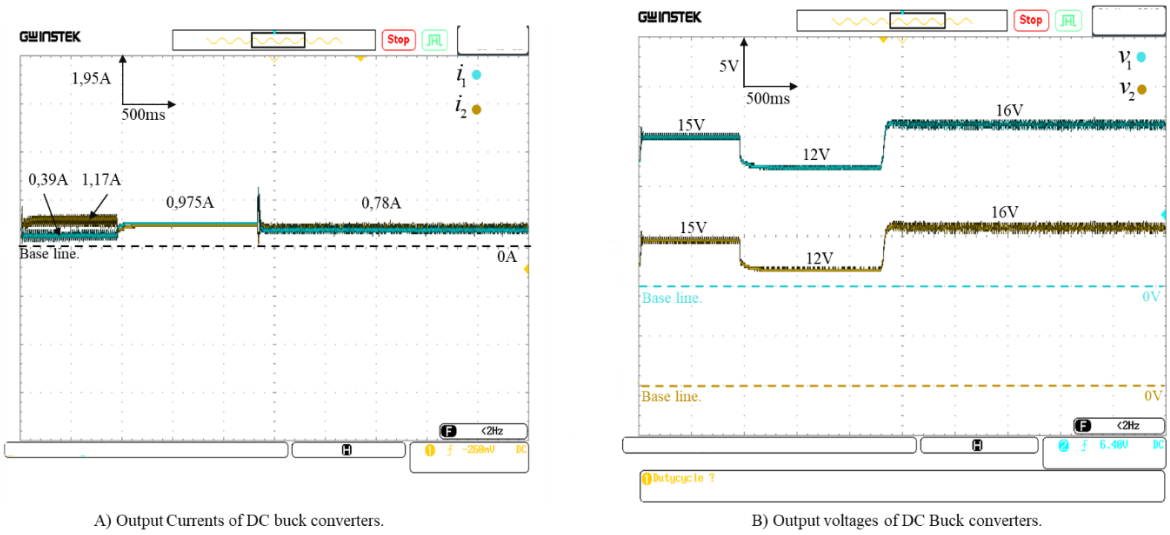

Fig 5.7. Output currents and voltages of DC buck converters resulted from the first scenario in the case of CPL load.

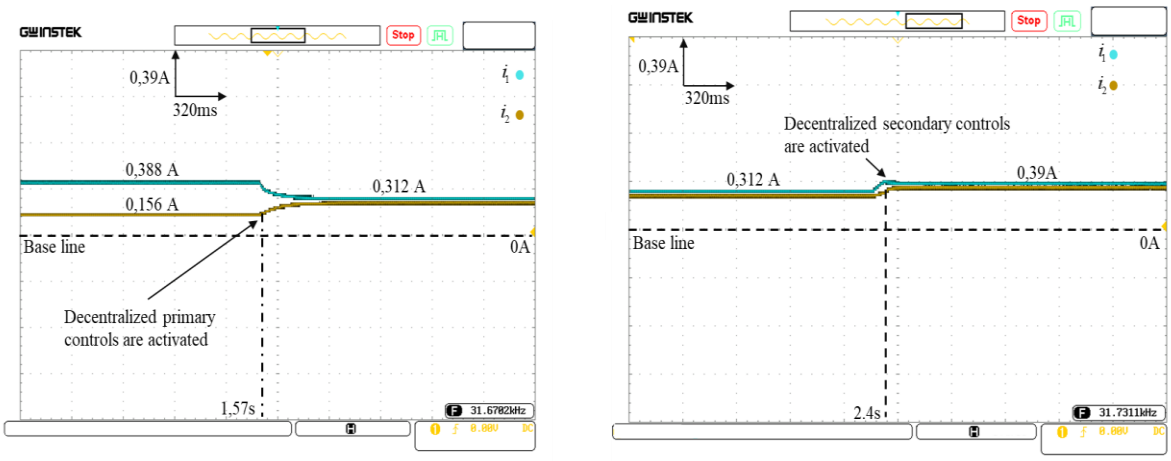

Fig 5.8. Outputs current of DC buck converters resulted from the first scenario in the case of resistive load.

The second scenario is carried out to exhibit the designed control's effectiveness to mitigate the disturbance arising from the sudden load variation. This scenario is performed in the case of resistive and CPL loads. Their sudden changes are realized in both cases, as illustrated in Fig 5.9 and Fig 5.10. According to the results, the sudden change of loads causes small voltage deviations appeared during a short time. After that, these deviations will be smoothed, and the DC bus voltage remains at the rated value $v^* = 15V$. Moreover, these results show that the system stability is maintained during system operation in both cases, and the sudden change does not affect the system stability.

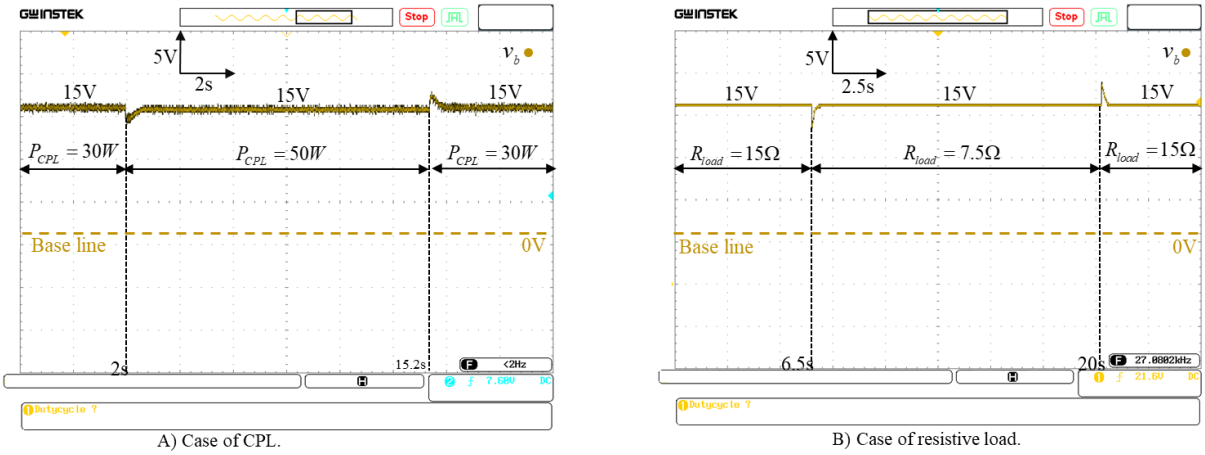

Fig 5.9. Common Dc bus voltage resulted from the second scenario.

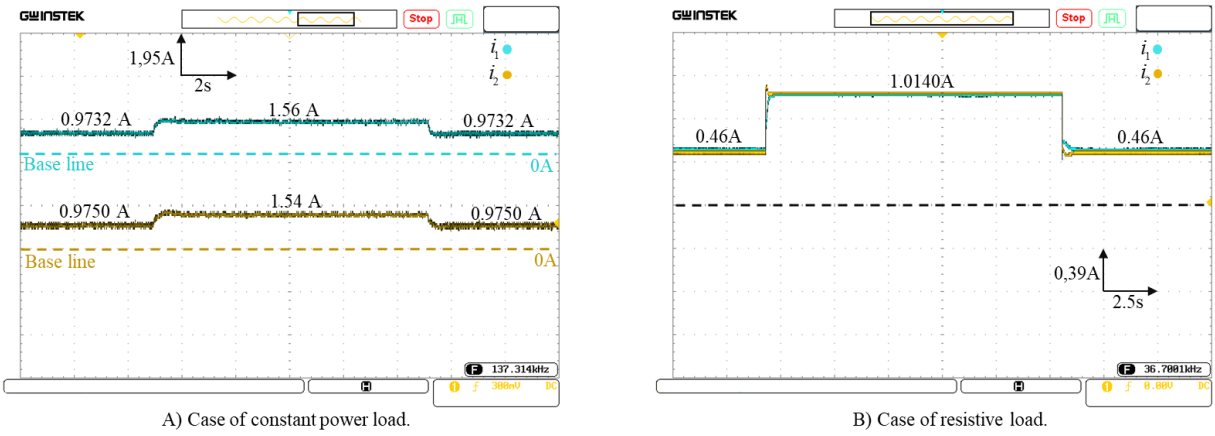

Fig 5.10. Output currents of DC buck converters resulted from the second scenario.

The third scenario is realized to test the play and plug system propriety. This scenario is performed by disconnecting one DC buck converter at 1.5s and reconnecting again at 5.1s. In this scenario, the system supplies a fixed CPL load, which consumes 30W. The whole results of this scenario are depicted in Fig 5.11. According to Fig 5.11, disconnecting and reconnecting the DC Buck converter causes small voltage deviations appeared during a short time. After

that, these deviations are smoothed, and the designed control restores the common DC bus voltage to the rated value $v^* = 15V$ with maintaining the power-sharing.

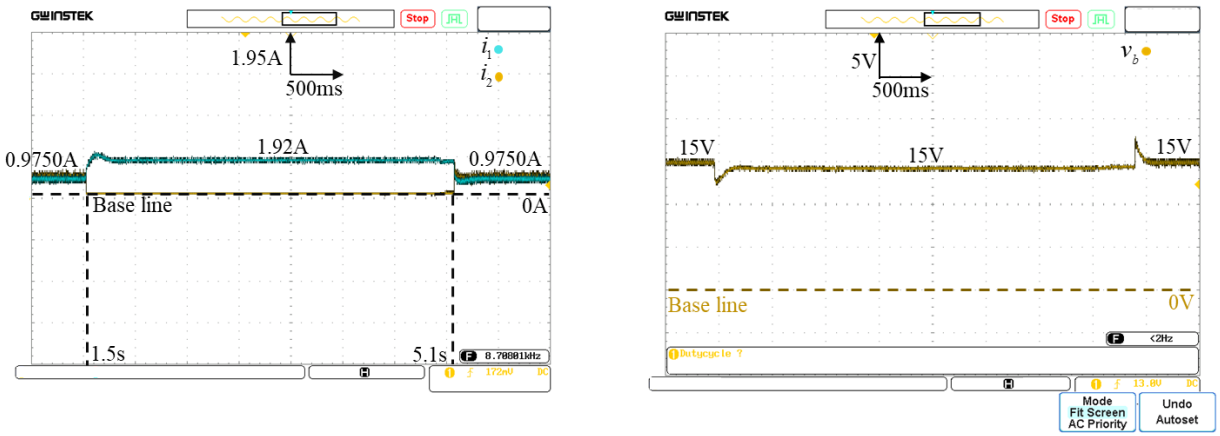

Fig 5.11. Output currents and Common DC bus voltage resulted from the third scenario.

5.4. Experimental validation robust online diagnosis

An experimental platform of DC-MG used to produce the green H_2 fuel is exploited to validate the developed robust online diagnosis. It consists of a parallel interconnection of the WT generator (350–400 W power), PV panels (200 W power per panel), fuel cell (700 W), and battery, as illustrated in Fig 5.12. The WT generator and PV panels converters the wind and solar energies to electrical power. The electrolyzer will use this electrical power to decompose the water in H_2 and O_2 gases. The H_2 is stored in the metallic cylinders. The mass flow of H_2 is firmly regulated to be constant at the desired value. Thus, the electrolyzer consumes, in this case, a constant power. The stability of electrical production cannot be ensured due to the intermittency of wind and solar energies. For that, The battery and fuel cell are incorporated into the system to ensure enough energy for the electrolyzer and stabilize the electrical power production. The whole system elements are integrated using the converters placed in the electrical enclosure. The parameters of platform components are listed in Tab a.1

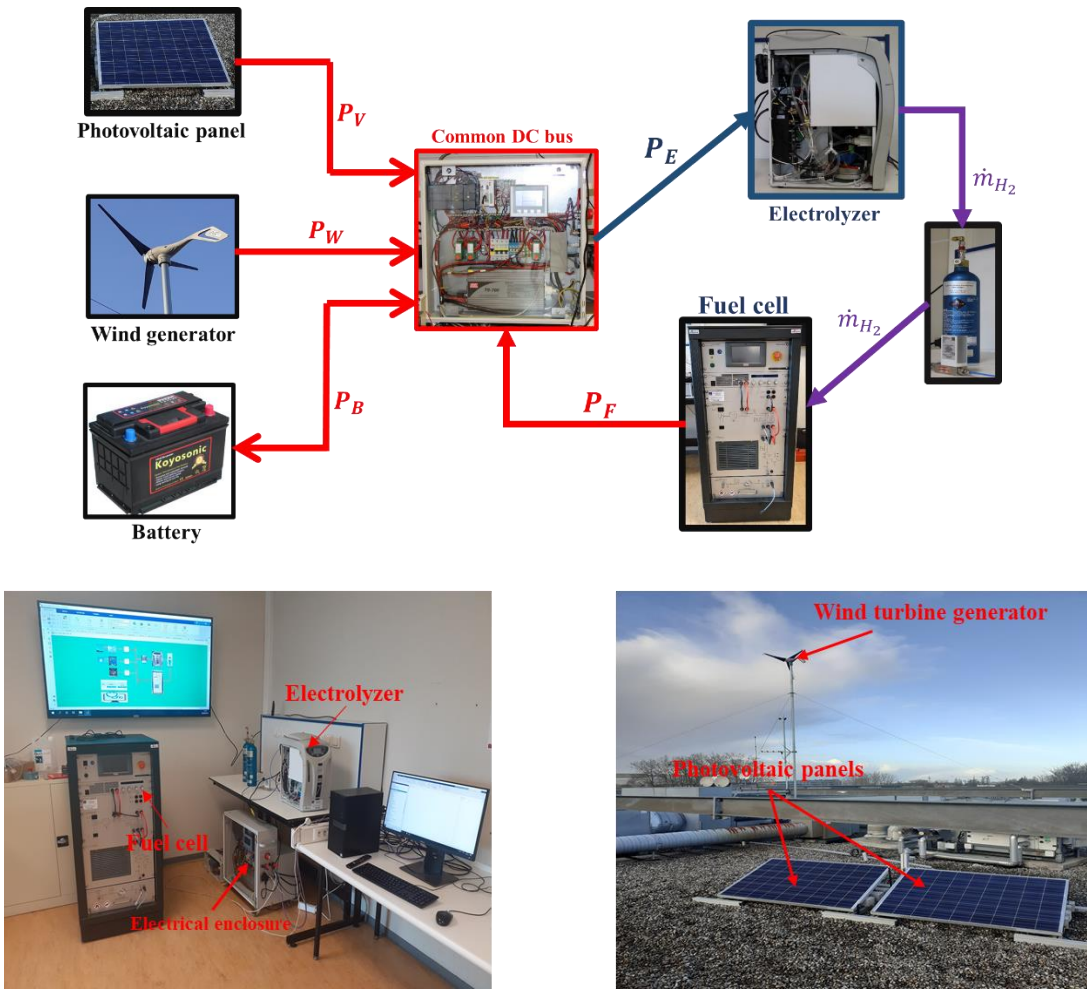

Fig 5.12. DC/DC Microgrid applied for green H_2 production.

The data acquisition system illustrated in Fig 5.13 is developed using PLC S7-1200 to exchange the measurement data and control law signals between the windows system and sensors and actuators of the DC-MG platform. Another communication is established between the windows system and Matlab software by using keyserver software. This kepserver software makes a Chanel that allows feeding Simulink of Matlab software by the data measurement. An algorithm implemented in Simulink/Matlab treats these data. Based on this data treatment, the implemented algorithm will provide the control signals, which will be used to act on the actuator of the DC-MG platform.

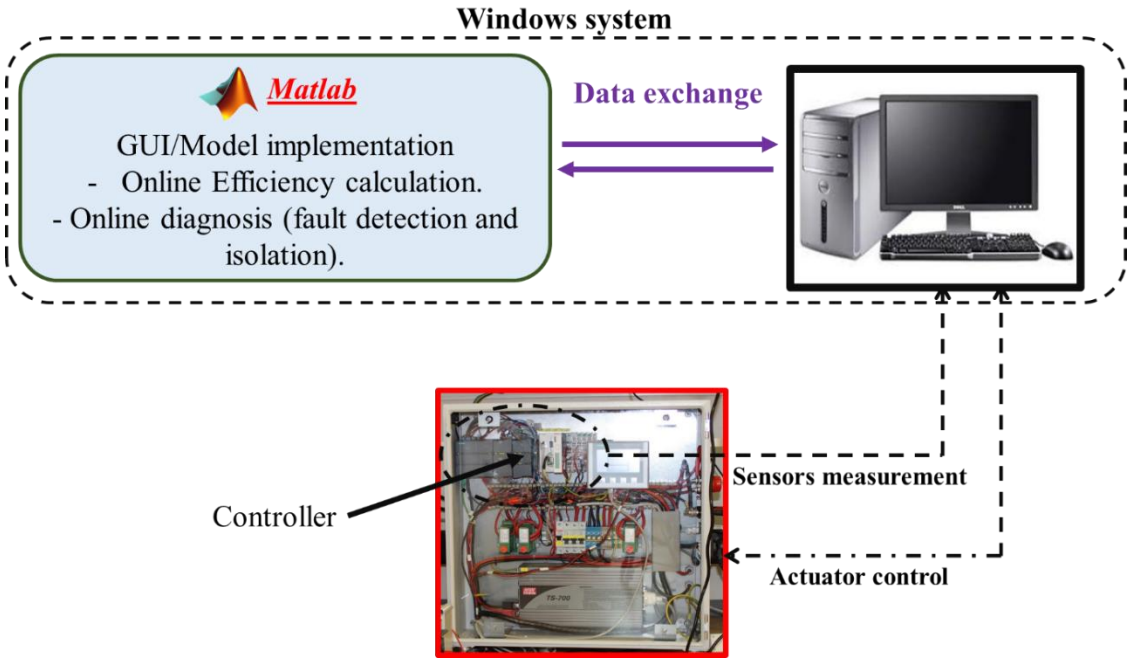

Fig 5.13. Data acquisition system of DC microgrid platform.

The graphical user interface (GUI) illustrated in Fig 5.14 is developed with the help of a Data acquisition system. It allows monitoring the system components by implementing the ARRs and generators of the adaptive thresholds in the form of Simulink blocks, as illustrated in Fig 5.14.

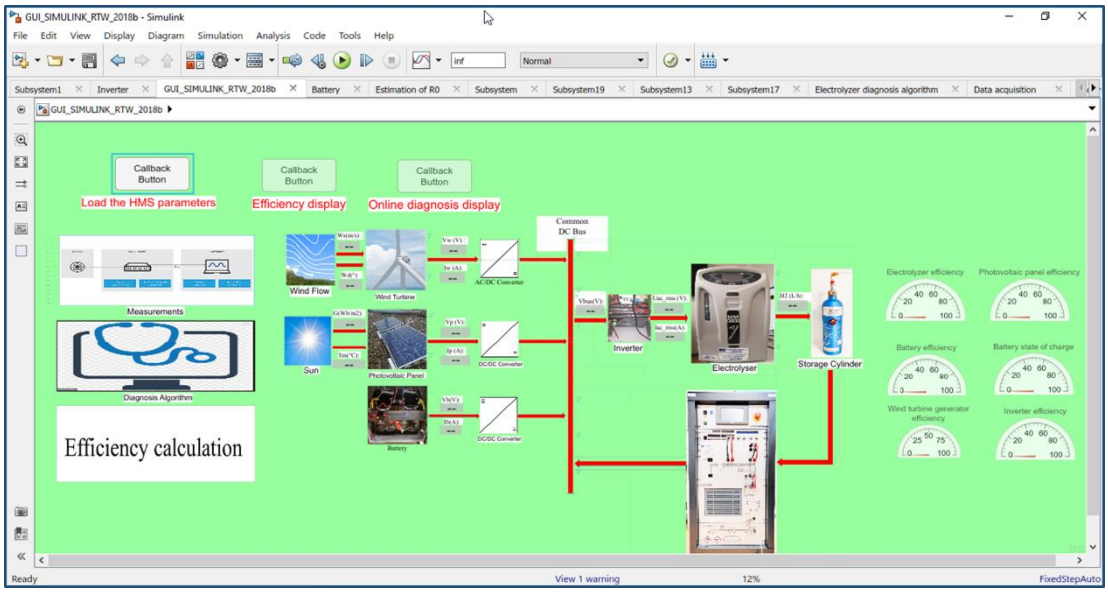

Fig 5.14. Graphical user interface of DC-MG platform developed in Matlab.

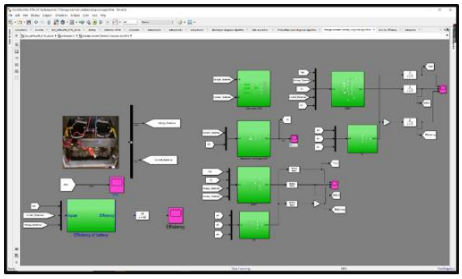

Battery diagnosis algorithm

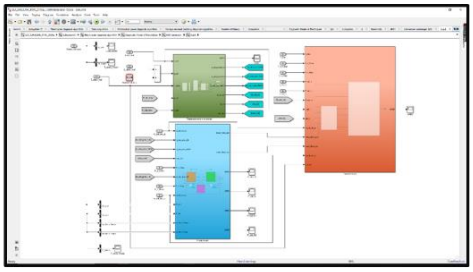

Electrolyzer diagnosis algorithm

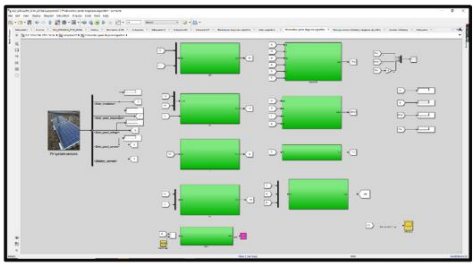

Photovoltaic diagnosis algorithm

Fig 5.15. Analytical redundancy relations implemented in Simulink in the form of blocks.

Only one scenario is performed for this experimental validation. There are two faults injected into the system by using the rheostat illustrated in Fig 5.16. These faults are injected into the battery and PV panel at the 20s and 35s to affect the series R_s and internal R_i resistances. The rheostat causes a variation in these parameters. In this case, these parameters variate and exceed the accepted limits ($R_{s_0} - R_{s_0} \cdot 5\% \le R_s \le R_{s_0} + R_{s_0} \cdot 5\%$, $R_{i_0} - R_{i_0} \cdot 5\% \le R_i \le R_{i_0} + R_{i_0} \cdot 5\%$). The obtained results are depicted in Fig 5.17. As long the faults are only injected in the PV panel and battery, we show only the residual signals generated from ARR_4, ARR_5, and ARR_6 illustrated in Fig 5.17. According to the obtained results, in the absence of the faults, the residual signals generated from the ARRs mentioned before are comprised in the bounds limited by their adaptive thresholds. The adaptive thresholds evolve with the evolution of system inputs (wind and solar irradiation) to prevent false alarms. When the faults occur in the system, the residual signals generated from ARR_4 and ARR_6 go out of the adaptive thresholds. These residuals return to their bounds limited by the adaptive thresholds when the faults are avoided from the system. Only the residual signal generated from ARR_5 is not affected because it is not sensitive to these faults. The injection of faults at a different time, which are not sensitive to the residual signal provided by ARR_5, have been performed to validate the monitorability and isolability analysis presented in section 4.7. This way shows the ability of the developed robust online diagnosis to detect and isolate the faults.

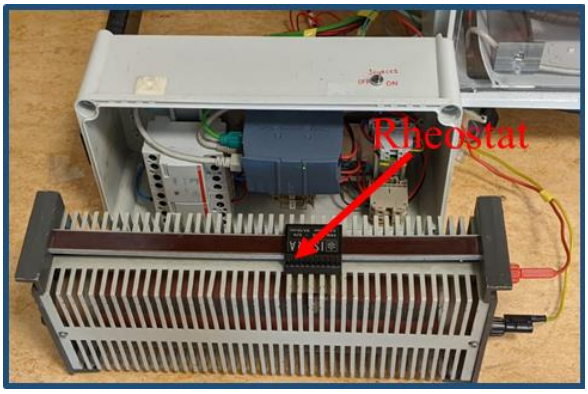

Fig 5.16. Rheostat used for emulating faults in panel.

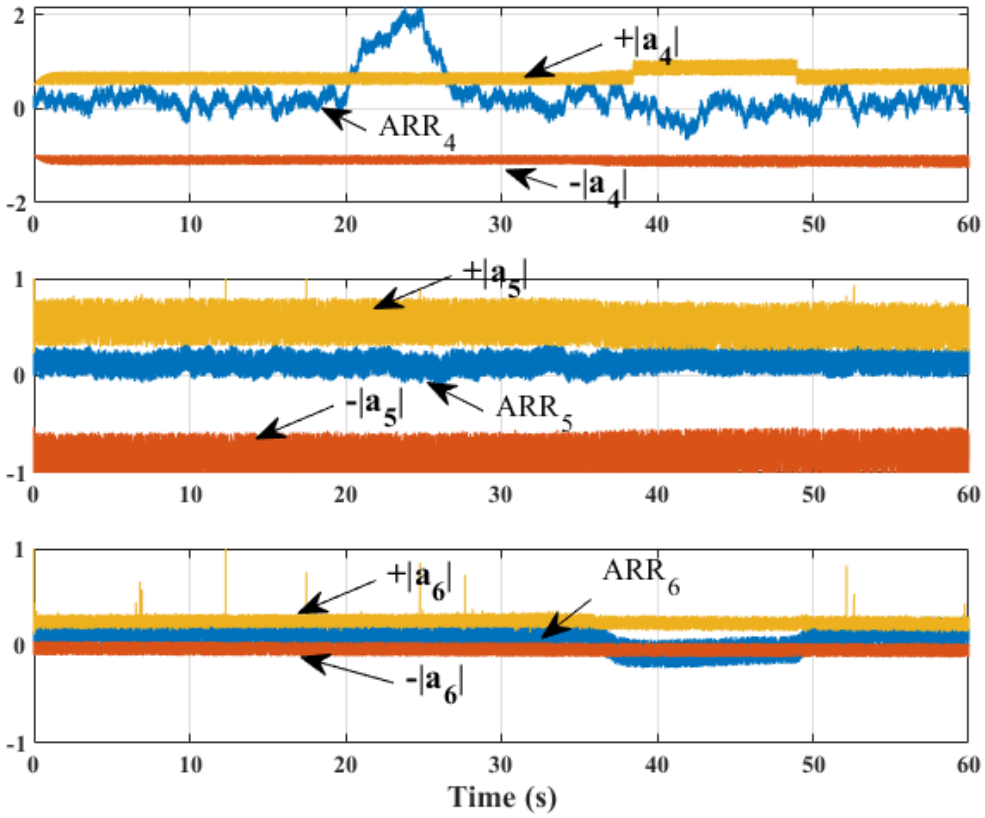

Fig 5.17. numerical evaluation of ARR4, ARR5, and ARR6 derived from the experimental validation.

5.5. Conclusion

The experimental validations presented in this chapter show the Active FTC element's effectiveness in realizing their objectives in control and diagnosis. The different scenarios performed to validate the robust hierarchical control show the robust hierarchical control to ensure the power flow needed to feed the load, where system stability is ensured in the presence of CPL and parameter variations. The H_∞-based control avoids the use of capacitance current measurement to prevent the filtering degradation problem. The experimental validation carried out on the DC-MG platform used for the green H_2 production shows the ability of robust online

diagnosis to prevent the possibility of false alarms. The adaptive thresholds of the online diagnosis evolve the evolution of the system inputs. The residual signals go outside the bounds limited by these adaptive thresholds when the fault occurs in the system.

General conclusion

In the thesis, an active (FTC) is developed to ensure energy availability in the DC MG system, which can be lost due to the INI characteristic of CPL and component faults that severely affects the system components. The developed active FTC consists of two elements: Robust Hierarchical control and online diagnosis. The Hierarchical control is formed by two levels of control: Primary and secondary control levels. The primary control level consists of decentralized controllers. Each decentralized controller consists of droop and voltage controls. The droop control uses a virtual impedance to avoid the current circulating and channel the power from the DC MG source to the electrolyzer and local loads. The voltage control receives the voltage reference from the droop control and controls the output voltages of DC/DC converters to avoid the difference in the voltage appearing between the output voltages of DC/DC converters, which is the cause of the current circulating. The secondary control level has a decentralized structure. It also consists of decentralized controllers, which provide the voltage composition signals to the droop controls to stabilize the DC bus's voltage at the desired voltage value. In this secondary control level, only one decentralized secondary controller has access to the bus voltage measurement. This decentralized secondary controller exchanges the information regarding the DC bus with the other decentralized secondary controllers through a network, which has the laplacian graph properties.

The Hierarchical control earns its robustness from two robust controllers: H_∞ and structured H_∞ based controllers. The H_∞ based controller is implemented in the primary control. It is obtained using the Golver Doyle (GD) optimization algorithm, which requires an augmented plant derived from the DC/DC converters model, where the uncertainties and disturbances take part in the DC/DC buck converters model. The augmented plants include the weight functions, representing the constraints of the optimization problem solved by the GD optimization algorithm. These weight functions are used to derive the H_∞ based control needed to achieve the suited performance. The structured H_∞ based control is developed using the Nonsmooth optimization algorithm that also requires an augmented plant including the weight functions. The model used to derive the augmented plant corresponds to the parallel interconnection of DC-MG components. The simulation study validates the effectiveness of the developed robust controller to improve the robustness of the Hierarchical control the perturbation arising from component faults. They increase the damping factor. Due to that, the voltage and current oscillations due to CPL and component faults will be damped.

However, the proposed robust Hierarchical control cannot keep the damping factor at desired value for the overall component faults. In some cases, the developed robust Hierarchical control cannot mitigate the faults that severely affect the DC-MG component. Therefore, the Hierarchical control must be reconfigured to correspond to the system when the faults are present. The thesis develops a robust online diagnosis, which estimates the variations of the parameters that are caused due to faults and provides them the control reconfiguration process. The control reconfiguration will recalculate H_∞ and structured H_∞ based controller to compensate for the damping factor decrease. The robust online diagnosis consists of the analytical redundancy relations and generators of adaptive thresholds. They are derived from the model of the whole DC MG system modeled by the linear fractional transformation modeling approach. This approach is powerful in modeling the hybrid multi-physical systems as DC-MG and allows incorporating the disturbances and uncertainties as part of the model. The LFT-BG modeling tool also facilitates performing the observers used to get the measurements from some part of the system, where placing a physical system is impossible. This way increases the ability of the robust online diagnosis to isolate the faults. The derived adaptive thresholds evolve with the evolution of system inputs and uncertainties to prevent the false alarm. The results obtained from the simulation study have proved the effectiveness of the Active FTC. It mitigates the current and voltage fluctuations that appeared due to the occurrence of the faults.

The results obtained from the simulation study have been confirmed experimentally by using the experimental setup built by the TMS320F28335 controller, controlling parallel interconnection of two DC/DC buck converters feeding a CPL emulated by DC/DC buck converter, and another DC MG platform used to produce the green hydrogen fuel, which consists of real RESs and operates under supervision platform performed by data acquisition system and Matlab /Simulink. Actually, these experimental setups have only validated the elements of Active FTC. The control reconfiguration process is not validated due to some technical problems. Using the H-based control implemented in the primary control improves the DC-MG system because it avoids using capacitance current measurement, having some drawbacks as a filtering degradation problem.

Perspectives

In this thesis, fault-tolerant control has been focused on the DC microgrid part. The concerned faults mitigated by the developed approach are the actuators (DC/DC converters) and physical

faults (faults in renewable energy sources). In terms of perspectives and within the framework of the industrial project, the future study will be extended to the process faults, mainly hydrogen leakage and electrolyzer faults. But in this new configuration where the system to be supervised (in terms of fault tolerant control and Fault Detection and Isolation) is described by a non-linear model due to the interactions of thermal, fluidic, and thermochemical energies, it is required to use the hybrid methods performed by combining the model-based and data based methods using artificial intelligence techniques and digital twin. The benefit of the combination of model-based and artificial intelligence-based techniques can also be oriented towards prognosis: for the estimation of remaining useful time. The introduction of the prognosis task provides the possibility to extend fault-tolerant control to degradation–tolerant control.

References

[1] D.-H. Dam and H.-H. Lee, “An adaptive power distributed control method to ensure proportional load power-sharing in DC microgrid considering equivalent line impedances,” 2 016 IEEE Energy Conversion Congress and Exposition (ECCE), Sep. 2016.

[2] X. Lu, K. Sun, J. M. Guerrero, J. C. Vasquez, and L. Huang, “Double-Quadrant Stat e-of-Charge-Based Droop Control Method for Distributed Energy Storage Systems in Autono mous DC Microgrids,” IEEE Transactions on Smart Grid, vol. 6, no. 1, pp. 147–157, Jan. 201 5.

[3] Sung-Hwan Park, Jin-Young Choi, and Dong-Jun Won, “Cooperative control betwe en the distributed energy resources in AC/DC hybrid microgrid,” ISGT 2014, Feb. 2014.

[4] Z. Zhong, “Modeling, Control, Estimation, and Optimization for Microgrids,” Oct. 2 019.

[5] T. Ma, H. Yahoui, H. Vu, N. Siauve, and H. Morel, “A Control Strategy of DC Buil ding Microgrid Connected to the Neighborhood and AC Power Network,” Buildings, vol. 7, n o. 4, p. 42, May 2017.

[6] M. Shahid, M. Khan, K. Hashmi, S. Habib, H. Jiang, and H. Tang, “A Control Meth odology for Load Sharing System Restoration in Islanded DC Micro Grid with Faulty Comm unication Links,” Electronics, vol. 7, no. 6, p. 90, Jun. 2018.

[7] J.-C. Choi, H.-Y. Jeong, J.-Y. Choi, D.-J. Won, S.-J. Ahn, and S. Moon, “Voltage C ontrol Scheme with Distributed Generation and Grid-Connected Converter in a DC Microgri d,” Energies, vol. 7, no. 10, pp. 6477–6491, Oct. 2014.

[8] F. Locment and M. Sechilariu, “Modeling and Simulation of DC Microgrids for Electr ic Vehicle Charging Stations,” Energies, vol. 8, no. 5, pp. 4335–4356, May 2015.

[9] “Interconnecting Microgrids via the Energy Router with Smart Energy Management,” Energies, vol. 10, no. 9, p. 1297, Aug. 2017.

[10] S. Serna-Garcés, D. González Montoya, and C. Ramos-Paja, “Control of a Charger/Di scharger DC/DC Converter with Improved Disturbance Rejection for Bus Regulation,” Energ ies, vol. 11, no. 3, p. 594, Mar. 2018.

[11] D.-K. Jeong, H.-S. Kim, J.-W. Baek, H.-J. Kim, and J.-H. Jung, “Autonomous Control Strategy of DC Microgrid for Islanding Mode Using Power Line Communication,” Energies, vol. 11, no. 4, p. 924, Apr. 2018.

[12] Z. Lv, Y. Xia, J. Chai, M. Yu, and W. Wei, “Distributed Coordination Control Based o n State-of-Charge for Bidirectional Power Converters in a Hybrid AC/DC Microgrid,” Energi es, vol. 11, no. 4, p. 1011, Apr. 2018.

[13] M. Hassan, M. Worku, and M. Abido, “Optimal Design and Real-Time Implementatio n of Autonomous Microgrid Including Active Load,” Energies, vol. 11, no. 5, p. 1109, May 2 018.

[14] P. Shaikh, Z. Leghari, N. Mirjat, F. Shaikh, A. Solangi, T. Jan, and M. Uqaili, “Wind–PV-Based Hybrid DC Microgrid (DCMG) Development: An Experimental Investigation and Comparative Economic Analysis,” Energies, vol. 11, no. 5, p. 1295, May 2018.

[15] C. Lv, X. Zheng, N. Tai, and S. Chen, “Single-Ended Protection Scheme for VSC-Bas ed DC Microgrid Lines,” Energies, vol. 11, no. 6, p. 1440, Jun. 2018.

[16] K. J. Bunker, “MULTIDIMENSIONAL OPTIMAL DROOP CONTROL FOR WIND RESOURCES IN DC MICROGRIDS.”

[17] A. Howlader, H. Matayoshi, S. Sepasi, and T. Senjyu, “Design and Line Fault Protecti on Scheme of a DC Microgrid Based on Battery Energy Storage System,” Energies, vol. 11, n o. 7, p. 1823, Jul. 2018.

[18] R. Salas-Puente, S. Marzal, R. Gonzalez-Medina, E. Figueres, and G. Garcera, “Practi cal Analysis and Design of a Battery Management System for a Grid-Connected DC Microgri d for the Reduction of the Tariff Cost and Battery Life Maximization,” Energies, vol. 11, no. 7 , p. 1889, Jul. 2018.

[19] A. Kihal, F. Krim, B. Talbi, A. Laib, and A. Sahli, “A Robust Control of Two-Stage G rid-Tied PV Systems Employing Integral Sliding Mode Theory,” Aug. 2018.

[20] N. Guler, S. Demirbas, and E. Irmak, “Design and Analyse of a Parallel Connection M odel for Hybrid Energy Systems,” Elektronika ir Elektrotechnika, vol. 21, no. 2, Apr. 2015.

[21] T. Dragicevic, X. Lu, J. C. Vasquez, and J. M. Guerrero, “DC Microgrids—Part II: A Review of Power Architectures, Applications, and Standardization Issues,” IEEE Transactions on Power Electronics, vol. 31, no. 5, pp. 3528–3549, May 2016.

[22] L. B. G. Campanhol, S. A. O. da Silva, A. A. de Oliveira, and V. D. Bacon, “Power Flow and Stability Analyses of a Multifunctional Distributed Generation System Integrating a Photovoltaic System With Unified Power Quality Conditioner,” IEEE Transactions on Power Electronics, vol. 34, no. 7, pp. 6241–6256, Jul. 2019.

[23] A. M. Othman, H. A. Gabbar, and N. Honarmand, “Performance Analysis of Grid Connected and Islanded Modes of AC/DC Microgrid for Residential Home Cluster,” Intelligent Control and Automation, vol. 06, no. 04, pp. 249–270, 2015.

[24] J. A. Pecas Lopes, C. L. Moreira, and A. G. Madureira, “Defining control strategies for analyzing microgrids islanded operation,” 2005 IEEE Russia Power Tech, Jun. 2005.

[25] H. Kakigano, Y. Miura, and T. Ise, “Low-Voltage Bipolar-Type DC Microgrid for Super High-Quality Distribution,” IEEE Transactions on Power Electronics, vol. 25, no. 12, pp. 3066–3075, Dec. 2010.

[26] L. Meng, T. Dragicevic, J. C. Vasquez, J. M. Guerrero, and J. R. Perez, “Modeling and sensitivity analysis of consensus algorithm based distributed hierarchical control for DC microgrids,” 2015 IEEE Applied Power Electronics Conference and Exposition (APEC), Mar. 2015.

[27] C. Wu, X. Hou, Y. Wang, X. Chen, and C. Liao, “SOC-featured Distributed Tertiary Control for Energy Management in DC Microgrid Clusters,” 2019 22nd International Conference on Electrical Machines and Systems (ICEMS), Aug. 2019.

[28] M.-A. Rodríguez-Licea, F.-J. Pérez-Pinal, J.-C. Nuñez-Perez, and C.-A. Herrera-Ramirez, “Nonlinear Robust Control for Low Voltage Direct-Current Residential Microgrids with fault Loads,” Energies, vol. 11, no. 5, p. 1130, May 2018.

[29] A. El Aroudi, B. Martínez-Treviño, E. Vidal-Idiarte, and A. Cid-Pastor, “Fixed Switching Frequency Digital Sliding-Mode Control of DC-DC Power Supplies Loaded by Constant Power Loads with Inrush Current Limitation Capability,” Energies, vol. 12, no. 6, p. 1055, Mar. 2019.

[30] I. Abdallah, A.-L. Gehin, and B. Ould Bouamama, “Event-driven Hybrid Bond Graph for Hybrid Renewable Energy Systems part I: Modelling and operating mode management,” I nternational Journal of Hydrogen Energy, vol. 43, no. 49, pp. 22088–22107, Dec. 2018.

[31] S. Sood, O. Prakash, M. Boukerdja, J.-Y. Dieulot, B. Ould-Bouamama, M. Bressel, an d A.-L. Gehin, “Generic Dynamical Model of PEM Electrolyser under Intermittent Sources,” Energies, vol. 13, no. 24, p. 6556, Dec. 2020.

[32] N. Mahdavi Tabatabaei, E. Kabalci, and N. Bizon, “Overview of Microgrid,” Microgr id Architectures, Control and Protection Methods, pp. 3–19, Jul. 2019.

[33] S. Peyghami, S. F. Zarei, M. A. Ghasemi, P. Palensky, and F. Blaabjerg, “A Decentral ized Frequency Regulation Scheme in AC Microgrids,” 2020 IEEE 21st Workshop on Contro l and Modeling for Power Electronics (COMPEL), Nov. 2020.

[34] M. Naderi, Q. Shafiee, F. Blaabjerg, and H. Bevrani, “Low-Frequency Small-Signal M odeling of Interconnected AC Microgrids,” IEEE Transactions on Power Systems, pp. 1–1, 20 20.

[35] A. Radwan, I. Khouri, and X. Jiang, “Modeling and Control of Current-Source Conver ter-Based AC Microgrids,” 2020 IEEE 8th International Conference on Smart Energy Grid En gineering (SEGE), Aug. 2020.

[36] A. O. Rousis, I. Konstantelos, and G. Strbac, “A Planning Model for a Hybrid AC–DC Microgrid Using a Novel GA/AC OPF Algorithm,” IEEE Transactions on Power Systems, vo l. 35, no. 1, pp. 227–237, Jan. 2020.

[37] A. A. Eajal, A. H. Yazdavar, E. F. El-Saadany, and K. Ponnambalam, “On the Loadab ility and Voltage Stability of Islanded AC–DC Hybrid Microgrids During Contingencies,” IE EE Systems Journal, vol. 13, no. 4, pp. 4248–4259, Dec. 2019.

[38] M. Biglarahmadi, A. Ketabi, H. Reza Baghaee, and J. M. Guerrero, “Integrated Nonlin ear Hierarchical Control and Management of Hybrid AC/DC Microgrids,” IEEE Systems Jour nal, pp. 1–12, 2021.

[39] M. Boukerdja, A. Chouder, and K. Louassaa, “Realizing the Accurate power-sharing i n DC Microgrid Using Droop Control Strategy.,” 2019 International Conference on Advanced Electrical Engineering (ICAEE), Nov. 2019.

[40] F. Guo, L. Wang, and C. Wen, “Distributed voltage restoration and power allocation c ontrol in islanded DC microgrids,” Distributed Control Methods and Cyber Security Issues in Microgrids, pp. 29–58, 2020.

[41] J. Liu, X. Lu, and C. Chen, “Secondary Control for DC Microgrids with Optimal Spar se Feedback,” 2019 IEEE Energy Conversion Congress and Exposition (ECCE), Sep. 2019.

[42] J. J. Justo, F. Mwasilu, J. Lee, and J.-W. Jung, “AC-microgrids versus DC-microgrids with distributed energy resources: A review,” Renewable and Sustainable Energy Reviews, v ol. 24, pp. 387–405, Aug. 2013.

[43] S. Dahale, A. Das, N. M. Pindoriya, and S. Rajendran, “An overview of DC-DC conve rter topologies and controls in DC microgrid,” 2017 7th International Conference on Power S ystems (ICPS), Dec. 2017.

[44] J. M. Guerrero, J. C. Vasquez, and R. Teodorescu, “Hierarchical control of droop-cont rolled DC and AC microgrids — a general approach towards standardization,” 2009 35th Ann ual Conference of IEEE Industrial Electronics, Nov. 2009.

[45] M. Cespedes, T. Beechner, L. Xing, and J. Sun, “Stabilization of constant-power loads by passive impedance damping,” 2010 Twenty-Fifth Annual IEEE Applied Power Electronics Conference and Exposition (APEC), Feb. 2010.

[46] M. Cespedes, L. Xing, and J. Sun, “Constant-Power Load System Stabilization by Pas sive Damping,” IEEE Transactions on Power Electronics, vol. 26, no. 7, pp. 1832–1836, Jul. 2 011.

[47] X. Liu and S. Ma, “Large signal stabilization method of constant power loads by addin g R parallel damping filters,” 2015 IEEE Energy Conversion Congress and Exposition (ECCE), Sep. 2015.

[48] M. K. AL-Nussairi, R. Bayindir, S. Padmanaban, L. Mihet-Popa, and P. Siano, “Const ant Power Loads (CPL) with Microgrids: Problem Definition, Stability Analysis, and Compen sation Techniques,” Energies, vol. 10, no. 10, p. 1656, Oct. 2017.

[49] X. Lu, K. Sun, L. Huang, J. M. Guerrero, J. C. Vasquez, and Y. Xing, “Virtual impeda nce-based stability improvement for DC microgrids with constant power loads,” 2014 IEEE E nergy Conversion Congress and Exposition (ECCE), Sep. 2014.

[50] M. Boukerdja, A. Chouder, L. Hassaine, B. O. Bouamama, W. Issa, and K. Louassaa, “H∞ based control of a DC/DC buck converter feeding a constant power load in uncertain DC microgrid system,” ISA Transactions, vol. 105, pp. 278–295, Oct. 2020.

[51] T. Dragicevic, “Dynamic Stabilization of DC Microgrids With Predictive Control of P oint-of-Load Converters,” IEEE Transactions on Power Electronics, vol. 33, no. 12, pp. 1087 2–10884, Dec. 2018.

[52] S. Singh, A. R. Gautam, and D. Fulwani, “Constant power loads and their effects in D C distributed power systems: A review,” Renewable and Sustainable Energy Reviews, vol. 72 , pp. 407–421, May 2017.

[53] X. Zhang, X. Ruan, and Q.-C. Zhong, “Improving the Stability of Cascaded DC/DC C onverter Systems via Shaping the Input Impedance of the Load Converter With a Parallel or S eries Virtual Impedance,” IEEE Transactions on Industrial Electronics, vol. 62, no. 12, pp. 74 99–7512, Dec. 2015.

[54] M. A. Hassan, E. Li, X. Li, T. Li, C. Duan, and S. Chi, “Adaptive Passivity-Based Co ntrol of dc-dc Buck Power Converter With Constant Power Load in DC Microgrid Systems,” IEEE Journal of Emerging and Selected Topics in Power Electronics, vol. 7, no. 3, pp. 2029–2040, Sep. 2019.

[55] A. Yasin, M. Ashraf, and A. Bhatti, “Fixed Frequency Sliding Mode Control of Power Converters for Improved Dynamic Response in DC Micro-Grids,” Energies, vol. 11, no. 10, p . 2799, Oct. 2018.

[56] Q. Shafiee, T. Dragicevic, J. C. Vasquez, and J. M. Guerrero, “Modeling, stability ana lysis and active stabilization of multiple DC-microgrid clusters,” 2014 IEEE International Ene rgy Conference (ENERGYCON), May 2014.

[57] V. Thomas, Kumaravel S., and Ashok S., “Control of parallel DC-DC converters in a DC microgrid using virtual output impedance method,” 2016 2nd International Conference on Advances in Electrical, Electronics, Information, Communication, and Bio-Informatics (AEEI CB), Feb. 2016.

[58] B. Babaiahgari, Y. Jeong, and J.-D. Park, “Stability Analysis for Interconnected DC M icrogrids with Constant Power Loads,” 2019 IEEE Energy Conversion Congress and Expositi on (ECCE), Sep. 2019.

[59] Q. Xu, W. Jiang, F. Blaabjerg, C. Zhang, X. Zhang, and T. Fernando, “Backstepping C ontrol for Large Signal Stability of High Boost Ratio Interleaved Converter Interfaced DC Mi crogrids With Constant Power Loads,” IEEE Transactions on Power Electronics, vol. 35, no. 5, pp. 5397–5407, May 2020.

[60] X. Li, X. Zhang, W. Jiang, J. Wang, P. Wang, and X. Wu, “A Novel Assorted Nonline ar Stabilizer for DC-DC Multilevel Boost Converter With Constant Power Load in DC Micro grid,” IEEE Transactions on Power Electronics, vol. 35, no. 10, pp. 11181–11192, Oct. 2020.

[61] D. K. Fulwani and S. Singh, “Mitigation of Negative Impedance Instabilities in DC Di stribution Systems,” Springer Briefs in Applied Sciences and Technology, 2017.

[62] Dragicevic T. Dynamic stabilization of DC microgrids with predictive control of point -of-load converters. IEEE Trans Power Electron 2018;33(12):10872–84.

[63] N. Vafamand, M. H. Khooban, T. Dragicevic, and F. Blaabjerg, “Networked Fuzzy Pr edictive Control of Power Buffers for Dynamic Stabilization of DC Microgrids,” IEEE Transa ctions on Industrial Electronics, vol. 66, no. 2, pp. 1356–1362, Feb. 2019.

[64] S. Yousefizadeh, J. D. Bendtsen, N. Vafamand, M. H. Khooban, T. Dragicevic, and F. Blaabjerg, “EKF-Based Predictive Stabilization of Shipboard DC Microgrids With Uncertain Time-Varying Load,” IEEE Journal of Emerging and Selected Topics in Power Electronics, v ol. 7, no. 2, pp. 901–909, Jun. 2019.

[65] N. Vafamand, S. Yousefizadeh, M. H. Khooban, J. D. Bendtsen, and T. Dragicevic, “ Adaptive TS Fuzzy-Based MPC for DC Microgrids With Dynamic CPLs: Nonlinear Power O bserver Approach,” IEEE Systems Journal, vol. 13, no. 3, pp. 3203–3210, Sep. 2019.

[66] R. Cheng, J. F. Forbes, and W. S. Yip, “Price-driven coordination method for solving plant-wide MPC problems,” Journal of Process Control, vol. 17, no. 5, pp. 429–438, Jun. 200 7.

[67] Q. Xu, C. Zhang, C. Wen, and P. Wang, “A Novel Composite Nonlinear Controller fo r Stabilization of Constant Power Load in DC Microgrid,” IEEE Transactions on Smart Grid, vol. 10, no. 1, pp. 752–761, Jan. 2019.

[68] S. Yousefizadeh, J. D. Bendtsen, N. Vafamand, M. H. Khooban, F. Blaabjerg, and T. Dragicevic, “Tracking Control for a DC Microgrid Feeding Uncertain Loads in More Electric Aircraft: Adaptive Backstepping Approach,” IEEE Transactions on Industrial Electronics, vol . 66, no. 7, pp. 5644–5652, Jul. 2019.

[69] S. Pang, B. Nahid-Mobarakeh, S. Pierfederici, M. Phattanasak, Y. Huangfu, G. Luo, a nd F. Gao, “Interconnection and Damping Assignment Passivity-Based Control Applied to O n-Board DC-DC Power Converter System Supplying Constant Power Load,” IEEE Transactio ns on Industry Applications, vol. 55, no. 6, pp. 6476–6485, Nov. 2019.

[70] S. Pang, B. Nahid-Mobarakeh, S. Pierfederici, Y. Huangfu, G. Luo, and F. Gao, “Tow ard Stabilization of Constant Power Loads Using IDA-PBC for Cascaded LC Filter DC/DC C onverters,” IEEE Journal of Emerging and Selected Topics in Power Electronics, vol. 9, no. 2 , pp. 1302–1314, Apr. 2021.

[71] T. Wang, L. Liang, S. K. Gurumurthy, F. Ponci, A. Monti, Z. Yang, and R. W. De Do ncker, “Model-Based Fault Detection and Isolation in DC Microgrids Using Optimal Observe rs,” IEEE Journal of Emerging and Selected Topics in Power Electronics, pp. 1–1, 2020.

[72] L. Kong and H. Nian, “Transient Modeling Method for Faulty DC Microgrid Consider ing Control Effect of DC/AC and DC/DC Converters,” IEEE Access, vol. 8, pp. 150759–1507 72, 2020.

[73] N. Yadav and N. R. Tummuru, “A Real-Time Resistance Based Fault Detection Techn ique For Zonal Type Low-Voltage DC Microgrid Applications,” IEEE Transactions on Indust ry Applications, vol. 56, no. 6, pp. 6815–6824, Nov. 2020.

[74] P. M. Frank, “Fault diagnosis in dynamic systems using analytical and knowledge-bas ed redundancy,” Automatica, vol. 26, no. 3, pp. 459–474, May 1990.

[75] R. Isermann and P. Ballé, “Trends in the Application of Model-Based Fault Detection and Diagnosis of Technical Processes,” IFAC Proceedings Volumes, vol. 29, no. 1, pp. 6325–6336, Jun. 1996.

[76] R. Isermann, “Supervision, fault-detection and diagnosis methods – a short introductio n,” Fault-Diagnosis Applications, pp. 11–45, 2011.

[77] R. Isermann, “Model-Based Fault Detection and Diagnosis - Status and Applications,” IFAC Proceedings Volumes, vol. 37, no. 6, pp. 49–60, Jun. 2004.

[78] J. J. Gertler, “Survey of model-based failure detection and isolation in complex plants, ” IEEE Control Systems Magazine, vol. 8, no. 6, pp. 3–11, Dec. 1988.

[79] Blanke, M., Kinnaert, M., Lunze, J., Staroswiecki, M. and Schröder, J., 2006. Diagnos is and fault–tolerant control. 2nd Eds., New York, USA: Springer.

[80] S. Jadidi, H. Badihi, and Y. Zhang, “Passive Fault-Tolerant Control Strategies for Pow er Converter in a Hybrid Microgrid,” Energies, vol. 13, no. 21, p. 5625, Oct. 2020.

[81] F. Shariatzadeh, N. Kumar, and A. K. Srivastava, “Optimal Control Algorithms for Re configuration of Shipboard Microgrid Distribution System Using Intelligent Techniques,” IEE E Transactions on Industry Applications, vol. 53, no. 1, pp. 474–482, Jan. 2017.

[82] S. Augustine, J. E. Quiroz, M. J. Reno, and S. Brahma, “DC Microgrid Protection: Re view and Challenges.,” Aug. 2018.

[83] Yi-Liang Chen and G. Provan, “Modeling and diagnosis of timed discrete event syste ms-a factory automation example,” Proceedings of the 1997 American Control Conference (C at. No.97CH36041), 1997.

[84] M. Sampath, R. Sengupta, S. Lafortune, K. Sinnamohideen, and D. Teneketzis, “Failu re diagnosis using discrete-event models,” Proceedings of 1994 33rd IEEE Conference on De cision and Control.

[85] A. Termeche, D. Benazzouz, B. O. Bouamama, and I. Abdallah, “Augmented analytic al redundancy relations to improve the fault isolation,” Mechatronics, vol. 55, pp. 129–140, N ov. 2018.

[86] M. Zhong, T. Xue, and S. X. Ding, “A survey on model-based fault diagnosis for linea r discrete time-varying systems,” Neurocomputing, vol. 306, pp. 51–60, Sep. 2018.

[87] D. Wang, F. Fu, W. Li, Y. Tu, C. Liu, and W. Liu, “A review of the diagnosability of control systems with applications to spacecraft,” Annual Reviews in Control, vol. 49, pp. 212 –229, 2020.

[88] X. Wang, Y. Li, Y. Li, Q. Zhang, and H. Chai, “Closed-loop parity-space based fault d etection: Application to simplified quadruped robot model,” 2017 Chinese Automation Congr ess (CAC), Oct. 2017.

[89] Y. Song, M. Zhong, J. Chen, and Y. Liu, “An Alternative Parity Space-Based Fault Di agnosability Analysis Approach for Linear Discrete-Time Systems,” IEEE Access, vol. 6, pp. 16110–16118, 2018.

[90] Z. Li, P. Wheeler, A. Watson, A. Costabeber, B. Wang, Y. Ren, Z. Bai, and H. Ma, “A Fast Diagnosis Method for Both IGBT Faults and Current Sensor Faults in Grid-Tied Three-P hase Inverters With Two Current Sensors,” IEEE Transactions on Power Electronics, vol. 35, no. 5, pp. 5267–5278, May 2020.

[91] T. Sun, D. Zhou, Y. Zhu, and M. V. Basin, “Stability, l_2-Gain Analysis, and Parity Spa ce-Based Fault Detection for Discrete-Time Switched Systems Under Dwell-Time Switching, ” IEEE Transactions on Systems, Man, and Cybernetics: Systems, vol. 50, no. 9, pp. 3358–33 68, Sep. 2020.

[92] H. Alikhani, M. A. Shoorehdeli, and N. Meskin, “A Functional Unknown Input Obser ver for Linear Singular Fornasini–Marchesini First Model Systems: With Application to Fault Diagnosis,” IEEE Systems Journal, pp. 1–12, 2021.

[93] Y. Yang, C. Lin, B. Chen, and Q.-G. Wang, “Functional Observer Design for Time-D elayed Systems With Application to Fault Diagnosis,” IEEE Access, vol. 7, pp. 14558–14568 , 2019.

[94] Q. Liu, T. Liang, Z. Huang, and V. Dinavahi, “Real-Time FPGA-Based Hardware Ne ural Network for Fault Detection and Isolation in More Electric Aircraft,” IEEE Access, vol. 7 , pp. 159831–159841, 2019.

[95] D. Long, X. Wen, W. Zhang, and J. Wang, “Recurrent Neural Network Based Robust Actuator and Sensor Fault Estimation for Satellite Attitude Control System,” IEEE Access, v ol. 8, pp. 183165–183174, 2020.

[96] W. Javed and D. Chen, “Data-Driven Fault Localization of a DC Microgrid with Refin ed Data Input,” 2020 IEEE 29th International Symposium on Industrial Electronics (ISIE), Ju n. 2020.

[97] C. Skliros, M. Esperon Miguez, A. Fakhre, and I. Jennions, “A review of model-based and data-driven methods targeting hardware systems diagnostics,” Diagnostyka, vol. 20, no. 1 , pp. 3–21, Nov. 2018.

[98] “Buck PWM DC-DC Converter,” Pulse-Width Modulated DC-DC Power Converters, Wiley, pp. 23–83, Feb. 2012.

[99] “Small-Signal Models of PWM Converters for CCM and DCM,” Pulse-Width Modula ted DC-DC Power Converters, Wiley, pp. 397–436, Feb. 2012.

[100] P. Wang, X. Lu, X. Yang, W. Wang, and D. Xu, “An Improved Distributed Secondary Control Method for DC Microgrids With Enhanced Dynamic Current Sharing Performance,” IEEE Transactions on Power Electronics, vol. 31, no. 9, pp. 6658–6673, Sep. 2016.

[101] J.-L. Hong and C.-C. Teng, “A derivation of the Glover-Doyle algorithms for general H∞ control problems,” Automatica, vol. 32, no. 4, pp. 581–589, Apr. 1996.

[102] A. S. Meghani and H. A. Latchman, “H_∞ vs. classical methods in the design of feedba ck control systems,” Proceedings IEEE Southeastcon ’92.

[103] L. Sedghi and A. Fakharian, “Robust voltage regulation in islanded microgrids: A LM I based mixed H_2/H_∞ control approach,” 2016 24th Mediterranean Conference on Control and Automation (MED), Jun. 2016.

[104] P. Lundstrom, S. Skogestad, and Z.-Q. Wang, “Uncertainty weight selection for H-infi nity and mu-control methods,” [1991] Proceedings of the 30th IEEE Conference on Decision and Control.

[105] P. Apkarian and D. Noll, “Nonsmooth Optimization for Multidisk H∞ Synthesis,” Eur opean Journal of Control, vol. 12, no. 3, pp. 229–244, Jan. 2006.

[105] A.K. Samantray and B. Ould bouamama, “Introduction to Process Supervision,” Adva nces in Industrial Control, pp. 1–12.

[106] D. Wang, M. Yu, C. B. Low, and S. Arogeti, “Quantitative Hybrid Bond Graph-Based Fault Detection and Isolation,” Model-based Health Monitoring of Hybrid Systems, pp. 81–14 6, 2013.

[107] R. Loureiro, R. Merzouki, and B. O. Bouamama, “Extension of the bond graph causali ty inversion method for fault detection and isolation: application to a mechatronic system*,” I FAC Proceedings Volumes, vol. 45, no. 20, pp. 150–155, Jan. 2012.

[108] M.-S. Jha, G. Dauphin-Tanguy, and B. Ould-Bouamama, “Robust fault detection with Interval Valued Uncertainties in Bond Graph Framework,” Control Engineering Practice, vol. 71, pp. 61–78, Feb. 2018.

[109] O. Prakash, A. K. Samantaray, and R. Bhattacharyya, “Optimal Adaptive Threshold a nd Mode Fault Detection for Model-Based Fault Diagnosis of Hybrid Dynamical Systems,” F ault Diagnosis of Hybrid Dynamic and Complex Systems, pp. 45–78, 2018.

[110] I. Abdallah, A.-L. Gehin, and B. Ould Bouamama, “On-line robust graphical diagnose r for hybrid dynamical systems,” Engineering Applications of Artificial Intelligence, vol. 69, pp. 36–49, Mar. 2018.

[111] M. Liao, L. Dong, L. Jin, and S. Wang, “Study on Rotational Speed Feedback Torque Control for Wind Turbine Generator System,” 2009 International Conference on Energy and E nvironment Technology, 2009.

[112] I. Colak, H. I. Bulbul, S. Sagiroglu, and M. Sahin, “Modeling a permanent magnet syn chronous generator used in wind turbine and the realization of voltage control on the model w ith artificial neural networks,” 2012 International Conference on Renewable Energy Research and Applications (ICRERA), Nov. 2012.

[113] A. E. Badoud, Y. Ayat, and S. Mekhilef, “Development and experimental validation o f novel robust MPPT controller based on bond graph and fuzzy logic for PV system under va riable weather conditions,” International Transactions on Electrical Energy Systems, Sep. 202 1.

[114] J. Badeda, M. Huck, D. U. Sauer, J. Kabzinski, and J. Wirth, “Basics of lead–acid batt ery modelling and simulation,” Lead-Acid Batteries for Future Automobiles, pp. 463–507, 20 17.

Tab a.1. Sources parameters of the hydrogen production platform.

$R_s = 0.004\Omega$	$R_{sh} = 1000\Omega$
$N_s = 54$ (Cells number)	$N_p = 2$ (Number of panels connected in parallel)
$C_{dl} = 55Ah$	$R_i = 6.5 \cdot 10^{-3}\Omega$
$R_{dl} = 0.002$	$N_b = 2$ (number of batteries connected in series)
$L_d = L_q = 0.25mH$	$R_d = R_q = 3.01\Omega$
$p = 3$	$\lambda = 2\,\mathrm{Wb}$
$f = 0.0016 \frac{N \cdot m \cdot s}{Rad}$	$J = 0.02 \frac{N \cdot m \cdot S^2}{Rad}$